Studies of coated and polycrystalline superconductors using the time-dependent Ginzburg-Landau equations

George James Carty

A thesis submitted in partial fulfilment of the

requirements for the degree of Doctor of Philosophy

Department of Physics, University of Durham

2006

Studies of coated and polycrystalline superconductors using the time-dependent Ginzburg-Landau equations

Abstract

Time-dependent Ginzburg-Landau equations are used to model 2D and 3D systems containing both superconductors and normal metals, in which both T_c and normal-state resistivity are spatially dependent. The equations are solved numerically using an efficient semi-implicit Crank-Nicolson algorithm. The algorithm is used to model flux entry and exit in homogenous superconductors with metallic coatings of different resistivities. For an abrupt boundary there is a minimum field of initial vortex entry occurring at a kappa-dependent finite ratio of the normal-state resistivities of the superconductor and the normal metal. Highly reversible magnetization characteristics are achieved using a diffusive layer several coherence lengths wide between the superconductor and the normal metal.

This work provides the first TDGL simulation in both 2D and 3D of current flow in polycrystalline superconductors, and provides some important new results both qualitative and quantitative. Using a magnetization method we obtain J_c for both 2D and 3D systems, and obtain the correct field and kappa dependences in 3D, given by $F_p = 3.6\times10^{-4}\frac{B_{c2}^{5/2}(T)}{\mu_0\kappa^2}\sqrt{\frac{2\pi}{\phi_0}}b^{1/2}(1-b)^2$. The pre-factor is different (about 3 to 5 times smaller) from that observed in technological superconductors, but evidence is provided showing that this prefactor depends on the details of H_{c3} effects at the edges of superconducting grains. In 2D, the analytic flux shear calculation developed by Pruymboom in his thin-film work gives good agreement with our computational results.

Visualization of $|\psi|^2$ and dissipation (including movies in the 2D case) shows that in both 2D and 3D, J_c is determined by flux shear along grain boundaries. In 3D the moving fluxons are confined to the grain boundaries, and cut through stationary fluxons which pass through the grains and are almost completely straight.

Thesis Contents

Declaration and Copyright

I hereby declare that the work contained within this thesis is my own original work and northing that is the result of collaboration unless otherwise stated. No part of this thesis has been submitted for a degree or other qualification at this or any other university.

G. J. Carty

May 2006.

Acknowledgements

I would like to thank the many people who have provided me with much valuable assistance during the course of my research. First of all, I must thank Damian Hampshire for being an excellent supervisor, with all that this implies. Particular thanks must also be given to Duncan Rand for his many hours of assistance in dealing with various problems I have come across when writing and debugging Fortran programs, and also for solving miscellaneous Unix-related problems. Masahiko Machida provided the original Fortran 77 code which was the first step in the computational work, and Thomas Winiecki provided invaluable assistance in making computational use of the new, more efficient semi-implicit algorithm, which proved vital throughout my research. Thanks to the fellow members of my research group: David Taylor, Nicola Morley and Matthew King who have helped in many different ways , and to the other support staff in Durham such as Lydia Heck, David Stockdale, Gerry Fuller, Norma Twomey and others for their most valuable assistance. I must also give special thanks to my parents for keeping me going during the frequent occasions when I have encountered difficulties during the course of my work.

Financial support from the Durham University Scholarship Fund and access to computing facilities both from the University of Durham IT Service and from Computer Services for Academic Research at the University of Manchester are also acknowledged.

Publications

Numerical studies on the effect of normal metal coatings on the magnetization characteristics of type-II superconductors

G. Carty, M. Machida, and D. P. Hampshire, Phys. Rev. B **71**, 144507 (2005)

Conferences and courses attended

Conferences (with poster presentations)

1. SET for Britain, House of Commons, London, November 2005.
2. Annual Superconductivity Group Conference, University of Bristol, June 2005
3. IoP meeting on Applied Superconductivity, Birmingham, November 2004
4. Annual Superconductivity Group Conference, University of Cambridge, January 2004
5. CMMP, University of Belfast, April 2003
6. Annual Superconductivity Group Conference, University of Cambridge, January 2003
7. CMMP, Brighton, April 2002

Courses

Superconductivity Winter School, University of Cambridge, January 2002

1 Introduction

1.1 Overview of superconductor technology

Superconductivity is a fascinating phenomenon by which the electrical resistance of some materials suddenly disappears when they are cooled below a critical temperature T_c. Superconductivity is interesting from a fundamental physics perspective as it is an example of a macroscopic quantum state.

Nobel Prizes have been won in the field of superconductivity in four years. In 1972, John Bardeen, Leon Cooper and J. Robert Schrieffer won the Nobel Prize for their microscopic theory of superconductivity[1] and in the following year Ivar Giaever won a quarter of the prize and Brian David Josephson half of the prize, both for their work on superconducting tunnel junctions. The discovery of the high-T_c cuprate materials won the 1987 Nobel Prize for Johannes Bednorz and Karl Müller[2], and in 2003, Alexei Abrikosov and Vitely Ginzburg won the Nobel Prize for their crucial studies of the flux-line lattice in type-II superconductivity.

Devices making use of these macroscopic quantum effects, such as the SQUID (superconducting quantum interference device) have interesting characteristics and applications. However, by far the most important application of superconductivity is in the production of superconducting magnets, which take advantage of the low resistivity of superconductors in order to create powerful electromagnets which produce little heat and can produce much higher magnetic fields than conventional electromagnets. Some large-scale research equipment such as particle accelerators and fusion reactor prototypes can only be constructed using superconducting magnets.

Since superconductors can carry current with negligible applied EMF, it is possible to operate superconducting magnets in a 'persistent mode' where the field is more stable than that produced by any conventional electromagnet. This extreme stability of the magnetic field is

crucial for medical magnetic resonance imaging (MRI) equipment, which is the main commercial application of superconductors: of a worldwide superconductivity market in 2000 of €2.37bn[3], €1.9bn was MRI equipment. Nuclear magnetic resonance (NMR) equipment used in analytical chemistry is a related application.

The discovery of the high-T_c cuprates led to an explosion of interest in superconductivity. As these new materials could be cooled using liquid nitrogen – this has a specific heat capacity more than an order of magnitude higher than that of liquid helium at 4.2K and costs only 12p per litre (compare £3.50 per litre for liquid helium), many possibilities were seen for new applications not cost-effective with traditional superconductors. These include fault current limiters, transformers, motors and generators, and superconducting magnetic energy storage (SMES). However, most of these applications remain at the experimental stage. Magnesium diboride, a common compound only discovered to be superconducting in 2001, has also aroused a great deal of interest despite not superconducting at liquid nitrogen temperatures, as its T_c is nevertheless far higher than any other non-cuprate material, and as it lacks the cuprate materials' anisotropy and grain boundary problems.

1.2 Aim of the work

The main concern when developing superconductors for large-scale applications such as superconducting magnets is the critical current density J_c in high magnetic fields. A higher J_c means that less material is required in order to build a given superconducting magnet, and allows higher fields to be achieved.

The ultimate theoretical limit for the current-carrying capacity of a superconductor is the *depairing current density* J_D – this is the current at which the kinetic energy of the Cooper pairs exceeds their binding energy, causing them to break up. However, superconducting magnets are made of Type II superconductors, and operate in the mixed state. This results in the formation of fluxons in the material – unless these fluxons are strongly pinned within the

material they will move and cause energy loss at a current far below J_D. For most superconductors used in magnet applications, J_c is about three orders of magnitude below J_D.

The ultimate aim of the work is to use the time-dependent Ginzburg-Landau equations to find a way to calculate the J_c values for superconductors with realistic flux pinning behaviour – this will lead to greater understanding of flux behaviour in superconductors, invaluable for future materials development aimed at improving superconductor performance. The work focuses on pinning of fluxons by grain boundaries in polycrystalline superconductors, as this is the dominant pinning mechanism in many practical superconductors, including both the A15 materials (eg Nb_3Sn, Nb_3Al) and the high-T_c cuprates. It is suggested[4] that the boundaries between grains dominate the current-carrying capacity of these materials, and that fluxons bend in order to remain within these boundaries.

Modelling a granular superconductor using the TDGL equations is a formidable challenge. In addition, features of the flux line structure in polycrystalline materials – such as flux line bending – cannot occur in 2D, necessitating a full 3D approach to the problem. 3D simulations are computationally expensive and therefore had only previously been used for qualitative simulations. In addition, an acceptable means of modelling non-superconducting materials within the context of the TDGL calculation, and a way of minimizing the effects of surfaces on the calculation results, are required. For these reasons, several simpler two-dimensional problems have been solved before attempting the main problem.

1.3 Thesis Structure

Chapter 2 gives a general introduction to the basics of superconductivity – it explains the fundamental properties of superconductors and briefly introduces the computational modelling – in more detail, and gives some examples of analytical calculations relating to surface barriers and to SNS junctions. The various considerations involved in setting up an efficient time-dependent Ginzburg-Landau computation are discussed in Chapter 4.

Before attempting to model a full 3D granular superconductor it is necessary to ensure that it is the bulk superconductor, rather than its surfaces, which are being measured. This is especially important as the exactness of computation may expose anomalies not seen in experimental work, and also due to the limited size of the systems for which computation is feasible.

Chapter 5 investigates the magnetization of homogenous 2D superconductors with various coatings. These showed that in order to obtain a reversible magnetization characteristic, eliminating the effects of the Bean-Livingston surface barrier (see Section 3.3) not only must the superconductor be coated with a normal metal, but a weakly superconducting transition region several coherence lengths wide must also be added. The effect of adding a normal layer encircling an inner superconductor within an outer superconductor is also investigated, with computational data compared with a calculation based on a Dew-Hughes pinning model (Section 5.5.4). Chapter 6 combines the Bean-Livingston principle of a surface barrier to flux entry caused by an 'anti-fluxon' on the other side of the barrier with the Clem model. This corrects the value of the initial penetration field, which was a factor of $\sqrt{2}$ out in the original Bean-Livingston calculation. The calculation is then extended to the mixed-state system, correctly predicting the magnetization irreversibility of the superconductors modelled computationally in the previous chapter.

Chapter 7 investigates the use of the TDGL model for modelling current flow through 2D junctions with and without an external applied field, while Chapter 8 moves onto the final problem – the critical current of granular superconductors. The structure of the simulated material is explained here, including the use of periodic boundary conditions, and consistency tests are presented for a single 2D test system. Chapter 9 then considers the effects on J_c in the 2D system of changing grain size, kappa, grain boundary resistivity and temperature, and compares a 2D system with a 3D system. Finally, chapter 10 discusses possible future developments from the presented work.

2 Basics of Superconductivity

2.1 Introduction

This chapter provides a review of the fundamental principles of superconductivity and the basic elements of the principle theories of superconductivity. Section 2.2 introduces the two basic defining properties of superconductors – zero resistivity and the Meissner effect, while section 2.3 gives selected examples of conventional and unconventional superconducting materials. London, BCS and Ginzburg-Landau theories are summarized in section 2.4, while section 2.5 gives some of the basic results stemming from Ginzburg-Landau theory. Finally section 2.6 discusses the factors which limit the current capacity of Type-II superconductors.

2.2 Fundamental properties of superconductors

The first material discovered to be a superconductor was mercury – during his experiments with liquid helium, Onnes[5] discovered that as the temperature was lowered through 4.19 K, its resistance dropped abruptly to zero. This **complete absence of dc electrical resistivity** below the superconducting critical temperature T_c and in small magnetic fields is the first fundamental property of superconductors – persistent current experiments[6] have fixed an upper resistivity limit 16 orders of magnitude lower than for copper at room temperature, allowing current to circulate in a superconducting ring for over 100,000 years!

The **Meissner effect**[7] is the second fundamental property of superconductors. When a superconductor in a small magnetic field is cooled below T_c, the magnetic flux is completely expelled from the bulk of the material. The material is therefore perfectly diamagnetic. The way superconductors respond to higher magnetic fields allows superconductors to be divided into two classes – **type-I** and **type-II** superconductors. Figure 2.1 demonstrates the difference in the magnetic properties.

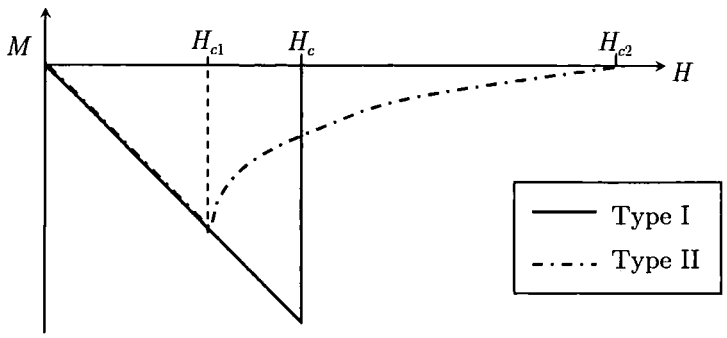

Figure 2.1: Reversible magnetization of type-II and type-II superconductors

Most superconducting elements are **Type-I superconductors**. When the magnetic field applied to a Type-I superconductor is increased, the material remains in the Meissner state until the thermodynamic critical field H_c is reached. At this point, the magnetic flux penetrates the sample completely – the magnetic moment of the sample becomes zero – and the resistivity returns to its normal-state value.

In **Type-II superconductors** – most alloys and compounds, including all commercially-used superconductors, are of this type – the material remains in the Meissner state up to the lower critical field H_{c1}. Above this field magnetic flux penetrates the sample in the form of quantized flux lines, each carrying a magnetic flux of $\phi_0 = h/2e$, leading to a mixed state of normal and superconducting regions. The sample remains in the mixed state until the upper critical field H_{c2} is reached, at which point the entire material becomes normal.

2.3 Superconducting materials

2.3.1 Elemental superconductors

Table 2.1 lists the properties of some superconducting elements – note that almost all type-I superconductors are elements.

Material	T_c (K)	Type	$B_c(T=0)$ (mT)
Hg	4.15	I	41
Al	1.2	I	10.5
Pb	7.2	I	80
Sn	3.72	I	30.5
Nb	9.2	II	$B_{c2} = 206$ mT

Table 2.1 – Properties of superconducting elements[8]

2.3.2 Other conventional superconductors

The term *conventional superconductors* is usually taken to mean superconductors which display *s*-wave pairing and the isotope effect, consistent with BCS theory. **Table 2.2** gives examples of alloy and compound conventional superconductors which are used commercially or have aroused particular interest among the scientific community.

Material	T_c (K)	Notes
$Nb_{0.6}Ti_{0.4}$ (alloy)	9.8	Most commonly used commercial superconductor (best performing ductile material)
Nb_3Sn	18.0	Known collectively as *A15* superconductors, after their crystal structure. These are used in applications where H_{c2} values higher than that of NbTi are required (eg prototype fusion reactors)
Nb_3Al	18.8	
V_3Si	17.1	
Nb_3Ge	23.2	
MgB_2	39	Discovered 2001. Highest-T_c conventional superconductor
$PbMo_6S_8$	15.3	Potentially higher B_{c2} than A15 materials

Table 2.2 – Conventionally superconducting alloys and compounds

2.3.3 Cuprate superconductors

The **cuprate superconductors** are a class of materials containing planes of copper and oxygen atoms. These materials are all type-II superconductors with extremely high κ values, and are important as their T_c values tend to be much higher that those of conventional superconductors, opening up a new range of possible applications.

An important fundamental aspect of the cuprates is that the electron pairing responsible for superconductivity is *d*-wave, rather than *s*-wave as in conventional superconductors. This

means that the Cooper pairs (see section 2.4.2) have an angular momentum quantum number $l = 2$, rather than the $l = 0$ predicted by BCS theory. This means that the energy gap Δ becomes a function of the wavevector $\mathbf{k}$ and changes sign when $\mathbf{k}$ is rotated through an angle of $\pi/2$

$$\Delta_{d-wave}\left(\hat{\mathbf{k}}\right) = \frac{\hat{\Delta}}{\sqrt{2}}\left(\hat{k}_x^2 - \hat{k}_y^2\right) \tag{2.1}$$

Table 2.3 gives information about some of these materials – note that the oxygen content of some of these materials is non-stoichiometric.

Material	T_c (K)	Notes
$La_{2-n}Sr_nCuO_4$	38	First cuprate superconductor to be discovered (1986). Simple structure
$YBa_2Cu_3O_{7-\delta}$	92	First material to superconduct at liquid nitrogen temperature (77 K). Bulk J_c limited by granular weak links
$Bi_2Sr_2Ca_2Cu_3O_{10-\delta}$	110	Most popular candidate material for tape conductors. Weak pinning due to 2D layered structure
$HgBa_2Ca_2Cu_3O_{8-\delta}$	132.5	Highest recorded T_c, but chemically unstable and toxic due to mercury content

Table 2.3 – high-T_c cuprate materials[9]

2.3.4 Other unconventional superconductors

Although the cuprates are the only technologically important class of unconventional superconductors, there are other unconventional superconductors which are interesting from a fundamental physics perspective – some examples are listed in Table 2.4.

Material	T_c (K)	Notes
Sr_2RuO_4	1.4	Electron pairing in this material is p-wave
UPt_3	0.45	These are *heavy-fermion* materials – m^* in these materials is
URu_2Si_2	1.5	hundreds of times the free electron mass due to s-f hybridization

Table 2.4 – Non-cuprate unconventional superconductors

2.4 Summary of Superconductivity Theories

2.4.1 London theory

The London theory[10], formulated shortly after discovery of the Meissner effect, was one of the first attempts to describe the behaviour of a superconductor mathematically. The London equations link the electric and magnetic fields **E** and **B** to the local current density **J**:

$$\frac{\partial \mathbf{J}}{\partial t} = \frac{\mathbf{E}}{\mu_0 \lambda_L^2} \tag{2.2}$$

$$\nabla \times \mathbf{J} = -\frac{\mathbf{B}}{\mu_0 \lambda_L^2}. \tag{2.3}$$

(2.2) is an 'acceleration equation' which allows a current to persist even without a driving electric field, while (2.3), when combined with Ampère's law, leads to the Meissner effect. λ_L is the London penetration depth, and is the characteristic decay length of the magnetic field on entering a superconductor.

2.4.2 BCS theory

BCS theory[1] explains the fundamental microscopic mechanism behind superconductivity. It is based on an electron-electron attraction, mediated by phonons in the crystal lattice. Electrons are bound into *Cooper pairs* – each electron has equal and opposite momentum. Cooper pairs cannot interact with the lattice and change momentum, and can therefore pass through the material without resistance. There is an *energy gap* Δ which divides the Cooper pairs from the unpaired electrons[1]

$$\Delta = 2\hbar\omega_D \exp\left(-\frac{1}{N(0)V}\right) \tag{2.4}$$

where ω_D is the angular Debye frequency, $N(0)$ is the density of states at the Fermi energy and V is the coupling energy. The critical temperature is given by[1]

$$T_c = 1.14\frac{\hbar\omega_D}{k_B}\exp\left(-\frac{1}{N(0)V}\right) \tag{2.5}$$

The electrons are bound over the BCS coherence length[1] ξ_0:

$$\xi_0 = 0.18\frac{\hbar v_F}{k_B T_c} \tag{2.6}$$

where v_F is the Fermi velocity. BCS theory also predicts a sudden rise in the electronic specific heat on entering the superconducting state, along with its sharp exponential decrease at low temperatures. The original BCS theory assumed that the phonon-mediated electronic interaction was weak. A more general microscopic theory was later developed[11] which dealt with strong phonon coupling. This strong-coupling theory was vital to explain the behaviour of conventional superconductors with the higher T_c values[12].

2.4.3 Ginzburg-Landau theory

The Ginzburg-Landau theory of superconductivity[13] is a phenomenological theory more general than the London theory – it allows spatial variation in superconductivity to be considered. It is descended from the Landau theory of second-order phase transitions, but uses a complex order parameter ψ such that $|\psi|^2$ equals the density of superconducting electrons. The theory is based on two coupled partial differential equations:

$$\alpha\psi + \beta|\psi|^2\psi + \frac{1}{2m_e}\left(-i\hbar\nabla - 2e\mathbf{A}\right)^2\psi = 0 \tag{2.7}$$

$$\mathbf{J}_e = -\frac{ie\hbar}{m_e}\left(\psi^*\nabla\psi - \psi\nabla\psi^*\right) - \frac{4e^2}{m_e}|\psi|^2\,\mathbf{A} \tag{2.8}$$

Ginzburg-Landau theory predicts that a superconductor should have two characteristic lengths:

$$\text{Coherence length } \xi = \frac{\hbar}{\sqrt{2m_e|\alpha|}} \tag{2.9}$$

$$\text{Penetration depth } \lambda = \sqrt{\frac{m_e\beta}{4e^2\mu_0|\alpha|}} \tag{2.10}$$

The Ginzburg-Landau parameter $\kappa = \lambda/\xi$. This ratio distinguishes Type-I superconductors, for which $\kappa \leq 1/\sqrt{2}$, from type-II superconductors which have higher κ values.

Two critical fields are also given by Ginzburg-Landau theory, the **thermodynamic critical field** H_c where the Meissner state and the normal state have equal energies, and the **second-order critical field** H_{c2}. In type-II superconductors, H_{c2}, the higher of these fields, is the maximum field at which superconductivity is possible, while in type-I superconductors, H_c is higher and is the maximum field for superconductivity, with H_{c2} being the limiting field for the metastable normal phase.

2.5 Results from Ginzburg-Landau theory

2.5.1 Critical fields

At the critical field H_c, the Gibbs free energies for superconducting and normal phases are equal. For the superconducting phase $\mathbf{B} = 0$, and for the normal phase $\psi = 0$:

$$\Rightarrow \qquad H_c = \frac{|\alpha|}{\sqrt{\mu_0 \beta}} \tag{2.11}$$

In Type I superconductors H_c is the critical field at which superconductivity is destroyed – ψ drops abruptly to zero in a first-order phase transition.

Type II superconductors undergo a second order transition into the normal state at H_{c2}. Immediately below H_{c2} ψ is low everywhere, and the 1st GL equation can be linearized. The magnetization can also be assumed to be negligible. Using the $\mathbf{A} = (0, \mu_0 H_0 x, 0)$ gauge for the vector potential gives:

$$\Rightarrow \qquad -\frac{\hbar^2}{2m_e}\frac{\partial^2 \psi}{\partial x^2} + \frac{1}{2m_e}\left(-i\hbar\frac{\partial}{\partial y} - 2e\mu_0 H_0 x\right)^2 \psi - \frac{\hbar^2}{2m_e}\frac{\partial^2 \psi}{\partial x^2} = |\alpha|\psi \tag{2.12}$$

The order parameter is factorized – $\psi = f(x)\ \exp\ i(k_y y + k_z z)$

$$\Rightarrow \qquad -\frac{\hbar^2}{2m_e}\frac{d^2 f}{dx^2} + \frac{1}{2m_e}\left(\hbar k_y - 2e\mu_0 H_0 x\right)^2 f = \left(|\alpha| - \frac{\hbar^2 k_z^2}{2m_e}\right) f \tag{2.13}$$

It can be noted that any eigenvalue is highly degenerate as k_y does not enter into the eigenvalue. Different k_y values correspond to different centres x_0 for the eigenfunction $f(x)$.

Using the substitution $x_0 = \dfrac{\hbar k_y}{2e\mu_0 H_0}$ we obtain

$$-\frac{\hbar^2}{2m_e}\frac{d^2 f}{dx^2} + \frac{2e^2\mu_0^2 H_0^2}{m_e}\left(x_0 - x\right)^2 f = \left(|\alpha| - \frac{\hbar^2 k_z^2}{2m_e}\right) f \tag{2.14}$$

The asymmetry between the x and y co-ordinates in this equation results from the asymmetric gauge used for $\mathbf{A}$. Use of a symmetric gauge would have resulted in a symmetric equation. This equation is a form of the quantum harmonic oscillator equation $\left(-\dfrac{\hbar^2}{2m_e}\dfrac{d^2}{dx^2} + \dfrac{m_e\omega^2 x^2}{2}\right)\psi = E\psi$, which has the general solution $E = (n + \tfrac{1}{2})\hbar\omega$. This gives the expression:

$$|\alpha| - \frac{\hbar^2 k_z^2}{2m_e} = (n + \tfrac{1}{2})\left(\frac{2e\hbar\mu_0 H_0}{m_e}\right) \tag{2.15}$$

However, instead of finding the eigenvalue, the value of H_0 is what is required. H_{c2} is the largest possible value of H_0 (which occurs at $n = k_z = 0$):

$$H_{c2} = \frac{m_e |\alpha|}{e\hbar\mu_0} = \frac{\phi_0}{2\pi\mu_0\xi^2} \tag{2.16}$$

An even higher critical field H_{c3} can also exist in superconductors with certain types of boundary. Between H_{c2} and H_{c3} (which can be as high as $1.69H_{c2}$), superconductivity does not exist in the bulk material, but it does exist within a surface sheath about a few coherence lengths thick.

2.5.2 Abrikosov lattice

In homogenous type-II superconductors the fluxons usually tend to arrange themselves into a regular flux-line lattice. The magnetization of such a lattice can be determined using a calculation based on a series wavefunction[14], which uses perturbative analysis of a periodic solution to the Ginzburg-Landau equations near H_{c2} to give the magnetization

$$M = -\frac{(H_{c2} - H_0)}{(2\kappa^2 - 1)\beta_A} \tag{2.17}$$

where

$$\beta_A = \frac{\langle |\psi|^4 \rangle}{\left(\langle |\psi|^2 \rangle\right)^2} \tag{2.18}$$

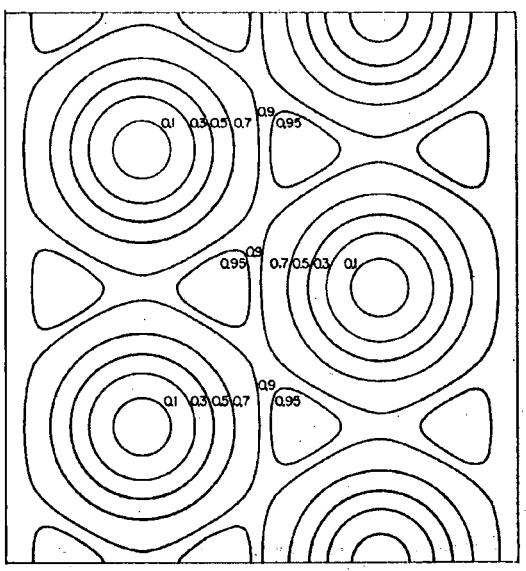

Figure 2.2: The Abrikosov flux-line lattice[15]

The free energy decreases as β_A decreases – lower β_A values are more energetically favourable. To calculate β_A, it is necessary to use the complex exponential integral

$$\int_{-\pi/k}^{\pi/k} \exp(iky(n-m))\,dy = \frac{2\pi}{k}\delta(n-m) \tag{2.19}$$

and the integral substitution

$$\int_{x=-\frac{k\xi^2}{2}}^{x=\frac{k\xi^2}{2}} \sum_{n=-\infty}^{\infty} \exp\left(-\frac{\left(x-nk\xi^2\right)^2}{\xi^2}\right)dx = \sum_{n=-\infty}^{\infty} \int_{\theta=(-\frac{1}{2}-n)k\xi^2}^{\theta=(\frac{1}{2}-n)k\xi^2} \exp\left(-\frac{\theta^2}{\xi^2}\right)d\theta = \xi\sqrt{\pi} \tag{2.20}$$

The original Abrikosov calculation[14] set all c_n's equal, giving a square lattice with $\beta_A = 1.18$. An improved calculation by Kleiner[15], set $c_{n+2} = c_n$, $c_{n+1} = ic_n$ – this lead to a triangular lattice with $\beta_A = 1.1596$. This triangular arrangement, shown in Fig. 2.2, is the one most commonly observed experimentally.

2.5.3 Relation between GL and BCS theory

The Ginzburg-Landau theory was originally derived on a purely phenomenological basis. However Gor'kov rewrote the microscopic BCS theory in terms of Green's functions[16]. In the $T \approx T_c$ limit, this was expanded in powers of ψ, leading to the Ginzburg-Landau equations – **Table 2.5** gives ξ and λ in the clean[17] and dirty[18] limits:

	Clean limit	Dirty limit
Ginzburg-Landau coherence length	$\xi = \sqrt{\frac{7\zeta(3)\hbar^2 v_F^2}{48k_B^2 T_c(T_c - T)}}$	$\xi = \sqrt{\frac{\pi\hbar v_F^2 \tau}{24k_B(T_c - T)}}$
Penetration depth	$\lambda = \sqrt{\frac{7m_e\zeta(3)}{2\mu_0 \mathsf{N}\ e^2\pi^2\left(\frac{T_c - T}{T_c}\right)}}$	$\lambda = \sqrt{\frac{7m_e\hbar\zeta(3)}{4\mu_0 \mathsf{N}\ e^2\tau\pi^3 k_B(T_c - T)}}$

Table 2.5 - Ginzburg-Landau lengths in terms of microscopic parameters. ζ is the Riemann zeta function, m_e is the electronic mass, T is temperature, v_F is Fermi velocity and $\mathcal{N}$ is electron number density.

2.6 Current flow in superconductors

2.6.1 Depairing and critical currents

The theoretical maximum possible current density in a superconductor is the **depairing current** J_D. This is defined as the current density for which equals the kinetic energy of the super-electrons. If any further increase in current is attempted, the super-electrons are destroyed and the material reverts to the normal state.

The standard expression for the depairing current at zero applied field is[19]

$$J_D = \frac{2H_{c2}}{3\sqrt{3}\kappa^2\xi} = 0.385\frac{H_{c2}}{\kappa^2\xi} \tag{2.21}$$

This expression does not account for the fact that the super-electron number density is related to the London penetration depth λ_L not the Ginzburg-Landau penetration depth, nor does it allow for the effect of non-spherical Fermi surfaces. A more complete expression, this time for use in high magnetic fields, is[20,21]

$$J_D = \frac{1.65(H_{c2} - H)}{\kappa^2 S^* \xi}\sqrt{\frac{P}{2\pi}} \tag{2.22}$$

P is the purity parameter $\left(P = \frac{\xi_0}{l} \approx \frac{\lambda^2}{\lambda_L^2}\right)$ where ξ_0 is the BCS coherence length, l is the electron mean free path and λ_L and λ are the London and Ginzburg-Landau penetration depths respectively. S^* is the Fermi surface enhancement factor, which can range from 1 (NbTi) to 0.26 ($PbMo_6S_8$).

When a current flows through a superconductor in the mixed state, the fluxons are subject to a Lorentz force. Unless the fluxons are pinned securely they will move through the superconductor, resulting in dissipation of energy. For a maximum pinning force per unit volume of $\mathbf{F}_p$, one may define a current density J_c such that:

$$\mathbf{F}_p = \mathbf{J}_c \times \mathbf{B} \tag{2.23}$$

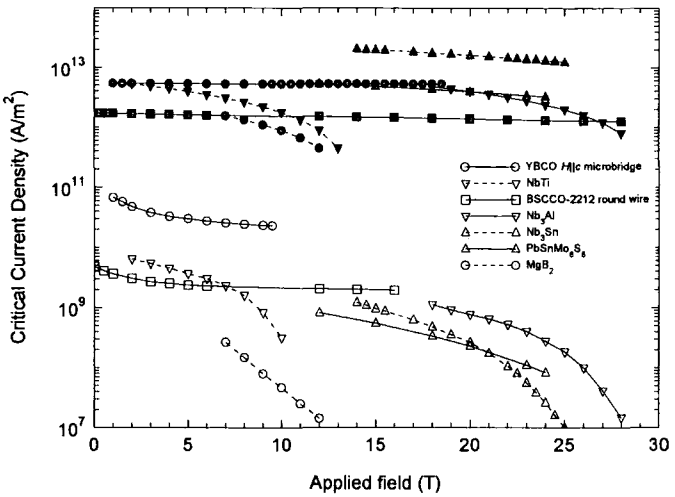

Figure 2.3: Depairing currents (solid symbols) calculated from (2.22) compared with experimentally measured J_c values (open symbols) for various superconductors at 4.2 K[22]

If J_c is exceeded, the fluxons are pulled out of their pinning sites and move through the material, dissipating energy. For this reason, J_c is referred to as the **critical current density**, and represents the practical maximum current density which can be passed through a superconductor. J_c is typically 2 or 3 orders of magnitude lower than J_D – Fig. 2.3 compares depairing and critical currents for several important superconducting materials.

2.6.2 Bean Critical State Model

The **Bean critical state model**[23,24] is a simple model for describing the macroscopic field and current distribution in an extreme type-II superconductor (negligible B_{c1}, negligible reversible magnetization) with pinned vortices. The basic assumption in the Bean critical state model is that any currents within the superconductor are equal in magnitude to the critical current density J_c – in the original model this was assumed to be field-independent.

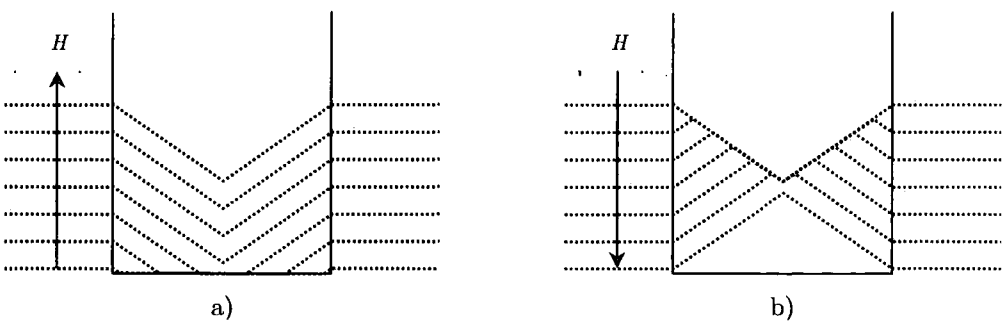

Figure 2.4: Field distribution according to the Bean critical state model for a) increasing and b) decreasing fields

When a field is applied to the sample flux penetrates a distance $d = B/\mu_0 J_c$. A high enough field will penetrate the sample completely. When the field is decreased the screening currents at the sample edge switch direction but still have the same density J_c. Flux remains trapped by the pinning sites in the superconductor even when the applied field is returned to zero – this is demonstrated in Fig. 2.4.

2.6.3 Microstructural defects affecting J_c

Bulk J_c is determined by material defects, which can have a range of properties[25]:

- Defects can be **non-superconducting regions** (δT_c pinning) or regions of **locally-enhanced resistivity** due to composition fluctuation, dislocations or martensite transformation ($\delta\kappa$ pinning).
- Defects can be characterized by their number of dimensions larger than the fluxon-fluxon-separation:
    - **Surface defects (2D):** – this is the most important form of defect in many practical superconductors such as the A15 materials, resulting from grain boundaries. The titanium ribbons which pin fluxons in NbTi, though differing in topology, are also 2-dimensional.
    - **Line defects (1D):** – this type of defect mostly results in neutron-irradiated samples, as the passage of the neutrons distorts the lattice and destroys superconductivity.
    - **Point pinning (0D):** – Although voids or impurity atoms could in theory act as point pinning sites, in practice the pinning from these is negligible as they are much smaller than the coherence length ξ. In practice, point pinning results mostly from non-superconducting precipitates, or from artificially-engineered non-superconducting particles.

The dimensionality of the defects in a material has important implications for the field dependence of J_c, as the way in which the defects interact with the fluxons is affected.

3 Review of Analytic Calculations

3.1 Introduction

This chapter of the thesis considers the important analytical calculation issues relating to my work. In section 3.2, various mechanisms are reviewed that consider the value of the critical current density J_c within a bulk superconductor. Pinning of isolated fluxons, the Kramer flux shear model, collective pinning, and grain boundary diffraction are all considered.

In the computational work it was important to ensure that the properties measured were those of the bulk superconductor, not of the surfaces – section 3.3 is a review of the literature on calculations related to the surface barrier in superconductors. Section 3.4 discusses how the Ginzburg-Landau equations can be derived from the Usadel equations to describe a system containing multiple or inhomogeneous materials for the computational work. This section is reasonably detailed as the equations included here are one of the most important components of the thesis. Finally, section 3.5 introduces the time-dependent Ginzburg-Landau equations.

3.2 Critical Current Calculations

3.2.1 Scaling laws

Scaling laws[26] are an empirical model for describing pinning in superconductors, based on several widely-found experimental observations:

- There is always a maximum in the $F_p(B)$ characteristic
- The reduced pinning force f_p is a function of reduced field $b = B/B_{c2}$ only
- Metallurgical treatment can affect the maximum pinning force and the reduced field at which it occurs.
- Metallurgical treatment does not affect the functional form of $F_p(b)$ at high b

The scaling law is normally written in the form[26]

$$F_p = \alpha(T,\varepsilon) b^p (1-b)^q \qquad (3.1)$$

where α is a function of temperature T and strain ε, p and q are constants, and b is the reduced field B/B_{c2}. For NbTi, p and q are both approximately equal to 1. For A15 class materials, Chevrel-phase superconductors and cuprates p is approximately 0.5 and q is approximately 2. This is due to the nature of the pinning in the materials.

3.2.2 Pin Breaking

If a superconductor contains regions which are totally non-superconducting, there is an energy gain δG per unit length resulting from a flux line passing through a non-superconducting region[27]

$$\delta G = \tfrac{1}{2}\mu_0 H_c^2 \pi \xi^2 \tag{3.2}$$

In a flux line lattice the average condensation energy is reduced by a factor $(1 - b)$ where b is the reduced field. In order to convert the energy gain into a pinning force, the expression must be divided by the characteristic distance over which the order parameter changes. For an abrupt S/N boundary the appropriate distance is found by differentiating $|\psi|^2$ with respect to distance[28]. This gave a pinning force per unit length of[27]

$$f_p = \frac{\pi (\tfrac{3}{4})^{1/4}}{4}\left(\frac{B_{c2}^{3/2}\phi_0^{1/2}}{\mu_0 (2\kappa^2 - 1)}\right) b^{1/2}(1-b) \tag{3.3}$$

For pinning by grain boundaries, the total length of pinned flux is S_v/a_0, where a_0 is the mean fluxon-fluxon spacing and S_v is the total area of grain boundary per unit volume correctly oriented to provide pinning. Summing to get the total pinning force gave

$$F_p = \frac{\pi (\tfrac{3}{4})^{1/2}}{4}\left(\frac{S_v B_{c2}^2}{\mu_0 (2\kappa^2 - 1)}\right) b(1-b) \tag{3.4}$$

For pinning sites which are superconducting but which have a shorter normal mean free path, pinning results from an enhancement of κ, and expression (3.3) should be multiplied by $\delta\kappa/\kappa$. Metallic conduction in the pinning sites induces superconductivity via the proximity effect[29] – this gives the expression (t = thickness of pinning boundary, assumed to be less than ξ)

$$F_p = \frac{\pi (\tfrac{3}{4})^{1/2}}{4}\left(\frac{S_v B_{c2}^2}{\mu_0 (2\kappa^2 - 1)}\right)\left(\frac{t}{\pi\xi}\right)^2 b(1-b) \tag{3.5}$$

3.2.3 Pin Avoidance – the Kramer Model

In some materials the pinning interaction is too strong for the Lorentz force to pull fluxons out of their pinning sites. The transport current is limited not by the strength of the individual pinning sites, but by the shearing of the flux-line lattice around the pinned fluxons. According to the Kramer model J_c is determined in the low-field regime by the weak pinning sites – the critical current is reached when the Lorentz force pushes fluxons from the weak sites. However, there are also strong pinning sites from which fluxons cannot be forced out by any fields below B_{c2}. In the high-field regime J_c is determined not by the forcing of fluxons out of pinning sites, but rather by the Lorentz force and fluxon-fluxon interactions producing a shear stress which exceeds the shear strength of the flux-line lattice. This allows the flux line lattice to shear around the strongly-pinned fluxons, and suggests that increasing the defect density will not increase J_c in the high-field regime. Kramer[30] predicted that F_p was given by

$$F_p = \frac{C_{66}}{12\pi^2 a_0 \left(1 - a_0/d\right)^2} \tag{3.6}$$

where d is the spacing of pinning sites. The shear modulus C_{66} of the flux-line lattice has a $(1 - b)^2$ dependence at high magnetic fields, suggesting that F_p is proportional $b^{1/2}(1 - b)^2$ dependence. Much work is done using Labusch's simple expression[31] for C_{66}, applicable in the high-field limit:

$$\lim_{b\to 1} C_{66} = 0.36\frac{B_{c2}^2}{4\mu_0\kappa^2}(1-b)^2 . \tag{3.7}$$

Using $a_0 = (1/3)^{1/4}\sqrt{\frac{\phi_0}{B}}$, we can combine (3.6) and (3.7) to get F_p in the large-grain limit:

$$\lim_{d\to\infty} F_p = 2.82\times 10^{-4}\frac{B_{c2}^{5/2}}{\mu_0\kappa^2}\sqrt{\frac{2\pi}{\phi_0}}b^{1/2}(1-b)^2 . \tag{3.8}$$

This expression has a reduced-field dependence consistent with many experimental results, but predicts a smaller magnitude for F_p than is usually observed.

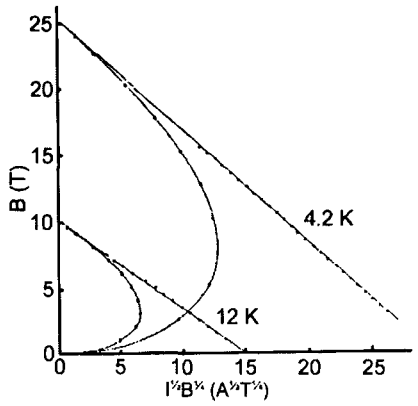

Figure 3.1: Pinning force from flux shear predicted from Kramer model with corrected C_{66} (curves), compared with experimental results in $(NbTa)_3Sn$ (fitted to straight lines)[32]

However, expression (3.7) is not correct across the entire field range. An accurate expression for C_{66}, valid in the entire field range, is[33]

$$C_{66} = \frac{B_{c2}^2}{8\mu_0\kappa^2} b(1-b)^2(1-0.29b)\exp\left(\frac{b-1}{3\kappa^2 b}\right). \tag{3.9}$$

When (3.9) is substituted into (3.6), the reduced-field dependence of F_p becomes very different[32] from that observed experimentally (see Fig. 3.1). Dew-Hughes[27] suggested that the Kramer expression for flux-shear F_p was wrong in the case of pinning by grain boundaries, and that the expression for F_p for grains of size D becomes

$$F_p = \frac{C_{66}}{\pi(D-a_0)} \tag{3.10}$$

This gives a dependence which can appear similar to the Kramer dependence, as shown in Figure 3.2. However, the form of the reduced-field dependence is critically dependent on grain size.

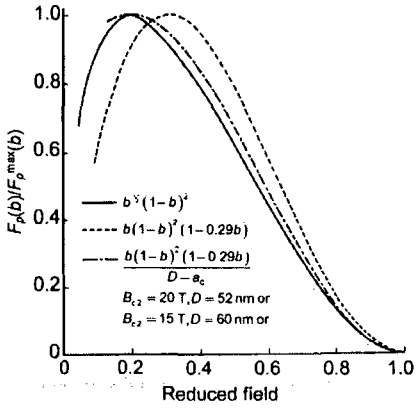

Figure 3.2: Pinning force from flux shear, as predicted by Dew-Hughes model[27]

3.2.4 Collective Pinning

The forces which pin individual fluxons can only be pinned in a simple manner in the low-field regime, where the fluxons are far enough apart that fluxon-fluxon interactions are negligible. However, the Kramer model of flux shear is oversimplified in that it assumes long-range order of the flux-line lattice and that the only forces acting on fluxons not held by pinning sites come from other fluxons. In addition, some superconductors exhibit a 'peak effect' in which J_c displays a narrow and very high maximum at a field close to H_{c2}. Neither individual flux pinning nor the flux shear model can account for such behaviour. The theory of collective pinning[34] solves this problem. In this theory it is postulated that short-range order exists within a volume V_c. When a current below J_c flows through the material the Lorentz force displaces the volume by a distance $< \xi$. If the density of pinning sites is n_p and f_p is the interaction force for a single pinning site, the critical current is given by[34]

$$J_c = \frac{f_p}{B}\sqrt{\frac{n_p}{V_c}} \tag{3.11}$$

In magnetic fields where the deformations of the flux-line lattice are elastic, the volume $V_c = R_c^2 L_c$, where R_c and L_c are the transverse and longitudinal lengths across which short-range order exists. R_c and L_c were given by

$$R_c = 4\sqrt{2}\,\frac{C_{66}^{3/2} C_{44}^{1/2} a_0^2}{n_p f_p^2} \tag{3.12}$$

and

$$L_c = \frac{8 C_{66} C_{44} a_0^2}{n_p f_p^2} \tag{3.13}$$

where C_{66} and C_{44} are respectively the shear and tilt moduli of the flux-line lattice, and a_0 is the fluxon-fluxon-separation. This gives the pinning force

$$F_p = \frac{n_p^2 f_p^4}{16 a_0^3 C_{44} C_{66}^2} \tag{3.14}$$

The Peak Effect: As H_{c2} is approached two physical effects cause the system to deviate from the behaviour given by expression (3.14). Both of these lead to the 'peak effect' of a high narrow maximum in J_c in the high-field regime:

- *Heavy concentration of pinning sites* ($n_p V_f \gg 1$), The effective field penetration depth $\lambda_{eff} = \lambda(1 - b)^{-1/2}$ becomes comparable to R_c. V_c decreases exponentially with field, thus increasing J_c. This stops when R_c reaches a value $\approx a_0$.
- *Sparse pinning sites* ($n_p V_f \ll 1$); The elastic moduli decrease in high fields, deformation from individual centre increases. When deformation becomes order of lattice parameter, deformation becomes plastic and J_c becomes equal to $f_p n_p / B$: this is much higher than the previous J_c value. The condition for this to occur is[34]

$$1 - b < \frac{f_p^2 \kappa^2}{a_0^4 C_{44} C_{66}}. \tag{3.15}$$

This condition allows materials to be separated into three categories:

- *(3.15) is true for all fields* (strong, sparse pinning sites): There is no peak effect, as the total pinning force can be found by a simple direct summation of the contributions of individual pins. F_p has a simple $b^p(1 - b)^q$ dependence.
- f_p *is moderately small and proportional to* $(1 - b)$: (3.15) is only true in very high or low fields, while in the intermediate field range weak pinning as described by (3.14) applies. Peaks are observed in the J_c characteristic both near H_{c2} and in the low-field regime.
- *(3.15) is always false (weak pinning sites)*: Weak collective pinning as described by (3.14) applies throughout the entire field range, and again there is no peak effect.

3.2.5 Weak Link Diffraction Model

The critical current in polycrystalline superconductors is often three or more orders of magnitude less than the depairing current J_D. An alternative model to investigate the origin of this restriction of J_c is to consider the weak links in a polycrystalline material, which in effect form a complex multi-junction SQUID[21]. In this model an exponential field-dependence of the critical current of a single junction[35,36] was assumed

$$J_c = J_D \exp\left(-\frac{B}{B_0}\right) \tag{3.16}$$

where J_D is the depairing current and B_0 is a field characteristic of the junction. In the dirty limit this field was given by[36]

$$B_0 = \frac{\phi_0}{2\pi d^2} \tag{3.17}$$

where d is the half-thickness of the junction, and for the clean limit it was[35]

$$B_0 = \frac{\phi_0}{4\pi\sqrt{3}dl} \tag{3.18}$$

where l is the mean free path. In addition to the effect of the junctions themselves, the consequences of diffraction also need to be considered. Taking the polycrystalline superconductor to be an N-junction SQUID, it was seen that in order to avoid any major peaks in J_c within the mixed state, H_1 should be set equal to B_{c2}. In the Meissner state, there are no fluxons in the sample and the current density is equal to the depairing current. This means that $H_1/N = H_{c1}$. This means that $J_c(B)$ could be approximated as[21]

$$J_c = J_D \frac{B_{c1}}{B_{c2}} = J_D \frac{\ln\kappa}{2\kappa^2} \tag{3.19}$$

Combining (3.16) with (3.19) and (2.22) gave a pinning force of the form

$$F_p = \frac{0.82\mu_0 B_{c2}^2 \ln\kappa}{\kappa^4 S^* \xi} \sqrt{\frac{P}{2\pi}} b(1-b)\exp\left(-\frac{B}{B_0}\right) \tag{3.20}$$

where P is the purity parameter and S^* is the Fermi surface enhancement factor.

3.3 Surface Barrier Calculations

3.3.1 Bean-Livingston calculation

When a type-II superconductor has a clean surface, the magnetic field initially penetrates the superconductor not at the lower critical field H_{c1}, but at a somewhat higher field H_p, which is of order H_c. This is due to the way in which the surface of the superconductor interacts with an entering fluxon[37]. Bean and Livingston assumed that no supercurrent passed through the boundary (this can be shown to be correct for an insulating boundary and for a highly-conductive boundary) – this boundary condition can be met by adding an antivortex at an equal and opposite displacement from the surface. This led to an image force which tends to attract the fluxon towards the surface, making flux entry more difficult. In an extreme type-II superconductor the interaction energy for a vortex and antivortex separated by a distance x » ξ was given by[37]

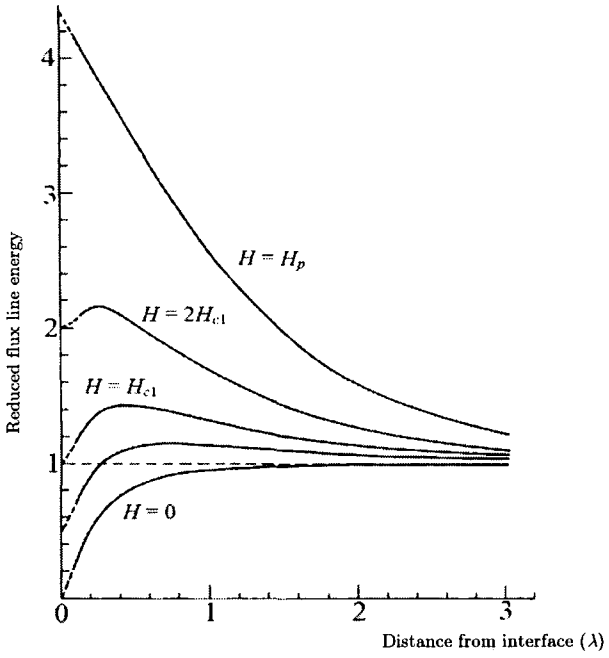

Figure 3.3: Dependence of line energy on position[37] for various fields at $\kappa = 10$

$$E(x) = -\frac{\phi_0^2}{4\pi\mu_0\lambda^2} K_0\left(\frac{2x}{\lambda}\right) \tag{3.21}$$

where K_0 is a modified Bessel function of the second kind. A second force results from the interaction with the screening current – the applied magnetic field H_0 penetrates the superconductor as $H = H_0 \exp(-x/\lambda)$ in the Meissner state. This field interacts with an entering fluxon, producing a repulsion which contributes to the total energy as $\phi_0 H_0 \exp(-x/\lambda)$. Note that as $x \to \infty$, this function decays more slowly than the image force expression.

The resultant total energy is dependent on the applied field H. At a field just above H_{c1}, flux entry is energetically favourable, but it is blocked until a field $H_p \approx H_c$ is reached. Figure 3.3 shows how the total energy depends on the depth of the fluxon inside the superconductor.

3.3.2 Matricon calculation

The Bean-Livingston calculation was based on the London theory, and is therefore only accurate in the extreme-type-II limit. Matricon carried out a more complete calculation of the initial vortex entry field using the one-dimensional Ginzburg-Landau equations[38]. Matricon's

calculation used the normalized units $\lambda = 1$ and $B_c = 1/\sqrt{2}$ (note that these are not the same as the normalized units from Chapter 4 onwards) giving the equations[38]

$$\left(\left|\hat{\psi}\right|^2 + A^2 - 1\right)\hat{\psi} + \frac{1}{\kappa^2}\frac{\partial^2\hat{\psi}}{\partial x^2} = 0 \tag{3.22}$$

$$\frac{d^2A}{dx^2} = \left|\hat{\psi}\right|^2 A \tag{3.23}$$

where $\hat{\psi}$ is the normalized order parameter, and A is the normalized vector potential in one dimension. Note that the local field $B = \frac{dA}{dx}$.

For a Meissner state, the required boundary conditions were $B = \mu_0 H$ and $\frac{d\hat{\psi}}{dx} = 0$ at $x = 0$ (the boundary of superconductor) and $A = B = 0$ at $x = +\infty$ (well within superconductor). The Matricon prediction for the initial vortex entry field was higher than the Bean-Livingston prediction because flux quantization makes it impossible for flux to directly enter a Meissner-state superconductor. Instead a small normal region must be created at the edge of the material (see Figure 3.4), allowing flux to enter – the difference in the initial vortex entry field predictions is the result of the extra energy input required to create this normal region.

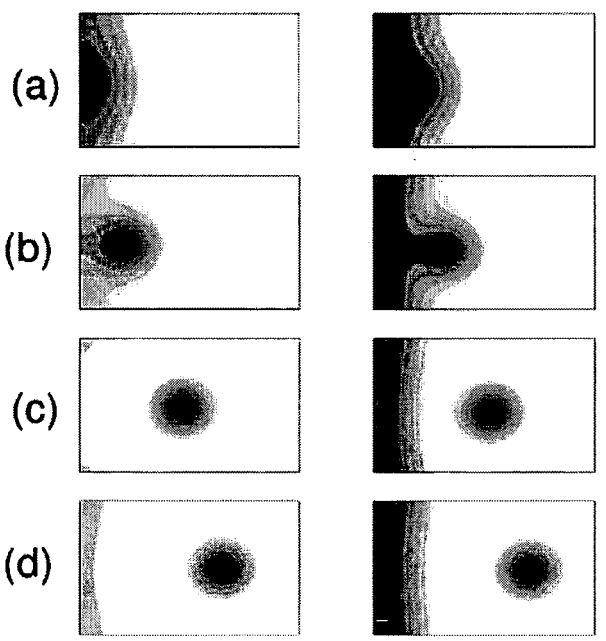

Figure 3.4: Entry of a fluxon from an insulator (left) and from a normal metal (right)[39]

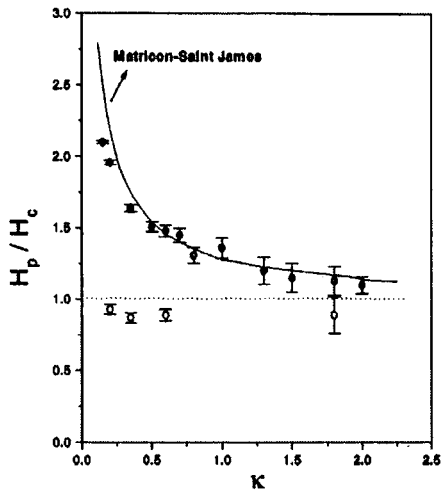

Figure 3.5: Comparison of Matricon analytic result (solid line) with computational results for insulating (solid circles) and metallic (open circles) boundaries[39]

The initial vortex entry field for a superconductor surrounded by insulator has been calculated numerically using the TDGL equations[39] – these computational results were broadly similar to Matricon's analytic results, as shown by Figure 3.5.

It may be noted that fluxons cannot enter into a perfect Meissner state along a straight edge due to symmetry considerations – in Kato's work[40] and in my own work the first fluxons enter near the corners, before more fluxons enter along the whole length of the edge. The fact that fluxons enter along the entire length of the edge once the first fluxons enter shows that the corners are needed only to break symmetry, and that the one-dimensional energy-based argument is valid. This is considered in more detail in Chapter 5.

3.4 Dirty-limit equations for a system with two materials

3.4.1 Introduction

Two factors must be taken into account when modelling a system which may contain different superconducting and non-superconducting materials:

- Determining the correct Ginzburg-Landau equations for all materials involved in the system.
- Determining appropriate boundary conditions for the order parameter and vector potential

It is more convenient to write the Ginzburg-Landau equations in a form using a normalized order parameter $\hat{\psi}$, equal to 1 within the Meissner state. In this form, the Ginzburg-Landau equations (2.7) and (2.8) can be rewritten as

$$\frac{1}{\xi^2}\left(\left|\hat{\psi}\right|^2 - 1\right)\hat{\psi} + \left(\frac{\nabla}{i} - \frac{2e}{\hbar}\mathbf{A}\right)^2 \hat{\psi} = 0 \tag{3.24}$$

$$\mathbf{J}_e = \frac{\hbar}{2e\mu_0\lambda^2}\mathrm{Re}\left(\hat{\psi}^*\left(\frac{\nabla}{i} - \frac{2e}{\hbar}\mathbf{A}\right)\hat{\psi}\right) \tag{3.25}$$

where ξ and λ are the coherence length and penetration depth. Analytic solutions of simple multimaterial systems in the dirty limit have often been solved using the Usadel equations[41]. However, the full Usadel theory is too complicated to be used for multidimensional, time-dependent numerical computation. In the appropriate temperature regime, the Usadel equations can be reduced to the Ginzburg-Landau equations – thus providing a method for using the Ginzburg-Landau equations to simulate systems containing more than one material in a way that is consistent with microscopic theory.

3.4.2 The Usadel equations

In 1958 Gor'kov rewrote the microscopic BCS theory[16] in terms of the Green's functions $F_\omega(t, \mathbf{r}, \mathbf{r}')$ and $G_\omega(t, \mathbf{r}, \mathbf{r}')$ and demonstrated that in a single material in the limit $T \approx T_c$, they reduce to the Ginzburg-Landau equations[17,18]. However, in the general case the Gor'kov equations were extremely difficult to handle because the Green's functions depended on two separate spatial points. The Eilenberger theory[42] greatly simplified the Gor'kov equations while maintaining all of the physics, by eliminating t and Fourier-transforming $\mathbf{r}'$ to give $\mathbf{k}$, then integrating over $|\mathbf{k}|$ (though the unit vector $\hat{\mathbf{k}}$ is retained). The Usadel equations[41] result from a further dirty-limit simplification of Eilenberger theory, which assumes isotropic behaviour. The $\hat{\mathbf{k}}$ dependence is expanded in spherical harmonics ignoring $l > 1$ terms, giving functions dependent on two variables only, $F_\omega(\mathbf{r})$ and $G_\omega(\mathbf{r})$:

$$\hbar\omega F_\omega(\mathbf{r}) - \frac{\hbar D}{2}\left(\nabla - \frac{2ie}{\hbar}\mathbf{A}\right)\left\{G_\omega(\mathbf{r})\left(\nabla - \frac{2ie}{\hbar}\mathbf{A}\right)F_\omega(\mathbf{r}) + \frac{F_\omega(\mathbf{r})}{2G_\omega(\mathbf{r})}\nabla\left|F_\omega(\mathbf{r})\right|^2\right\} = \Delta(\mathbf{r})G_\omega(\mathbf{r}) \tag{3.26}$$

$$\mathbf{J} = 2\pi e g(\varepsilon_F) D k_B T \sum_\omega \mathrm{Im}\left[F_\omega(\mathbf{r})\left(\nabla - \frac{2ie}{\hbar}\mathbf{A}\right)F_\omega^*(\mathbf{r})\right] \tag{3.27}$$

$$\Delta(\mathbf{r})\ln\frac{T_c}{T} = 2\pi k_B T \sum_\omega \left[\frac{\Delta(\mathbf{r})}{\hbar\omega} - F_\omega(\mathbf{r})\right] \tag{3.28}$$

$$G_\omega^2(\mathbf{r}) = 1 - \left|F_\omega^2(\mathbf{r})\right|. \tag{3.29}$$

Here D $\left(= \frac{1}{3}v_F^2\tau\right.$, with v_F the Fermi velocity and τ the scattering time$\left.\right)$ is the diffusivity of the material, Δ is the local BCS gap function, $g(\varepsilon_F)$ is the Fermi-level density of states and T is temperature. $F_\omega(\mathbf{r})$ is a pair condensation amplitude (analogous to ψ in Ginzburg-Landau theory), with $G_\omega(\mathbf{r})$ a related function. ω is a quantized frequency given by $\omega = (2n+1)\frac{\pi k_B T}{\hbar}$ $(n \in \mathbb{Z})$, originating the Fourier transformation of the original Gor'kov equations. Using the expression for resistivity

$$\rho = \frac{1}{2e^2 g(\varepsilon_F) D} \tag{3.30}$$

the following boundary conditions are obtained for an interface between two materials[43]:

$$F_\omega^{(1)} = F_\omega^{(2)} \tag{3.31}$$

$$\frac{\hat{\mathbf{n}}}{\rho_{(1)}}\cdot\left(\nabla - \frac{2ie}{\hbar}\mathbf{A}\right)F_\omega^{(1)} = \frac{\hat{\mathbf{n}}}{\rho_{(2)}}\cdot\left(\nabla - \frac{2ie}{\hbar}\mathbf{A}\right)F_\omega^{(2)}. \tag{3.32}$$

3.4.3 Reduction to the Ginzburg-Landau equations

First Ginzburg-Landau equation – linear form: The gradient term of the first Ginzburg-Landau equation was obtained by setting $F_\omega(\mathbf{r}) \approx 0$, $G_\omega(\mathbf{r}) = 1$ to linearize Usadel equation (3.26)[44]

$$\Rightarrow \qquad \hbar\omega F_\omega(\mathbf{r}) - \frac{\hbar D}{2}\left(\nabla - \frac{2ie}{\hbar}\mathbf{A}\right)^2 F_\omega(\mathbf{r}) = \Delta(\mathbf{r}). \tag{3.33}$$

The following *ansatz* was used to separate ω and $\mathbf{r}$[44].

$$\Delta(\mathbf{r}) = \left(\hbar\omega + \frac{\hbar D}{2\xi^2}\right)F_\omega(\mathbf{r}) \tag{3.34}$$

This *ansatz* was shown to be correct[45] in N/S bilayers where the superconductor is much thicker than the normal metal. This was substituted into (3.33):

$$\Rightarrow \qquad \left(\nabla - \frac{2ie}{\hbar}\mathbf{A}\right)^2 F_\omega(\mathbf{r}) + \frac{F_\omega(\mathbf{r})}{\xi^2} = 0 \tag{3.35}$$

This equation had the form of the linearized first Ginzburg-Landau equation, demonstrating that ξ in (3.34) is the coherence length. ξ was found by substituting (3.34) into (3.28) – Ψ is the digamma function[44]:

$$\ln\frac{T}{T_c} = \Psi(\tfrac{1}{2}) - \Psi\left(\frac{1}{2} + \frac{\hbar D}{4\pi k_B T \xi^2}\right) \tag{3.36}$$

In the Ginzburg-Landau regime ($T \approx T_c$) one can use a Taylor expansion to find ξ:

$$\frac{T}{T_c} - 1 = -\frac{\hbar D}{4\pi k_B T \xi^2}\Psi'(\tfrac{1}{2}) \tag{3.37}$$

Now $\Psi'(\tfrac{1}{2}) = \tfrac{1}{2}\pi^2$ – this gives the standard Ginzburg-Landau coherence length[18].

$$\xi(T \approx T_c) = \sqrt{\frac{\hbar\pi D}{8k_B T\left(1 - T/T_c\right)}} \tag{3.38}$$

Adding the non-linear Term: The non-linear term in the first Ginzburg-Landau equation is calculated below using the zero-field Usadel equations, using an approach broadly similar to section 45.1 in Ketterson and Song [46], which considers the zero-field gap function given directly by BCS theory. Eliminating the spatially-dependent terms in the Usadel equation (3.26) gives

$$\hbar\omega F_\omega = \Delta G_\omega \tag{3.39}$$

This was substituted into the Usadel equation (3.28)

$$\ln\frac{T_c}{T} = 2\pi k_B T \sum_\omega \left[\frac{1}{\hbar\omega} - \frac{1}{\sqrt{\hbar^2\omega^2 + |\Delta|^2}}\right]. \tag{3.40}$$

In the Ginzburg-Landau regime $\hbar\omega \gg \Delta$. Following Ketterson and Song[46]:

$$\frac{T_c}{T} - 1 = \pi k_B T |\Delta|^2 \sum_\omega \frac{1}{\hbar^3\omega^3}$$

$$\Rightarrow \qquad |\Delta|^2 = \frac{8(\pi k_B T)^2}{7\zeta(3)}\left(1 - \frac{T}{T_c}\right) \tag{3.41}$$

where ζ is the Riemann zeta function. Comparing with (3.34) and using $T \approx T_c$ gives a value for F_0 (F_ω for the lowest possible ω) of

$$|F_0|^2 = \frac{8}{7\zeta(3)}\left(1-\frac{T}{T_c}\right) \tag{3.42}$$

Combining this with the linear equation given by (3.35) and using (3.38) gives an equation in the form of the nonlinear first Ginzburg-Landau equation, namely:

$$\left(\frac{\nabla}{i}-\frac{2e}{\hbar}\mathbf{A}\right)^2 F_0(\mathbf{r}) + \frac{8k_BT\left(1-T/T_c\right)}{\hbar\pi D}\left(\frac{7\zeta(3)|F_0|^2}{8\left(1-\frac{T}{T_c}\right)}-1\right)F_0(\mathbf{r}) = 0 \ . \tag{3.43}$$

The second Ginzburg-Landau equation: the Usadel equation (3.27) was rewritten[36] using (3.34) in terms of the lowest frequency contribution F_0:

$$\mathbf{J} = 2\pi e g(\varepsilon_F) D k_B T \,\mathrm{Im}\left[F_0(\mathbf{r})\left(\nabla-\frac{2ie}{\hbar}\mathbf{A}\right)F_0^*(\mathbf{r})\right]\sum_n\left(\frac{\pi k_BT+\frac{\hbar D}{2\xi^2}}{\pi k_BT(2n+1)+\frac{\hbar D}{2\xi^2}}\right)^2 \tag{3.44}$$

Now in the Ginzburg-Landau regime $\pi k_BT \gg \frac{\hbar D}{2\xi^2}$. Also $\sum_n\left(\frac{1}{2n+1}\right)^2 = \frac{\pi^2}{4}$:

$$\Rightarrow \qquad \mathbf{J} = \frac{\pi^3}{2} e g(\varepsilon_F) D k_B T \,\mathrm{Im}\left[F_0(\mathbf{r})\left(\nabla-\frac{2ie}{\hbar}\mathbf{A}\right)F_0^*(\mathbf{r})\right] \tag{3.45}$$

Renormalizing to Ginzburg-Landau $|\hat{\psi}|$: In order to compare these to the Ginzburg-Landau equations (3.24) and (3.25) it is necessary to replace F_0 by $\hat{\psi}$. Material (1) is taken to be the main superconductor within the system and the general substitution for F_0 used is

$$|F_0|^2 = \frac{8}{7\zeta(3)}\left(1-\frac{T}{T_{c(1)}}\right)|\hat{\psi}|^2 \tag{3.46}$$

where $\hat{\psi}$ is the Ginzburg-Landau order parameter normalized to be 1 in the Meissner state in material (1). This gives the expressions

$$\frac{D_{(1)}}{\xi_{(1)}^2 D}\left(|\hat{\psi}|^2-\frac{T_c-T}{T_{c(1)}-T}\right)\hat{\psi}+\left(\frac{\nabla}{i}-\frac{2e}{\hbar}\mathbf{A}\right)^2\hat{\psi}=0 \tag{3.47}$$

$$\mathbf{J} = \frac{4\pi^3 e g(\varepsilon_F) D k_B T}{7\zeta(3)}\left(1-\frac{T}{T_{c(1)}}\right)\mathrm{Im}\left[\hat{\psi}\left(\nabla-\frac{2ie}{\hbar}\mathbf{A}\right)\hat{\psi}^*\right] \tag{3.48}$$

where D, $g(\varepsilon_F)$ and T_c are the local diffusivity, Fermi-level density of states and critical temperature respectively. Within material (1), (3.47) and (3.48) are equivalent to (3.24) and (3.25) for a penetration depth λ given by[18]

$$\lambda_{(1)}\left(T \approx T_{c(1)}\right) = \sqrt{\frac{7\hbar\zeta(3)\rho_{(1)}}{4\mu_0\pi^3 k_B T\left(1-\frac{T}{T_{c(1)}}\right)}}. \tag{3.49}$$

Hence, the equations for the main superconductor (1) and an alternate material (2) are thus obtained.

Material 1:

$$\frac{1}{\xi_{(1)}^2}\left(\left|\hat{\psi}\right|^2 - 1\right)\hat{\psi} + \left(\frac{\nabla}{i} - \frac{2e}{\hbar}\mathbf{A}\right)^2\hat{\psi} = 0 \tag{3.50}$$

$$\mathbf{J}_s = \frac{\hbar}{2e\mu_0\lambda_{(1)}^2}\mathrm{Re}\left(\hat{\psi}^*\left(\frac{\nabla}{i} - \frac{2e}{\hbar}\mathbf{A}\right)\hat{\psi}\right) \tag{3.51}$$

Material 2:

$$\frac{D_{(1)}}{\xi_{(1)}^2 D_{(2)}}\left(\left|\hat{\psi}\right|^2 + \alpha_N\right)\hat{\psi} + \left(\frac{\nabla}{i} - \frac{2e}{\hbar}\mathbf{A}\right)^2\hat{\psi} = 0 \tag{3.52}$$

$$\mathbf{J}_s = \frac{\hbar}{2e\mu_0\lambda_{(1)}^2}\left(\frac{\rho_{(1)}}{\rho_{(2)}}\right)\mathrm{Re}\left(\hat{\psi}^*\left(\frac{\nabla}{i} - \frac{2e}{\hbar}\mathbf{A}\right)\hat{\psi}\right) \tag{3.53}$$

while the boundary conditions are obtained by substituting (3.46) into (3.31) and (3.32)

$$\hat{\psi}^{(1)} = \hat{\psi}^{(2)} \tag{3.54}$$

$$\frac{\hat{\mathbf{n}}}{\rho_{(1)}}\cdot\left(\nabla - \frac{2ie}{\hbar}\mathbf{A}\right)\hat{\psi}^{(1)} = \frac{\hat{\mathbf{n}}}{\rho_{(2)}}\cdot\left(\nabla - \frac{2ie}{\hbar}\mathbf{A}\right)\hat{\psi}^{(2)} \tag{3.55}$$

and α_N is given by

$$\alpha_N = \frac{T - T_{c(2)}}{T_{c(1)} - T} \tag{3.56}$$

In simple terms, these represent conservation of superelectron density and supercurrent respectively.

3.5 Time-Dependent Ginzburg-Landau theory

3.5.1 Introduction

Finally, we introduce the time-dependent Ginzburg-Landau equations, which were initially postulated by Schmid[47] in order to calculate the resistivity of a type-II superconductor in the flux-flow regime[47,48]. However Gor'kov and Eliashberg[49] found that they were not rigorously consistent with microscopic theory due to the singularity in the BCS density of states, except in a material with a very high concentration of paramagnetic impurities. In my own work the

Schmid equations are used in a phenomenological manner. The time-dependent Ginzburg-Landau equations are[47-49]

$$\frac{1}{\xi^2}\left(\left|\hat{\psi}\right|^2-1\right)\psi+\left(\frac{\nabla}{i}-\frac{2e}{\hbar}\mathbf{A}\right)^2\hat{\psi}+\frac{1}{D}\left(\frac{\partial}{\partial t}+i\frac{2e\varphi}{\hbar}\right)\hat{\psi}=0 \tag{3.57}$$

$$\mathbf{J}_e=\frac{\hbar}{2e\mu_0\lambda^2}\mathrm{Re}\left(\hat{\psi}^*\left(\frac{\nabla}{i}-\frac{2e}{\hbar}\mathbf{A}\right)\hat{\psi}\right)-\frac{1}{\rho}\left(\nabla\varphi+\frac{\partial\mathbf{A}}{\partial t}\right) \tag{3.58}$$

where λ and ξ are the penetration depth and coherence length, D is the diffusivity, and ρ is the normal-state resistivity. The time-dependent terms are the final brackets in each equation, while the remaining parts of the equations are the same as (3.24) and (3.25). The time-dependent term in (3.57) is a relaxation term, accounting for the finite time required for the system to relax into equilibrium, whereas the additional term in (3.58) is simply the normal current. The terms in φ are required by gauge invariance considerations. The scalar and vector potentials may be set in an arbitrary way, as when the following gauge transformations are applied (with χ an arbitrary scalar field), the equations and all measurable parameters remain the same[50].

$$\mathbf{A}\rightarrow\mathbf{A}'-\frac{\phi_0}{2\pi}\nabla\chi,\qquad\varphi\rightarrow\varphi'+\frac{\phi_0}{2\pi}\frac{\partial\chi}{\partial t},\qquad\hat{\psi}\rightarrow\hat{\psi}'\exp(-i\chi) \tag{3.59}$$

This is known as **gauge invariance**. For the purposes of computation the $\varphi=0$ gauge was used[50].

3.5.2 Normalizing the TDGL equations

The normalization of the TDGL equations is relatively straightforward. Rewriting (3.57) and (3.58) in the $\varphi=0$ gauge gives the time derivatives explicitly[50]

$$\frac{\partial\hat{\psi}}{\partial t}=-\left[\frac{D}{\xi^2}\left(\left|\hat{\psi}\right|^2-1\right)+D\left(\frac{\nabla}{i}-\frac{2e}{\hbar}\mathbf{A}\right)^2\right]\hat{\psi} \tag{3.60}$$

$$\frac{\partial\mathbf{A}}{\partial t}=\frac{\rho\hbar}{2e\mu_0\lambda^2}\mathrm{Re}\left(\hat{\psi}^*\left(\frac{\nabla}{i}-\frac{2e}{\hbar}\mathbf{A}\right)\hat{\psi}\right)-\frac{\rho}{\mu_0}(\nabla\times\mathbf{B}) \tag{3.61}$$

The equations are normalized by rescaling with the following units[50]:

$$\mathbf{r}\text{ in units of }\xi$$

$$t\text{ in units of }\frac{\mu_0\lambda^2}{\rho}$$

$$\mathbf{A} \text{ in units of } \frac{\hbar}{2e\xi} = B_{c2}\xi$$

$$\mathbf{J} \text{ in units of } \frac{\hbar}{2e\mu_0\xi^3} = \frac{H_{c2}}{\xi}.$$

This involves the following substitutions:

$$\nabla \to \frac{\nabla}{\xi}, \qquad \frac{\partial}{\partial t} \to \frac{\rho}{\mu_0\lambda^2}\frac{\partial}{\partial t}, \qquad \frac{2e}{\hbar}\mathbf{A} \to \frac{\mathbf{A}}{\xi} \tag{3.62}$$

$$\Rightarrow \qquad \frac{\partial\hat{\psi}}{\partial t} = -\frac{1}{\zeta'}\left[\left(\left|\hat{\psi}\right|^2 - 1\right) + \left(\frac{\nabla}{i} - \mathbf{A}\right)^2\right]\hat{\psi} \tag{3.63}$$

$$\frac{\partial\mathbf{A}}{\partial t} = \mathrm{Re}\left(\hat{\psi}^*\left(\frac{\nabla}{i} - \mathbf{A}\right)\hat{\psi}\right) - \kappa^2(\nabla\times\mathbf{B}) \tag{3.64}$$

where ζ' is a time-scale ratio given by

$$\zeta' = \frac{D\mu_0\kappa^2}{\rho} \tag{3.65}$$

As the ratio between the characteristic time scales of the two TDGL equations, ζ' can be compared to κ, which is the ratio between the characteristic lengths found in the two Ginzburg-Landau equations. However, while κ can have any of a wide range of values, depending on the superconductor, ζ' has only a few specific values. For superconductors in the dirty limit with non-magnetic impurities, $\zeta' = \pi^4/14\zeta(3) \approx 5.78$, while for superconductors dominated by paramagnetic impurities, $\zeta' = 12$.

This thesis uses the convention that a single normalization for $\hat{\psi}$ is used throughout the multipart system – in particular the equations (see section 3.4) are normalized in terms of the main superconductor (which shall be defined as material (1)). Hence for a second material (2) – such as a normal metal coating or a grain boundary – the equivalent non-dimensionalized TDGL equations are

$$\frac{\partial\hat{\psi}}{\partial t} = -\frac{1}{\zeta'}\left[\left(\left|\hat{\psi}\right|^2 + \alpha_N\right) + \frac{D_{(2)}}{D_{(1)}}\left(\frac{\nabla}{i} - \mathbf{A}\right)^2\right]\hat{\psi} \tag{3.66}$$

$$\frac{\partial\mathbf{A}}{\partial t} = \mathrm{Re}\left(\hat{\psi}^*\left(\frac{\nabla}{i} - \mathbf{A}\right)\hat{\psi}\right) - \kappa_{(1)}^2\frac{\rho_{(2)}}{\rho_{(1)}}(\nabla\times\mathbf{B}) \tag{3.67}$$

4 Computational Method

4.1 Introduction

The range of problems in superconductivity which can be solved by analytic methods is extremely limited. More complex problems must be solved numerically. The time dependent Ginzburg-Landau theory will be described briefly in section 4.2, while section 4.3 is concerned with how these equations can be written in a dimensionless form amenable to computation. Section 4.4 describes the popular explicit U-ψ method used in most numerical computation work on superconductivity, while sections 4.5 and 4.6 describe the more efficient semi-implicit algorithm which is used in my own work.

4.2 The explicit U-ψ method

It is necessary to discretize the normalized TDGL equations (3.63) and (3.64) for computational purposes – we define δx_i as the grid spacing and δt as the timestep. In order to achieve second-order spatial accuracy, the vector potential components must be placed at the midpoints between the order parameter grid points[51]. In the U-ψ algorithm, widely used for solving the TDGL equations[40,52,53], a **link variable** between $\mathbf{r}_1$ and $\mathbf{r}_2$ has been defined as[54]

$$\mathbf{U}(\mathbf{r}) = \begin{pmatrix} \exp i \int_{\mathbf{r}}^{\mathbf{r}+\mathrm{i}\delta x} \mathbf{A}.d\mathbf{r} \\ \exp i \int_{\mathbf{r}}^{\mathbf{r}+\mathrm{j}\delta y} \mathbf{A}.d\mathbf{r} \\ \exp i \int_{\mathbf{r}}^{\mathbf{r}+\mathrm{k}\delta z} \mathbf{A}.d\mathbf{r} \end{pmatrix}. \tag{4.1}$$

When the equations are discretized, they are expressed in terms of the link variable rather than the vector potential itself. The exponentiation is required to conserve the gauge invariance of the TDGL equations under discretization. The link variables can be treated as part of a complex vector field $\mathbf{U}$, in which each of the vectorial components are unimodular. This may be compared and contrasted with the order parameter ψ (a complex scalar), and with the magnetic field B (which was a real scalar in 2D simulations, or a real vector in 3D simulations).

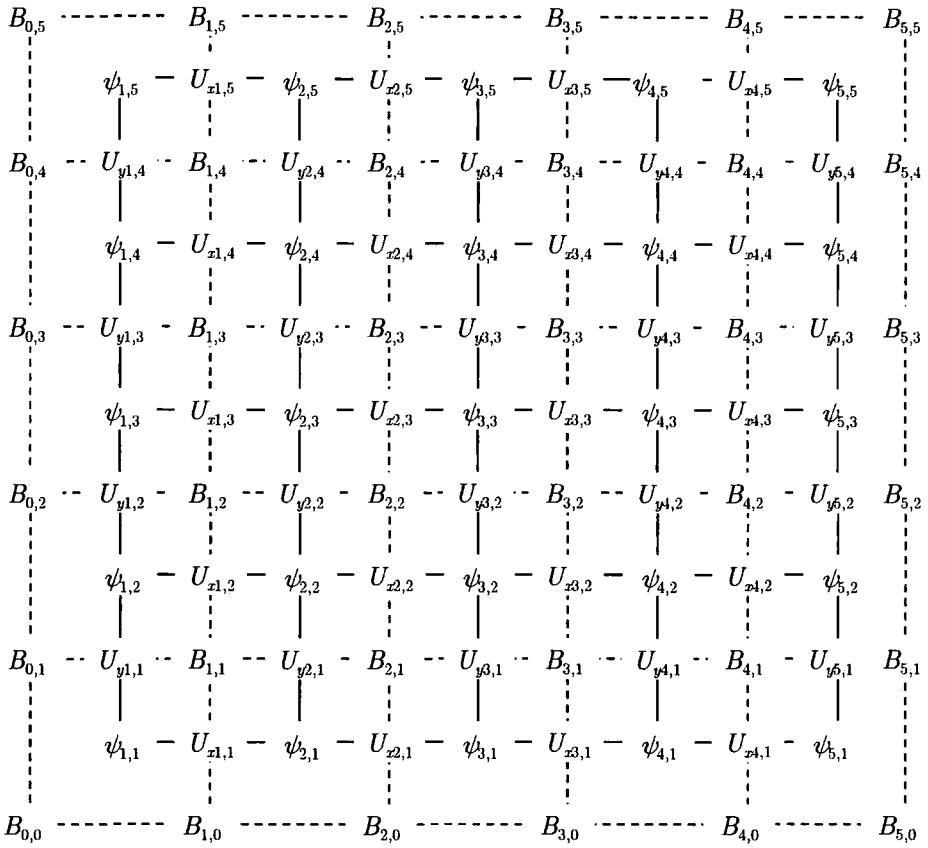

Figure 4.1: Diagram showing the ψ, U_x, U_y and B grid positions on a 5 × 5 grid[55]

The absolute phase of **U** is arbitrary – it is normally set to be zero throughout the system when there is no field applied. In terms of the link variable U, the discretized TDGL equations are[40]

$$\frac{\delta\hat{\psi}}{\delta t} = -\frac{1}{\zeta'}\left[\left(\left|\hat{\psi}\right|^2 - 1\right)\hat{\psi} - \sum_{i=x,y,z} \frac{U_i(\mathbf{r})\hat{\psi}(\mathbf{r}+\delta x_i\hat{\mathbf{r}}_i) + U_i^*(\mathbf{r}-\delta x_i\hat{\mathbf{r}}_i)\hat{\psi}(\mathbf{r}-\delta x_i\hat{\mathbf{r}}_i) - 2\hat{\psi}(\mathbf{r})}{(\delta x_i)^2}\right] \tag{4.2}$$

$$U_i(t+\delta t) = U_i(t)\exp\left[-i\left(\mathrm{Im}\left(\frac{U_i(\mathbf{r})\hat{\psi}(\mathbf{r})\hat{\psi}^*(\mathbf{r}+\delta x_i\hat{\mathbf{r}}_i)}{\delta x_i}\right) + \kappa^2(\nabla\times\mathbf{B})_i\right)\delta t\right] \tag{4.3}$$

$$B_i = \frac{\varepsilon_{ijk}}{2\delta r_j \delta r_k}\left(U_k(\mathbf{r})U_j(\mathbf{r}+\hat{\mathbf{r}}_k\delta r_k)U_k^*(\mathbf{r}+\hat{\mathbf{r}}_j\delta r_j)U_j^*(\mathbf{r})\right) \tag{4.4}$$

4.3 The semi-implicit algorithm for the TDGL equations

4.3.1 Stability of finite differencing algorithms

The U-ψ method is a simple algorithm which is easy to understand and follow, and which can be done using only the four basic arithmetical operations. However, it has a major flaw which

renders it very computationally expensive. The Ginzburg-Landau equations are members of a family of partial differential equations known as *diffusion equations*, which relate the first time derivative of a quantity to its second spatial derivative. The principles of solving diffusion equations was demonstrated using a general 1-D diffusion equation[56] for a function u:

$$\frac{\partial u}{\partial t} = C\frac{\partial^2 u}{\partial x^2}. \tag{4.5}$$

For the purposes of numerical computation, it is necessary to discretize this equation. An obvious way of discretizing the equation to solve for u is

$$\frac{u_j^{n+1} - u_j^n}{\delta t} = C\left[\frac{u_{j+1}^n + u_{j-1}^n - 2u_j^n}{\delta x^2}\right] \tag{4.6}$$

where j and n are integers representing spatial and temporal indices respectively. This method of discretization is known as an *explicit* scheme, as it involves calculating the values of the function at the new timestep entirely from values of the function at the old timestep. This is a very simple method of solving the equation, and is first-order accurate in time. However it has stability problems if δt is too large. The stability or otherwise of a numerical algorithm for solving partial differential equations can be determined by means of Von Neumann stability analysis[56]. In this analysis it is assumed that the coefficients of the equations are constant in space and time. In the case of the diffusion equation, the eigenstates of the discretized equations are taken to be of the form

$$u_j^n(x) = \xi^n(k)\exp(ik_x j\delta x) \tag{4.7}$$

Here k is a spatial wavenumber, and ξ (the *amplification factor*) is a complex function of k. The time dependence of the function is given by the increasing powers of ξ. Therefore, if $|\xi| > 1$ for any value of k, the algorithm is unstable. Substitution of (4.7) into (4.6) gives

$$\xi = 1 - \frac{4C\delta t}{\delta x^2}\sin^2\left(\frac{k_x\delta x}{2}\right) \tag{4.8}$$

For $|\xi|$ to be less than 1 for all k's, the maximum value of δt was given by

$$\delta t_{\max} = \frac{\delta x^2}{2C} \tag{4.9}$$

If the system is to be studied with any significant level of detail (δx small), this restriction imposes a very small δt, with the resulting computational expense. In Ginzburg-Landau

computation, this is especially severe for high-κ superconductors as in the second Ginzburg-Landau equation $C = \kappa^2$. This can be seen by taking the curl of (3.64) $\left[\frac{\partial \mathbf{B}}{\partial t} = \nabla \times \mathbf{J}_s + \kappa^2 \nabla^2 \mathbf{B}, \text{ where } \mathbf{J}_s \text{ is the supercurrent}\right]$. For example, for a grid spacing of $\delta x =$ 0.5, and a Ginzburg-Landau parameter $\kappa = 2$, the maximum timestep is given by:

$$\delta t < \frac{\delta x^2}{2\kappa^2} = \frac{(0.5)^2}{2 \cdot 2^2} = 0.03125 \tag{4.10}$$

Note that in practice, a smaller timestep such as 0.01 is used to ensure stability. One alternative algorithm is the *fully-implicit* differencing scheme[56]:

$$\frac{u_j^{n+1} - u_j^n}{\delta t} = C\left[\frac{u_{j+1}^{n+1} + u_{j-1}^{n+1} - 2u_j^{n+1}}{\delta x^2}\right] \tag{4.11}$$

This scheme is better in that it drives the values of u towards their *equilibrium* values (ie the LHS is zero). For this method, the amplification factor is

$$\xi = \frac{1}{1 + \frac{4C\delta t}{\delta x^2}\sin^2\left(\frac{k_x \delta x}{2}\right)} \tag{4.12}$$

This shows that the fully implicit algorithm is stable at all timesteps. The implicit equation is solved by re-arrangement as a tridiagonal matrix equation:

$$\left[1 + \frac{2C\delta t}{\delta x^2}\right]u_j^{n+1} - \frac{C\delta t}{\delta x^2}\left(u_{j+1}^{n+1} + u_{j-1}^{n+1}\right) = u_j^n \tag{4.13}$$

The fully-implicit algorithm is best for reaching equilibrium forms, but is still only first-order accurate in time. Another possible algorithm is the *Crank-Nicolson*[57] method, which combines the explicit and implicit calculations:

$$\frac{u_j^{n+1} - u_j^n}{\delta t} = C\left[\frac{\left(u_{j+1}^n + u_{j-1}^n - 2u_j^n\right) + \left(u_{j+1}^{n+1} + u_{j-1}^{n+1} - 2u_j^{n+1}\right)}{\delta x^2}\right] \tag{4.14}$$

As both the LHS and RHS are centred at n + ½, this method is second-order accurate in time. The Crank-Nicolson amplification factor is given by[56]

$$\xi = \frac{1 - \frac{2C\delta t}{\delta x^2}\sin^2\left(\frac{k_x \delta x}{2}\right)}{1 + \frac{2C\delta t}{\delta x^2}\sin^2\left(\frac{k_x \delta x}{2}\right)} \tag{4.15}$$

showing that this algorithm is also stable for any δt.

It is essential to solve these implicit formulae by means of matrix inversion. If an attempt is made to time-evolve explicitly, and then iterate to correct this value, this does not restore stability. This is because the instability results in physical terms from the fact that the numerical diffusion (restricted by the dependence on nearest neighbour elements only) is unable to keep up with the actual diffusion in the system. The matrix inversion introduces a long-range dependence into the system.

4.3.2 Method of fractional steps

The U-ψ algorithm is an explicit algorithm, and is therefore extremely inefficient. However, because of the non-linear nature of the Ginzburg-Landau equation, it would be very difficult to use a fully-implicit method to calculate the equations in their entirety. The Crank-Nicolson method is therefore used only on the diffusive terms (which are the cause of the instability problem), while the remaining terms are treated explicitly. This is known as the *method of fractional steps*. In this approach, fundamental matrix operators are defined[58]:

$$I^{+}_{ii'}u_{i'} = u_{i+1}, \qquad I^{-}_{ii'}u_{i'} = u_{i-1} \tag{4.16}$$

The method considers a general diffusion equation for a scalar field of the form:

$$\left(\frac{\partial u}{\partial t}\right)_{ijk} = P_{ijk} + Q^{x}_{ii'}u_{i'jk} + Q^{y}_{jj'}u_{ij'k} + Q^{z}_{kk'}u_{ijk'} \tag{4.17}$$

where P_{ijk} is the section of the RHS to be calculated explicitly, and the Q operators are the diffusive terms to be calculated implicitly. Equation (4.17) is now substituted into (4.14) giving:

$$\begin{aligned}\frac{u^{(n+1)}_{ijk} - u^{(n)}_{ijk}}{\delta t} = {} & \frac{1}{2}\left[P^{(n)}_{ijk} + Q^{x(n)}_{ii'}u^{(n)}_{i'jk} + Q^{y(n)}_{jj'}u^{(n)}_{ij'k} + Q^{z(n)}_{kk'}u^{(n)}_{ijk'}\right] \\ & + \frac{1}{2}\left[P^{(n+1)}_{ijk} + Q^{x(n+1)}_{ii'}u^{(n+1)}_{i'jk} + Q^{y(n+1)}_{jj'}u^{(n+1)}_{ij'k} + Q^{z(n+1)}_{kk'}u^{(n+1)}_{ijk'}\right]\end{aligned} \tag{4.18}$$

The expression is rearranged to separate 'new' and 'old' timestep terms

$$\begin{aligned}&\left\{I_{ii'}I_{jj'}I_{kk'} - \frac{\delta t}{2}\left[Q^{x(n+1)}_{ii'}I_{jj'}I_{kk'} + I_{ii'}Q^{y(n+1)}_{jj'}I_{kk'} + I_{ii'}I_{jj'}Q^{z(n+1)}_{kk'}\right]\right\}u^{(n+1)}_{i'j'k'} \\ &= \left\{I_{ii'}I_{jj'}I_{kk'} + \frac{\delta t}{2}\left[Q^{x(n)}_{ii'}I_{jj'}I_{kk'} + I_{ii'}Q^{y(n)}_{jj'}I_{kk'} + I_{ii'}I_{jj'}Q^{z(n)}_{kk'}\right]\right\}u^{(n)}_{i'j'k'} + \frac{\delta t}{2}\left[P^{(n)}_{ijk} + P^{(n+1)}_{ijk}\right]\end{aligned} \tag{4.19}$$

Now, the method of *approximate factorization* can be used[58] so that

$$\left[I_{ii'}-\frac{\delta t}{2}Q_{ii'}^{x(n+1)}\right]\left[I_{jj'}-\frac{\delta t}{2}Q_{jj'}^{y(n+1)}\right]\left[I_{kk'}-\frac{\delta t}{2}Q_{kk'}^{z(n+1)}\right]u_{i'j'k'}^{(n+1)}$$
$$=\left[I_{ii'}+\frac{\delta t}{2}Q_{ii'}^{x(n)}\right]\left[I_{jj'}+\frac{\delta t}{2}Q_{jj'}^{y(n)}\right]\left[I_{kk'}+\frac{\delta t}{2}Q_{kk'}^{z(n)}\right]u_{i'j'k'}^{(n)}+\frac{\delta t}{2}\left[P_{ijk}^{(n)}+P_{ijk}^{(n+1)}\right] \tag{4.20}$$

The RHS of the equation can be calculated explicitly, and the LHS matrices can be inverted consecutively using fast tridiagonal matrix inversion routines.

4.3.3 The link variable in the semi-implicit algorithm

The fractional steps Crank-Nicolson method uses a different link variable from the explicit U-ψ method. This alternative link variable ϕ is given by[59]

$$\phi(\mathbf{r}_1,\mathbf{r}_2)=\int_{\mathbf{r}_1}^{\mathbf{r}_2}\mathbf{A}.d\mathbf{r} \tag{4.21}$$

The arrangement of the grid points is the same as for the U-ψ method. In the canonical derivatives the exponentiation is retained in order to preserve gauge invariance. This gives the following discretized equations[59]:

$$\frac{\delta\hat{\psi}}{\delta t}=-\frac{1}{\zeta'}\left\{\left(\left|\hat{\psi}\right|^2-1\right)\psi-\sum_{i=x,y,z}\frac{1}{(\delta x_i)^2}\begin{bmatrix}\exp(\phi_i(\mathbf{r}))\hat{\psi}(\mathbf{r}+\delta x_i\hat{\mathbf{r}}_i)-2\hat{\psi}(\mathbf{r})\\+\exp(-i\phi_i(\mathbf{r}-\delta x_i\hat{\mathbf{r}}_i))\hat{\psi}(\mathbf{r}-\delta x_i\hat{\mathbf{r}}_i)\end{bmatrix}\right\} \tag{4.22}$$

$$\frac{\delta\phi_i}{\delta t}=\mathrm{Im}\left(\frac{\exp(i\phi_i(\mathbf{r}))\hat{\psi}(\mathbf{r})\hat{\psi}^*(\mathbf{r}+\delta x_i\hat{\mathbf{r}}_i)}{\delta x_i}\right)+\kappa^2(\nabla\times\mathbf{B})_i \tag{4.23}$$

$$B_i=\frac{\varepsilon_{ijk}}{2\delta r_j\delta r_k}\left(\phi_k(\mathbf{r})+\phi_j(\mathbf{r}+\hat{\mathbf{r}}_k\delta r_k)-\phi_k(\mathbf{r}+\hat{\mathbf{r}}_j\delta r_j)-\phi_j(\mathbf{r})\right) \tag{4.24}$$

The first step in implementing the Crank-Nicolson method is to separate the diffusive terms from the non-diffusive terms. The normalized Ginzburg-Landau equations are written in terms of matrices[59]:

$$\left(\frac{\partial\hat{\psi}}{\partial t}\right)_{ijk}=F_{ijk}(\hat{\psi})+D_{ii'}^x(\phi^x)\hat{\psi}_{i'jk}+D_{jj'}^y(\phi^y)\hat{\psi}_{ij'k}+D_{kk'}^z(\phi^z)\hat{\psi}_{ijk'} \tag{4.25}$$

$$\left(\frac{\partial\phi^x}{\partial t}\right)_{ijk}=G_{ijk}^x(\hat{\psi},\phi^x,\phi^y,\phi^z)+E_{jj'}^y\phi_{ij'k}^x+E_{kk'}^z\phi_{ijk'}^x \tag{4.26}$$

$$\left(\frac{\partial\phi^y}{\partial t}\text{ and }\frac{\partial\phi^y}{\partial t}\text{ are found by cyclic permutation of } x,y,z\right)$$

The matrix operators F, D, G and E are now given by

$$F_{ijk}=-\frac{1}{\zeta'}\left(\left|\hat{\psi}_{ijk}\right|^2+1\right)\hat{\psi}_{ijk} \tag{4.27}$$

$$D^x_{ii'} = \frac{1}{\zeta'\delta x^2}\Big[I^+_{ii'}\exp\big(-i\phi^x_{ijk}\big) + I^-_{ii'}\exp\big(i\phi^x_{i'jk}\big) - 2I_{ii'}\Big] \tag{4.28}$$

$$\begin{aligned} G^x_{ijk} = \mathrm{Im}\Big(\hat{\psi}^*_{ijk} I^+_{ii'}\hat{\psi}_{i'jk}\exp\big(-i\phi^x_{ijk}\big)\Big) &+ \frac{\kappa^2 I^+_{ii'}I^-_{jj'}}{\delta y^2}\Big[\phi^y_{ijk} + \phi^y_{i'j'k} - \phi^y_{i'jk} - \phi^y_{ij'k}\Big] \\ &+ \frac{\kappa^2 I^+_{ii'}I^-_{kk'}}{\delta z^2}\Big[\phi^z_{ijk} + \phi^z_{i'jk'} - \phi^z_{i'jk} - \phi^z_{ijk'}\Big] \end{aligned} \tag{4.29}$$

$$E^x_{ii'} = \frac{\kappa^2}{\delta x^2}\big[I^+_{ii'} + I^-_{ii'} - 2I_{ii'}\big] \tag{4.30}$$

(the y- and z-components of D, G, and E were found by cyclic permutation of x, y, z)

By analogy with (4.20) the equations are factorized

$$\Big[I_{ii'} - \frac{\delta t}{2}D^{x(n+1)}_{ii'}\Big]\Big[I_{jj'} - \frac{\delta t}{2}D^{y(n+1)}_{jj'}\Big]\Big[I_{kk'} - \frac{\delta t}{2}D^{z(n+1)}_{kk'}\Big]\hat{\psi}^{(n+1)}_{i'j'k'} \tag{4.31}$$

$$\begin{aligned} &= \Big[I_{ii'} + \frac{\delta t}{2}D^{x(n)}_{ii'}\Big]\Big[I_{jj'} + \frac{\delta t}{2}D^{y(n)}_{jj'}\Big]\Big[I_{kk'} + \frac{\delta t}{2}D^{z(n)}_{kk'}\Big]\hat{\psi}^{(n)}_{i'j'k'} + \frac{\delta t}{2}\Big[F^{(n)}_{ijk} + F^{(n+1)}_{ijk}\Big] \\ &\quad \Big[I_{jj'} - \frac{\delta t}{2}E^{y(n+1)}_{jj'}\Big]\Big[I_{kk'} - \frac{\delta t}{2}E^{z(n+1)}_{kk'}\Big]\phi^{x(n+1)}_{i'j'k'} \\ &= \Big[I_{jj'} + \frac{\delta t}{2}E^{y(n)}_{jj'}\Big]\Big[I_{kk'} + \frac{\delta t}{2}E^{z(n)}_{kk'}\Big]\phi^{x(n)}_{i'j'k'} + \frac{\delta t}{2}\Big[G^{(n)}_{ijk} + G^{(n+1)}_{ijk}\Big] \end{aligned} \tag{4.32}$$

(other equations for ϕ can be obtained by cyclic permutation.)

These equations are written in a more compact form as

$$\alpha^x_{ii'}\alpha^y_{jj'}\alpha^z_{kk'}\hat{\psi}^{(n+1)}_{i'j'k'} = \beta^x_{ii'}\beta^y_{jj'}\beta^z_{kk'}\hat{\psi}^{(n)}_{i'j'k'} + \frac{\delta t}{2}\Big[F^{(n)}_{ijk} + F^{(n+1)}_{ijk}\Big] \tag{4.33}$$

$$\gamma^{y-}_{jj'}\gamma^{z-}_{kk'}\phi^{x(n)}_{ij'k'} = \gamma^{y+}_{jj'}\gamma^{z+}_{kk'}\phi^{x(n)}_{ij'k'} + \frac{\delta t}{2}\Big[G^{(n)}_{ijk} + G^{(n+1)}_{ijk}\Big] \tag{4.34}$$

where the matrices α, β, γ are given by

$$\alpha^x_{ii'} = \left[\left(1 + \frac{\delta t}{\zeta'\delta x^2}\right)I_{ii'} - \frac{\delta t}{2\zeta'\delta x^2}\Big(I^+_{ii'}\exp\big(-i\phi^{x(n+1)}_{ijk}\big) + I^-_{ii'}\exp\big(i\phi^{x(n+1)}_{i'jk}\big)\Big)\right] \tag{4.35}$$

$$\beta^x_{ii'} = \left[\left(1 - \frac{\delta t}{\zeta'\delta x^2}\right)I_{ii'} + \frac{\delta t}{2\zeta'\delta x^2}\Big(I^+_{ii'}\exp\big(-i\phi^{x(n)}_{ijk}\big) + I^-_{ii'}\exp\big(i\phi^{x(n)}_{i'jk}\big)\Big)\right] \tag{4.36}$$

$$\gamma^{x\pm}_{ii'} = \left[\left(1 \mp \frac{\kappa^2\delta t}{\delta x^2}\right)I_{ii'} \pm \frac{\kappa^2\delta t}{2\delta x^2}\big(I^+_{ii'} + I^-_{ii'}\big)\right] \tag{4.37}$$

(cyclic permutation of x, y, z gives the equivalent y and z matrices).

Note that in the order parameter equation, the diffusive terms are time-dependent (via the link variables). For this reason, an iterative method is needed to solve the equations It was found[59] that 3 iterations were normally sufficient. To speed up computation, those terms on the RHS of the equations depending only on the state of the system at the start of the timestep are calculated and stored before the iterations begin. Also, the γ^+ and γ^- have no time-dependent terms, unless the timestep δt itself changes during the course of the calculation. This means that γ^+ and γ^- may be calculated once only, and then stored for use in the main calculation.

4.3.4 Boundary Conditions

At the edge of the grid a boundary condition was applied representing an insulator $\left(\hat{\mathbf{n}}.(\hbar\nabla - 2ie\mathbf{A})\hat{\psi} = 0\right)$ or a highly-conductive metal[39] $\left(\hat{\psi} = 0\right)$. Periodic boundary conditions may also be used provided the system has broken symmetry (due to a junction or internal inhomogeneity) to permit fluxon entry. Periodic boundary conditions are implemented using dummy grid points (as this is more efficient computationally than direct referencing), while other boundary conditions are implemented within the calculation matrices themselves. At interfaces between materials within the grid, it is important to maintain the boundary conditions given by (3.55). Maintaining the continuity of $\hat{\psi}$ is trivial, but maintaining the continuity of supercurrent requires careful consideration. When calculating the $\left(\frac{\nabla}{i} - \mathbf{A}\right)^2 \hat{\psi}$ term in the first TDGL equation, $\hat{\psi}$ is differentiated once, then divided by ρ before being differentiated a second time. When the numerical calculation is done in this manner, the correct boundary conditions follow naturally.

5 The Magnetization Surface Barrier - Effect of Coatings

5.1 Introduction

The new Crank-Nicolson algorithm for solving the time-dependent Ginzburg-Landau equations, described in the previous chapter, improves computational efficiency of one or two orders of magnitude. Combined with the 100-fold increase in PC processor speed within the past decade, this now permits TDGL computation to model superconductors with high finite κ values in contact with non-superconducting materials.

The phenomenological TDGL equations provide a way of modelling superconductivity more complete than simple macroscopic models[60,61], but without the extreme complexity of microscopic theory which makes such calculations impractical for the mixed state. The TDGL equations have been used to calculate I-V characteristics for superconductors with insulating-boundary surface pinning[52] and with bulk pinning by point pinning sites[62]. The initial vortex penetration field of a superconductor with a notch[63] has also been investigated using TDGL theory, along with the current flow in a 3D layered superconductor[64,65]. Some of the systems considered in the literature consider spatially varying material properties by invoking a variation in the critical temperature T_c[53,64-66].

The effect of surface barriers on superconductors is a phenomenon which has been researched in detail for most of the history of superconductivity. The effect of coatings on the surface critical field H_{c3} has been determined by using linearized equations to obtain H_{c3} as a function of coating resistivity[67]. The question of initial vortex penetration into a coated superconductor was first posed by Bean and Livingston[37], and solved in the high-κ limit using London theory, and using 1-D Ginzburg-Landau theory[68]. The Bean-Livingston model is based on competition between the attraction from an 'image force' and repulsion due to the screening currents, and predicts an initial vortex penetration field $H_p \approx H_c$. Much later, it was confirmed computationally[39] that their result is valid for the extreme metallic limit irrespective of κ. The case of the superconductor with an insulating surface was solved by

Matricon and Saint-James using the 1-D Ginzburg-Landau equations[38], showing that H_p was noticeably higher than the Bean-Livingston value, due to the need to force the material normal at the insulating edge before fluxons can enter. This has more recently been followed by computational work[39,40] which confirmed the Matricon result.

This chapter (and the associated paper[69]) extends our understanding of coated superconductors from the insulating and extreme metallic limits to the case of superconductors coated with metals of arbitrary resistivity. These systems involve spatial variation of both T_c and normal-state resistivity ρ. The generalization of the computation to include spatially-dependent ρ necessitates implementation of internal boundary conditions, but enables the direct computational simulation of new classes of systems. Hence coated superconductors, polycrystalline bulk materials (where the grain boundaries may be non-superconducting) and superconducting composite conductors (which may include normal metal matrix materials) can all begin to be addressed computationally. The aim of our work is to determine the effect of the surface barrier on the hysteretic magnetic response to an applied magnetic field. As part of our long-standing interest in bulk superconducting properties, we have also considered how best to eliminate the surface pinning barrier from a superconductor. For this reason the properties of bilayer coatings, which consist of a weakly superconducting S' layer interposed between the superconductor and normal coating are calculated. This bilayer structure was chosen in light of the experimental finding[70] that the creation of a diffusion layer between a superconductor and its normal metal coating reduces the superconductor's magnetic irreversibility.

In Section 5.2 the appropriate parameters for the time-dependent Ginzburg-Landau model (described in Chapter 4) based on normal-state material properties are determined. The general impact of symmetry considerations on TDGL computation, the numerical method itself, and the optimization of the calculations are also discussed.

Section 5.3 considers a superconductor coated with a normal metal. The magnetization characteristics themselves are calculated along with the initial vortex penetration field H_p and the hysteresis. The minimum possible H_p and corresponding ρ_N/ρ_S are also found. (ρ_N/ρ_S is

the ratio of the coating resistivity to the normal-state resistivity of the superconductor.) In Section 5.3.3 a weakly superconducting region is introduced between the superconductor and the main normal metal coating.

Sections 5.4 considers the magnetization properties trilayer-coated superconductors, while section 5.5 considers a trilayer-coated superconductor enclosed within another superconductor. These systems are investigated because of their similarities with individual grains in polycrystalline superconductors – the focus of Chapters 8 and 9. An analytic calculation of ΔM across a trilayer boundary between two superconductors, based on the Dew-Hughes pinning calculation[25], is included in section 5.5.4.

The implications of the results obtained are discussed further in section 5.6. Finally, section 5.7 gives a summary of the results and conclusions.

5.2 Setting up the calculations

5.2.1 Varying coating resistivity

This chapter considers simple normal metal coatings, bilayer and trilayer coatings which include an additional weakly superconducting layer to represent a diffusion layer. Changing the resistivity of the normal metal coating leaves complete freedom in setting its diffusivity. In this chapter the Fermi-level density of states $g(\varepsilon_F)$, given by

$$g(\varepsilon_F) = \frac{1}{2e^2 D\rho}, \tag{5.1}$$

was held constant throughout the grid, while T_c and ρ were used to define material properties. This is appropriate if changes in resistivity are determined mainly by impurity concentration (and therefore by changes in D). In the bilayer (S'/N) coating simulations, T_c and ρ were varied linearly across the S' layer. Since the core superconductor in the computation is the critical part of the system, and in most relevant experiments is far larger than the coatings, the magnetization data were obtained from a sum over the core superconductor alone (i.e. not including the S' layer). The approach ensures that the magnitudes of our calculated magnetizations are representative of large samples.

5.2.2 Symmetry Problems

Explicit consideration of symmetry-breaking is required to describe the changes in a physical system when a local energy minimum becomes a local maximum while the system remains in equilibrium throughout. Whereas an analytic calculation can check for the point at which a minimum becomes a maximum and then identify the correct minimum-energy equilibrium state, a time-dependent computation without symmetry breaking can remain indefinitely at a state which has become a local maximum in energy. In a superconductor, either the Meissner state or the normal state may be erroneously preserved if symmetry breaking is absent.

In the Meissner state of an infinitely long superconductor, every point along the edge is equivalent to every other point, which may mean that the superconductor remains trapped in this state even above H_p. We have addressed this symmetry problem by considering finite rectangular (where the corners break the symmetry) and circular (where roughness is imposed by the rectilinear discretization) superconductors. If the surface barrier is not weakened by the corners, H_p obtained from both rectangular and circular computations will agree with analytic values in the large-grid limit.

Similarly if the superconductor becomes completely normal it is impossible for superconductivity to renucleate even if this is energetically favourable. When $\hat{\psi}$ is zero everywhere, $\frac{\partial \hat{\psi}}{\partial t'} = 0$ (c.f. equation (3.57)) and the normal state is erroneously preserved whatever the shape of the superconductor. Renucleation of superconductivity can be enabled by adding random Gaussian noise to both real and imaginary components of $\hat{\psi}$ after every 50 iterations. This noise is of mean zero and standard deviation 10^{-6}. Within the superconducting regime this noise has negligible effect on the results, as noise 10^4 times more intense was found to have negligible effect on the results[40] except for the time scale – more noise leads to faster equilibration.

5.2.3 Optimizing the Computation

In Schmid's dirty-limit TDGL theory, the ratio of the time constants $\zeta' = \frac{\pi^4}{14\zeta(3)} = 5.78$, while in TDGL theory as obtained for superconductors dominated by paramagnetic

impurities[49], $\zeta' = 12$. In Figure 5.1, where the time evolution is of explicit interest, our calculation uses $\zeta' = 5.78$. The remaining work in this chapter considers equilibrium properties, where the time-dependent terms ultimately tend to zero. As a result, ζ' was set to 1 to reduce computational expense. We have confirmed that this value of ζ' does not affect the results, while reducing computation times considerably – this is consistent with work in the literature[63]. In order to obtain the equilibrated magnetic properties, the applied magnetic field was ramped from one value to the next, and then held constant. The field increment was typically $0.05H_{c2}$, ramped over $100\tau^{J}_{(1)}$, although when obtaining precise H_p values much smaller increments were used. The equilibration time (typically $400\tau^{J}_{(1)}$, although this varied depending on the system) was determined by confirming convergence of M to 3 significant figures.

In all computations included in this chapter, a grid spacing of 0.5ξ in both x and y directions was used. H_p is dependent on grid size – it is higher for small superconductors, as the screening current on the near side of the superconductor which induces flux entry is partially cancelled by the opposite screening current at the far side. This meant it was necessary to check that the grid size was large enough to obtain H_p results consistent with analytic results in the literature for the insulating and extreme metallic limits. For the rectangular grid, for $\kappa = 2$ the grid size was $50\xi \times 40\xi$, with a 10ξ thick coating. For $\kappa = 5$ calculations, a $100\xi \times 80\xi$ grid with a 10ξ thick coating was used, $250\xi \times 200\xi$ with a 20ξ coating for $\kappa = 10$ and $625\xi \times 500\xi$ for $\kappa = 20$ with a 20ξ coating. For the circular superconductors referred to in Figure 5.3, the diameters used were 50ξ for $\kappa = 2$, 100ξ for $\kappa = 5$, 250ξ for $\kappa = 10$ and 500ξ for $\kappa = 20$, with the same coating. The large grid sizes for $\kappa = 10$ and $\kappa = 20$ use up to 1 GB of RAM – to reduce the computational expense the superconductor was divided into symmetric quarters, and the computation was restricted to a single quarter. The same S grid sizes and N thicknesses are used in the bilayer coating calculations.

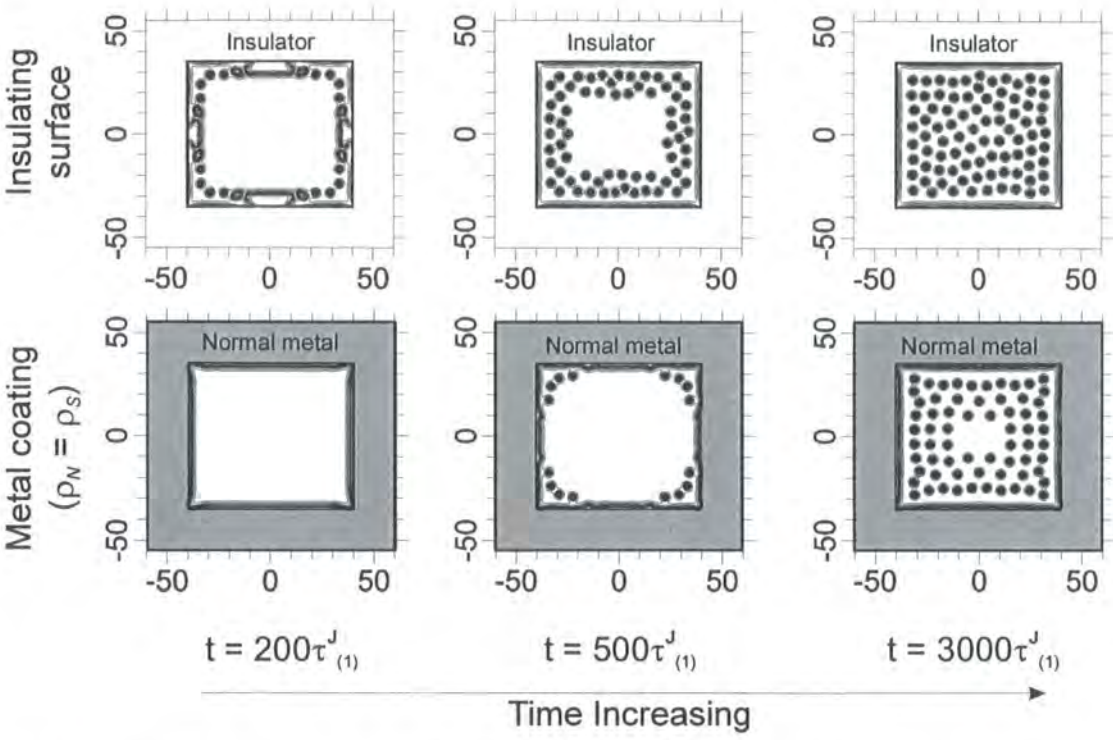

Figure 5.1: Time evolution of $\left|\tilde{\psi}\right|^2$ showing vortex entry into a $\kappa = 2$ superconductor of dimensions $80\xi \times 70\xi$ with an insulating surface and with a $\rho_N = \rho_S$, 20ξ thick metal coating (partly shown for clarity) and insulating outer surface. The applied magnetic field is increased above the initial vortex penetration field (i.e. to $H_p + 0.01H_{c2}$) at $t = 0$. Time frames at $200\tau^J_{(1)}$, $500\tau^J_{(1)}$ and $2000\tau^J_{(1)}$ are shown. $\left|\tilde{\psi}\right|^2$ contours are at intervals of 0.1

5.3 Results

5.3.1 Flux Entry Behaviour

Figure 5.1 shows the time evolution of $\left|\tilde{\psi}\right|^2$ as flux enters a superconductor with an insulating surface and a superconductor with a $\rho_N = \rho_S$ normal metal coating (the outer surface of the coating was set to be insulating). For each system, the superconductor was equilibrated in the Meissner state with an applied field of $H_p - 0.01H_{c2}$, (where H_p is the minimum field at which flux entry occurs) then the field was increased to $H_p + 0.01H_{c2}$. In the analytic work on initial vortex penetration, the non-superconducting side of the barrier is not explicitly considered. In both the insulating[38] and extreme metallic[37] limits, $\psi = 0$ outside the superconductor, and the fluxons first nucleate just inside the superconductor. For a superconductor coated with a normal metal this leads to the question as to where current

vortices first form. The mechanism of flux entry is quite different in the two cases – in the insulating surface case a continuous normal region forms at the edges which then breaks up into fluxons, while in the metal-coated superconductor individual fluxons enter the superconductor from the edge of the material where $\left|\hat{\psi}\right|^2$ has been depleted by the proximity effect. When the magnetization response was calculated for a superconductor with normal metal coatings of various thicknesses, it was found that any thickness above $2\xi_{(1)}$ gave the same result for H_p. This shows that the order parameter within the coating becomes negligible within $2\xi_{(1)}$ for $H \approx H_p$, and so the normal metal coatings used here can be considered to be infinitely thick. A metal coating slows the diffusion of fluxons into the superconductor compared to an insulating surface because H_p, and therefore the driving force on the fluxons, is lower for the metal-coated superconductor.

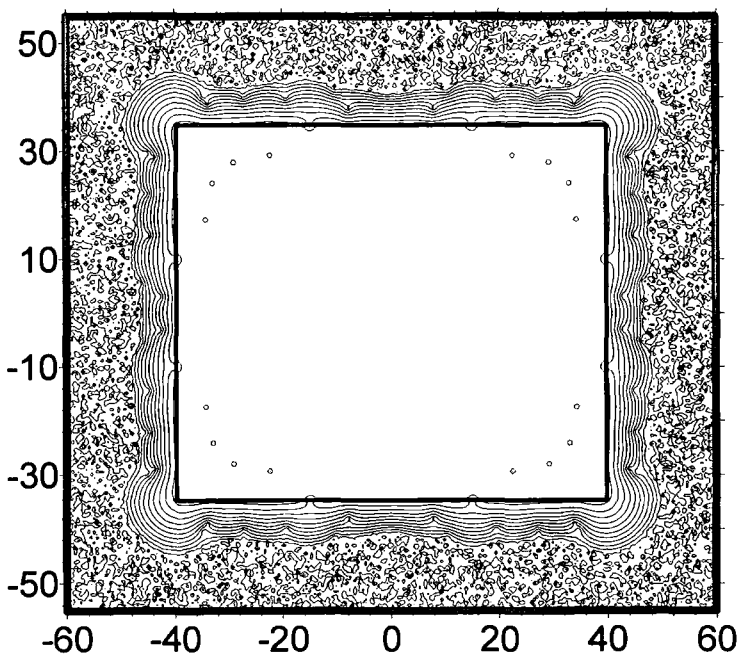

Figure 5.2: Contour plot of $\log_{10}\left(\left|\hat{\psi}\right|^2\right)$ for a $\kappa = 2$ superconductor of dimensions $80\xi \times 70\xi$ coated with a $\rho_N = \rho_S$, 20ξ thick normal metal and bounded by an insulating outer surface. The applied magnetic field was increased to above the initial vortex penetration field (i.e. to $H_p + 0.01H_{c2}$) at $t = 0$ and data obtained at $t = 500\tau_{(1)}$. $\log_{10}\left(\left|\hat{\psi}\right|^2\right)$ contours are at intervals of 1 – the outer region has random $\log_{10}\left(\left|\hat{\psi}\right|^2\right)$ due to noise.

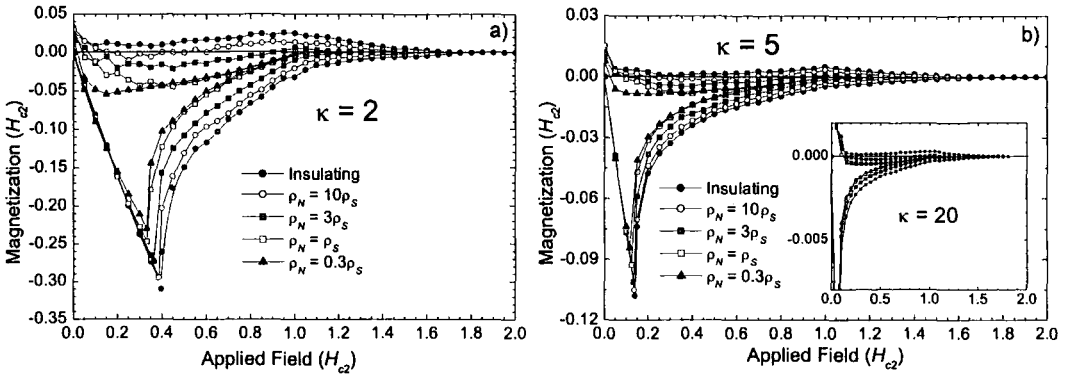

Figure 5.3: Magnetization of superconductors with an insulating surface or normal metal coatings of various resistivities – a) $\kappa = 2$, b) $\kappa = 5$ with $\kappa = 20$ inset.

Figure 5.2 is a logarithmic contour plot for such a system. It consists of three main regions, an outer region in the normal coating dominated by noise where $\left|\hat{\psi}\right|^2 < 10^{-10}$, a second region containing screening currents which circulate near the superconductor-normal interface and exists in both regions and an inner region which contains a few fluxons, but where the order parameter is in most regions close to unity (Meissner state). It can be seen that there are small depressions of ψ within the normal metal layer, which have associated vortex currents. These proto-fluxons do not have quantized flux of $h/2e$ associated with them. We have found that unlike the two extreme limits considered analytically, the proto-fluxons first nucleate within the 'noisy' region in the normal coating, then cross the screening current region into the superconductor.

5.3.2 Normal Metal Coatings

Figure 5.3 shows the complete magnetization characteristics for superconductors coated with insulator and with metals of various resistivities. The sample magnetization M was calculated by subtracting the applied magnetic field H from the internal magnetic field B (calculated by $\nabla \times \mathbf{A}$), and then averaging over the S region only (the demagnetization factor can be ignored for a 2D system). Adding a metal coating reduces the surface critical field H_{c3} from its insulating-surface value of $1.69H_{c2}$ to H_{c2} when $\rho_N \leq \rho_S$, consistent with the Hurault result[67]. (Note that superconductivity can persist in corners even above H_{c3}, as noted in the

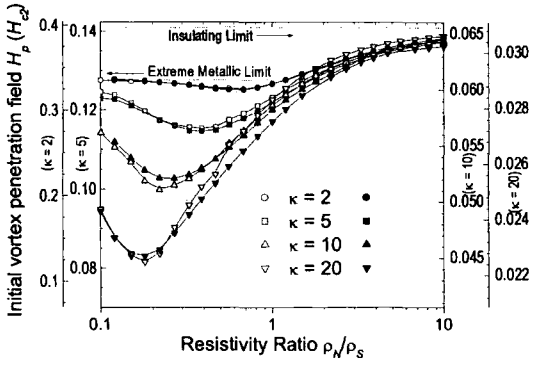

Figure 5.4: Initial vortex penetration field H_p as a function of ρ_N/ρ_S for κ = 2, 5, 10 and 20 for rectangular (open symbols) and circular (closed symbols) superconductors. The y-axes are scaled so that the asymptotic values of H_p in both the insulating and extreme metallic limits are at the same position for all κ values.

literature[40]). The magnitude of the magnetic hysteresis decreases as ρ_N/ρ_S decreases, or as κ increases. However, the field dependence of the hysteresis is a property not only of the coating itself but also of the shape of the superconductor because in superconductors with small dimensions, fluxons which have already entered the superconductor impede the entry of further fluxons[39]. In contrast to the hysteresis, the initial vortex penetration field H_p is characteristic of the coating alone, and is considered in more detail below.

Figure 5.4 shows the results of H_p calculations for coating resistivity values ranging from $\rho_N = 0.1\rho_S$ to $\rho_N = 10\rho_S$ at κ values of 2, 5, 10 and 20. H_p was calculated for both rectangular (open symbols) and circular superconductors (closed symbols). It is clear that $H_p(\rho_N/\rho_S)$ has a minimum value ($H_{p(min)}$) that is *lower* than the extreme metallic limit ($H_p(0)$), and that the resistivity ratio at which the minimum occurs $(\rho_N/\rho_S)_{opt}$, decreases as κ increases. The y-axes on Fig. 5.4 have been scaled so that the extreme metallic ($\rho_N = 0$) and insulating ($\rho_N = \infty$) limits are at the same positions for all values of κ (the H_p values at these two limits converge in the extreme high-κ limit[38]). The rectangular and circular H_p results agree to within a reasonable accuracy and the computed H_p values in Fig. 5.4 for the extreme limits are equivalent to values determined by the Bean-Livingston and Matricon calculations. We

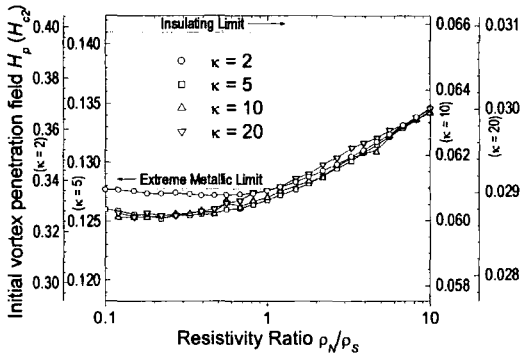

Figure 5.5: Initial vortex penetration field H_p as a function of ρ_N/ρ_S for κ = 2, 5, 10 and 20 for coated rectangular superconductors where $T_{c(N)} = -2T_{c(S)}$. The y-axes are scaled so that the asymptotic values of H_p in both insulating and extreme metallic limits are aligned for all κ values.

therefore conclude that corners are not responsible for determining H_p in the rectangular superconductor and that the grid size is sufficiently large. The literature result that notches[63] reduce H_p and the observation in Fig. 5.1 that fluxons do not enter directly at corners suggest that convex features increase H_p, and in particular that corners do not weaken the surface barrier, thus confirming that the calculated H_p values are those for a straight edge rather than a corner. To confirm that the minimum in Fig. 5.4 is not specific to the conditions $T = T_{c(2)} = 0$, Fig. 5.5 shows the effect of pair-breaking on H_p. The same system is considered as in Fig. 5.4, but at $T = \frac{2}{3}T_{c(1)}$ and $T_{c(2)} = 0$ (this is also equivalent to $T = 0$ and $T_{c(2)} = -2T_{c(1)}$).

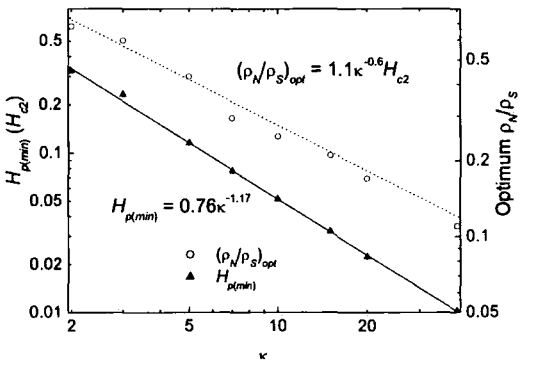

Figure 5.6: Minimum initial vortex penetration field $H_{p(min)}$ (left axis) and required resistivity ratio ρ_N/ρ_S (right axis) as a function of κ.

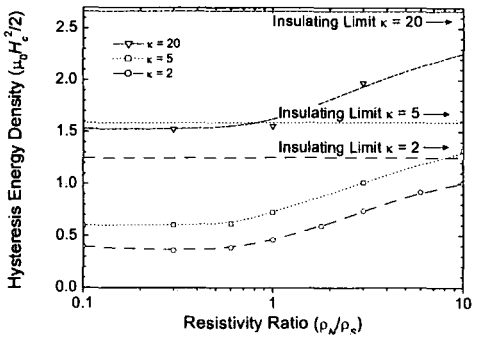

Figure 5.7: Hysteretic energy density as a function of ρ_N/ρ_S at $\kappa = 2$, 5 and 20.

In this system the minimum is attenuated considerably, as the pair-breaking forces $\hat{\psi}$ rapidly to zero in the normal metal, reinforcing the surface barrier for $\rho_N < \rho_S$, while weakening it for $\rho_N > \rho_S$. However, the minimum is not suppressed completely. The convergence of the data at high ρ_N/ρ_S in Figs. 5.4 and 5.5 suggests that in the $\rho_N \gg \rho_S$ limit, $\dfrac{H_p\left(\rho_N/\rho_S\right) - H_p(0)}{H_p(\infty) - H_p(0)}$ depends primarily on ρ_N/ρ_S and T, not κ. Figure 5.6 focuses on the minima in the $H_p(\rho_N/\rho_S)$ characteristics on figure 5.4 (with some additional κ values), and demonstrates that for $T = T_{c(2)} = 0$, $H_{p(min)}$, and $(\rho_N/\rho_S)_{opt}$ have approximate power-law dependences. Figure 5.7 shows the ρ_N/ρ_S dependence of the hysteresis energy, which calculated from the area enclosed by the M-H loop. For $\rho_N > \rho_S$, the hysteresis energy increases with ρ_N/ρ_S, while for $\rho_N < \rho_S$ it is approximately independent of ρ_N/ρ_S. The minimum observed in the H_p characteristic does not appear in the hysteresis energy characteristic because hysteresis energy depends on both flux entry and flux exit, and the barrier for flux exit drops monotonically as ρ_N/ρ_S decreases in the important low field region. This cancels the effect of the H_p minimum on the hysteresis energy.

5.3.3 Bilayer (S'/N) coatings

It is clear from the results presented so far that single normal metal coatings cannot destroy the surface barrier in any significant field range. The effect of a weakly superconducting S' layer between the S and N layers was therefore investigated with the intention of reducing the magnetic hysteresis further and obtaining reversible magnetic behaviour over the widest possible field range.

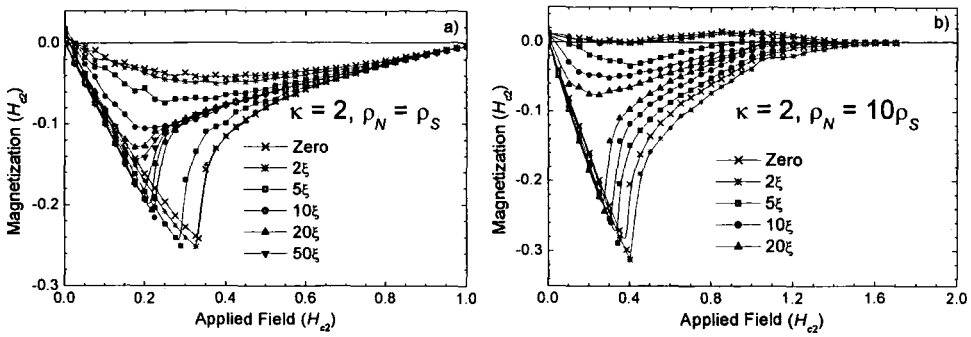

Figure 5.8: Magnetization of a $\kappa = 2$ superconductor coated with weakly superconducting S' layers of thicknesses up to 20ξ and an outer normal layer with a) $\rho_N = \rho_S$ and b) $\rho_N = 10\,\rho_S$.

Figure 5.8 shows examples of magnetization curves calculated for $\kappa = 2$, bilayer coated superconductors. For an N layer with $\rho_N = \rho_S$, adding a 2ξ -thick S' layer has minimal effect, while an S' layer at least 10ξ thick makes the magnetization essentially reversible above $0.4H_{c2}$. For an N layer with $\rho_N = 10\rho_S$ adding an S' layer results in a less pronounced reduction of the hysteresis, and for a 2ξ-thick S' layer there is an anomalous increase in both H_p and hysteresis energy, which is discussed below. It may be noted that the calculations in Fig. 5.8b are more computationally expensive – not only does the large ρ_N require the simulation time-step to be reduced, but the equilibration itself is slower – taking up to 10 times longer in normalized time than for a system with a simple normal metal coating.

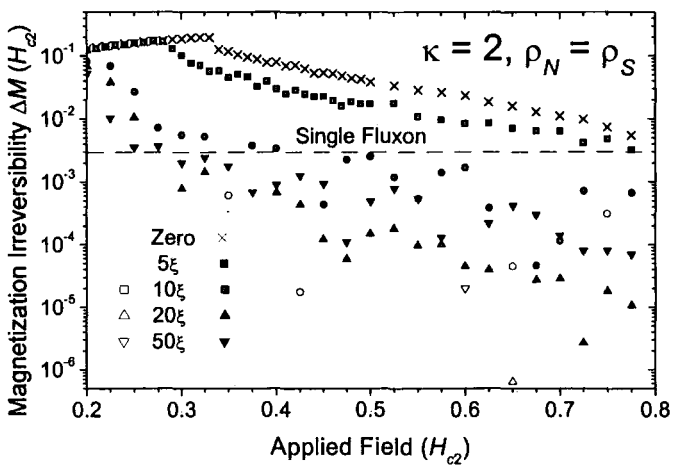

Figure 5.9: Magnetization irreversibility on a logarithmic scale for $\kappa = 2$ superconductors with $\rho_N = \rho_S$ normal metal coatings and S' layers of various thicknesses. (Negative values are indicated by open symbols).

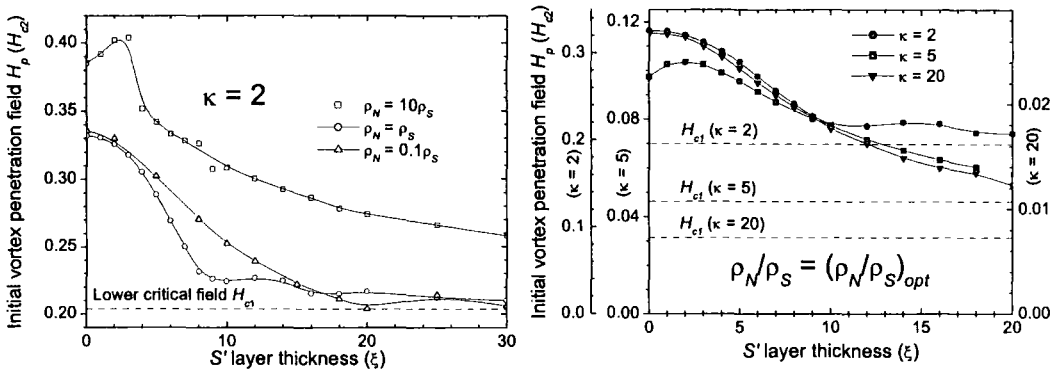

Figure 5.10: Initial vortex penetration field H_p as function of S' thickness for a) $\kappa = 2$ superconductors with $\rho_N = \rho_S$ and $\rho_N = 10\rho_S$ normal metal coatings, and b) $\kappa = 2$, 5 and 20 superconductors with coating resistivity given by $(\rho_N/\rho_S)_{opt}$. The y-axes are normalized to the lower critical field H_{c1}.

In Figure 5.8a the magnetization characteristics for S' thicknesses of 10ξ or more appear to be reversible for fields above $0.3H_{c2}$, which opens the possibility of the existence of an irreversibility field. Since the irreversibility field marks the point at which critical current density J_c becomes zero, it is an important issue both experimentally[71-73] and theoretically[71,72]. The magnetization irreversibility ΔM obtained from the data in Fig. 5.8a is plotted on a logarithmic scale in Fig. 5.9. It is clear that there is no evidence for a phase transition in high fields. For S' thicknesses of 20ξ, ΔM eventually becomes less than that resulting from a single fluxon for $H \geqslant 0.35H_{c2}$. A limited set of calculations for a much larger grid of $250\xi \times 200\xi$, where one fluxon would make a much smaller contribution to M, still showed a non-zero ΔM, thus confirming that the apparent irreversibility field in Fig. 5.8a is not the result of any phase transition.

Figure 5.10a shows H_p as a function of the thickness of S' for $\kappa = 2$ and ρ_N values of $0.1\rho_S$, ρ_S and $10\rho_S$. The anomalous increase in H_p first noted in Figure 5.8b ($\rho_N = 10\rho_S$) is found for S' thicknesses of 3ξ or less and confirmed to exist even when the grid spacing is reduced from 0.5ξ to 0.1ξ. In equation (3.66) for $\rho_N = 10\rho_S$, diffusivity D is decreased within the S' layer, which lowers the kinetic energy term and thus increases $\hat{\psi}$ at the S'/S interface, increasing the energy penalty associated with moving fluxons into the superconductor. For S' thickness of 3ξ or less this effect dominates, resulting in the anomalous H_p increase, while for thicker S'

layers, H_p decreases because the Bean-Livingston image force begins to dominate again. The initial vortex penetration field never reaches the lower critical field value[74] of $0.195H_{c2}$, but instead tends asymptotically to a somewhat higher value of $0.205\ H_{c2}$. This difference and hysteretic behaviour is found even for a 50ξ-thick S' layer (cf Fig 5.8a) and is discussed in the next section. Figure 5.10b demonstrates the effect of changing κ on the H_p characteristic as a function of S' thickness – for all values of κ there is a general trend of decreasing H_p as S' thickness is increased, but again full reversibility is not achieved for thicknesses up to 20ξ.

5.3.4 Irreversible surface current of coated superconductors

In previous sections, we have focused on the magnetization characteristics in their own right, and on the field H_p when the first fluxon enters a Meissner-state superconductor. As our focus in later chapters will be on critical current densities both of single junctions (in chapter 7) and polycrystalline systems (in chapter 9), investigation of the irreversible screening current in a homogenous coated superconductor is potentially useful.

The magnetization of a homogenous macroscopic superconductor as a function of field does not depend on its size – this means that the relevant size-independent quality is the critical current per unit depth in the z-direction (I_{cl}). In the system of normalized units established in Sec. 3.5.2, the natural unit for current per unit depth is H_{c2}/κ^2, and in normalized units it is found from Maxwell's equations using the expression

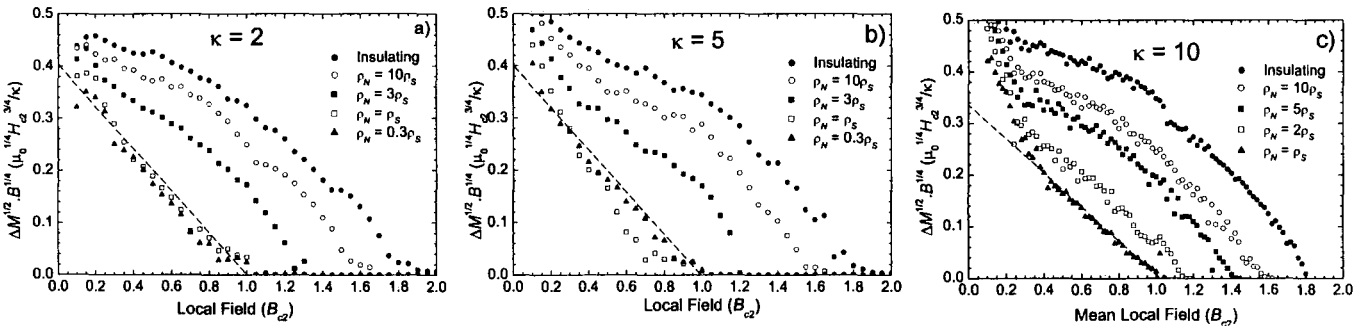

Figure 5.11: Irreversible surface magnetization ΔM presented as a Kramer plot for superconductors with an insulating surface or normal metal coatings of various resistivities – a) $\kappa = 2$, b) $\kappa = 5$, c) $\kappa = 10$.

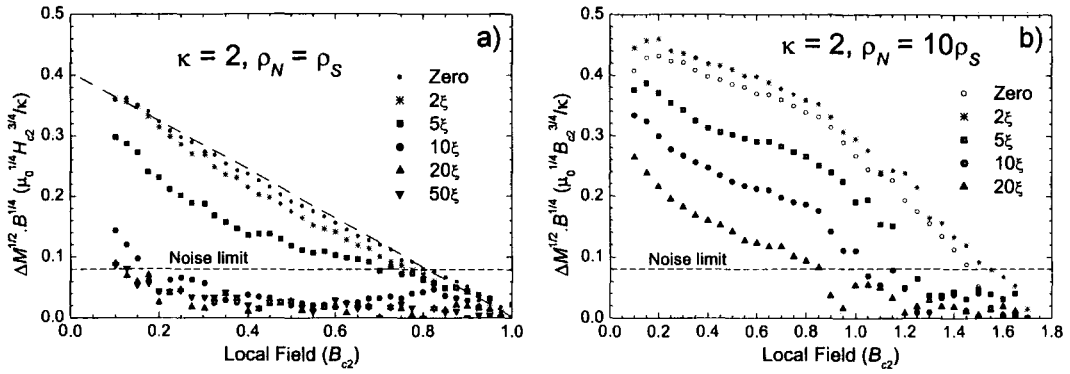

Figure 5.12: Irreversible surface magnetization presented as a Kramer plot for $\kappa = 2$ superconductors coated with weakly superconducting S' layers of thicknesses up to 20ξ and an outer normal layer with a) $\rho_N = \rho_S$ and b) $\rho_N = 10\,\rho_S$.

$$I_{cl} = \frac{\kappa^2 \Delta M}{2} \tag{5.2}$$

A Kramer plot provides $I_{cl}^{1/2}B^{1/4}$ as a function of B – so called because the field dependence $I_{cl} \propto B^{-1/2}(1 - B/B_{c2})^2$, predicted by Kramer's flux-shear model of flux pinning[75] appears as a straight line. The magnetization data from Fig. 5.3 is re-plotted as a Kramer plot in Fig. 5.11. The normalized I_{cl} for a superconductor with a simple coating is approximately independent of κ (this means the actual current is proportional to $1/\kappa^2$). In high fields, I_{cl} obeys the Kramer dependence rather accurately. When the coating $\rho_N \leq \rho_S$, I_{cl} follows the Kramer dependence across the entire field range. The bilayer coating data from Fig. 5.8 has also been re-plotted as a Kramer plot in Fig. 5.12 – this shows that I_{cl} only exhibits the Kramer-like dependence for an abrupt superconducting/normal interface where $\rho_N \leq \rho_S$. A high-field Kramer-like dependence is however still noticeable in Fig. 5.12b. Below $0.08\mu_0^{1/4}H_{c2}^{3/4}/\kappa$, the data become unreliable as the magnetization irreversibility is equivalent to that of only one or two fluxons.

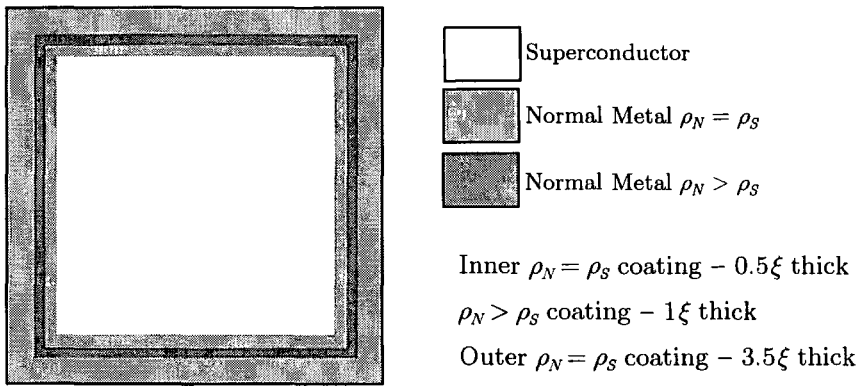

Figure 5.13: Diagram of the trilayer coated superconductor

5.4 Trilayer coatings

Microstructural analysis shows that in grain boundaries in polycrystalline superconductors, $\rho_N > \rho_S$ due to increased electron scattering at the dislocations present along the grain boundary. However, significant H_{c3} effects are not generally observed in polycrystalline superconductors. This could possibly be explained by the region over which superconductivity is destroyed being wider than the region of increased resistivity – this proposition for grain boundary properties is discussed in more detail in Sec. 6.6. Hence a trilayer-coated superconductor as shown in Fig. 5.13, with a thin $\rho_N = \rho_S$ normal metal layer between the superconductor and the $\rho_N > \rho_S$ layer, is considered in this section as a possible building block for polycrystalline superconductors. The magnetization characteristics of such as system can be compared with that resulting from the simple metal coating studied in Sec. 5.3.2. As in section 5.3.4, the magnetization irreversibility is plotted on a Kramer plot:

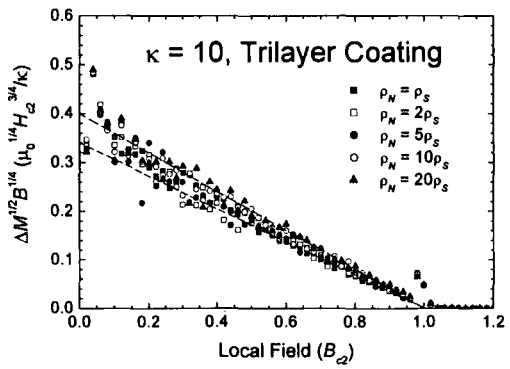

Figure 5.14: Magnetization per unit depth presented as a Kramer plot for $\kappa = 10$ superconductors with a trilayer coating shown in Fig. 13. The anomaly at $H \approx H_{c2}$ results from the delay in the nucleation of superconductivity on the downward ramp. This shows that ρ_N/ρ_S in a trilayer coating has a small effect on ΔM

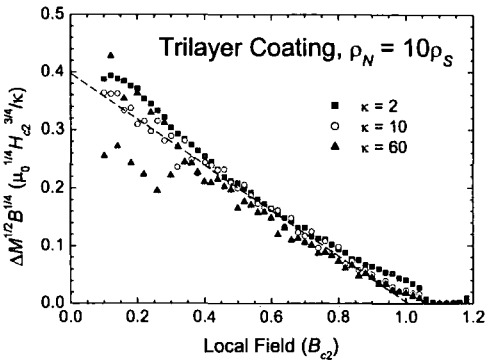

Figure 5.15: Magnetization irreversibility presented as a Kramer plot for superconductors with κ values of 2, 10 and 60 superconductors and with a $\rho_N = 10\rho_S$ trilayer coating.

Fig. 5.14 shows the effect of changing ρ_N/ρ_S on the magnetization irreversibility of a $\kappa = 10$ superconductor. It can thus be shown that the magnetization of a trilayer-coated superconductor is thus similar to that of one simply coated with a superconductor with $\rho_N = \rho_S$. ΔM is proportional to $1/\kappa^2$, while increasing the resistivity of the inner normal metal layer from ρ_S to $20\rho_S$ increases ΔM by $\approx 40\%$. For $\rho_N \geq \rho_S$, the magnetization irreversibility of a trilayer-coated superconductor can be approximated by the expression

$$\Delta M \approx \left(0.17 - 0.06 \exp\frac{-\rho_N}{6\rho_S}\right) \frac{H_{c2}}{\kappa^2} b^{-1/2} (1-b)^2 \qquad (5.3)$$

where b is the reduced local field B/B_{c2}. Figure 5.15 investigates the κ-dependence of ΔM for a superconductor coated with a $\rho_N = 10\rho_S$ trilayer coating – the κ-independence of the normalized current per unit depth confirms the κ dependence of (5.3). We shall return to this result in Chapter 8.

5.5 Trilayer annular superconductors

5.5.1 Introduction

We conclude our magnetization studies of barriers to flux entry and exit in relatively simple superconductor systems by considering one superconductor inside another, with a trilayer barrier at the interface. The outer superconductor has a normal coating with $\rho_N = \rho_S$. Such a system will help us consider the pinning of fluxons against perpendicular grain boundaries.

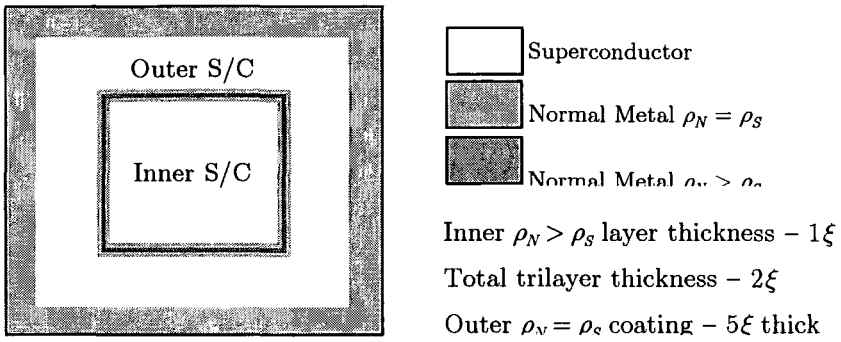

Figure 5.16: Diagram of the trilayer annular superconductor system

This system is illustrated in Fig. 5.16 – it is expected that the inner superconductor will have little effect on the screening current that flows around the outer region, which will be the same as for a homogenous 2D superconductor coated in a $\rho_N = \rho_S$ normal metal (ie the $\rho_N = \rho_S$ results in Section 5.3.2, or the data in Fig. 5.11a). However, the trilayer impedes flux entering the inner superconductor, and thus generates a second inner screening current.

5.5.2 ΔM_{inner} and ΔM_{outer}

We have chosen to define the magnetization of the inner region M_{inner} in terms of the inner screening current, so that

$$M_{inner} = \frac{B_{inner} - B_{outer}}{\mu_0} \tag{5.4a}$$

$$M_{outer} = \frac{B_{outer} - B_{applied}}{\mu_0} \tag{5.4b}$$

In Fig. 5.17 we indeed see that the magnetization irreversibility is greater for the inner region (in fact about twice as large) than for the outer region.

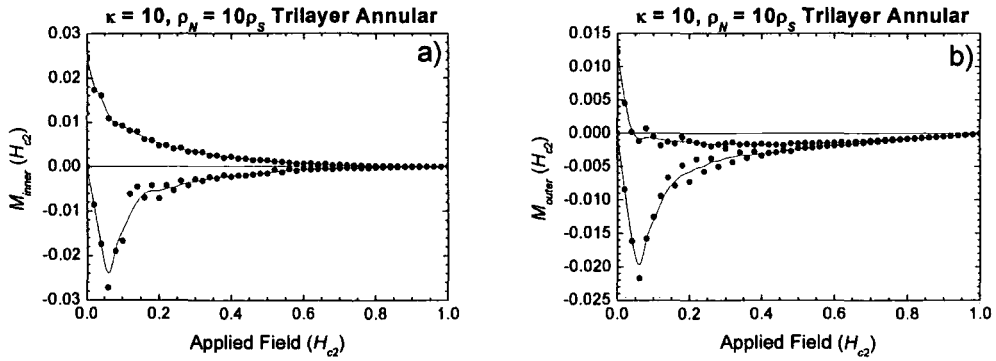

Figure 5.17: Magnetization characteristics for a) inner and b) outer regions of annular superconductor system with trilayer boundary ($T = T_c/2$, $\kappa = 10$, $\rho_N = 10\rho_S$)

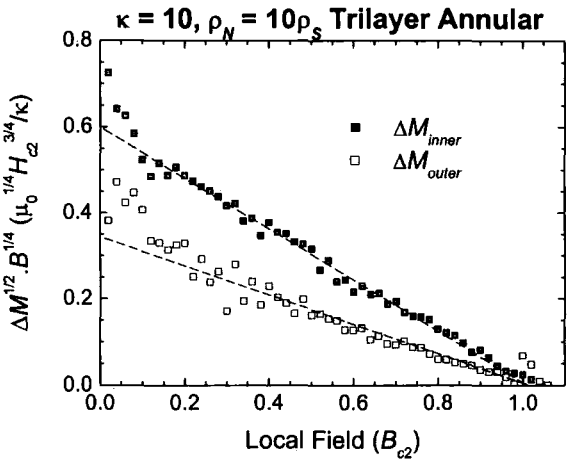

Figure 5.18: Magnetization irreversibility for inner and outer regions of annular superconductor system with trilayer boundary ($T = T_c/2$, $\kappa = 10$, $\rho_N = 10\rho_S$)

Figure 5.18 shows $(\Delta M_{outer})^{1/2}B^{1/4}$ and $(\Delta M_{inner})^{1/2}B^{1/4}$. It shows that the magnetization irreversibility contribution from the trilayer barrier follows the $\Delta M \propto b^{-1/2}(1-b)^2$ dependence even more closely than that from the outer superconducting-normal interface, and for this system is $\approx 2.1\Delta M_{outer}$.

5.5.3 κ and T dependence of ΔM_{inner}

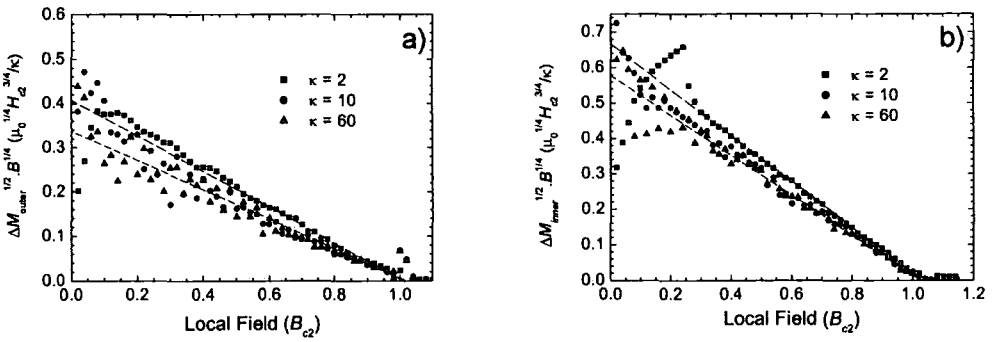

Figure 5.19: Magnetization irreversibility contributions in annular superconductor system from a) the outer S/N interface and b) the trilayer barrier as a function of κ ($T = T_c/2$, $\rho_N = 10\rho_S$). In both cases $\Delta M/\kappa^2$ is 33% larger for $\kappa = 2$ than for the higher κ values – this is because ΔM is in fact proportional to $(2\kappa^2 - 1)^{-1}$.

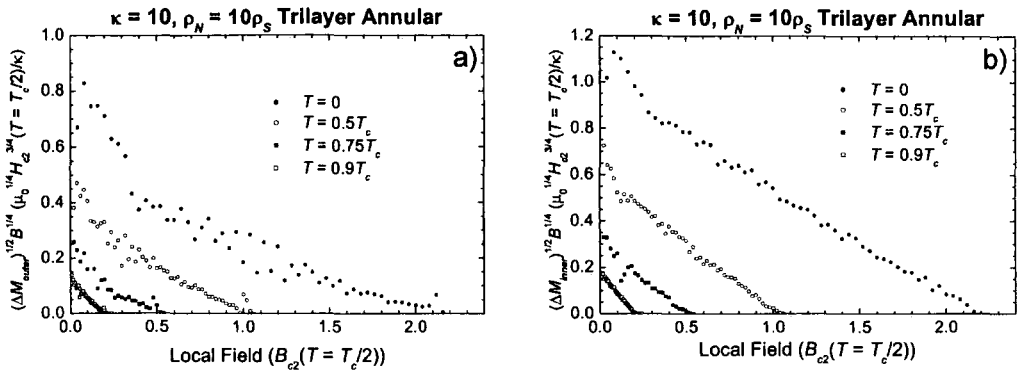

Figure 5.20: Magnetization irreversibility contributions from a) the outer S/N interface and b) the trilayer barrier for inner and outer regions of annular superconductor system with trilayer boundary as a function of temperature ($\kappa = 10$, $\rho_N = 10\rho_S$)

In addition to the applied magnetic field, the magnetization irreversibility contributions from both the outer superconductor surface and the trilayer barrier will depend on κ and temperature. The κ-dependence checks in Fig. 5.19 show no noticeable difference in $\Delta M/\kappa^2$ between $\kappa = 10$ and $\kappa = 60$, but a value of $\Delta M/\kappa^2$ about 33% higher for $\kappa = 2$. This is significant as it suggests that in fact $\Delta M \propto (2\kappa^2 - 1)^{-1}$ – this is significant as it is the same κ dependence predicted by Abrikosov[14] for M itself in a reversible superconductor.

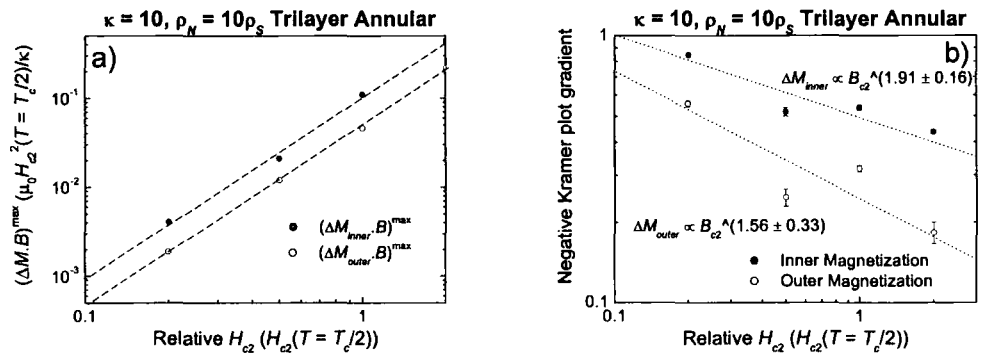

Figure 5.21: a) maximum pinning pressure on the outer S-N interface and the trilayer barrier as a function of relative H_{c2}. This suggests an H_{c2}^2 dependence. b) Kramer plot (see Fig. 5.) gradients for the outer and inner irreversible magnetization – H_{c2} dependence calculated from these are also shown. These are different because they are calculated from the high-field gradient, not the P_f maximum (which is at low fields)

The temperature dependence must also be checked. Calculations were made on the $\kappa = 10$, $\rho_N = 10\rho_S$ inner layer system corresponding to operating temperatures of zero, $0.5T_c$, $0.75T_c$ and $0.9T_c$. The effect of changing temperature on the differential magnetizations of the trilayer annular superconductor is shown in Fig. 5.20. In scaling laws for critical current density[26,30], the temperature dependence is normally expressed in terms of dependence on the upper critical field. The H_{c2}-dependence of data obtained experimentally is checked by plotting the maximum pinning force $F_p^{\max}$ against the upper critical field H_{c2} on a log-log scale[28]. The gradient gives the dependence $F_p \propto {H_{c2}}^n$, with n usually between 2 and 3. In Fig. 5.21 the inner and outer differential magnetizations are analyzed using a similar method. Instead of $F_p^{\max}$, $(\Delta M.B)^{\max}$ is plotted against H_{c2}. It may be noted that $\Delta M.B$ is equivalent to the pressure applied to the flux line lattice at a surface by the magnetic field differential. Both the outer and inner contributions $\Delta M.B$ are found to be proportional to ${H_{c2}}^2$. Assuming the same relative ρ_N/ρ_S dependence as for the outer coating, we obtain a final expression for ΔM_{inner} based on the computational results, given by:

$$\Delta M_{inner} \approx \left(0.76 - 0.27 \exp \frac{-\rho_N}{6\rho_S}\right) \frac{H_{c2}}{\left(2\kappa^2 - 1\right)} b^{-1/2} (1-b)^2 . \qquad (5.5)$$

ΔM_{inner} is about 2½ times the value of ΔM_{outer}, which is given by (5.3).

5.5.4 Analytic calculation of ΔM_{inner}

The maximum differential magnetic field supportable by the (trilayer) normal barrier can be approximated using a simple pinning argument, following the approach used by Dew-Hughes[25] for a range of pinning sites in 3D superconductors. The Lorentz force expression in superconductors is[28]

$$\mathbf{F}_p = \mathbf{J} \times \mathbf{B} \qquad (5.6)$$

where $\mathbf{F}_p$ is the pinning force per unit volume and $\mathbf{J}$ is the current density. Applying Ampère's law we get

$$\mathbf{F}_p = -\frac{1}{\mu_0} \mathbf{B} \times \nabla \times \mathbf{B} \qquad (5.7)$$

If we take a line integral through the barrier, connecting regions far away from the barrier on either side, we obtain a pressure P_f which the normal metal barrier must exert on the FLL to prevent flux flow:

$$P_f = -\int_{inside}^{outside} \mathbf{F}_p.\mathbf{dr} = \frac{1}{\mu_0}\int_{inside}^{outside} (\mathbf{B}\times\nabla\times\mathbf{B}).\mathbf{dr}$$

$$= \frac{1}{\mu_0}\left[\frac{B_{out}^2 - B_{in}^2}{2} + \int_{inside}^{outside} (\mathbf{B}.\nabla)\mathbf{B}.\mathbf{dr}\right] \tag{5.8}$$

The integral $\int_{inside}^{outside} (\mathbf{B}.\nabla)\mathbf{B}.\mathbf{dr}$ is zero for any 2D system as $\mathbf{B}$ points in the z-direction while being dependent only on x and y. We define ΔB as $B_{out} - B_{in}$ and B as $\frac{1}{2}(B_{out} + B_{in})$ – note that in high fields or high-κ superconductors, B, B_{in}, $B_{out} \gg \Delta B$:

$$\Rightarrow \qquad \Delta B = \frac{\mu_0 P_f}{B}. \tag{5.9}$$

The Lorentz pressure P_f is given by[25]

$$P_f = \frac{f_p}{a_0} = \frac{\Delta W}{a_0 x} \tag{5.10}$$

where f_p is the pinning force per unit length on an individual fluxon, which is ΔW – the work done moving a fluxon from a pinned to an unpinned position – divided by x – the range of the pinning interaction. a_0 is the fluxon-fluxon spacing, given by[76]:

$$a_0 = (\tfrac{1}{3})^{1/4}\sqrt{\frac{\phi_0}{B}} \tag{5.11}$$

For a normal layer of thickness much less than the fluxon-fluxon spacing a_0, the range x of the pinning interaction is approximately equal to the coherence length ξ, while ΔW is approximately equal to the Gibbs energy per unit volume multiplied by the area of the fluxon core[77]:

$$\Rightarrow \qquad \Delta W = \frac{\pi\xi^2\mu_0 H_{c2}^2}{2\beta_A\left(2\kappa^2 - 1\right)}(1-b)^2. \tag{5.12}$$

Combining (5.9) through (5.12) we get the final expression for ΔM_{inner} $(= \Delta B/\mu_0)$

$$\Delta M_{inner} = \frac{3^{1/4}\sqrt{\pi}}{4\beta_A}\frac{H_{c2}}{\left(2\kappa^2 - 1\right)} b^{-1/2}(1-b)^2. \tag{5.13}$$

This predicted ΔM_{inner} is within about 6% of the computed value given by (5.5) for $\rho_N = \rho_S$.

5.6 Discussion of magnetization results and H_p

5.6.1 The effect of coatings on H_p

The value of H_p is determined principally by two considerations. The first is the gradient of the order parameter at the interface of the superconductor. The dependence of H_p on the gradient explains the existence of the minimum. Both very low and very high ρ_N/ρ_S have high H_p as the interface boundary conditions force a steep gradient: on the N side of the interface for high ρ_N/ρ_S and on the S side for low ρ_N/ρ_S. This means that in both of theses cases the Bean-Livingston 'image force' is close to full strength. Close to $(\rho_N/\rho_S)_{opt}$, the screening supercurrent extends somewhat into the normal metal, weakening the image force and lowering H_p. This dependence of H_p on $\nabla\hat{\psi}$ also explains why adding a weakly superconducting S' layer reduces H_p, as $\hat{\psi}$ is gradually reduced to zero over the width of the S' layer. The decrease in $(\rho_N/\rho_S)_{opt}$ as κ increases results from the second Ginzburg-Landau equation – at high κ values the screening current can penetrate further into the normal metal, meaning gradients at the interface are optimized at a lower ρ_N/ρ_S value. The first Ginzburg-Landau equation only plays a minor role – it was found that changing the relation between D_N/D_S and ρ_N/ρ_S changed $H_{p(min)}$ but not $(\rho_N/\rho_S)_{opt}$.

The second consideration in determining H_p is the value of $\hat{\psi}$ itself at the interface. In the extreme metallic limit, $\hat{\psi} = 0$ at the interface while in the insulating limit $\hat{\psi}$ at zero field is the Meissner state value. $\hat{\psi}$ must be reduced to zero near the edge of the superconductor before any fluxons can enter, which results in a greater energy penalty for fluxon entry in the insulating limit, and thus a higher H_p than for the extreme metallic limit[39]. This 'condensation energy' consideration also explains the anomalous increase in H_p observed in Figure 5.8b.

Finally we consider the general issue of the field-dependence of the hysteretic magnetization data. Clearly, the reversible magnetization of a superconductor does not depend on its shape or size, provided that the separation between parallel surfaces size is much larger than $\sim 20\lambda$ (λ = penetration depth). The surface barrier contribution to the irreversible magnetization

can be interpreted as a critical current along the surface of the superconductor per unit length in the z-direction, and is thus also independent of shape and size. This means that the magnetization characteristics presented in Figs. 5.3 and 5.8 are completely general for a given κ value and type of surface (as long as the surfaces are well-separated), rather than being specific to a given shape or size. These calculations have also confirmed that thick smooth S' layers cannot completely destroy the surface barrier, to achieve complete reversibility surface defects such as notches or surface roughness are required[63]. Finally, we also note from the hysteretic data in Fig. 5.3 that the magnitude of ΔM for the superconductors with insulating coatings can be approximated by

$$\Delta M \approx \frac{0.35}{\kappa^2 \sqrt{H_{c2}}} (H_{c3} - H)^{3/2} . \tag{5.14}$$

If we consider a thin film conductor of thickness $\sim \lambda$, for example of a high-temperature superconducting RABITS conductor[73], the surface contribution to the average current density (J_c) is $\Delta M/\lambda$ which can be rewritten: $J_c \approx 0.64 J_D/\kappa$ (where $J_D \approx H_c/\lambda$ is the theoretical upper limit known as the depairing current density[19]). Such high current densities are clearly of technological interest.

5.6.2 Comparison with experimental results

In general it is difficult to compare theoretical or computational predictions on the behaviour of the surface barrier with experimental results. In most samples the barrier is removed by suppression of the superconductivity near the surface (due for example to oxidation), by roughness of the surface (the effect of notches on H_p has been investigated computationally[63]), or by the presence of twins boundaries or other defects. In such samples the effect of the surface barrier is only seen in the immediate vicinity of H_{c1}, and is usually therefore obscured by the effects of bulk pinning.

Surfaces which are flat on the scale of the coherence length are needed to observed the full Bean-Livingston barrier, meaning that most observations of a significant surface barrier have been in single crystals of YBCO[78] and Bi-2212[79]. However, surface barriers strong enough for

the characteristic asymmetric irreversibility have also been observed in a thin well-annealed sample of elemental niobium[79] and in powdered MgB_2[80].

There has been very little experimental work on the effect of plating a superconductor with a normal metal, although measurements on cylindrical samples of a niobium-zirconium alloy[81] showed a small decrease in magnetization irreversibility on plating with silver, although this was not considered significant by the authors. The computational work presented in Section 5.3.3 of this chapter shows that diffusing the boundary between a superconductor and its normal-metal coating reduces surface hysteresis. Such behaviour has been observed in metallic interdiffusion experiments on a lead-thallium alloy[70] and in oxide-coated niobium[82].

5.7 Conclusions

Magnetic properties of superconductors coated with metals of arbitrary resistivity ρ_N are calculated using the time-dependent Ginzburg-Landau equations, with generalized boundary conditions applicable for systems in which both T_c and ρ_N vary. The initial vortex penetration field $H_p(\rho_N)$ is maximized at the insulating (Matricon) limit, but is minimized not at the extreme metallic (Bean-Livingston) limit, but at a finite coating resistivity $\rho_{N(\mathrm{opt})}$: this is because for a coating of finite resistivity (i.e. not in the extreme metallic or insulating limits) the surface barrier is weakened by proximity-effect penetration of superelectrons into the coating. When a magnetic field is applied to a coated superconductor, local depressions in ψ nucleate in the coating which do not have the well-know quantum of magnetic flux ($h/2e$) until they have crossed the coating and entered the superconductor. In the specific case where $T = T_{c(\mathrm{coating})} = 0$, the minimum vortex penetration field $H_{p(\mathrm{min})} \approx 0.76\kappa^{-1.17}H_{c2}$ which occurs for a coating resistivity $\rho_{N(\mathrm{opt})} \approx 1.1\kappa^{-0.6}\rho_S$. For $T > 0$ the minimum is attenuated but not completely suppressed. Adding a very thick weakly superconducting S' layer between the superconductor and normal metal coating reduces the irreversibility markedly but does not eliminate it entirely.

We have also found that the irreversible component of the magnetization (and therefore the associated surface currents) for some simple, bilayer and trilayer coatings follow a Kramer-like $b^{-\frac{1}{2}}(1 - b)^2$ field dependence – this is not predicted by the standard analytic work on surface barriers and is in fact more similar (though smaller in magnitude) to the pinning of fluxons by planar normal metal barriers – normal metal barriers of trilayer cross section were tested computationally and found to correspond reasonably well with the simple analytic model postulated by Dew-Hughes[25].

These results are discussed in the context of polycrystalline materials in Chapter 9.

6 New analytic calculations of surface-barrier ΔM

6.1 Introduction

The well-known Bean-Livingston surface barrier calculation[14] was the first attempt to explain the barrier to initial flux entry into a superconductor. It featured an easily-understandable physical model, in which the force produced by the applied field, tending to pull a fluxon into the superconductor, is opposed by a force produced by an 'image fluxon' which represents the distortion of the fluxon caused by the edge of the superconductor.

The original calculation by Bean and Livingston is based on the London model. As a result it fails to describe the fluxon core correctly and gives a final result for the penetration field which is a factor of $\sqrt{2}$ too small. In section 6.2 we use a new formulation of the Ginzburg-Landau equations to replace the London equations, coupled with Clem's simple approximate model of the flux core, to repeat the calculation for the penetration field (H_p) with a more realistic core, and thus achieve the correct result for H_p, while keeping the physical transparency of the original model.

In section 6.3 we calculate the surface barrier for a fluxon entering the mixed state of a superconductor, based on the force between partial Abrikosov lattices of opposing polarity. This new calculation provides a rigorous explanation for the magnetization characteristics observed in the previous chapter.

6.2 Calculation of initial entry field for Meissner state

6.2.1 Simplifying the Ginzburg-Landau functional

In Ginzburg-Landau theory the Helmholtz free energy density is[13]:

$$f = \frac{\phi_0^2}{8\pi^2\mu_0\lambda^2}\left[\frac{1}{2\xi^2}\left(1-\left|\hat{\psi}\right|^2\right)^2 + \left|\left(\frac{\nabla}{i}-\frac{2\pi}{\phi_0}\mathbf{A}\right)\hat{\psi}\right|^2\right] + \frac{\mathbf{B}^2}{2\mu_0} \qquad (6.1)$$

while the vector potential **A** is given by the second Ginzburg-Landau equation

$$\nabla\times\nabla\times\mathbf{A}=\frac{\phi_0}{2\pi\lambda^2}\mathrm{Re}\left[\hat{\psi}^*\left(\frac{\nabla}{i}-\frac{2\pi}{\phi_0}\mathbf{A}\right)\hat{\psi}\right] \tag{6.2}$$

We use the gauge transformation given by (3.59) to set $\hat{\psi}$ to be always real. This gauge was used in 1D by Matricon[38], but is used below for a 2D problem. Equations (6.1) and (6.2) can thus be rewritten:

$$f=\frac{\phi_0^2}{8\pi^2\mu_0\lambda^2}\left[\frac{1}{2\xi^2}\left(1-\hat{\psi}^2\right)^2+\left|\nabla\hat{\psi}\right|^2+\frac{4\pi^2}{\phi_0^2}\mathbf{A}^2\hat{\psi}^2\right]+\frac{\mathbf{B}^2}{2\mu_0} \tag{6.3}$$

$$\mu_0\mathbf{J}=\nabla\times\nabla\times\mathbf{A}=-\frac{\hat{\psi}^2\mathbf{A}}{\lambda^2} \tag{6.4}$$

Re-writing to replace **A** with the magnetic field **B**, we get

$$f=\frac{\phi_0^2}{8\pi^2\mu_0\lambda^2}\left(\frac{1}{2\xi^2}\left(1-\hat{\psi}^2\right)^2-\left|\nabla\hat{\psi}\right|^2\right)+\frac{1}{2\mu_0}\left(\mathbf{B}^2+\frac{\lambda^2}{\hat{\psi}^2}\left|\nabla\times\mathbf{B}\right|^2\right) \tag{6.5}$$

$$\nabla\times\nabla\times\mathbf{B}=-\frac{\hat{\psi}^2\mathbf{B}}{\lambda^2}+\frac{\nabla\left(\hat{\psi}^2\right)}{\hat{\psi}^2}\times\nabla\times\mathbf{B} \tag{6.6}$$

The second term in (6.5) resembles the London expression[19] for f, but with a $\hat{\psi}^2$ in the denominator of the $|\nabla\times\mathbf{B}|^2$ term, which ensures that no arbitrary cut-off at the fluxon core is needed. (6.5) can be re-arranged to give this London-like term as a divergence of a vector field, reducing the double integral for F to a single integral. Using the vector identity[83] $|\nabla\times\mathbf{B}|^2\equiv\mathbf{B}.\nabla\times\nabla\times\mathbf{B}+\nabla.(\mathbf{B}\times\nabla\times\mathbf{B})$ and substituting from (6.6) the expression becomes

$$\Rightarrow\quad f=\frac{\phi_0^2}{8\pi^2\mu_0\lambda^2}\left(\frac{1}{2\xi^2}\left(1-\hat{\psi}^2\right)^2+\left|\nabla\hat{\psi}\right|^2\right)+\frac{\lambda^2}{2\mu_0\hat{\psi}^2}\left[\mathbf{B}.\left(\frac{\nabla\left(\hat{\psi}^2\right)}{\hat{\psi}^2}\times\nabla\times\mathbf{B}\right)+\nabla.(\mathbf{B}\times\nabla\times\mathbf{B})\right] \tag{6.7}$$

Applying the identities[83] $f\nabla.\mathbf{a}\equiv\nabla.(f\mathbf{a})-\mathbf{a}.\nabla f$ and $(\mathbf{a}.\mathbf{b}\times\mathbf{c}+\mathbf{b}.\mathbf{a}\times\mathbf{c}\equiv 0)$ we reach the final expression for f in terms of $\hat{\psi}$ and **B**. The expression includes $f_{condensation}$ (Landau terms and kinetic energy term from depression of $\hat{\psi}$) and f_{M+K} (term corresponding to London terms):

$$f=\underbrace{\frac{\phi_0^2}{8\pi^2\mu_0\lambda^2}\left(\frac{1}{2\xi^2}\left(1-\hat{\psi}^2\right)^2+\left|\nabla\hat{\psi}\right|^2\right)}_{f_{condensation}}+\underbrace{\frac{\lambda^2}{2\mu_0}\nabla.\left(\frac{\mathbf{B}}{\hat{\psi}^2}\times\nabla\times\mathbf{B}\right)}_{f_{M+K}} \tag{6.8}$$

The field term can be integrated using the divergence theorem, and thus its pointwise value is only needed at the edges of a superconductor, or in the immediate vicinity of singularities (these occur at the centres of fluxons as $\psi^2\to 0$).

6.2.2 Energy per unit length of a single fluxon in an infinitely large superconductor

The order parameter and field associated with a single fluxon at the origin can be approximated[84] as:

$$\psi^2 = \frac{r^2}{r^2 + \xi_v^2} \tag{6.9}$$

$$\mathbf{B} = \frac{\phi_0}{2\pi\lambda\xi_v} \frac{K_0\left(\sqrt{r^2+\xi_v^2}/\lambda\right)}{K_1\left(\xi_v/\lambda\right)} \hat{\mathbf{z}} \tag{6.10}$$

Substituting into (6.8):

$$\begin{aligned} f_{condensation} &= \frac{\phi_0^2}{8\pi^2\mu_0\lambda^2}\left(\frac{\xi_v^4}{2\xi^2\left(r^2+\xi_v^2\right)^2} - \frac{\xi_v^4}{\left(r^2+\xi_v^2\right)^3}\right) \\ f_{M+K} &= \frac{\phi_0^2}{8\pi^2\mu_0\lambda\xi_v^2}\nabla.\left(\frac{\sqrt{r^2+\xi_v^2}}{r}\frac{K_0\left(\sqrt{r^2+\xi_v^2}/\lambda\right)K_1\left(\sqrt{r^2+\xi_v^2}/\lambda\right)}{K_1^2\left(\xi_v/\lambda\right)}\hat{\mathbf{r}}\right) \end{aligned} \tag{6.11}$$

Integrating $f_{condesmation}$ and f_{M+K} over all space gives the free energy per unit length F_l:

$$F_{l(condensation)} = \frac{\phi_0^2\left(\xi^2+\xi_v^2\right)}{16\pi\mu_0\lambda^2\xi^2} \tag{6.12}$$

$$F_{l(M+K)} = -\frac{\phi_0^2}{8\pi^2\mu_0\lambda\xi_v^2}\iint_{all\ space}\nabla.\left(\frac{\sqrt{r^2+\xi_v^2}}{r}\frac{K_0\left(\sqrt{r^2+\xi_v^2}/\lambda\right)K_1\left(\sqrt{r^2+\xi_v^2}/\lambda\right)}{K_1^2\left(\xi_v/\lambda\right)}\hat{\mathbf{r}}\right)dS$$

The singularity at the origin can be dealt with by converting to polar co-ordinates – this is simplified by the lack of angular dependence:

$$\begin{aligned} &\iint_{all\ space}\nabla.\left(\frac{\sqrt{r^2+\xi_v^2}}{r}\frac{K_0\left(\sqrt{r^2+\xi_v^2}/\lambda\right)K_1\left(\sqrt{r^2+\xi_v^2}/\lambda\right)}{K_1^2\left(\xi_v/\lambda\right)}\hat{\mathbf{r}}\right)dx\,dy \\ &= 2\pi\int_0^\infty r\nabla.\left(\frac{\sqrt{r^2+\xi_v^2}}{r}\frac{K_0\left(\sqrt{r^2+\xi_v^2}/\lambda\right)K_1\left(\sqrt{r^2+\xi_v^2}/\lambda\right)}{K_1^2\left(\xi_v/\lambda\right)}\hat{\mathbf{r}}\right)dr = -2\pi\xi_v\frac{K_0\left(\xi_v/\lambda\right)}{K_1\left(\xi_v/\lambda\right)} \end{aligned}$$

$$\Rightarrow \qquad F_{l(M+K)} = \frac{\phi_0^2}{4\pi\mu_0\lambda\xi_v}\frac{K_0\left(\xi_v/\lambda\right)}{K_1\left(\xi_v/\lambda\right)} \tag{6.13}$$

6.2.3 Energy per unit length of a fluxon-antifluxon pair in an infinitely large superconductor

The next step is to consider a superconductor containing a fluxon and an anti-fluxon separated by a distance $2X$. We shall first calculate $F_{l(M+K)}$ as this is the more important term, corresponding with the free energy obtained from London theory. We can approximate the magnetic field from the fluxon and antifluxon as:

$$\mathbf{B}_{F/A} = \frac{\phi_0}{2\pi\lambda\xi_v}\left(\frac{K_0\left(\sqrt{(x-X)^2+y^2+\xi_v^2}/\lambda\right)}{K_1\left(\xi_v/\lambda\right)} - \frac{K_0\left(\sqrt{(x+X)^2+y^2+\xi_v^2}/\lambda\right)}{K_1\left(\xi_v/\lambda\right)}\right)\hat{\mathbf{z}} \quad (6.14)$$

Note that ψ^2 is even in both x and y, while $\mathbf{B}_{F/A}$ is odd in x and even in y. By the divergence theorem we get

$$F_{l(M+K)} = \frac{\lambda^2}{2\mu_0}\iint \nabla.\left(\frac{\mathbf{B}_{F/A}}{\hat{\psi}^2}\times\nabla\times\mathbf{B}_{F/A}\right)dS = \frac{\lambda^2}{2\mu_0}\oint\left(\frac{\mathbf{B}_{F/A}}{\hat{\psi}^2}\times\nabla\times\mathbf{B}_{F/A}\right).\mathbf{dr} \quad (6.15)$$

Since $\mathbf{B}_{F/A}$ tends exponentially to zero as $x^2 + y^2 \to \infty$, the line integral at infinity is zero-valued. However the divergence theorem is not valid when applied over all space, due to the two singularities. For this reason, we choose an area of integration that consists of all space except for two circles of infinitesimal radius δr around the singularities at $(X, 0)$ and $(-X, 0)$.

$$\Rightarrow \qquad F_{l(M+K)} = -\frac{\lambda^2}{2\mu_0}\left[\oint_{+X}\left(\frac{\mathbf{B}_{F/A}}{\hat{\psi}^2}\times\nabla\times\mathbf{B}_{F/A}\right).\mathbf{dr}_+ + \oint_{-X}\left(\frac{\mathbf{B}_{F/A}}{\hat{\psi}^2}\times\nabla\times\mathbf{B}_{F/A}\right).\mathbf{dr}_-\right] \quad (6.16)$$

where

$$\mathbf{d\hat{r}}_\pm = (x \mp X)\,\hat{\mathbf{x}} + y\hat{\mathbf{y}} \quad (6.17)$$

Since $\mathbf{B}_{F/A}$ runs in the z-direction, and can considered constant in the region of dimension δr, we can take it outside the integrals:

$$F_{l(M+K)} = \frac{\lambda^2}{2\mu_0}\left[B_{F/A}(X\hat{\mathbf{x}})\oint_{+X} r_+\frac{\left(\nabla\times\mathbf{B}_{F/A}\right)}{\hat{\psi}^2}.\mathbf{d\theta}_+ + B_{F/A}(-X\hat{\mathbf{x}})\oint_{-X} r_-\frac{\left(\nabla\times\mathbf{B}_{F/A}\right)}{\hat{\psi}^2}.\mathbf{d\theta}_-\right] \quad (6.18)$$

Now along the circle of the line integral, only the field from the fluxon centred within that circle has its $\nabla \times \mathbf{B}_{F/A}$ orientated in the $\mathbf{d\theta}$ direction. The contributions to $\nabla \times \mathbf{B}_{F/A}$ from

other fluxons or external applied fields sum to zero. We can thus substitute in using (6.9) and (6.10):

$$F_{l(M+K)} = \frac{\phi_0}{4\pi\mu_0\xi_v}\left[\begin{array}{l} B_{F/A}(X\hat{\mathbf{x}})\oint_{+X}\sqrt{r_+^2+\xi_v^2}\,\dfrac{K_1\left(\sqrt{r_+^2+\xi_v^2}/\lambda\right)}{K_1\left(\xi_v/\lambda\right)}d\theta_+ \\ -B_{F/A}(-X\hat{\mathbf{x}})\oint_{-X}\sqrt{r_-^2+\xi_v^2}\,\dfrac{K_1\left(\sqrt{r_-^2+\xi_v^2}/\lambda\right)}{K_1\left(\xi_v/\lambda\right)}d\theta_- \end{array}\right]$$

$$= \frac{\phi_0}{2\mu_0}\left(B_{F/A}(X\hat{\mathbf{x}}) - B_{F/A}(-X\hat{\mathbf{x}})\right) \qquad (6.19)$$

And substituting for $B_{F/A}(X\hat{\mathbf{x}})$ and $B_{F/A}(-X\hat{\mathbf{x}})$ using (6.14) gives the final result:

$$F_{l(M+K)} = \frac{\phi_0^2}{2\pi\mu_0\lambda\xi_v}\left(\frac{K_0\left(\xi_v/\lambda\right)}{K_1\left(\xi_v/\lambda\right)} - \frac{K_0\left(\sqrt{4X^2+\xi_v^2}/\lambda\right)}{K_1\left(\xi_v/\lambda\right)}\right) \qquad (6.20)$$

The first term comes from the fluxon self-energies, while the second term comes from the fluxon-antifluxon interaction. Differentiation gives the pinning force per unit length of fluxon:

$$\mathsf{F}_{l(M+K)} = -\frac{dF_{l(M+K)}}{d(2X)} = -\frac{\phi_0^2}{2\pi\mu_0\lambda^2\xi_v}\frac{2X}{\sqrt{4X^2+\xi_v^2}}\frac{K_1\left(\sqrt{4X^2+\xi_v^2}/\lambda\right)}{K_1\left(\xi_v/\lambda\right)} \qquad (6.21)$$

If X, $\lambda \gg \xi_v$, this expression tends toward the London result[19]:

$$\lim_{X,\lambda\gg\xi_v}\left|\mathsf{F}_{l(M+K)} = -\frac{\phi_0^2}{2\pi\mu_0\lambda^3}\mathrm{sgn}(X)K_1\left(\frac{2|X|}{\lambda}\right) \qquad \left(\mathrm{sgn}(X) = \frac{X}{|X|}\right)\right. \qquad (6.22)$$

To complete the calculation we need the force per unit length resulting from $F_{l(condensation)}$. This attractive interaction is significant when the fluxons are within ~ ξ of each other, as the fluxons 'share' each other's normal regions. Calculation of the force per unit length based on the Clem approximation for $\hat{\psi}$ gives a non-physical result, as the Clem approximation for $\hat{\psi}$ converges to 1 less rapidly than the exact solution for $\hat{\psi}$ when moving away from the fluxon core. A more accurate form for the order parameter of a fluxon at the origin in the London ($\hat{\psi}$ real) gauge is[19]

$$\hat{\psi} = \tanh\left(\frac{\nu\sqrt{x^2+y^2}}{\xi}\right) \qquad (6.23)$$

where ν is a constant of order unity. We approximate the order parameter for a fluxon-antifluxon pair of separation X in the London (ψ real) gauge as

$$\hat{\psi}(x,y) = \tanh\left(\frac{\nu\sqrt{|x-X|^2+y^2}}{\xi}\right) \tag{6.24}$$

A drawback of this expression for $\hat{\psi}$ is that when the fluxon and anti-fluxon coincide ($X = 0$), the order parameter is the same as that for a single fluxon, rather than rising to 1 everwhere as the fluxon and antifluxon annihilate. However, we confirmed using our TDGL computations that the fluxon and antifluxon are only slightly distorted (with $\hat{\psi}$ remaining zero at their centres) right up until the moment of annihilation, at which point the order parameter rapidly increases in time to its Meissner value. This shows that (6.24) is a reasonable approximation to use here.

Subsituting (6.24) into (6.8) gives $f_{condensation}$:

$$f_{condensation} = \frac{\phi_0^2\left(1+2\nu^2\right)}{16\pi^2\mu_0\lambda^2\xi^2}\operatorname{sech}^4\left(\frac{\nu\sqrt{|x-X|^2+y^2}}{\xi}\right) \tag{6.25}$$

As performing a double integral of $f_{condensation}$ to obtain $F_{l(condensation)}$ is extremely difficult, we instead use a single integral to directly obtain the force per unit length of fluxon $\mathcal{F}_{l(condensation)}$:

$$\mathsf{F}_{l(condensation)} = -\frac{dF_{l(condensation)}}{d(2X)} \tag{6.26}$$

Using the fundamental theorem of calculus we can obtain $\mathcal{F}_{l(condensation)}$ from (6.25) by a single integral:

$$\begin{aligned}\mathsf{F}_{l(condensation)} &= -\frac{\phi_0^2\left(1+2\nu^2\right)}{16\pi^2\mu_0\lambda^2\xi^2}\frac{d}{dX}\int_{x=0}^{x=\infty}\int_{y=-\infty}^{y=\infty}\operatorname{sech}^4\left(\frac{\nu\sqrt{|x-X|^2+y^2}}{\xi}\right)dy\,dx \\ &= -\frac{\phi_0^2\left(1+2\nu^2\right)}{16\pi^2\mu_0\lambda^2\xi^2}\int_{y=-\infty}^{y=\infty}\operatorname{sech}^4\left(\frac{\nu\sqrt{X^2+y^2}}{\xi}\right)dy\end{aligned} \tag{6.27}$$

$\mathcal{F}_{l(condensation)}$ is negative (it is an attractive force), and has its largest magnitude at $X = 0$, where we can integrate simply.

$$\begin{aligned}\mathsf{F}_{l(condensation)}(X=0) &= -\frac{\phi_0^2\left(1+2\nu^2\right)}{16\pi^2\mu_0\lambda^2\xi^2}\int_{y=-\infty}^{y=\infty}\operatorname{sech}^4\left(\frac{\nu y}{\xi}\right)dy \\ &= -\frac{\phi_0^2\left(1+2\nu^2\right)}{12\pi^2\mu_0\lambda^2\xi\nu}\end{aligned} \tag{6.28}$$

At the $X \gg \xi$ extreme, we can integrate by approximating the hyperbolic cosine with an exponential.

$$\mathsf{F}_{l(condensation)}(X \gg \xi) \approx -\frac{\phi_0^2(1+2\nu^2)}{\pi^2\mu_0\lambda^2\xi^2}\int_{y=-\infty}^{y=\infty}\exp\left(-\frac{4\nu\sqrt{X^2+y^2}}{\xi}\right)dy$$

$$= -\frac{2\phi_0^2(1+2\nu^2)}{\pi^2\mu_0\lambda^2\xi^2}XK_1\left(\frac{4\nu X}{\xi}\right) \qquad (6.29)$$

In any type-II superconductor, the $K_1\left(4\nu X/\xi\right)$ term in $\mathscr{F}_{l(condensation)}$ decays far faster than the $K_1\left(\sqrt{4X^2+\xi_v^2}/\lambda\right)$ term in $\mathscr{F}_{l(M+K)}$, thus at long range only the magnetic term of the attractive force is significant. $\mathscr{F}_{l(condensation)}(X=0)$ as given by (6.28) is of the same order of magnitude as the maximum magnetic force per unit length, which in the extreme type-II limit is $\mathsf{F}^{\max}_{l(M+K)} = -\frac{\phi_0^2}{4\sqrt{2}\pi\mu_0\lambda^2\xi}$ (we shall see later that this maximum magnetic force per unit length corresponds with a fluxon-antifluxon separation of $\xi/\sqrt{2}$).

We have thus obtained an expression for the force between a fluxon and antifluxon which is more accurate than that given by the London theory. While the London result (6.22) becomes inaccurate when the separation decreases to a few coherence lengths, our own result, given by expressions (6.21), (6.28) and (6.29) only becomes inaccurate when $X \ll \xi$, due to the approximation made in (6.24).

6.2.4 Modelling the Bean-Livingston Barrier (Meissner state)

When an external field is applied to the system, the Helmholtz free energy is no longer the relevant energy describing the system – the Gibbs free energy must be used instead. For an external applied field $\mathbf{H}_{ext}$, the Gibbs energy density is obtained from the Helmholtz energy density by:

$$g = f - \mathbf{H}_{ext}.\mathbf{B} \qquad (6.30)$$

In the Bean-Livingston model for flux entry into a superconductor, we consider only the $x > 0$ region. The field from the fluxon within the superconductor is balanced by an image fluxon field centred at a point outside the superconductor, in order that no current pass through the edge. The magnetic field in the system is given by $\mathbf{B} = \mathbf{B}_{F/A} + \mathbf{B}_{ext}$, where:

$$\mathbf{B}_{ext} = \mu_0 H_{ext} \exp\left(-\frac{x}{\lambda}\right)\hat{\mathbf{z}} \qquad (x > 0) \tag{6.31}$$

Multiplying out the Helmholtz energy term f_{M+K} we get the expression for the Gibbs energy – the Helmholtz terms are within the square bracket (note that for now we ignore the $f_{condensation}$ term – we shall return to this at the end of the section):

$$G_{l(M+K)} = \iint_{x>0} \left\{ \begin{bmatrix} \nabla.\left(\frac{\mathbf{B}_{F/A}}{\hat{\psi}^2} \times \nabla \times \mathbf{B}_{F/A}\right) + \nabla.\left(\frac{\mathbf{B}_{ext}}{\hat{\psi}^2} \times \nabla \times \mathbf{B}_{F/A}\right) \\ + \nabla.\left(\frac{\mathbf{B}_{F/A}}{\hat{\psi}^2} \times \nabla \times \mathbf{B}_{ext}\right) + \nabla.\left(\frac{\mathbf{B}_{ext}}{\hat{\psi}^2} \times \nabla \times \mathbf{B}_{ext}\right) \end{bmatrix} - \mathbf{H}_{ext}.\mathbf{B} \right\} dS \tag{6.32}$$

We can get the first of the four Helmholtz terms (the fluxon self-energy and fluxon-antifluxon interaction) by halving (6.20) – f_{M+K} is symmetric about the y-axis for this system:

$$F_{l(M+K)}^{(F/A)} = \frac{\phi_0^2}{4\pi\mu_0\lambda\xi_v}\left(\frac{K_0\left(\xi_v/\lambda\right)}{K_1\left(\xi_v/\lambda\right)} - \frac{K_0\left(\sqrt{4X^2+\xi_v^2}/\lambda\right)}{K_1\left(\xi_v/\lambda\right)}\right) \tag{6.33}$$

The fourth Helmholtz term and the $-\mathbf{H}_{ext}.\mathbf{B}_{ext}$ term are both problematic as they tend to infinity when integrated over y, but they can be removed from the expression as they do not depend on the position of the fluxon and are therefore not physically important. The third Helmholtz term can also be omitted as it is zero – around the fluxon it is zero as $\nabla \times \mathbf{B}_{ext}.\mathbf{dr}_+$ averages to zero over all angles, and along the y-axis it is zero because $\mathbf{B}_{F/A}(y=0) \equiv 0$. We therefore get an expression for the Gibbs energy per unit length:

$$\begin{aligned} G_{l(M+K)} = {} & \frac{\phi_0^2}{4\pi\mu_0\lambda\xi_v}\left(\frac{K_0\left(\xi_v/\lambda\right)}{K_1\left(\xi_v/\lambda\right)} - \frac{K_0\left(\sqrt{4X^2+\xi_v^2}/\lambda\right)}{K_1\left(\xi_v/\lambda\right)}\right) \\ & + \iint_{x>0}\left\{\frac{\lambda^2}{2\mu_0}\nabla.\left(\frac{\mathbf{B}_{ext}}{\hat{\psi}^2} \times \nabla \times \mathbf{B}_{F/A}\right) - \mathbf{H}_{ext}.\mathbf{B}_{F/A}\right\} dS \end{aligned} \tag{6.34}$$

Applying the divergence theorem we now get:

$$\begin{aligned} G_{l(M+K)} = {} & \frac{\phi_0^2}{2\pi\mu_0\lambda\xi_v}\left(\frac{K_0\left(\xi_v/\lambda\right)}{K_1\left(\xi_v/\lambda\right)} - \frac{K_0\left(\sqrt{4X^2+\xi_v^2}/\lambda\right)}{K_1\left(\xi_v/\lambda\right)}\right) + \phi_0 H_{ext}.\left\{\frac{1}{2}\exp\left(-\frac{X}{\lambda}\right)\right. \\ & \left. - \frac{\lambda^2}{2\phi_0}\int_{-\infty}^{\infty}\frac{1}{\hat{\psi}^2}\frac{dB_{F/A}}{dx}\bigg|_{x=0} dy - \frac{1}{\xi_v K_1\left(\xi_v/\lambda\right)}\int_0^X \exp\left(-\frac{\sqrt{x^2+\xi_v^2}}{\lambda}\right) dx\right\} \end{aligned} \tag{6.35}$$

Substituting $\hat{\psi}$ and $B_{F/A}$ into the integral $\displaystyle\int_{-\infty}^{\infty}\frac{1}{\hat{\psi}^2}\frac{dB_{F/A}}{dx}\bigg|_{x=0} dy$ we get

$$\int_{-\infty}^{\infty} \frac{1}{\hat{\psi}^2}\frac{dB_{F/A}}{dx}\bigg|_{x=0} dy = \frac{\phi_0 X}{\pi\lambda^2\xi_v K_1\left(\xi_v/\lambda\right)}\int_{-\infty}^{\infty}\frac{X^2+y^2+\xi_v^2}{X^2+y^2}\frac{K_1\left(\sqrt{X^2+y^2+\xi_v^2}/\lambda\right)}{\sqrt{X^2+y^2+\xi_v^2}}dy$$

$$= \frac{\phi_0 X}{\lambda\xi_v K_1\left(\xi_v/\lambda\right)}\left\{\frac{\exp\left(-\sqrt{X^2+\xi_v^2}/\lambda\right)}{\sqrt{X^2+\xi_v^2}} + \frac{1}{\pi\lambda}\int_{-\infty}^{\infty}\frac{\xi_v^2}{X^2+y^2}\frac{K_1\left(\sqrt{X^2+y^2+\xi_v^2}/\lambda\right)}{\sqrt{X^2+y^2+\xi_v^2}}dy\right\} \quad (6.36)$$

The remaining integral cannot be evaluated exactly in closed form, so we use the following approximation, valid for large λ ($K_1(x \approx 0) \approx 1/x$):

$$\int_{-\infty}^{\infty}\frac{\xi_v^2 K_1\left(\sqrt{y^2+X^2+\xi_v^2}/\lambda\right)}{\left(y^2+X^2+\xi_v^2\right)^{3/2}}dy = \frac{\pi\lambda\xi_v^2}{2\left(X^2+\xi_v^2\right)^{3/2}}\left(1+\sqrt{\frac{X^2+\xi_v^2}{\lambda^2}}\right)\exp\left(-\sqrt{\frac{X^2+\xi_v^2}{\lambda^2}}\right)$$

$$\int_{-\infty}^{\infty}\frac{\xi_v^2\lambda}{\left(y^2+X^2\right)\left(y^2+X^2+\xi_v^2\right)}dy = \frac{\pi\lambda\left(\sqrt{X^2+\xi_v^2}-X\right)}{X\sqrt{X^2+\xi_v^2}}$$

$$\int_{-\infty}^{\infty}\frac{\xi_v^2\lambda}{\left(y^2+X^2+\xi_v^2\right)^2}dy = \frac{\pi\lambda\xi_v^2}{2\left(X^2+\xi_v^2\right)^{3/2}}$$

$$\therefore \quad \int_{-\infty}^{\infty}\frac{\xi_v^2}{y^2+X^2}\frac{K_1\left(\sqrt{y^2+X^2+\xi_v^2}/\lambda\right)}{\sqrt{y^2+X^2+\xi_v^2}}dy \approx \frac{\pi\lambda\left(\sqrt{X^2+\xi_v^2}-X\right)}{X\sqrt{X^2+\xi_v^2}}\left(1+\sqrt{\frac{X^2+\xi_v^2}{\lambda^2}}\right)\exp\left(-\sqrt{\frac{X^2+\xi_v^2}{\lambda^2}}\right) \quad (6.37)$$

Substituting this in to (6.36) we get

$$-\frac{\lambda^2 H_{ext}}{2}\int_{-\infty}^{\infty}\frac{1}{\hat{\psi}^2}\frac{dB_{F/A}}{dx}\bigg|_{x=0}dy = -\frac{\phi_0 H_{ext}}{2\xi_v K_1\left(\xi_v/\lambda\right)}\left(\lambda+\sqrt{X^2+\xi_v^2}-X\right)\exp\left(-\frac{\sqrt{X^2+\xi_v^2}}{\lambda}\right) \quad (6.38)$$

We thus have the expression for $G_{I(M+K)}$ for the surface barrier:

$$G_{I(M+K)} = \frac{\phi_0^2}{2\pi\mu_0\lambda\xi_v}\left(\frac{K_0\left(\xi_v/\lambda\right)}{K_1\left(\xi_v/\lambda\right)} - \frac{K_0\left(\sqrt{4X^2+\xi_v^2}/\lambda\right)}{K_1\left(\xi_v/\lambda\right)}\right) + \phi_0 H_{ext}\left\{\tfrac{1}{2}\exp\left(-\frac{X}{\lambda}\right)\right.$$
$$\left. -\frac{\lambda+\sqrt{X^2+\xi_v^2}-X}{2\xi_v K_1\left(\xi_v/\lambda\right)}\exp\left(-\frac{\sqrt{X^2+\xi_v^2}}{\lambda}\right) - \frac{1}{\xi_v K_1\left(\xi_v/\lambda\right)}\int_0^X \exp\left(-\frac{\sqrt{x^2+\xi_v^2}}{\lambda}\right)dx\right\} \quad (6.39)$$

Differentiating to get the force per unit length we get:

$$\mathsf{F}_{I(M+K)} = -\frac{dG_{I(M+K)}}{dX} = -\frac{\phi_0^2}{\pi\mu_0\lambda^2\xi_v K_1\left(\xi_v/\lambda\right)}\frac{2X}{\sqrt{4X^2+\xi_v^2}}K_1\left(\frac{\sqrt{4X^2+\xi_v^2}}{\lambda}\right)$$
$$+\frac{\phi_0 H_{ext}}{2}\left\{\frac{1}{\lambda}\exp\left(-\frac{X}{\lambda}\right) + \left(1-\frac{X}{\lambda}+\frac{X^2}{\lambda\sqrt{X^2+\xi_v^2}}\right)\frac{\exp\left(-\sqrt{X^2+\xi_v^2}/\lambda\right)}{\xi_v K_1\left(\xi_v/\lambda\right)}\right\} \quad (6.40)$$

In the extreme type-II limit we can simplify (6.40) as $\lambda \gg X$, ξ, ξ_v. Expanding (6.40) in powers of $1/\lambda$ as far as $(1/\lambda)^2$ gives

$$\mathsf{F}_{I(M+K)} \approx -\frac{\phi_0^2}{\pi\mu_0\lambda^2}\frac{2X}{4X^2+\xi_v^2} + \frac{\phi_0 H_{ext}}{\lambda}\left[1-\frac{1}{2\lambda}\left(2X+\sqrt{X^2+\xi_v^2}-\frac{X^2}{\sqrt{X^2+\xi_v^2}}\right)\right] \quad (6.41)$$

Differentiating again (to find the point where $F_{I(M+K)}$ is most strongly attractive) we get

$$\frac{dF_{I(M+K)}}{dX} \approx \frac{2\phi_0^2}{\pi\mu_0\lambda^2}\frac{2\left(4X^2-\xi_v^2\right)}{\left(4X^2+\xi_v^2\right)^2} - \frac{\phi_0 H_{ext}}{2\lambda^2}\left(2 - \frac{X\xi_v^2}{\left(X^2+\xi_v^2\right)^{3/2}}\right) \tag{6.42}$$

For $\lambda \gg X, \xi, \xi_v$ the second term in (6.42) becomes negligible and the value of X at which the fluxon is pinned is:

$$X = \frac{\xi_v}{2} \tag{6.43}$$

H_p is the minimum H_{ext} to get $F_{I(M+K)} < 0$ for all values of X. This allows us to find H_p:

$$H_P = \frac{\phi_0}{2\pi\mu_0\lambda\xi_v\left(1-0.95\,\xi_v/\lambda\right)} \tag{6.44}$$

As Clem's paper[84] gives $\xi_v = \xi\sqrt{2}$ in the type-II limit

$$H_P = \frac{\phi_0}{2\sqrt{2}\pi\mu_0\lambda\xi\left(1-1.34/\kappa\right)} \tag{6.45}$$

This result is somewhat higher than the Bean-Livingston and Matricon results, because it assumes that the order parameter in the material in the Meissner state is spatially independent. In fact, for a superconductor coated in a normal metal, the proximity effect ensures that $\hat{\psi} \approx 0$ at the edge of the superconductor. This means that within a region at the edge approximately one coherence length thick, the external field penetrates fully instead of decaying exponentially. The bracket in the denominator of (6.45) has its origin in the assumption of (6.31) that the field decays exponentially from the very edge of the superconductor. In a metal-coated superconductor this bracket term vanishes as the decay within $\approx \xi$ of the edge is much slower than the exponential approximation (due to the suppression of ψ at the edge, which allows B to be $\approx \mu_0 H_{app}$ at the point of flux entry criticality). The expression for H_p thus simplifies to

$$H_p^{metal} = \frac{\phi_0}{2\sqrt{2}\pi\mu_0\lambda\xi} = H_p \tag{6.46}$$

This formula (6.46) gives values of H_p which are typically 10% higher than the numerical results given in Section 5.3, unlike the original Bean-Livingston formula, which is typically 30% too low. Equation (6.47) gives a good result even though $F_{I(condensation)}$ is not included in

the calculation, because the point of criticality is so close to the edge that $\hat{\psi} \approx 0$ there and thus $F_{(condensation)}$ at the critical point can be neglected.

In the high-κ limit the computation predicts that the H_p values for metal-coated and insulator-coated systems should converge. The H_p for an insulator-coated superconductor was calculated numerically by Matricon[38] using the one-dimensional Ginzburg-Landau equations, and converges in the high-κ limit to the value given by (6.46).

We have thus corrected the Bean-Livingston calculation, which uses a very simple and intuitive model, but which in its original form gave a value of H_p which was a factor $\sqrt{2}$ too small.

6.2.5 Calculating $\Delta\phi$ for flux entry

When the centre of the fluxon is a distance X inside the superconductor, the net flux inside the superconductor (fluxon contribution – antifluxon contribution) is given in the high-κ limit by

$$\phi_{partial} \approx \frac{\phi_0}{2K_1\left(\xi_v/\lambda\right)} = \frac{\phi_0}{\kappa\sqrt{2}} \tag{6.48}$$

Figure 6.1 shows a more accurate result obtained by numerically integrating **B** over the relevant area.

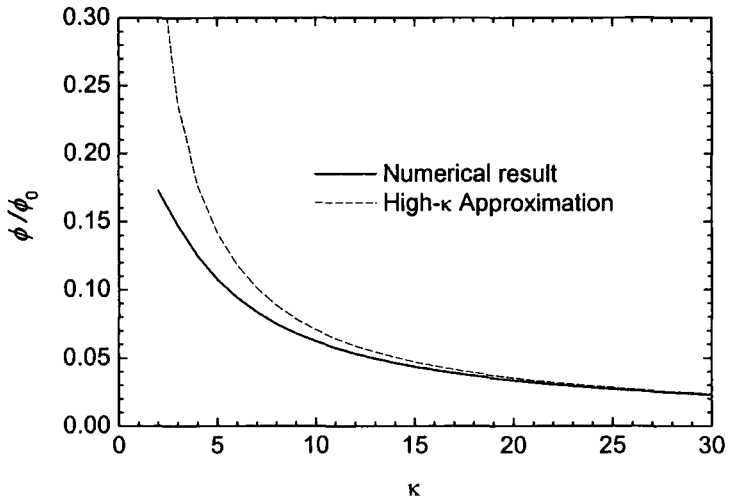

Figure 6.1: Net proportion of fluxon (flux – antiflux) inside the superconductor at criticality

6.3 Flux entry and exit in the mixed state

6.3.1 Calculation of ΔM for mixed state – general introduction

In order to extend the surface barrier calculation to the high-field regime, we shall replace the single fluxon of the Meissner-state with a semi-infinite flux-line lattice, as described by Abrikosov[14]. As in the Meissner-state calculation, the magnetization from the fluxon(s) within the superconductor is cancelled by anti-fluxon(s) outside the superconductor. Unlike the Meissner state calculation, it is possible to consider all the terms in the Gibbs energy expression, including the Landau condensation term. We move the *entire* flux-line lattice towards or away from the boundary, and calculate the resulting change of the Gibbs energy inside the superconductor (and thus the force exerted on the flux-line lattice).

6.3.2 General analytic considerations – lack of exact solution

A bulk superconductor in high magnetic fields (near H_{c2}) has a distribution of order parameter and magnetic field which is periodic in x and y and was described by Abrikosov[14]:

$$\hat{\psi} = \sum_{n=-\infty}^{\infty} C_n \exp(inky) \exp\left[-\frac{1}{2\xi^2}\left(x - nk\xi^2\right)^2\right] \tag{6.49}$$

$$\mathbf{J} = \frac{\hbar}{4e\mu_0\lambda^2}\left(-\frac{\partial}{\partial y}\left|\hat{\psi}\right|^2 \hat{\mathbf{x}} + \frac{\partial}{\partial x}\left|\hat{\psi}\right|^2 \hat{\mathbf{y}}\right) \tag{6.50}$$

(6.50) implies a simple relation between B and $\left|\hat{\psi}\right|^2$:

$$B = \mu_0 H - \frac{\hbar}{4e\lambda^2}\left|\hat{\psi}\right|^2 \tag{6.51}$$

Substituting the first Ginzburg-Landau equation into the Gibbs energy expression gives a simplified Gibbs energy expression:

$$g = -\frac{\mu_0 H_{c2}^2}{4\kappa^2}\left|\hat{\psi}\right|^4 + \frac{\mu_0 H_{c2}^2}{8\kappa^2}\xi^2\nabla^2\left|\hat{\psi}\right|^2 + \frac{\left(\mathbf{B} - \mu_0\mathbf{H}_{ext}\right)^2}{2\mu_0} \tag{6.52}$$

A standard (infinite) Abrikosov lattice is periodic in both x and y, and thus the Laplacian term in (6.52) averages to zero. If we set $\beta_A = \left\langle\left|\hat{\psi}\right|^4\right\rangle \Big/ \left(\left\langle\left|\hat{\psi}\right|^2\right\rangle\right)^2$ we get the expressions:

$$\left\langle\left|\hat{\psi}\right|^2\right\rangle = \frac{2\kappa^2(1-b)}{\beta_A\left(2\kappa^2 - 1\right)} \tag{6.53}$$

$$\left\langle \left|\hat{\psi}\right|^4 \right\rangle = \frac{4\kappa^4 (1-b)^2}{\beta_A \left(2\kappa^2 - 1\right)^2} \tag{6.54}$$

$$\Rightarrow \qquad \langle g \rangle = -\frac{\mu_0 H_{c2}^2 (1-b)^2}{2\beta_A \left(2\kappa^2 - 1\right)} \tag{6.55}$$

If a superconductor adjoins a normal metal, the order parameter is depressed at the edge. For a normal metal with $\rho_N \ll \rho_S$ (or for any normal metal, in high magnetic fields), we can approximate $\psi(x=0) \approx 0$ (Setting ψ to zero, or any other constant, also fulfils the necessary boundary condition of no current through the interface, via (6.50)). Following Abrikosov, we substitute $\mathbf{A} = B_{c2} x \hat{\mathbf{y}}$ into the linearized version of the first Ginzburg Landau equation:

$$-\frac{\hat{\psi}}{\xi^2} - \frac{\partial^2 \hat{\psi}}{\partial x^2} + \left(\frac{1}{i}\frac{\partial}{\partial y} - \frac{x}{\xi^2}\right)^2 \hat{\psi} = 0 \tag{6.56}$$

As the y dependence appears only via the derivative $\partial/\partial y$ it will be plane-wave in form. Separating the variables x and y according to $\hat{\psi}(x,y) = \hat{\varphi}(x)\exp(iky)$, we get

$$-\frac{\hat{\varphi}}{\xi^2} - \frac{d^2\hat{\varphi}}{dx^2} + \left(k - \frac{x}{\xi^2}\right)^2 \hat{\varphi} = 0 \tag{6.57}$$

This is the quantum harmonic oscillator equation, giving the general solution at H_{c2}:

$$\hat{\varphi} = \left\{C + D\mathrm{erf}\left[i\left(k\xi - \frac{x}{\xi}\right)\right]\right\}\exp\left(-\frac{\left(x - k\xi^2\right)^2}{2\xi^2}\right) \tag{6.58}$$

Now $D \equiv 0$ as $\mathrm{erf}(ix)$ tends to infinity faster than $\exp(-x^2/2)$ tends to zero. This means we can write the general wavefunction as:

$$\hat{\psi} = \int_{k=-\infty}^{k=\infty} C(k)\exp(iky)\exp\left(-\frac{\left(x - k\xi^2\right)^2}{2\xi^2}\right)dk \tag{6.59}$$

Now, solving for $\hat{\psi}(-X,y) \equiv 0$ (we are setting the edge at $x = -X$):

$$\hat{\psi}(-X,y) = \int_{k=-\infty}^{k=\infty} C(k)\exp(iky)\exp\left(-\frac{\left(X + k\xi^2\right)^2}{2\xi^2}\right)dk \equiv 0 \tag{6.60}$$

Now as the Fourier transform of zero is also zero:

$$\int_{k=-\infty}^{k=\infty} C(k)\exp\left(-\frac{\left(X + k\xi^2\right)^2}{2\xi^2}\right)\int_{y=-\infty}^{y=\infty}\exp\left(i\left(k - k'\right)y\right)dy\ dk \equiv 0$$

$$\Rightarrow \qquad C(k)\exp\left(-\frac{\left(X+k\xi^2\right)^2}{2\xi^2}\right)\equiv 0 \tag{6.61}$$

As $\exp\left(-\frac{\left(X+k\xi^2\right)^2}{2\xi^2}\right)\neq 0$, this shows that the linearized first GL equation has no non-trivial solution which has $\hat{\psi}(-X,y)\equiv 0$. This means it is impossible to obtain a non-trivial exact solution of the first linearized Ginzburg-Landau equation which includes an edge where ψ is set to zero.

6.3.3 Calculating the Gibbs energy contribution from the edge

From now onwards, the co-ordinate system is defined such that $x = 0$ is the edge. The Laplacian term in (6.52) is calculated first:

$$\Delta G_l^{\nabla^2} = \frac{\mu_0 H_{c2}^2 \xi^2}{8\kappa^2}\int_0^{\infty}\int_0^{\xi\sqrt{2\pi}} \nabla^2\left|\hat{\psi}\right|^2 dy\,dx \tag{6.62}$$

As $\left|\hat{\psi}\right|^2$ is periodic in y, the double derivative in y averages to zero:

$$\Delta G_l^{\nabla^2} = -\frac{\mu_0 H_{c2}^2 \xi^2}{8\kappa^2}\int_0^{2\pi/k}\frac{\partial}{\partial x}\left|\hat{\psi}\right|^2 dy\Bigg|_{x=0} \tag{6.63}$$

Now if we Fourier transform $\hat{\psi}$ in y

$$\hat{\psi}(x,y) = \sum_n e^{inky} f(n,x) \tag{6.64}$$

we can evaluate the y-integral:

$$\Delta G_l^{\nabla^2} = -\frac{\mu_0 H_{c2}^2 \xi^2}{4\kappa^2}\frac{2\pi}{k}(1-b)\sum_n f(n,0)\frac{df(n,0)}{dx} \tag{6.65}$$

As $f(n, 0) = 0$, so $\Delta G_l^{\nabla^2}$ is also zero. This allows expression (6.52) for the Gibbs energy density to be simplified to

$$g = -\frac{H_{c2}^2}{4\mu_0\kappa^2}\left|\hat{\psi}\right|^4 + \frac{\left(\mathbf{B}-\mu_0\mathbf{H}_{ext}\right)^2}{2\mu_0} \tag{6.66}$$

in which both terms (and thus the complete expression for ΔM) are proportional to $(1 - b)^2$. Substituting (6.51) we now get

$$g = -\frac{H_{c2}^2}{4\mu_0\kappa^2}\left(1-\frac{1}{2\kappa^2}\right)\left|\hat{\psi}\right|^4 \tag{6.67}$$

To calculated the force acting on each fluxon (and thus ΔM), we must calculate the total energy per unit length. This is obtained by integrating the Gibbs energy density over the xy plane. A normal integral to obtain the energy would give an infinite result, so a term corresponding to the bulk material is subtracted, leaving only the contribution from the edge itself. To prevent an oscillatory term unrelated to the edge entering into the integral from its upper limit (far from the edge, tending to infinity), this upper limit must move with the flux-line lattice. Thus we get:

$$\Delta G_l = -\frac{\mu_0 H_{c2}^2}{4\kappa^2}\left(1-\frac{1}{2\kappa^2}\right)\lim_{A\to\infty}\left[\int_0^{X+A}\int_0^{\frac{2\pi}{k}}\left(\left|\hat{\psi}\right|^4-\left\langle\left|\hat{\psi}_\infty\right|^4\right\rangle\right)dy\,dx\right] \tag{6.68}$$

where $\left\langle\left|\hat{\psi}_\infty\right|^4\right\rangle$ is given by (6.54) and where A is a dummy variable. The absolute value of this integral is dependent on A, but the difference between two values for the same A and different X (and therefore the force) is not dependent on A.

6.3.4 ΔM for wavefunction forced to zero using a tanh function

The simplest way to force ψ to zero at the edge is to multiply it by a function of x which is zero at $x = 0$, but which tends asymptotically to 1 as $x \to \infty$. Since the order parameter at the edge of a superconductor exhibits a hyperbolic tangent spatial dependence, this is a natural choice of function to use.

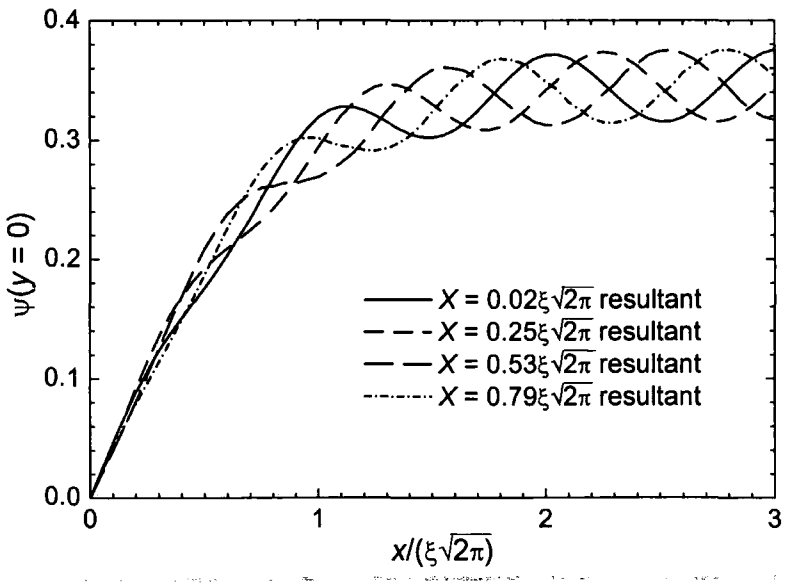

Figure 6.2: ψ at $y = 0$ with order parameter suppressed by tanh function with $\xi_{edge} = \xi$ (ψ normalized for $B = 0.9B_{c2}$)

We set

$$\hat{\psi}(x>0)=\sum_{n=-\infty}^{\infty}C_n\exp(inky)\exp\left[-\frac{1}{2\xi^2}\left(X+nk\xi^2-x\right)^2\right]\tanh\left(\frac{x}{\xi_{edge}}\right) \qquad (6.69)$$

where ξ_{edge} is an arbitrary parameter which is the characteristic length for the decay of to zero at the edge of the superconductor. Here X is a variable parameter which indicates the position of the flux-line lattice relative to the edge of the superconductor. We shall solve here for the square lattice considered originally by Abrikosov as this is the simplest possible case. For this lattice $k=\frac{\sqrt{2\pi}}{\xi}$ and $C_n\equiv\sqrt{\frac{2\sqrt{2}\kappa^2(1-b)}{\beta_A\left(2\kappa^2-1\right)}}$. Figure 6.2 shows examples of this order parameter for $\xi_{edge}=\xi$ and four different values of X. Substituting (6.69) into (6.68) gives

$$\Delta G_l=-\frac{2\pi\xi^2\mu_0H_{c2}^2(1-b)^2}{\beta_A^2\left(2\kappa^2-1\right)}\hat{G}_l \qquad (6.70)$$

where $\hat{G}_l$ is a dimensionless energy per unit length given by

$$\hat{G}_l=\frac{1}{2\pi\xi^2}\lim_{A\to\infty}\left[\int_0^{X+A}\int_0^{\frac{2\pi}{k}}\left\{\left[\tanh\left(\frac{x}{\lambda_{edge}}\right)\sum_{n=-\infty}^{\infty}\exp(inky)\exp\left[-\frac{1}{2\xi^2}\left(X+nk\xi^2-x\right)^2\right]\right]^4-\frac{\beta_A}{2}\right\}dy\,dx\right] \qquad (6.71)$$

If we normalize X, x and y in units of $\xi\sqrt{2\pi}$ (normalized units bearing caret signs), $\hat{G}_l$ now given by:

$$\hat{G}_l=\lim_{\hat{A}\to\infty}\left[\int_0^{\hat{X}+\hat{A}}\int_0^{1}\left\{\tanh\left(\frac{\hat{x}}{\hat{\xi}_{edge}}\right)\sum_{n=-\infty}^{\infty}\exp 2\pi in\hat{y}\exp\left[-\pi\left(X+n-x\right)^2\right]\right\}^4-\frac{\beta_A}{2}d\hat{y}\,d\hat{x}\right] \qquad (6.72)$$

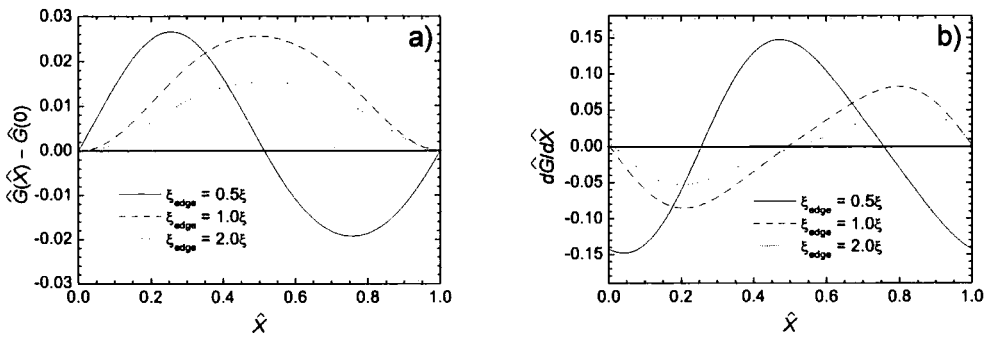

Figure 6.3: Normalized $\hat{G}_l$ (energy/unit length) and $d\hat{G}_l/d\hat{X}$ (force/unit length) for order parameter suppressed by a tanh function of three different length scales.

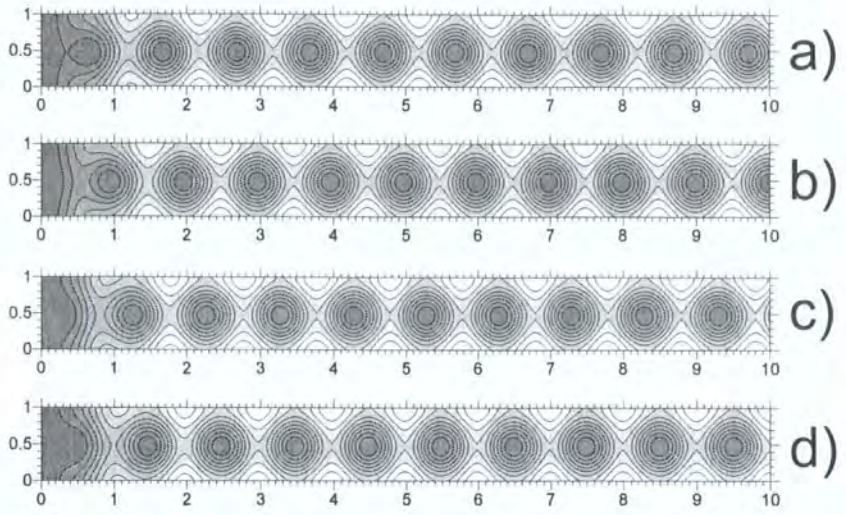

Figure 6.4: Part of the square Abrikosov lattice near the edge of a superconductor with the edge suppressed by a tanh function with $\xi_{edge} = \xi$. a) $\hat{X} = 0.21$ – flux entry critical state, b) $\hat{X} = 0.49$ – maximum energy state, c) $\hat{X} = 0.80$ – flux exit critical state, d) $\hat{X} = 0.00$ – minimum energy state

Numerical solution of this integral gives the Gibbs energy per unit length (and differentiating w.r.t. $\hat{X}$ gives the force per unit length on the fluxons). Results of these integrations for three different values of ξ_{edge} are shown in Figure 6.3. It can be seen that the amplitudes of $d\hat{G}_l/d\hat{X}$ as a function of $\hat{X}$ are approximately 0.15, 0.085 and 0.052 for ξ_{edge} values of 0.5ξ, ξ and 2ξ respectively. Figure 6.4 shows contour plots of ψ for $\xi_{edge} = \xi$ at the four critical points in the force profile. The energy per unit length is minimized for $\hat{X} = 0.00$ (which is identical to the $\hat{X} = 1.00$ position), so this is the equilibrium configuration associated with the reversible magnetization of the superconductor.

Increasing the external field pushes the vortices inwards, increasing $\hat{X}$ so as to approach the $\hat{X} = 0.21$ position. Once the force is sufficient to push the fluxons past the $\hat{X} = 0.21$ position, the fluxons move continuously into the superconductor until the internal field increases such that the force is no longer sufficient to overcome the force opposing flux entry at $\hat{X} = 0.21$. Similarly, if the external field is decreased, the fluxons move towards the edge, approaching the $\hat{X} = 0.80$ position. Once this position is reached, fluxons can exit continuously until the internal field decreases such that the force is no longer sufficient to overcome the force opposing flux entry at $\hat{X} = 0.80$.

The force per unit length restricting fluxon entry is found via

$$\mathsf{F}_{l}^{\max} = \left[\frac{d}{dX}(\Delta G_l)\right]_{\max} = \pm\frac{\sqrt{2\pi}\xi B_{c2}^2}{\mu_0\beta_A^2\left(2\kappa^2-1\right)}(1-b)^2\left[d\hat{G}_l\Big/d\hat{X}\right]_{\max} \tag{6.73}$$

For the system to be stable, the force exerted by the edge of the superconductor on the fluxons (as calculated above) must be opposed by a force exerted on the fluxons by an additional (irreversible) screening current component $\Delta\mathbf{J}$. Equating values of $\mathscr{F}_l^{(\max)}$ we get:

$$\int_0^{\infty}\int_0^{a_0}|\Delta\mathbf{J}\times\mathbf{B}|\,dy\,dx = \pm\frac{\sqrt{2\pi}\xi H_{c2}^2(1-b)^2}{\mu_0\beta_A^2\left(2\kappa^2-1\right)}\left[d\hat{G}_l\Big/d\hat{X}\right]_{\max} \tag{6.74}$$

For a superconductor in the high-field limit (the region of validity is larger in high-κ superconductors), $\mathbf{B}$ can be approximated as the applied field $\mu_0 H$. This allows it to be taken outside the integrals. Assuming that ΔJ is not y-dependent:

$$\mu_0 H a_0\int_0^{\infty}\Delta J\,dx = \pm\frac{\sqrt{2\pi}\xi H_{c2}^2(1-b)^2}{\mu_0\beta_A^2\left(2\kappa^2-1\right)}\left[d\hat{G}_l\Big/d\hat{X}\right]_{\max} \tag{6.75}$$

We can now obtain $\Delta M\left(=\int_0^{\infty}\Delta J\,dx\right)$

$$\Delta M = \pm\left[d\hat{G}_l\Big/d\hat{X}\right]_{\max}\frac{H_{c2}}{(\tfrac{1}{3})^{1/4}\,\beta_A^2\left(2\kappa^2-1\right)}b^{-1/2}(1-b)^2 \tag{6.76}$$

To be consistent with the computational results of Chapter 5 as given by (5.3) for $\rho_N = \rho_S$, $\left[d\hat{G}_l\Big/d\hat{X}\right]_{\max}$ must be 0.356, but $\left[d\hat{G}_l\Big/d\hat{X}\right]_{\max}$ in this model is only 0.15 even for the low ξ_{edge} value of 0.5.

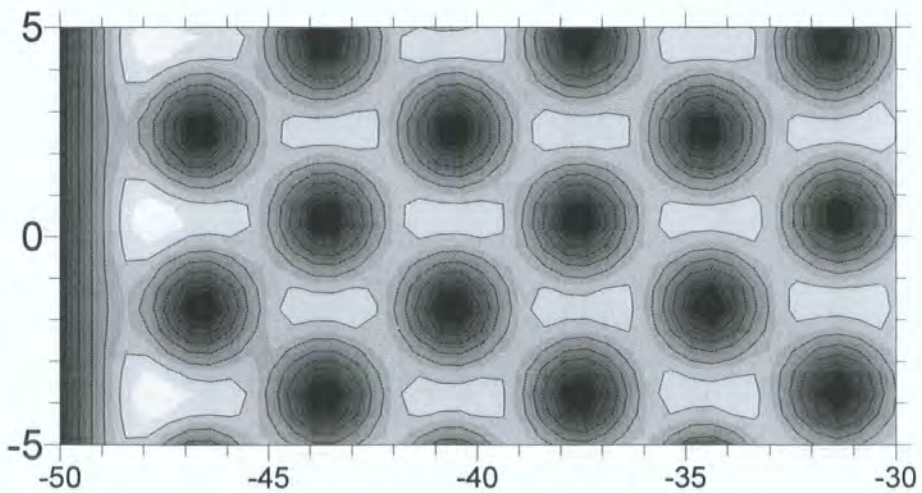

Figure 6.5: Example of edge from a TDGL computation

An even lower value of ξ_{edge} could be used to correct ΔM, but would give an order parameter profile grossly inconsistent with those visualized in the computational data of Chapter 5 – hence this simple model of the material edge is unsatisfactory. This low value of ΔM comes from the fact that $|\psi|$ near the edge of the superconductor is determined almost entirely by the tanh function itself, which is not $\hat{X}$-dependent. Another indication that this model is unsatisfactory comes from the shape of the ψ contours next to the edge. In this simple tanh-suppressed model these contours (shown in Fig. 6.4) have a significant curvature in conformity with the flux-line lattice for all values of $\hat{X}$, while in contour plots obtained from the TDGL computations in Chapter 5 (an example is shown in Fig. 6.5) the contours nearest to the edge are almost straight.

6.3.5 ΔM for wavefunction anti-symmetrized at edge

A better possibility for simulating the edge of a superconductor in a high magnetic field is suggested by the Bean-Livingston model for initial flux entry, which uses a virtual 'anti-fluxon' outside the superconductor. The flux-line lattice within the superconductor can be mirrored by an 'anti-flux line lattice' outside, such that the order parameter at the very edge ($x = 0$) is zero. We postulate the following expression for a semi-infinite Abrikosov lattice, which artificially anti-symmetrizes the wave function to force $\hat{\psi}(x=0,y) \equiv 0$. The function is made periodic in X, with the first fluxon always within $\xi\sqrt{2\pi}$ of the edge of the superconductor.

$$\hat{\psi}\left(x>0, 0<X<\xi\sqrt{2\pi}\right) = \sum_{n=0}^{\infty} C_n \exp(inky) \left\{ \begin{array}{l} \exp\left[-\frac{1}{2\xi^2}\left(X+nk\xi^2-x\right)^2\right] \\ -\exp\left[-\frac{1}{2\xi^2}\left(X+nk\xi^2+x\right)^2\right] \end{array} \right\} \tag{6.77}$$

$$\hat{\psi}\left(x, X+m\xi\sqrt{2\pi}\right) = \hat{\psi}(x,X) \qquad (m \in \mathbb{Z})$$

where $\hat{G}_l$ is a dimensionless energy per unit length given by

$$\hat{G}_l = -\int_0^{\infty}\int_0^{1}\left[\begin{array}{l} \left|\sum_{n=0}^{\infty} \exp 2\pi in\hat{y}\left\{\exp\left[-\pi\left(\hat{X}+n-\hat{x}\right)^2\right]-\exp\left[-\pi\left(\hat{X}+n+\hat{x}\right)^2\right]\right\}\right|^4 \\ -\left|\sum_{n=-\infty}^{\infty} \exp 2\pi in\hat{y}\exp\left[-\pi\left(\hat{X}+n-\hat{x}\right)^2\right]\right|^4 \end{array}\right] d\hat{y}\,d\hat{x} \tag{6.78}$$

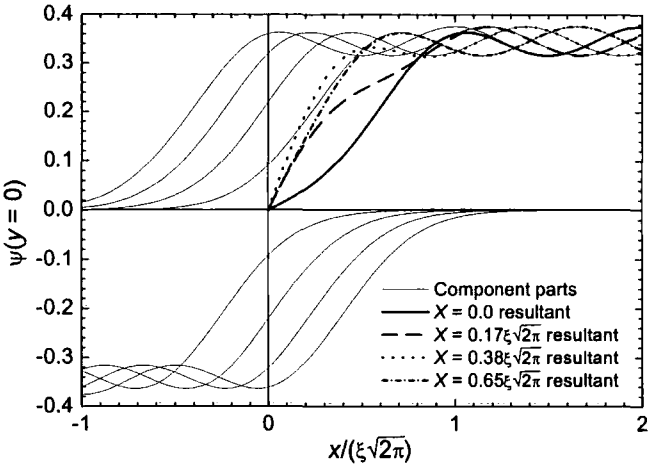

Figure 6.6: Anti-symmetrization of ψ at $y = 0$ (ψ normalized for $B = 0.9B_{c2}$)

The formulation of these wavefunctions is demonstrated graphically in Fig. 6.6. The integrals now contain no system-dependent parameters, and can thus be solved numerically and applied to the general case. The integral and its derivative are shown in Fig. 6.7 – it can be seen that in this system $d\hat{G}_l/d\hat{X}$ is much larger than that of the system in section 6.3.4., ranging from −0.57 to +0.78. These values would give a value of ΔM about twice as large as the computational results (which corresponds to $d\hat{G}_l/d\hat{X}$ extrema of ±0.356). In addition there is an unphysical 'cusp' in the $d\hat{G}_l/d\hat{X}$ data at $\hat{X} = 0.0$.

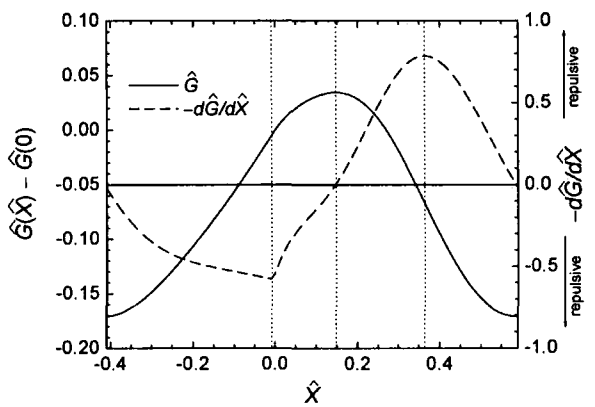

Figure 6.7: Normalized $\hat{G}_l$ (energy/unit length) and $d\hat{G}_l/d\hat{X}$ (force/unit length) as given by the anti-symmetrization model. The energy barrier which fluxons must cross as they enter or exit the superconductor is clearly visible between $\hat{X} = -0.41$ and $\hat{X} = +0.59$

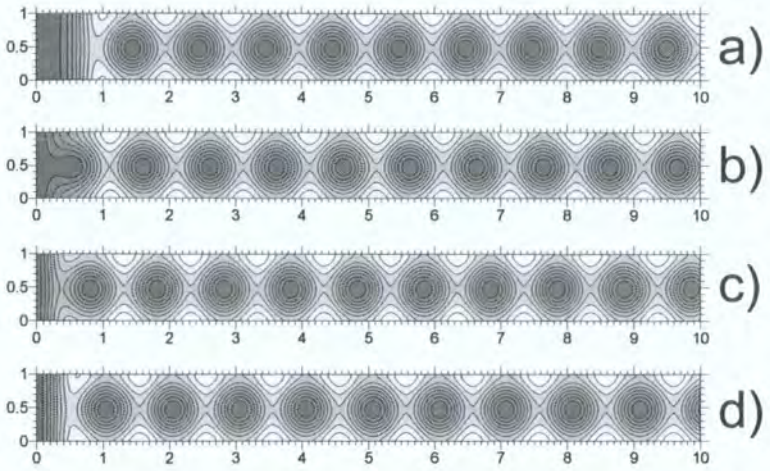

Figure 6.8: Part of a square Abrikosov lattice near the edge of a superconductor, simulated using the 'anti-symmetrization' model – a) $\hat{X} = -0.01$ – flux entry critical state, b) $\hat{X} = 0.15$ – maximum energy state, c) $\hat{X} = 0.36$ – flux exit critical state, d) $\hat{X} = 0.59$ – minimum energy state

Figure 6.8 demonstrates the four most important configurations of fluxons near the edge of the superconductor. This form of $\hat{\psi}$, unlike that used in section 6.3.4, gives near-straight ψcontours near the edge of the superconductor in most of the $\hat{X}$ range, including at $\hat{X} = -0.01$, $\hat{X} = 0.36$ and $\hat{X} = 0.59$. The order parameter behaviour is therefore much like that actually observed in our TDGL computations.

The cause of the unphysical 'cusp' in $d\hat{G}_l / d\hat{X}$ which exists in this model is that when $\hat{X}$ passes through zero a full new fluxon-antifluxon pair is suddenly created (for increasing $\hat{X}$) or destroyed (for decreasing $\hat{X}$). This suggests an obvious modification to the anti-symmetrization model, in which the flux from a new fluxon-antifluxon pair is phased in gradually over a distance $\approx \xi_{edge}$. The improved anti-symmetrized function for $\hat{\psi}$ is

$$\hat{\psi}(x>0) = \sum_{n=-\infty}^{\infty} C_n \exp(inky) \tanh\left(\frac{X+n}{\xi_{edge}}\right) \left\{ \begin{array}{l} \exp\left[-\frac{1}{2\xi^2}\left(X + nk\xi^2 - x\right)^2\right] \\ -\exp\left[-\frac{1}{2\xi^2}\left(X + nk\xi^2 + x\right)^2\right] \end{array} \right\}. \quad (6.79)$$

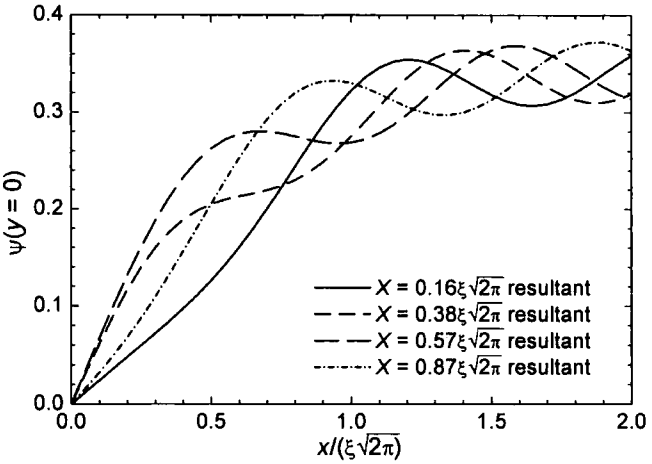

Figure 6.9: $\hat{\psi}$ at $y = 0$ obtained by modified anti-symmetrization model, with $\xi_{edge} = \xi\sqrt{2}$ (ψ normalized for $B = 0.9B_{c2}$)

The formulation of these new wavefunctions for $\xi_{edge} = \xi\sqrt{2}$ is demonstrated graphically in Fig. 6.9, while the integral and its derivative are shown in Fig. 6.10 – it can be seen that in this system $d\hat{G}_l/d\hat{X}$ ranges from −0.35 to +0.35, thus giving a value of ΔM within one percent of that found by the computational results. (Note that for a straight superconductor edge in the Meissner state, the order parameter is given by a tanh function with characteristic length $\xi\sqrt{2}$, which may explain why this value gives such a good result in this system). In addition, the 'cusp' in $d\hat{G}_l/d\hat{X}$ at $\hat{X} = 0.0$ has been removed.

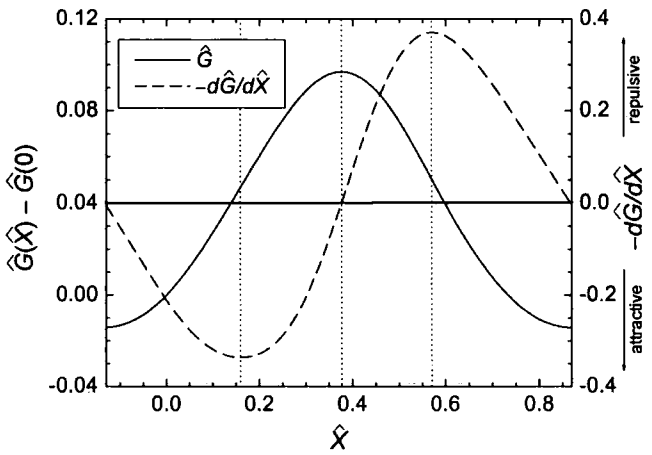

Figure 6.10: Normalized $\hat{G}_l$ (energy/unit length) and $d\hat{G}_l/d\hat{X}$ (force/unit length) as given by the modified anti-symmetrization model with $\xi_{edge} = \xi\sqrt{2}$. The energy barrier for fluxons entering or exiting the superconductor is visible between $\hat{X} = -0.13$ and $\hat{X} = +0.87$

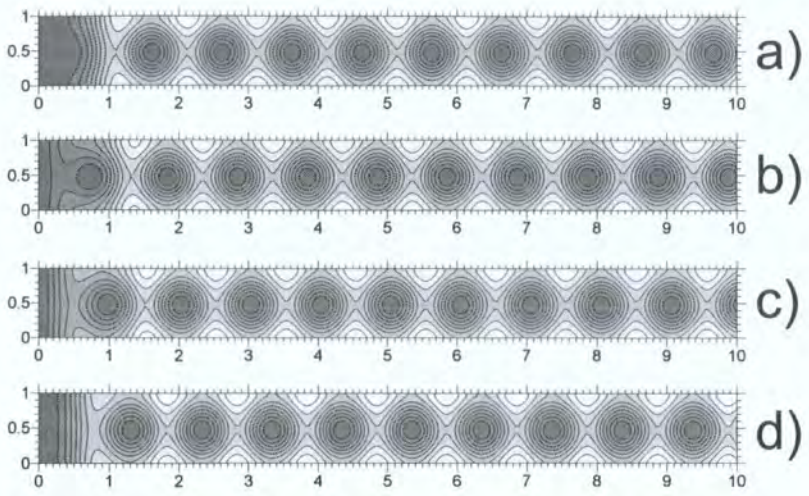

Figure 6.11: Part of a square Abrikosov lattice near the edge of a superconductor, simulated using the modified anti-symmetrization model with $\xi_{edge} = \xi\sqrt{2}$ – a) $\hat{X} = 0.16$ – flux entry critical state, b) $\hat{X} = 0.38$ – maximum energy state, c) $\hat{X} = 0.57$ – flux exit critical state, d) $\hat{X} = 0.87$ – minimum energy state

The maximum and minimum energy states are at $\hat{X} = 0.38$ and $\hat{X} = 0.87$ respectively, while the flux entry and exit critical states are at $\hat{X} = 0.16$ and $\hat{X} = 0.57$ respectively. Figure 6.11 shows the order parameter at these four critical points. As for the simple anti-symmetrization model, $\hat{\psi}$ following the modified has almost straight contours next to the edge.

6.3.6 Calculating $\Delta\phi$ for flux entry

In Sec. 6.2.5 we calculated the net fraction of fluxon which had entered the superconductor at the point of criticality. For the high-field mixed state system, the directly analogous number would be the additional flux per edge fluxon (as we now have not a single fluxon entering the superconductor, but an entire row of them) which is present in the superconductor in the 'flux entry critical' state, rather than in the 'minimum energy' state. Using the Abrikosov magnetic field expression (6.51), this additional flux per edge fluxon $\delta\phi$ can be written as follows (where $\Delta X = X_{entry\text{-}critical} - X_{min\text{-}energy}$):

$$\delta\phi = \mu_0 H \xi\sqrt{2\pi}\Delta X - \frac{\hbar}{4e\lambda^2}\int_0^{\xi\sqrt{2\pi}} \lim_{A\to\infty}\left[\int_0^{A+X_{entry-critical}} \left|\hat{\psi}\left(X_{entry-critical}\right)\right|^2 dx - \int_0^{A+X_{min-energy}} \left|\hat{\psi}\left(X_{min-energy}\right)\right|^2 dx\right] dy \qquad (6.80)$$

Re-writing this in normalized units we get

$$\delta\phi = \phi_0 \left\{ \frac{H}{H_{c2}} \Delta\hat{X} - \frac{1}{2\kappa^2} \int_0^1 \lim_{\hat{A}\to\infty} \left[\int_0^{\hat{A}+\hat{X}_{entry-critical}} \left|\hat{\psi}\left(\hat{X}_{entry-critical}\right)\right|^2 d\hat{x} - \int_0^{\hat{A}+\hat{X}_{min-energy}} \left|\hat{\psi}\left(\hat{X}_{min-energy}\right)\right|^2 d\hat{x} \right] d\hat{y} \right\} \tag{6.81}$$

For the modified anti-symmetrized wavefunction of (6.79) with $\xi_{edge} = \xi\sqrt{2}$ – the approximate function which gave the closest qualitative and quantitative match to our TDGL computational results, $\Delta\hat{X} = 0.16 - 0.87 \bmod 1 = 0.29$. Numerical solution of the integrals gives the final result for $\delta\phi$:

$$\delta\phi = \phi_0 \left[0.29b - \frac{0.0761}{2\kappa^2 - 1}(1-b) \right] \tag{6.82}$$

6.4 Conclusions

We have built on the simple physical model posited in 1964 by Bean and Livingston in order to gain an understanding of the behaviour of the surface barrier of a superconductor. The original London-model calculation could not model the fluxon core correctly, and therefore gave a value of H_p which was a factor of $\sqrt{2}$ too small. We have modelled the vortex core using the Clem approximation, and obtained the correct value of H_p

The calculation has also been extended to the mixed-state case, by assuming that the vortices form an Abrikosov lattice and that this entire lattice moves in or out of the superconductor. Since a non-trivial exact solution of the linearized Ginzburg-Landau equations where $\psi = 0$ along an edge is impossible, an approximate expression for ψ must be used. An approximate expression for ψ is postulated based on applying the Bean-Livingston 'fluxon-antifluxon' methodology to the Abrikosov lattice. When this approach is combined with a term which phases in new fluxon-antifluxon pairs using a hyperbolic tangent function of characteristic length $\xi\sqrt{2}$ (this tanh function is the same as the spatial dependence ψ at the edge of a metal-coated superconductor in the Meissner state), the predicted value of ΔM is within 1% of that observed in our TDGL computations of Chapter 5.

7 Critical current of SNS Junctions

7.1 Introduction

7.1.1 Motivation

One of the central aims of this thesis is to model current flow in polycrystalline superconductors. It is important to check that the computational method can model single SNS junctions correctly. In addition, we need to consider the role of junctions as a potential basic building block for polycrystalline materials. First current flow through a single planar SNS junction is modelled and compared to analytic predictions. The configuration of the basic SNS junction and the computational method used to obtain J_c are described in 7.1. One-dimensional analytic methods for obtaining J_c are reviewed and a new analytic calculation of J_c for a junction without pair-breaking (ie $\alpha_N = 0$) is provided in section 7.2. Section 7.3 compares zero-field computational J_c results with these analytic results, considering the dependences of J_c on kappa, junction thickness and width, junction resistivity and Cooper-pair breaking. The effect of small applied fields (that permit the superconductors on either side of the junction to remain in the Meissner state) on J_c is reviewed in section 7.4 – this includes both the Fraunhofer narrow-junction limit and the self-field-limited wide-junction case. Section 7.5 investigates the J_c of an SNS junction with the superconductors in the mixed state. To avoid surface critical field (H_{c3}) effects, especially when polycrystalline materials are simulated in Chapters 8 and 9, trilayer junctions (ie three normal metal layers) are considered, and compared with simple junctions in Section 7.6, while section 7.7 considers what we shall call 'trilayer cross junctions' which serve as the basic building blocks for the grain boundaries of the polycrystalline model. The conclusions are presented in section 7.8.

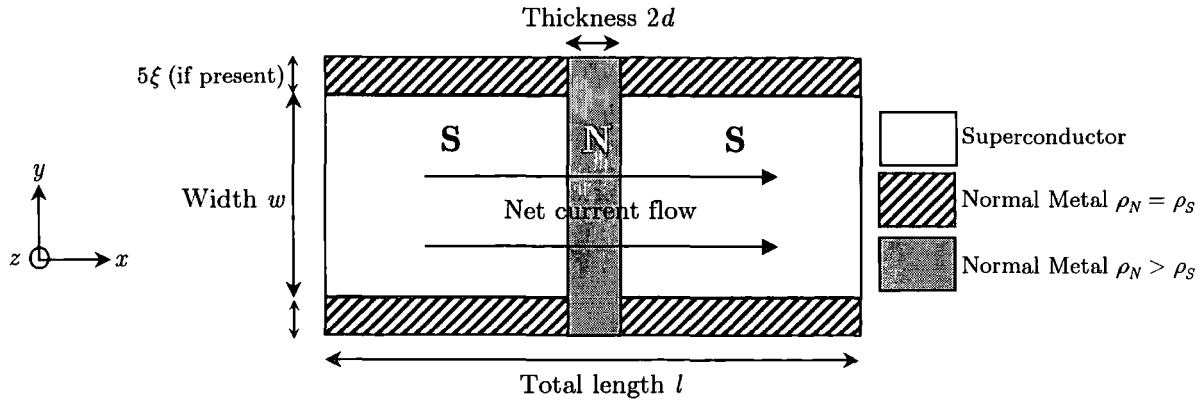

Figure 7.1: Diagram of an SNS junction as modelled computationally – the normal regions at top and bottom are optional

7.1.2 Calculation Method

The critical current of various junctions are computed in this chapter using a transport current measurement approach. The external applied field H has a gradient in the y-direction, which according to Maxwell's equations is equivalent to a current travelling in the x-direction. The current enters and leaves the system as normal current, and then becomes supercurrent some way inside the superconductor. For this reason the length l of superconductor modelled is typically set to 70ξ, though longer lengths are sometimes required for high-κ superconductors.

The current is ramped upwards in a series of steps, and the voltage across the junction is calculated and averaged over the second half of each step. The dependence of the voltage on the current density J is then used to obtain the critical current density J_c. To ensure that the J_c value is correct it is important to ensure that the calculated voltage for $J < J_c$ is as low as possible. The voltage is measured by integrating the electric field in the direction of current flow to within 4λ of the ends of the system – this allows sufficient space for the injected normal current to become supercurrent – and then summing over all y within the superconductor. This is equivalent to a standard four-terminal resistive measurement. J_c values less than $\approx 10^{-4} H_{c2}/\kappa^2\xi$ are very difficult to compute due to the slow equilibration of the voltage at such low current flows. The geometry of the system is shown by Fig. 7.1, while some examples of calculated current versus voltage characteristics are shown in Fig. 7.2.

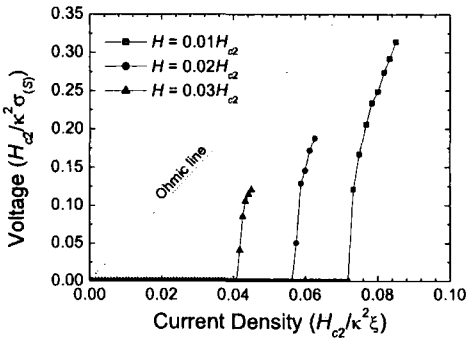

Figure 7.2: Computed *V-I* traces for a 30ξ wide, 0.5ξ thick junction with $\rho_N = 10\rho_S$.

It should be noted that measuring very low J_c values by the transport method is computationally expensive as the equilibration of the voltage is very slow.

7.2 1D analytic solutions for J_c

7.2.1 Introduction

We consider setting up the general problem of a current flowing through an SNS junction of thickness $2d$ in the x-direction. With the applied field along the z-axis, **A** can be defined as **A** $= Bx\hat{\mathbf{y}}$. $\hat{\psi}$ is assumed to depend on x only. Equations (3.52) and (3.53) inside the junction are rewritten in 1-D:

$$\frac{D_{(S)}}{D_{(N)}\xi_{(S)}^2}\left(\left|\hat{\psi}^{(N)}\right|^2 + \alpha_N\right)\hat{\psi}^{(N)} - \frac{d^2\hat{\psi}^{(N)}}{dx^2} + \left(\frac{2eBx}{\hbar}\right)^2\hat{\psi}^{(N)} = 0 \tag{7.1}$$

$$J = -\frac{\rho_{(S)}}{\rho_{(N)}}\frac{\hbar}{2e\mu_0\lambda_{(S)}^2}\,\mathrm{Im}\left(\hat{\psi}^{(N)*}\frac{d\hat{\psi}^{(N)}}{dx}\right) \tag{7.2}$$

The parameter α_N is given by (3.56) for a junction in the $T \approx T_{c(N)}$ regime, or by[36]

$$\alpha_N\left(T_{c(N)} = 0\right) = \frac{\pi^2 T}{2\left(T_{c(S)} - T\right)} \tag{7.3}$$

if the junction is totally non-superconducting. The pair-breaking in the normal barrier is typically described via a 'normal metal coherence length' $\xi_{(N)}$ – however unlike the original sources[36,67], we have chosen a 'Real = Superconducting' convention for ξ to give a consistent form for the equations in both the superconductor and normal metal, so that $\xi_{(N)}$ is imaginary. Its value is given by

$$\xi_{(N)} = i\xi_{(S)}\sqrt{\frac{D_{(N)}}{\alpha_N D_{(S)}}} \tag{7.4}$$

The magnitude of the order parameter at infinity was defined to be $\hat{\psi}_\infty$, and phase difference across the junction $\bar{\varphi}$. $\hat{\psi}_\infty = 1$ in the Meissner state, and can be approximated to $\sqrt{1-\frac{B}{B_{c2}}}$ in the mixed state.

Outside the junction, the order parameter was described as[36]:

$$\hat{\psi}^{(S)}(x > d) = \hat{\psi}_\infty \tanh\left(\frac{x_1 + x - d}{\xi_{(S)}\sqrt{2}}\right)\exp\left(-\frac{i\bar{\varphi}}{2}\right) \tag{7.5}$$

$$\hat{\psi}^{(S)}(x < -d) = \hat{\psi}_\infty \tanh\left(\frac{x_2 - x - d}{\xi_{(S)}\sqrt{2}}\right)\exp\left(\frac{i\bar{\varphi}}{2}\right) \tag{7.6}$$

From these expressions and the boundary conditions (3.54) and (3.55) an expression was obtained relating $\hat{\psi}^{(N)}(\pm d)$ and $\frac{d\hat{\psi}^{(N)}}{dx}(\pm d)$ to $\hat{\psi}_\infty$ and $\bar{\varphi}$:

$$\frac{d\hat{\psi}^{(N)}}{dx}(d) = \frac{\rho_{(N)}}{\xi_{(S)}\rho_{(S)}\sqrt{2}}\left(\hat{\psi}_\infty \exp\left(-\frac{i\varphi}{2}\right) - \frac{\hat{\psi}^{(N)2}(d)}{\hat{\psi}_\infty}\exp\left(+\frac{i\bar{\varphi}}{2}\right)\right) \tag{7.7}$$

Hence, the general solution for $\hat{\psi}^{(N)}$ was written in the form[36]

$$\hat{\psi}^{(N)}(x) = c_1 f_1(x) + ic_2 f_2(x) \tag{7.8}$$

Owing to the choice of phases in (7.5) and (7.6) and the symmetry of the junction, f_1 and f_2 are symmetric and antisymmetric functions respectively, while c_1 and c_2 are real constants. The general approach to obtain J is thus to solve for $\hat{\psi}^{(N)}$ and then substitute into (7.2). Specific cases are considered in the remainder of section 7.2.

7.2.2 Zero-field J_c – linear equations ($\alpha_N > 0$)

If there is a strong pair-breaking term (for example if T is relatively high) then $\left|\hat{\psi}^{(N)}\right|^2 \ll 1$ within the junction, and the nonlinear term can be ignored so a simple analytic solution is possible[36,85]. In the low-field limit, where $B \ll \frac{\hbar}{2ed\xi_{(N)}}$, the field term can also be ignored, allowing (7.1) to be simplified to[85]

$$\frac{d^2\hat{\psi}^{(N)}}{dx^2} + \frac{1}{\xi^2_{(N)}} = 0 \tag{7.9}$$

which has the solutions[36,85]

$$f_1 = \cosh\left(\frac{x}{\left|\xi_{(N)}\right|}\right), \qquad f_2 = \sinh\left(\frac{x}{\left|\xi_{(N)}\right|}\right) \tag{7.10}$$

Solving for c_1 and c_2 gave the results for J in the thick-junction limit of $\dfrac{2d}{\left|\xi_{(N)}\right|} \gg 1$ that:

$$J = \frac{\rho_{(S)}}{\rho_{(N)}} \frac{\hbar\left|\psi^{(N)}(d)\right|^2}{e\mu_0\lambda_{(S)}^2\left|\xi_{(N)}\right|} \exp\left(-\frac{2d}{\left|\xi_{(N)}\right|}\right) \sin\bar{\varphi} \tag{7.11}$$

Equation (7.11) is the famous De Gennes result[85] where J_c is exponentially dependent on d, and where the only field dependence comes in a long Josephson junction from diffraction effects. However, this expression is difficult to use as it requires knowledge of the interface order parameter $\psi^{(N)}(d)$.

In the thick-junction limit, we can write[85] $\dfrac{d\hat{\psi}^{(N)}}{dx}(d) = \dfrac{1}{\left|\xi_{(N)}\right|}\hat{\psi}^{(N)}(d)$. Solving with (7.7) gives

$$\hat{\psi}^{(N)}(d) = \hat{\psi}_\infty \exp\left(-\frac{i\varphi}{2}\right)\left\{\sqrt{\left(\frac{\xi_{(S)}\rho_{(S)}}{\sqrt{2}\left|\xi_{(N)}\right|\rho_{(N)}}\right)^2 + 1} - \frac{\xi_{(S)}\rho_{(S)}}{\sqrt{2}\left|\xi_{(N)}\right|\rho_{(N)}}\right\} \tag{7.12}$$

which gives J_c (the maximum J, found at $\bar{\varphi} = \pi/2$) in terms of the Meissner order parameter $\hat{\psi}_\infty$:

$$J_{D-J} = \frac{\rho_{(S)}}{\rho_{(N)}} \frac{\hbar\hat{\psi}_\infty^2}{e\mu_0\lambda_{(S)}^2\left|\xi_{(N)}\right|}\left\{\sqrt{\left(\frac{\xi_{(S)}\rho_{(S)}}{\sqrt{2}\left|\xi_{(N)}\right|\rho_{(N)}}\right)^2 + 1} - \frac{\xi_{(S)}\rho_{(S)}}{\sqrt{2}\left|\xi_{(N)}\right|\rho_{(N)}}\right\}^2 \exp\left(-\frac{2d}{\left|\xi_{(N)}\right|}\right) \tag{7.13}$$

The zero-field 1D J_c of a junction is referred to as $J_{D\text{-}J}$ in this thesis as it is an intrinsic property of the junction comparable to the depairing current for a superconductor.

7.2.3 Zero-field J_c – nonlinear equations ($\alpha_N = 0$)

In a junction where $T = T_{c(N)} = 0$, the α term is zero within the junction, and the non-linear β term determines the behaviour of the junction. This gives a d^{-3} dependence of J_c for these junctions which shall be explained in the following derivation. When the α_N term is zero, the zero-field version of (7.1) becomes

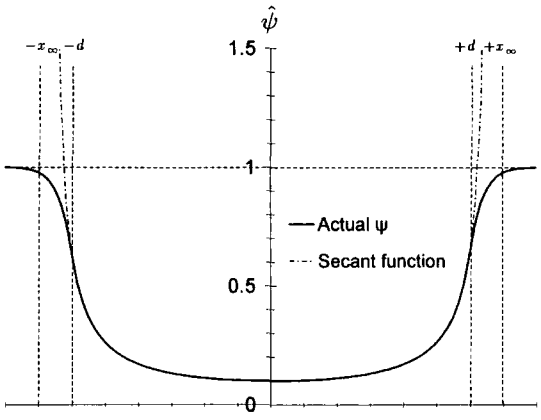

Figure 7.3: Approximate solution of non-linear Josephson junction for $\bar{\varphi} = 0$

$$\frac{D_{(S)}}{D_{(N)}}\left|\hat{\psi}^{(N)}\right|^2 \hat{\psi}^{(N)} = \xi_{(S)}^2 \frac{d^2\hat{\psi}^{(N)}}{dx^2} \tag{7.14}$$

As before we set $\hat{\psi}(-x) = \hat{\psi}^*(x)$ using (7.5) and (7.6). Note that as the first Ginzburg-Landau equation is now nonlinear, f_1 and f_2 are themselves dependent on c_1 and c_2. It is extremely difficult to solve the nonlinear Ginzburg-Landau expression exactly, so we have used an approximate solution to obtain the general trend of J_c for the junction. We find that one particular solution of (7.14) is

$$\hat{\psi}_{x_0} = \xi_S \sqrt{\frac{2D_{(N)}}{D_{(S)}}} \frac{\exp(i\varphi)}{x_0 \pm x} \tag{7.15}$$

where φ and x_0 are arbitrary real constants. However, this function does not have the required symmetry. This exact solution does however suggest that a trial solution should decay as $1/x$ when moving into the normal junction, with the function reaching a singularity were it extrapolated into the superconductor. Since the function $y = \sec x$ is an even function with singularities at $x = \pm\pi/2$ and the singularities in the extrapolation of ψ are at $\pm x_\infty$ ($x_\infty >$ d), we suggest the approximate f_1 (shown in Fig. 7.3) of

$$f_1 = \sec\left(\frac{\pi x}{2x_\infty}\right) \tag{7.16}$$

The flow of current through the junction, and therefore $\mathrm{Im}\left(\hat{\psi}^* \dfrac{\partial\hat{\psi}}{\partial x}\right)$, must be independent of x. Given f_1 this requirement determines the x-dependence of f_2:

$$f_2(x) \propto f_1 \int \frac{dx}{f_1^2(x)} \tag{7.17}$$

The functions in (7.10) which solve the linearized Ginzburg-Landau equations, automatically meet this requirement. For f_1 given as (7.16) f_2 is thus obtained

$$f_2 = \sin\left(\frac{\pi x}{2x_\infty}\right) + \frac{\pi x}{2x_\infty}\sec\left(\frac{\pi x}{2x_\infty}\right) \tag{7.18}$$

Next c_1 and c_2 must be found. Solving the real part of (7.14) at $x = x_\infty$ gives

$$c_1^2 + c_2^2\left(\frac{\pi}{2}\right)^2 = \frac{D_{(N)}}{2D_{(S)}}\left(\frac{\pi\xi_{(S)}}{x_\infty}\right)^2 \tag{7.19}$$

and solving the argument of (7.14) at $x = x_\infty$ gives

$$c_2 = -\frac{2c_1}{\pi}\tan\left(\frac{\overline{\varphi}}{2}\right) \tag{7.20}$$

This allows the values of c_1 and c_2 to be found

$$c_1 = \frac{\pi\xi_{(S)}}{x_\infty}\sqrt{\frac{D_{(N)}}{2D_{(S)}}}\cos\left(\frac{\overline{\varphi}}{2}\right) \tag{7.21}$$

$$c_2 = -\frac{2\xi_{(S)}}{x_\infty}\sqrt{\frac{D_{(N)}}{2D_{(S)}}}\sin\left(\frac{\overline{\varphi}}{2}\right) \tag{7.22}$$

Substituting into (7.2) at $x = 0$ gives the current density of J as a function of x_∞:

$$J = \frac{\rho_{(S)}}{\rho_{(N)}}\frac{D_{(N)}}{D_{(S)}}\frac{\hbar\pi^2}{4e\mu_0\kappa_S^2 x_\infty^3}\sin\overline{\varphi} \tag{7.23}$$

To complete the calculation it is necessary to find x_∞ as a function of the junction half-width d. This can be done using (7.7) – in the thick junction limit ($d \approx x_\infty$) we can use the following approximations

$$\sec\left(\frac{\pi d}{2x_\infty}\right) \approx \tan\left(\frac{\pi d}{2x_\infty}\right) \approx \frac{2}{\pi}\left(\frac{1}{1 - d/x_\infty}\right) \tag{7.24}$$

to obtain $\hat{\psi}^{(N)}(d)$ and $\dfrac{d\hat{\psi}^{(N)}}{dx}(d)$ using (7.16)

$$\hat{\psi}^{(N)}(d) = \frac{\xi_{(S)}}{x_\infty - d}\sqrt{\frac{2D_{(N)}}{D_{(S)}}}\exp\left(-\frac{i\overline{\varphi}}{2}\right)$$

$$\frac{d\hat{\psi}^{(N)}}{dx}(d) = \frac{\hat{\psi}^{(N)}(d)}{x_\infty - d}$$

This gives the value of x_∞:

$$x_\infty = d + \frac{\xi_{(S)}}{\hat{\psi}_\infty}\sqrt{\frac{2D_{(N)}}{D_{(S)}}\left(1+\frac{\hat{\psi}_\infty \rho_{(S)}}{\rho_{(N)}}\sqrt{\frac{D_{(S)}}{D_{(N)}}}\right)} \tag{7.25}$$

and we substitute into (7.23) to find the final J_c expression:

$$J_{D-J} = \frac{\rho_{(S)}}{\rho_{(N)}}\frac{D_{(N)}}{D_{(S)}}\frac{\hbar\pi^2}{4e\mu_0\kappa_{(S)}^2\left(d+\frac{\xi_{(S)}}{\hat{\psi}_\infty}\sqrt{\frac{2D_{(N)}}{D_{(S)}}\left(1+\frac{\hat{\psi}_\infty\rho_{(S)}}{\rho_{(N)}}\sqrt{\frac{D_{(S)}}{D_{(N)}}}\right)}\right)^3}. \tag{7.26}$$

7.2.4 High-field J_c

We now review the work of Dobrosavjlević-Grujić[36] et al which considers a 1D SNS junction where $\alpha_N > 0$ in high fields, such that the field-dependent term must be retained. The in-field linearized equation for the junction was given by

$$\frac{\hat{\psi}^{(N)}}{\xi_{(N)}^2} - \frac{d^2\hat{\psi}^{(N)}}{dx^2} + \left(\frac{2eBx}{\hbar}\right)^2\hat{\psi}^{(N)} = 0 \tag{7.27}$$

The substitution[36]

$$x^2 = \frac{\hbar}{2eB}t^2 \tag{7.28}$$

was used to transform the equation into a standard form for solution.

$$\Rightarrow \qquad \frac{d^2\hat{\psi}^{(N)}}{dt^2} = \left(\frac{\hbar}{2eB\left|\xi_{(N)}\right|^2} + t^2\right)\hat{\psi}^{(N)} \tag{7.29}$$

The forms of f_1 and f_2 were found by solving (7.29). With ${}_1F_1$ = Kummer's confluent hypergeometric function, the general solutions were[36]

$$f_1(x) = \exp\left(-\frac{eB}{\hbar}x^2\right){}_1F_1\left(\frac{1}{4}-\frac{\hbar}{8eB\left|\xi_N\right|^2},\tfrac{1}{2},\frac{2eB}{\hbar}x^2\right) \tag{7.30}$$

$$f_2(x) = x\exp\left(-\frac{eB}{\hbar}x^2\right){}_1F_1\left(\frac{3}{4}-\frac{\hbar}{8eB\left|\xi_N\right|^2},\tfrac{3}{2},\frac{2eB}{\hbar}x^2\right). \tag{7.31}$$

These expressions have the property

$$f_1(x)f_2'(x) - f_1'(x)f_2(x) = \sqrt{\frac{2eB}{\hbar}} \tag{7.32}$$

J can be expressed in terms of c_1, c_2 by substituting (7.8) and (7.32) into (7.2):

$$J = -\frac{\rho_{(S)}}{\rho_{(N)}} \frac{\hbar}{2e\mu_0 \lambda_{(S)}^2 \xi_{(S)}} \sqrt{\frac{B}{B_{c2}}} c_1 c_2 \tag{7.33}$$

In the low-field limit where $B \ll \frac{\hbar}{2ed\xi_{(N)}}$, the De Gennes solution of section 7.2.2 is returned, while in the $t^2 \to \infty$ limit, ${}_1F_1\left(a,b,t^2\right) \to \frac{\Gamma(b)}{\Gamma(a)} t^{2(a-b)} \exp\left(t^2\right)$.

This gave approximate high-field expressions[36, 86] for f_1 and f_2.

$$f_1(x) \approx \frac{\Gamma(1/2)}{\Gamma(1/4)} \left(\frac{\hbar}{2eBx^2}\right)^{1/4} \exp\left(\frac{eB}{\hbar} x^2\right) \tag{7.34}$$

$$f_2(x) \approx \operatorname{sgn}(x) \frac{\Gamma(3/2)}{\Gamma(3/4)} \left(\frac{\hbar}{2eBx^2}\right)^{1/4} \exp\left(\frac{eB}{\hbar} x^2\right) \tag{7.35}$$

c_1 and c_2 were then found in terms of $\hat{\psi}(d)$. Using $\frac{\Gamma(3/4)\Gamma(1/4)}{\Gamma(3/2)\Gamma(1/2)} = 2\sqrt{2}$ in the $\frac{\rho_{(N)}}{\rho_{(S)}} \ll \frac{eBd\xi_{(S)}}{\hbar}$ limit[36] we solve for J_c

$$J_c \approx \frac{\hbar \hat{\psi}_\infty^2 d}{2\sqrt{2} e\mu_0 \lambda_{(S)}^2 \xi_{(S)}^2} \frac{\rho_{(N)}}{\rho_{(S)}} \left(\frac{\hbar}{2ed^2B}\right) \exp\left(-\frac{2eBd^2}{\hbar}\right) \qquad \left(\frac{\rho_{(N)}}{\rho_{(S)}} \ll \frac{eBd\xi_{(S)}}{\hbar}\right) \tag{7.36}$$

Note that we have recalculated equation (7.36) and found that the correct result differs from the original result in the paper by a factor of $\sqrt{2}$. More generally, we can solve for $\hat{\psi}^{(N)}(d)$ using a method analogous to that used in section 7.2.3 to obtain a general solution applicable for all $\rho_{(N)}/\rho_{(S)}$ values:

$$J_c = \frac{\rho_{(S)}}{\rho_{(N)}} \frac{\sqrt{2}\hat{\psi}_\infty^2 Bd}{\mu_0 \lambda_{(S)}^2} \left| \sqrt{2\left(\frac{eBd\xi_{(S)}\rho_{(S)}}{\hbar\rho_{(N)}}\right)^2 + 1} - \frac{\sqrt{2}eBd\xi_{(S)}\rho_{(S)}}{\hbar\rho_{(N)}} \right|^2 \exp\left(-\frac{2eBd^2}{\hbar}\right) \tag{7.37}$$

In the $\frac{\rho_{(N)}}{\rho_{(S)}} \gg \frac{eBd\xi_{(S)}}{\hbar}$ limit, this becomes

$$J_c = \frac{\rho_{(S)}}{\rho_{(N)}} \frac{\sqrt{2}\hat{\psi}_\infty^2 Bd}{\mu_0 \lambda_{(S)}^2} \exp\left(-\frac{2eBd^2}{\hbar}\right) \tag{7.38}$$

In the high-field limit J_c has an exponential dependence on B and d^2 in addition to the B dependence to the phase-coherence related dependence found in a real 2D or 3D system, and does not depend on $|\xi_{(N)}|$. This exponential field dependence is observed in many polycrystalline samples – especially cuprate materials[87]. Note that expression (7.38) does not include $|\xi_{(N)}|$, implying that this high-field result is also valid for the $\alpha_N = 0$ system – the decrease in $\hat{\psi}^{(N)}$ in the junction results almost exclusively from the field itself – also as it is

the field which causes $\hat{\psi}^{(N)}$ to fall, the effective thickness $2d$ of the junction is not the geometric thickness but may include an extra thickness where the field penetrates into the superconductor[36].

7.3 Computational results for zero-field J_c

7.3.1 1-D computational results for $J_{D\text{-}J}$

Figure 7.4 shows J_c computed as a function of the junction thickness d, junction resistivity $\rho_{(N)}$ and superconductor κ value for $\alpha_N = +1$ and $\alpha_N = 0$. For comparison with the computation it is more convenient to use normalized units. For superconductors in the Meissner state, $\hat{\psi}_\infty^2 = 1$ and since we assume the junction to have the same density of states as the superconductor itself, $\frac{\rho_{(S)}}{\rho_{(N)}} = \frac{D_{(N)}}{D_{(S)}}$. Making these substitutions into the normalized form of (7.13) with $\alpha_N = +1$ gives

$$\hat{J}_{D-J} = 2\sqrt{\frac{\rho_{(S)}}{\rho_{(N)}}}\left\{\sqrt{\frac{\rho_{(S)}}{2\rho_{(N)}}+1} - \sqrt{\frac{\rho_{(S)}}{2\rho_{(N)}}}\right\}^2 \exp\left(-2\hat{d}\sqrt{\frac{\rho_{(N)}}{\rho_{(S)}}}\right), \tag{7.39}$$

while the $\alpha_N = 0$ expression results from substituting $\hat{\psi}_\infty^2 = 1$ and $D_{(N)}/D_{(S)} = \rho_{(S)}/\rho_{(N)}$ into (7.26):

$$\hat{J}_{D-J} = \frac{\pi^2}{2}\left(\frac{\rho_{(S)}}{\rho_{(N)}}\right)^2\left[\hat{d} + \sqrt{\frac{2\rho_{(S)}}{\rho_{(N)}}\left(1+\sqrt{\frac{\rho_{(S)}}{\rho_{(N)}}}\right)}\right]^{-3} \tag{7.40}$$

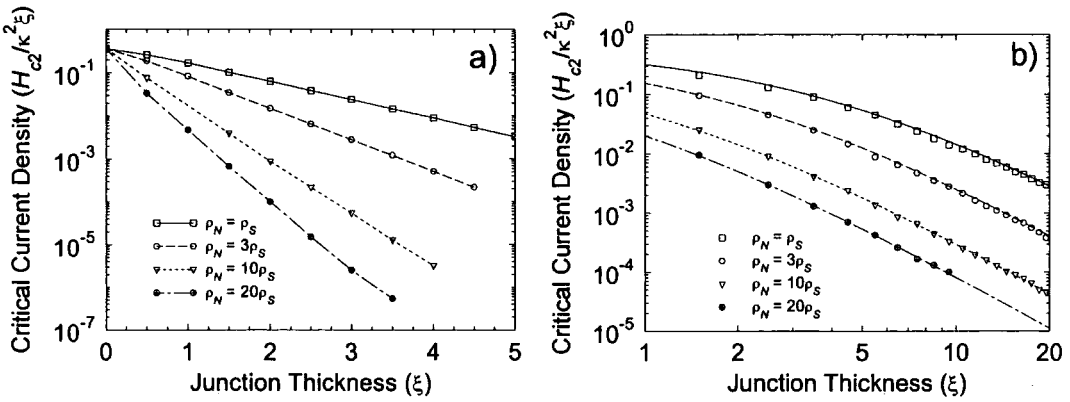

Figure 7.4: J_c values computed for a single 5ξ wide SNS junction with various junction resistivities for a) $\alpha_N = +1$ and b) $\alpha_N = 0$. The computational data (data points) correspond closely with the analytic results (7.39) and (7.40) respectively (lines).

The thickness dependences of J_c for the α_N =+1 and α_N = 0 SNS junctions are in almost exact accordance with (7.39) and (7.40) respectively, except for high J_c values where self-field limiting comes into effect. For both $\alpha_N = 0$ and α_N =+1, $\hat{J}_{D-J}$ for a single SNS junction is κ-independent.

7.3.2 Effect of T and $T_{c(N)}$

The effect of changing the ambient temperature T, or the critical temperature of the junction material can be encapsulated in the parameter α_N, given in the Ginzburg-Landau case by (3.56). Since SNS junctions in experiments use non-superconducting ($T_{c(N)} = 0$) metals in the N layer, and are measured at nonzero temperature, α_N is positive for SNS junctions measured experimentally. However, it is also possible for a junction to have a zero α_N value if the ambient temperature $T = 0$. This has a marked effect on the thickness dependence of J_c.

Figure 7.5 shows values of J_c we have computed for various SNS junctions and demonstrates how changes in α_N affect the thickness dependence of J_c. For $\alpha_N > 0$ a pair-breaking tendency within the junction gives an exponential thickness dependence as observed experimentally[36] for SNS junctions (see also section 3.3.3). For $\alpha_N = 0$, $J_c \propto d^{-3}$ while for $\alpha_N < 0$ the junction is itself superconducting (the junction is now S-S'-S), and the junction J_c tends asymptotically to a constant value in the thick junction limit. In most SNS junction experiments $\alpha_N > 0$ as the measurements are made at nonzero temperature.

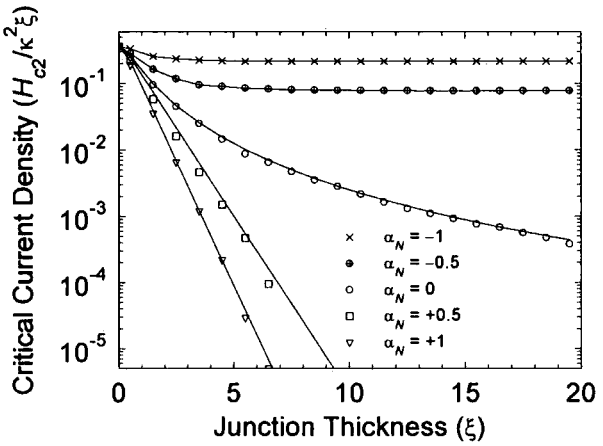

Figure 7.5: Zero-field J_c values computed for a single 5ξ wide, $\rho_N = 3\rho_S$ SNS junction with various α_N values in a $\kappa = 5$ superconductor. The edges at the y-extrema are insulating.

Nevertheless, the $\alpha_N = 0$ case is interesting because J_c has a different thickness dependence, and the zero-field J_c equals that of a thinner $\alpha_N > 0$ junction. This can be useful for simulating a high-J_c junction, which may otherwise be difficult due to the grid discretization imposed by computation.

7.3.3 Effect of Self-Field Limiting

The 1D analytic calculation of J_c for a planar SNS junction in zero applied field gives a limiting value independent of the width of the junction. In wide, thin junctions with high J_c values, the value of J_c for the junction as a whole is lowered as the current is excluded from the central region of the junction by the Meissner effect[88]. The importance of self-field limiting can be determined from the Josephson penetration depth λ_J, which is calculated from J_c via[88]:

$$\lambda_J = \sqrt{\frac{\hbar}{4eJ_c\mu_0(d+\lambda)}} \tag{7.41}$$

If $\lambda_J > w/4$ (w = junction width), then its J_c value will correspond with the value obtained by 1D calculation, while if $\lambda_J < w/4$, J_c will be reduced by self-field limiting[88]. The concept of self-field limiting also has important consequences for the dependence of J_c on an externally applied magnetic field, as shall be seen in the next section. The effect of self-field limiting on J_c can be seen in Fig. 7.6 – for widths up to 10ξ $J_c(H = 0) = J_{D\text{-}J}$, while this is not true for a 30ξ-wide junction.

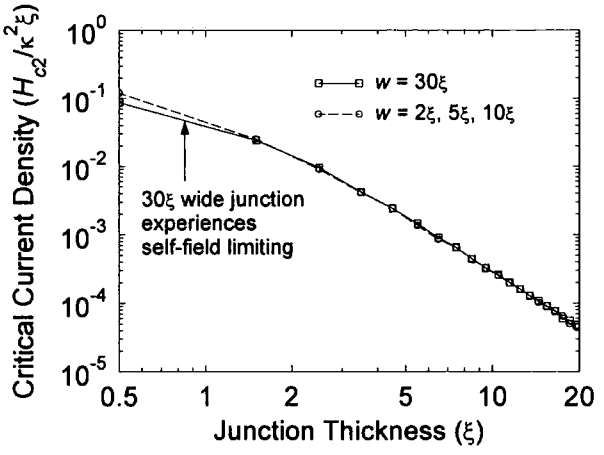

Figure 7.6: J_c computed for SNS junctions with various widths and $\rho_{(N)} = 10\rho_{(S)}$, $\kappa = 5$, $\alpha_N = 0$

7.4 Field Dependence of J_c – Bulk Meissner State

7.4.1 Introduction

For a narrow junction, the field dependence of J_c can be simply calculated using this Fraunhofer approximation. For wider junctions, or junctions with a higher zero-field J_c, the self-field resulting from the current flow becomes important. In the extreme limit, the self-field contribution causes the Fraunhofer sinc dependence to be replaced with a linear decrease of J_c with H, resulting from the confinement of the current to the edges. The computed field-dependence of J_c in the low field regime is shown for junctions of 4 different thicknesses in Fig. 7.7. As the junction thickness increases (and thus J_c decreases), the field dependence changes from the linear self-field decrease to the Fraunhofer pattern.

In low fields, the superconducting blocks on either side of the junction are in the Meissner state – this means that J_c as a function of field can be calculated simply by means of a flux argument[19,89]. At any point along the junction, the current density is determined by the phase difference across the normal junction:

$$J(y) = J_{D-J} \sin \bar{\varphi}(y) \tag{7.42}$$

and the phase difference itself is given by

$$\frac{\partial \bar{\varphi}}{\partial y} = \frac{4e\mu_0 (d+\lambda)}{\hbar} H(y) \tag{7.43}$$

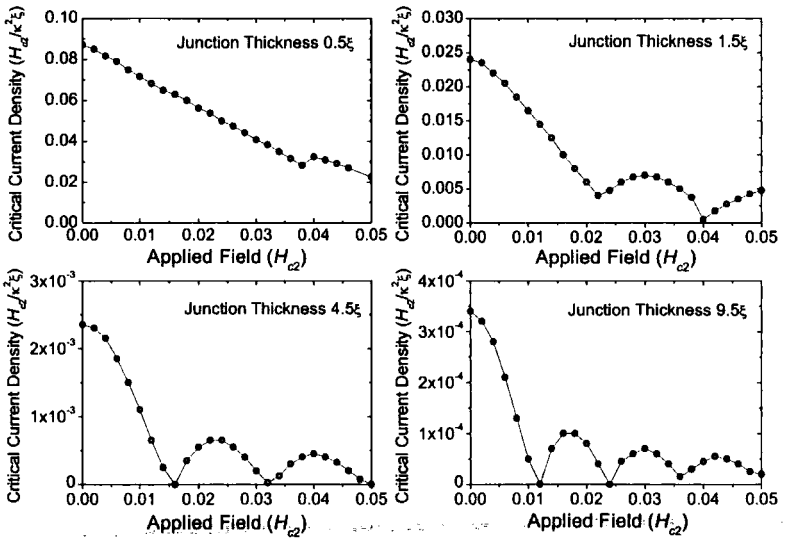

Figure 7.7: J_c computed for an $\alpha_N = 0$, $\rho_N = 10\rho_S$ junction in a 30ξ-wide $\kappa = 5$ superconductor.

Combining (7.42) and (7.43) with Maxwell's equations gives the stationary sine-Gordon equation:

$$\frac{\partial^2 \bar{\varphi}}{\partial y^2} = \frac{1}{\lambda_J^2} \sin \bar{\varphi}(y) \tag{7.44}$$

where λ_J is the Josephson penetration depth given by

$$\lambda_J = \sqrt{\frac{\hbar}{4e\mu_0 (d+\lambda) J_{D-J}}} \tag{7.45}$$

Before the general solutions of (7.44) are given it is important to note an integral parameter k which determines the solution[90]:

$$k = \frac{1}{\sqrt{\left(\frac{\lambda_J}{2}\frac{\partial \bar{\varphi}}{\partial y}\right)^2 + \cos^2 \frac{\bar{\varphi}}{2}}} \tag{7.46}$$

Depending on whether k is greater than or less than 1 there are two general solutions, which can be expressed in terms of Jacobian elliptical functions[90,91]:

$k > 1$:

$$\sin\left(\frac{\bar{\varphi}(y)}{2}\right) = \mathrm{sn}\left(\frac{y - y_0}{\lambda_J}\middle|\frac{1}{k^2}\right) \tag{7.47a}$$

$$\frac{4e\mu_0 (d+\lambda)}{\hbar} H(y) = \frac{\partial \bar{\varphi}}{\partial y} = \frac{2}{k\lambda_J} \mathrm{cn}\left(\frac{y - y_0}{\lambda_J}\middle|\frac{1}{k^2}\right) \tag{7.47b}$$

$k < 1$:

$$\sin\left(\frac{\bar{\varphi}(y)}{2}\right) = \mathrm{cn}\left(\frac{y - y_0}{k\lambda_J}\middle|k^2\right) \tag{7.48a}$$

$$\frac{4e\mu_0 (d+\lambda)}{\hbar} H(y) = \frac{\partial \bar{\varphi}}{\partial y} = \frac{2}{k\lambda_J} \mathrm{dn}\left(\frac{y - y_0}{k\lambda_J}\middle|k^2\right) \tag{7.48b}$$

In narrow junctions at all applied fields, and in wide junctions where $H > H_{c0}$, the $k < 1$ solution determines J_c. The critical value $k_c = 1$ is important, as solutions with $k > 1$ only exist for an applied field below H_{c0}, given by[90]

$$H_{c0} = \frac{\hbar}{2e\mu_0 (d+\lambda)\lambda_J} = \sqrt{\frac{\hbar J_{D-J}}{e\mu_0 (d+\lambda)}} \tag{7.49}$$

A wide Josephson junction can be thought of as being like a one-dimensional type-II superconductor, but with an important difference: while Abrikosov vortices are characterized by two length scales, the coherence length ξ (characterizing the core) and the penetration

depth λ (characterizing the electromagnetic properties), Josephson vortices, being core-less, only have one characteristic length, the Josephson penetration depth λ_J.

7.4.2 General numerical solution

In general, the dependence of J_c on applied field must be calculated numerically. This is done by fixing the magnetic field $H(w)$ and phase difference $\bar{\varphi}(w)$ at one end of the junction. This fixes the value of k, while (7.47) or (7.48) is used to obtain the translational shift y_0. This means that the solution has been completely determined, so $H(0)$, the magnetic field at the other end of the junction, can now be determined. Finding the critical current now becomes an optimization problem[90]:

$$J_c(H(w)) = \frac{1}{w} \max_{-\pi<\Theta(w)\leq\pi} |H(0) - H(w)| \tag{7.50}$$

Once J_c is obtained for all values of $H(w)$, it can be rewritten in terms of H_{app} using

$$H_{app} = H(w) - \tfrac{1}{2} J_c w \tag{7.51}$$

7.4.3 Narrow-junction limit

In the limit of a narrow junction we can take $\lambda_J \to \infty$, we can achieve a simple closed-form solution using the identities $\mathrm{cn}(x \mid 0) = \cos x$, $\mathrm{dn}(x \mid 0) = 1$. This gives the spatially-dependent J expression

$$J(y) = J_{D-J} \cos\left[(y - y_0)\left(\frac{4e\mu_0 (d+\lambda) H_{app}}{\hbar}\right)\right]$$

Integrating over the width of the junction leads to the familar sinc function[19,89]

$$J_c = \frac{1}{w} \max\left[\int_0^w \left|J_y(y, y_0)\right| dy, y_0\right] = \frac{\hbar J_{D-J}}{2e\mu_0 (d+\lambda) H_{app} w} \left|\sin \frac{2e\mu_0 w (d+\lambda) H_{app}}{\hbar}\right|. \tag{7.52}$$

7.4.4 High-field envelope

In high fields the phase-dependent term in (7.46) becomes negligible, so k approximates to

$$k_\infty = \frac{\hbar}{2e\mu_0 (d+\lambda) \lambda_J H_{app}} = \frac{H_{c0}}{H_{app}} \tag{7.53}$$

which gives the H expression

$$H(y) = H_{app} \,\mathrm{dn}\left(\frac{H_{app}}{H_{c0}\lambda_J}(y - y_0) \middle| \left(\frac{H_{c0}}{H_{app}}\right)^2\right) \tag{7.54}$$

The oscillation amplitude ΔH of this expression is

$$\Delta H(y) = \frac{H_{c0}^2}{2H_{app}} \tag{7.55}$$

leading[90] to an upper bound for J_c

$$J_c \leq \frac{H_{c0}^2}{2wH_{app}} = \frac{\hbar J_{D-J}}{2e\mu_0 w(d+\lambda)H_{app}} \tag{7.56}$$

It can thus be seen that the $J_c \propto 1/H_{app}$ envelope which clearly applies for the sinc function is also true in the case of a wide SNS junction. In the high-field limit the main difference between narrow and wide junctions is that J_c at the nodes is non-zero in the wide-junction case.

7.5 Field Dependence of J_c – Bulk Mixed State

When H is high enough that the bulk superconductors on either side of the junction enter the mixed state, the textbook low-field flux integration method[19] is no longer valid. It has been suggested by Nikulov[92] that when the superconductors on either side of an SNS junction enter the mixed state, the junction's properties are affected in two ways:

- The effective width of the junction is changed from $2(d+\lambda)$ to $2(d+\xi)$
- Due to the presence of fluxons and their associated screening currents near the junction, the relevant field for the junction is changed from H to $(H - k_J B)$ where k_J is a constant ≈ 1.

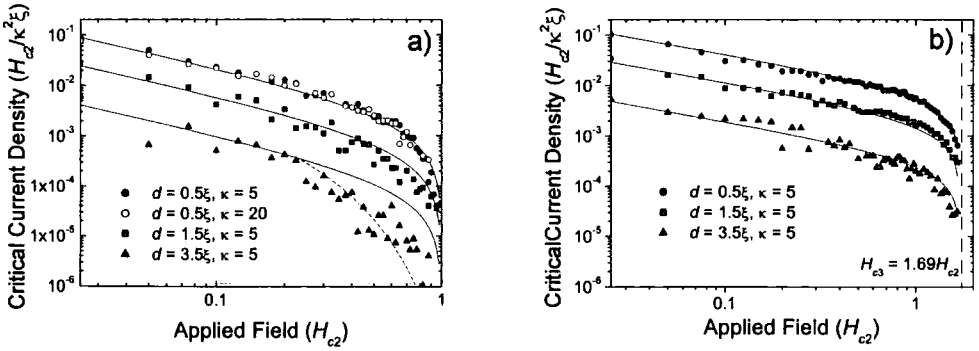

Figure 7.8: Field dependence of J_c up to H_{c2} for 30ξ-wide $\rho_N = 3\rho_S$, $\alpha_N = 0$ junctions of various thicknesses in a $\kappa = 5$ superconductor coated with a) $\rho_N = \rho_S$ metal and b) insulator.

Fig. 7.8 shows the field dependences for 30ξ-wide junction of varying thicknesses. If we start with the sinc field dependence of (7.52) and take into account that

- the individual nodes are not visible in the field dependence of J_c for these wide junctions and we can use the root mean square approximation of sin $x \rightarrow 1/\sqrt{2}$,
- the effective junction width has changed from $2(d + \lambda)$ to $2(d + \xi)$ – this is in accordance with Nikulov's prediction, and results from the disturbance of the field profile moving away from the junction caused by fluxons in the superconductors, and
- the in-field junction depairing current differs from the zero-field $J_{D\text{-}J}$ by a factor $\left(1-\frac{H}{H_{c2}}\right)$ due to the $\left(1-\frac{H}{H_{c2}}\right)$ dependence of $|\psi|^2$ within the bulk superconductors,

we get an analytic expression for the J_c data in Fig. 7.8a of the form

$$J_c(H) \approx \frac{J_{D-J}\xi_{(S)}^2}{2\sqrt{2}w\left(d+\xi_{(S)}\right)}\frac{H_{c2}}{H}\left(1-\frac{H}{H_{c2}}\right) \tag{7.57}$$

However, the second prediction of the Nikulov paper – that the crucial field within the junction was not H but $(H - k_J B)$ was found not to hold in the computations. This is because the paper neglected to consider that the current from the fluxons on one side of the normal junction is almost entirely cancelled by the effect of the similar current flowing on the opposite side of the junction. It can be noted that in Fig. 7.8a) the actual computed values of J_c for fields above $0.6H_{c2}$ (for $2d = 1.5$) or $0.2\ H_{c2}$ (for $2d = 3.5$) are considerably less than those predicted by (7.57). This is because $J_{D\text{-}J}$ is decreased further by the presence of the field following an exponential field dependence[36] consistent with (7.37). The dashed low-J_c line in Fig. 7.8a for $2d = 3.5$ is found by replacing the zero field $J_{D\text{-}J}$ in (7.57) with the high-field limit 1D J_c given by (7.38) with the effective half-width of the junction set to $d + \xi$ here consistent with Nikulov's prediction.

For the data in Fig. 7.8b, the SNS junction with an insulating boundary condition at the edges, we have fitted the expression

$$J_c(H) \approx \frac{J_{D-J}\xi_{(S)}^2}{2w\left(d+\xi_{(S)}\right)}\left(\frac{1.69H_{c2}}{H}\right)^{0.66}\left(1-\frac{H}{1.69H_{c2}}\right)^{0.66} \tag{7.58}$$

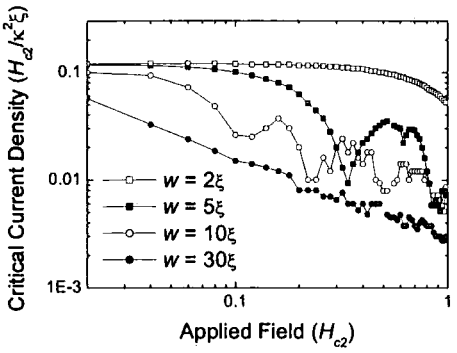

Figure 7.9: Computed field dependence of J_c for a 0.5ξ-thick $\rho_N = 10\rho_S$, $\alpha_N = 0$ junction up to H_{c2} for $\kappa = 5$ superconductors of various widths, with insulating edges.

In the junction with insulating edges, current travels preferentially along the edges due to the superconducting surface sheath – this means the current through the junction is also dominated by the edges, which via the Fourier transform changes the exponent from 1 to 0.66. H_{c2} is also replaced by $H_{c3} = 1.69H_{c2}$.

Another effect on the $J_c(H)$ chacteristic which mixed-state bulk superconductors have is to destroy the regularity of the node spacing. This can be seen in the width dependence of J_c in fields up to H_{c2} shown in Fig. 7.9. Nodes are clearly visible for widths of 5ξ and 10ξ, but for a 30ξ junction the nodes of the sinc function are washed out leaving the monotonic decay $\propto H^{-0.66}$. The fluxons within the bulk material affect the phase of ψ at the junction itself, destroying the J_c node spacing regularity.

7.6 Trilayer junctions

7.6.1 Motivation

In Fig. 7.8b, J_c does not become zero when the applied magnetic field reaches H_{c2}. This is because where $\rho_N > \rho_S$, superconductivity persists along the edges of the superconductors and of the junction even above H_{c2} – this is demonstrated in Fig. 7.10. However, in experimental data on polycrystalline superconductors there is no evidence of a significant surface superconductivity close to grain boundaries above H_{c2}. H_{c3} effects can be removed by:

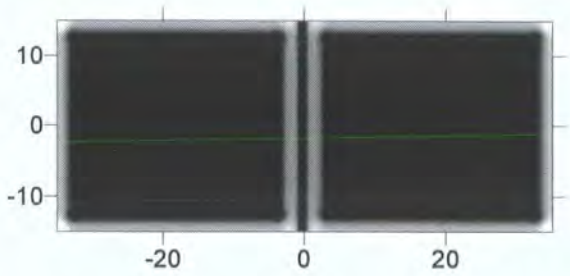

Figure 7.10: Order parameter within for a simple $\rho_{(N)} = 10\rho_{(S)}$ junction 1.5ξ thick at $H = 1.04H_{c2}$ with insulating edges and no applied current (black indicates $|\psi|^2 = 0$). Surface superconductivity exists both along the superconductor edges and the edges of the junction.

i) Applying a metallic boundary condition at the edges of the superconductor, rather than an insulating boundary conditions (this removes the superconducting surface sheaths on the edges of the superconductors), and

ii) replacing the simple normal metal junction with a trilayer junction (this deals with surface superconductivity along the edges of the junction).

We have considered a trilayer as shown in Fig. 7.11 – the inner junction has $\rho_{(N)} > \rho_{(S)}$, while the outer junctions have $\rho_{(N)} = \rho_{(S)}$. This structure is motivated by microstructural analysis (discussed in chapter 8) on grain boundaries showing significant strain several nanometres away from the actual position of lattice mismatch at a grain boundary. Transport measurements on strained superconductors show that a relatively small amount of strain destroys superconductivity[93], while increased scattering (which increases the resistivity in a grain boundary), occurs predominantly close to the region of the lattice mismatch itself.

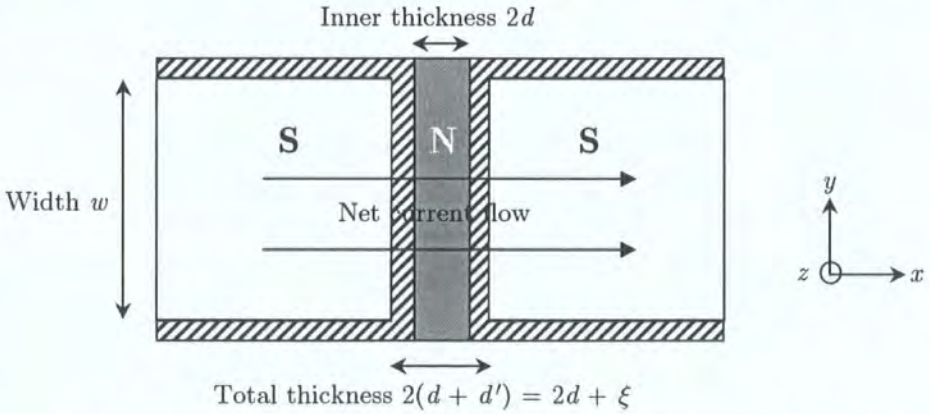

Figure 7.11: Diagram of the trilayer junction. The superconductor edges and outer N layers are $\rho_N = \rho_S$ metallic, while the inner barrier may have higher resistivity

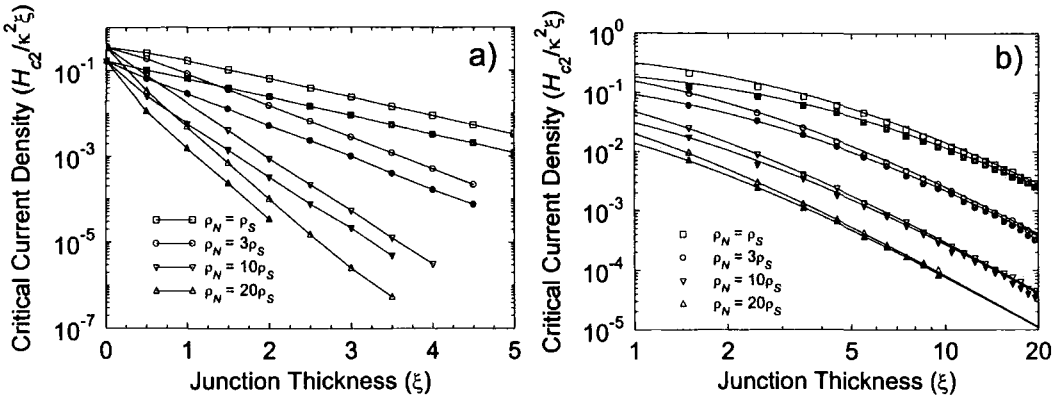

Figure 7.12: Comparison of computed zero-field J_c values for simple SNS junctions (open symbols) and trilayer junctions (closed symbols) for a) $\alpha_N = +1$ and b) $\alpha_N = 0$

7.6.2 Effect of Outer Layers on Zero-Field J_c

Figure 7.11 shows the geometry of the trilayer junctions considered here. The thickness d' of each outer junction is fixed at 0.5ξ, as it is desired that they should have as little effect as possible on the junction, other than eliminating surface superconductivity. Nevertheless, it is important to check the effect of the outer layers on the junction J_c.

Figure 7.12 compares the zero-field J_c of trilayer junctions with those of simple SNS junctions. The effect of adding the outer layers can be expressed by modifying the expressions for the zero-field J_c. For $\alpha_N = +1$, with an inner junction of thickness $2d$ and a total junction thickness of $2(d + d')$, we have found that the zero-field J_c expression (7.39) becomes

$$J_{D-J} = 2\sqrt{\frac{\rho_{(S)}}{\rho_{(N)}}}\frac{\left(\sqrt{\frac{\rho_{(S)}}{2\rho_{(N)}}+1}-\sqrt{\frac{\rho_{(S)}}{2\rho_{(N)}}}\right)^2}{\left(\cosh\hat{d}' + \sqrt{\frac{\rho_{(S)}}{\rho_{(N)}}}\sinh\hat{d}'\right)^2}\exp\left(-2\hat{d}\sqrt{\frac{\rho_{(N)}}{\rho_{(S)}}}\right) \tag{7.59}$$

while for $\alpha_N = 0$, we can use the following approximation:

$$J_{D-J} \approx \frac{\pi^2}{2}\left(\frac{\rho_{(S)}}{\rho_{(N)}}\right)^2\left(\hat{d} + \sqrt{\frac{\rho_{(S)}}{\rho_{(N)}}}\hat{d}' + \sqrt{\frac{2\rho_{(S)}}{\rho_{(N)}}\left(1+\sqrt{\frac{\rho_{(S)}}{\rho_{(N)}}}\right)}\right)^{-3} \tag{7.60}$$

These reductions in J_c can alternatively be expressed in terms of an effective junction thickness d_{eff} in equation (7.39) of

$$d_{eff} = d + \sqrt{\frac{\rho_{(S)}}{\rho_{(N)}}} \ln\left(\cosh d' + \sqrt{\frac{\rho_{(S)}}{\rho_{(N)}}} \sinh d'\right). \tag{7.61}$$

and in equation (7.40) of

$$d_{eff} \approx d + \sqrt{\frac{\rho_{(S)}}{\rho_{(N)}}} d' \tag{7.62}$$

7.6.3 Effect of Outer Layers on In-Field J_c

The effect on introducing the trilayer junction is much more marked in the in-field case than in the zero-field case, because in the simple junction it is difficult to suppress $|\psi|^2$ on the superconducting sides of the junction due to the boundary conditions, while in the trilayer junction, it is much easier to suppress $|\psi|^2$ in the outer normal layers. Figure 7.13 compares the field dependences of J_c for a trilayer junction, a simple junction with normal metal edges and a simple junction with insulating edges. It can be seen that the trilayer junction not only has a lower overall magnitude of J_c due to the reduction in $J_{D,J}$ because of the additional normal layers, but also has a different high-field dependence – as the applied field approaches H_{c2}, J_c drops to zero as $\left(1 - \frac{H}{H_{c2}}\right)^2$ rather than the $\left(1 - \frac{H}{H_{c2}}\right)$ associated with the single junction. This is due to an additional reduction in $|\psi|^2$ near the junction which results from the presence of the outer junctions.

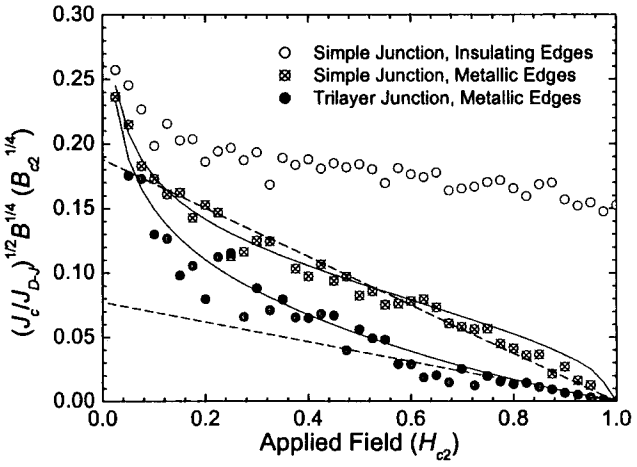

Figure 7.13: Comparison of in-field J_c for simple SNS junctions with insulating and metallic edges (data taken from Figs. 6.8b and 6.8a respectively) and trilayer junctions with metallic edges for a $\rho_{(N)} = 3\rho_{(S)}$, $\alpha_N = 0$, 0.5ξ-thick junction in a $\kappa = 5$ superconductor

The critical current density expression for the trilayer junction is therefore

$$J_c(H) \approx \frac{J_{D-J}\xi_{(S)}^2}{2\sqrt{2}w\left(d+\xi_{(S)}\right)}\frac{H_{c2}}{H}\left(1-\frac{H}{H_{c2}}\right)^2 \tag{7.63}$$

It can be seen in Fig. 7.13 that J_c for the single junction with normal metallic edges can look deceptively similar to the Kramer $b^{-\frac{1}{2}}(1-b)^2$ dependence. This is because (7.57) overestimates low-field J_c – the product HJ_c, peaks near $0.2H_{c2}$, the same field at which F_p peaks according to the Kramer model, rather than linearly increasing as H decreases from H_{c2} towards zero. The dashed lines in Fig. 7.13 are approximations to the high-field data with a $J_c \propto b^{-\frac{1}{2}}(1-b)^2$ dependences, while the solid curves follow the derived dependences. The simple-junction expression (7.57) can thus be approximated using the Kramer-like expression:

$$J_c(H) \sim 1.06\frac{J_{D-J}\xi_{(S)}^2}{w\left(d+\xi_{(S)}\right)}\sqrt{\frac{H_{c2}}{H}}\left(1-\frac{H}{H_{c2}}\right)^2 \tag{7.64}$$

7.7 'Cross' junctions

In order to get the best possible comparison between a single planar SNS junction and the granular systems in chapters 8 and 9, a 'cross' trilayer junction has also been modelled. As shown in Fig. 7.14, this is a trilayer junction which also includes layers of high-resistivity normal metal just outside the edges of the superconductors on either side of the barrier. These cross the high-resistivity junction layer at the two ends of the junction. This is thus directly equivalent to the multi-grain system, where the high-resistivity layer normal to the current corresponds to a grain boundary which the current must cross, while the high-resistivity layers parallel to the current corresponds to surfaces which must pin fluxons to enable a current to flow non-dissipatively through the superconductor.

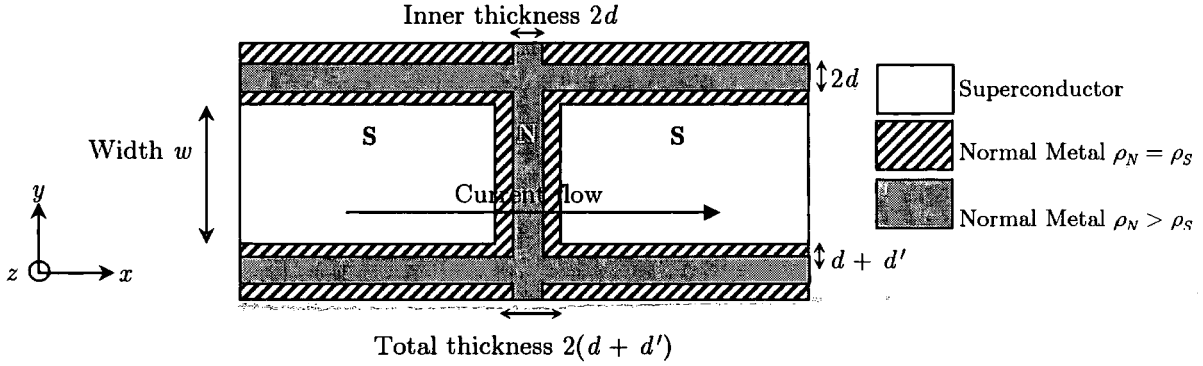

Figure 7.14: Diagram of the 'cross' junction.

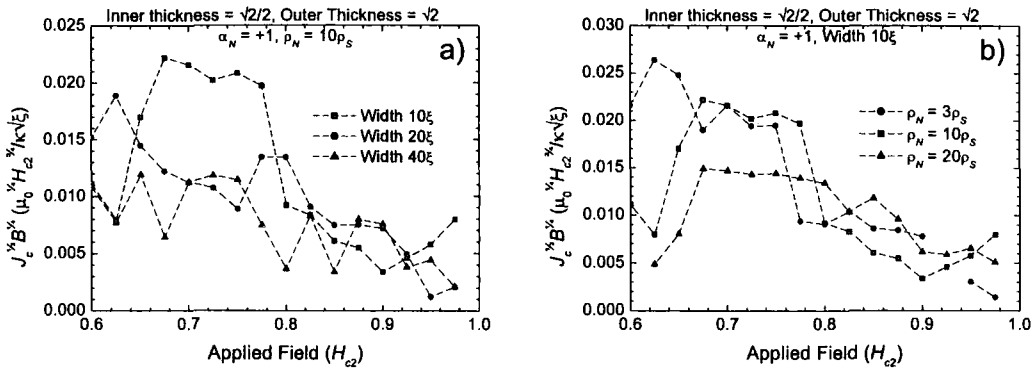

Figure 7.15: Critical current density for 'cross' junctions with $\alpha_N = +1$ as a function of a) width and b) ρ_N/ρ_S.

Typical data at fields above $0.6H_{c2}$ for these types of junctions is displayed in Fig. 7.15. The data is very noisy which suggests that the phase-dependent behaviour of single junctions is present in this trilayer system. Furthermore there is no simple resistivity dependence in this data, as higher resistivities tend to lower $J_{D\text{-}J}$ (which lowers J_c) but also tend to enhance the superconducting surface sheaths (which raise J_c). However, an approximately $1/w$ width dependence is still clearly visible, as is the strong sensitivity to field which is also characteristic of phase-dependent systems.

7.8 Conclusions

7.8.1 Zero-field J_c

A single planar SNS junction has been simulated using the TDGL equations. For a junction with pair-breaking ($\alpha_N > 0$) $J_c(H = 0)$ has an exponential thickness dependence – this famous De Gennes result[85] is the case for all SNS junctions at nonzero temperature. For a junction without pair-breaking (equivalent to zero ambient temperature) $J_c(H = 0)$ has an approximately inverse-cube dependence. This case is less directly applicable but is useful from a computational perspective.

7.8.2 Field dependence of J_c

In low fields (superconductors on either side of the junction in Meissner state) the field dependence of J_c follows the 'Fraunhofer' sinc function for narrow or poorly conducting junctions, and is limited by the current self-field in wide, high-J_c junctions – this is consistent with experimental data. In high applied fields (superconductors on either side of junction in mixed state), the field dependence changes from $J_c \propto \frac{1}{w(d+\lambda)}$ to $J_c \propto \frac{1}{w(d+\xi)}$ because the magnetic field penetrating the junction (which reaches a distance λ into a Meissner-state superconductor) is disrupted at a distance $\approx \xi$ from the junction by the fluxons within the superconductors.

For a superconductor with normal metallic edges, extending the analysis up to H_{c2} washes out the nodes of the sinc function, giving an $\frac{H_{c2}}{H}$ factor, while the decrease in the order parameter within the superconductors adds a $\left(1-\frac{H}{H_{c2}}\right)$ (c.f. (7.57)) factor, causing J_c to become zero at H_{c2}. On insulating superconducting edges, superconducting surface sheaths are formed which alter the current profile of the junction, and give a field dependence more like $J_c \propto \left(\frac{H_{c2}}{H}\right)^{2/3}\left(1-\frac{H}{H_{c3}}\right)^{2/3}$ (c.f. (7.58)). If the simple junction is replaced by a trilayer junction, the field dependence becomes $J_c \propto \frac{H_{c2}}{H}\left(1-\frac{H}{H_{c2}}\right)^2$ – see section 7.6.3.

7.8.3 Comparison with pinning model

In terms of the widely used 'pinning' model for describing the critical current of superconductors, the J_c of a single planar SNS junction can be interpreted as resulting from surface pinning of fluxons at the edges of the junction. Current flow through the junction results from their being an incomplete number of Josephson vortices across the junction. For an infinitely long junction all the currents from the Josephson vortices cancel each other out, leading to zero J_c – this manifests itself in the $1/w$ dependence in the J_c expressions.

8 The Critical State Model for Polycrystalline Superconductors

8.1 Introduction

The behaviour of fields and currents within a polycrystalline Type-II superconductor is very complex. Section 8.2 reviews the method of determining the critical current density of a superconductor by a magnetization measurement. We explain why we use such a method in our polycrystalline superconductor simulations, rather than the direct transport measurement used in Chapter 7. Section 8.3 explains the choice of system used in the simulations. This system has been chosen to be amenable to computation and simple to analyze, whilst preserving the essential physics of real polycrystalline superconductors. Nevertheless, all the calculations in this chapter are two-dimensional calculations, as these are less computationally expensive than 3D computations. The remainder of section 8.3 considers various other issues involved in computing J_c – separation of bulk and surface currents, matching effects and mathematical symmetry problems.

Section 8.4 describes a 'mainline + branches' approach to finding J_c which permits the E-fields associated with the measurements to be reduced to values comparable with those used experimentally. The later parts of this section uses this method to calculate J_c at fields above $0.84H_{c2}$ in a $\kappa = 10$ superconductor with 30ξ grains separated by $\rho_N = 10\rho_S$ trilayer grain boundaries (this is our computational 'hub' – all systems covered in Chapter 9 change only one of the three parameters of κ, grain size and grain boundary resistivity). The field range close to H_{c2} is chosen as it will give us the most interesting results in the next chapter. We ensure that our calculated J_c values are not unduly affected by sample size, the field ramping rate during the mainline run, or the resolution of the computational grid.

Section 8.5 extends these calculations to entire field range from zero to above H_{c2}, while section 8.6 gives a more detailed look at the computational resources required by our calculations. Section 8.7 concludes the chapter with a brief summary.

8.2 Measurement of J_c in polycrystalline superconductors

8.2.1 Obtaining J_c from a Bean profile

We have decided to use a magnetization measurement to obtain J_c, rather than the transport measurement method used in the previous chapter – reasons for this choice will become clear in Section 8.6. In chapter 5 we addressed the importance of the surface barrier when modelling a superconductor via computation. When considering the J_c of a polycrystalline superconductor for practical use, it is important to ensure that the J_c value being obtained is the *bulk* J_c value, and not that resulting from a surface current. The bulk J_c value can be obtained from the one-dimensional spatial profile of the local magnetic field within the material (see section 2.6.2). J_c can then be obtained from the one-dimensional form of Maxwell's equations:

$$J_c = \frac{1}{\mu_0}\frac{dB_z}{dy} \tag{8.1}$$

8.2.2 *E*-field associated with ramping of applied field

The electric field associated with ramping a field can be calculated from Maxwell's equations – when the applied field is ramped up or down, this induces electric fields in opposing directions on either side of the sample. For a sample of width $W\xi$, the magnitude of the electric field at the edges (where it is highest) is given by

$$E_{\max} = \frac{W}{2}\frac{\delta B}{\delta t} \tag{8.2}$$

The standard non-dimensionalizations of (3.62)-(3.64) are used in this formula: these give a normalized E_{max} in units of $H_{c2}\rho_S/\kappa^2\xi$.

8.3 A model for granular superconductors

8.3.1 A body–centred-cubic arrangement for grains in a polycrystalline superconductor

There were several considerations involve in deciding how to simulate a polycrystalline superconductor within the computation:

i) There should be only one characteristic grain size in the granular system.

ii) All grain boundaries should be planar and should be of the same thickness

iii) The system should be reasonably simple to model using the rectilinear grid.

iv) There should be no continuous straight paths for fluxons to follow through the superconductor

The 'single characteristic length' and 'rectilinear grid' requirements both point towards a system with cubic symmetry, but a simple cubic system is not suitable as there are continuous planes parallel to all three crystallographic axes – we had concerns about fluxons moving through a 3D superconductor without bending. It was decided to model the polycrystalline superconductor as a set of grains arranged in a b.c.c. structure. Given the requirement that the grain boundaries be planar, the grains take the form of truncated octahedra. An f.c.c. arrangement, in which the grains would take the form of rhombic dodecahedra, would also be possible, but this would have only half the volume per grain for a given unit cell size (and is therefore probably more computationally expensive). The b.c.c. granular structure is shown in Figure 8.1.

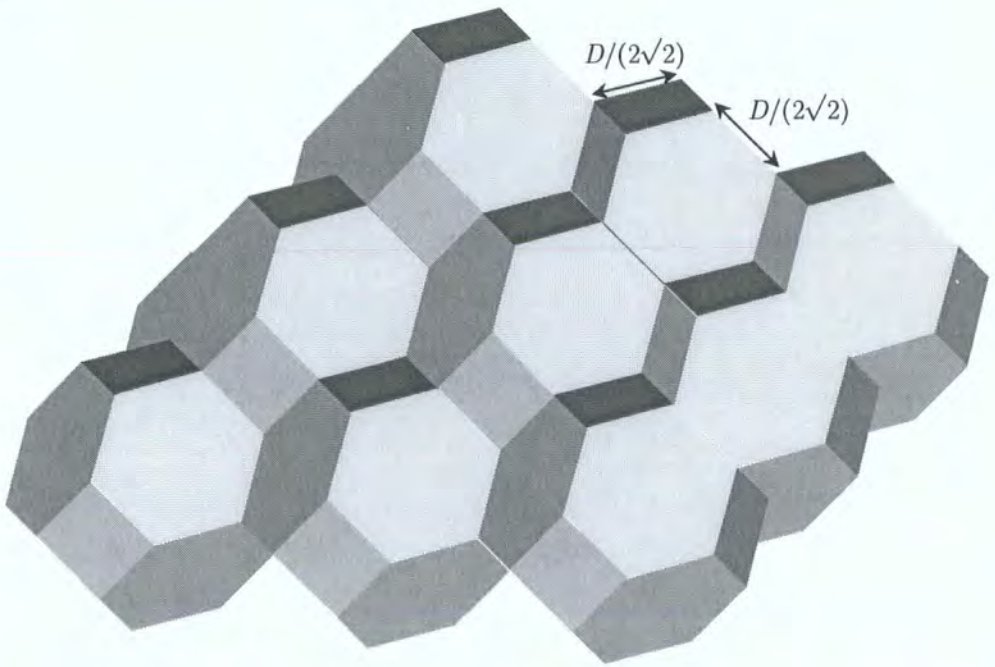

Figure 8.1: BCC arrangement of truncated octahedra as used in polycrystalline model. We define the 'grain size' as D, the distance between opposite square faces of a grain.

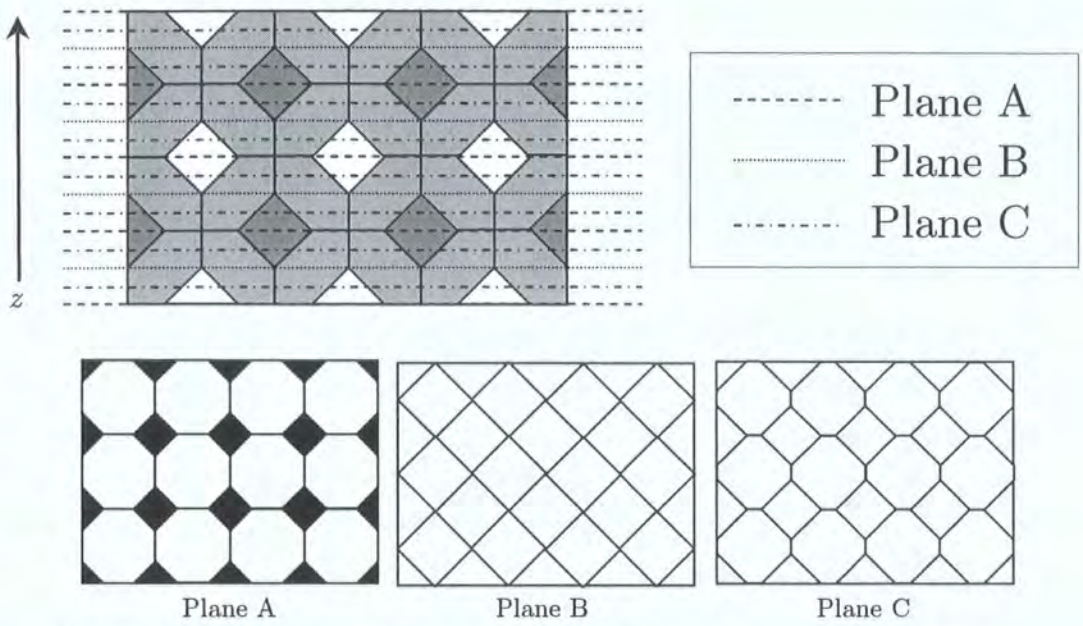

Figure 8.2: Possible cross-sectional planes of BCC truncated octahedral structure

Since 3D computations are extremely computationally expensive, it is also desirable to select a cross-section of this 3D structure for 2D calculations. There are three obvious cross-sections to choose, which are shown in Fig 8.2 – it was decided that the 2D polycrystalline calculations would be based on plane C, as it contains neither the large normal 'islands' of plane A, nor the continuous straight channels of plane B, both of which are not representative of 3D systems.

8.3.2 Matching effects and symmetry problems

Because the system has a regular structure with all grains of identical size and shape, matching of the flux-line lattice to the grain structure can cause problems when measuring J_c. If the grain boundaries to run parallel to the edges of the material the local field contributions from individual fluxons will interfere constructively when summed. As illustrated in Fig. 8.3, we rotate the edges of the superconductor rather than the grain boundaries themselves. Since the grain boundary thicknesses are only a very small number of length units in the discretized grid, running these along non-principal axes would unacceptably distort the grain boundaries. We define the a- and b-axes to lie along the grain structure principal axes (with periodic boundary conditions applying at the a-extremities), while the x- and y-directions are respectively parallel and normal to the superconductor edges. The c-axis and z-axis are

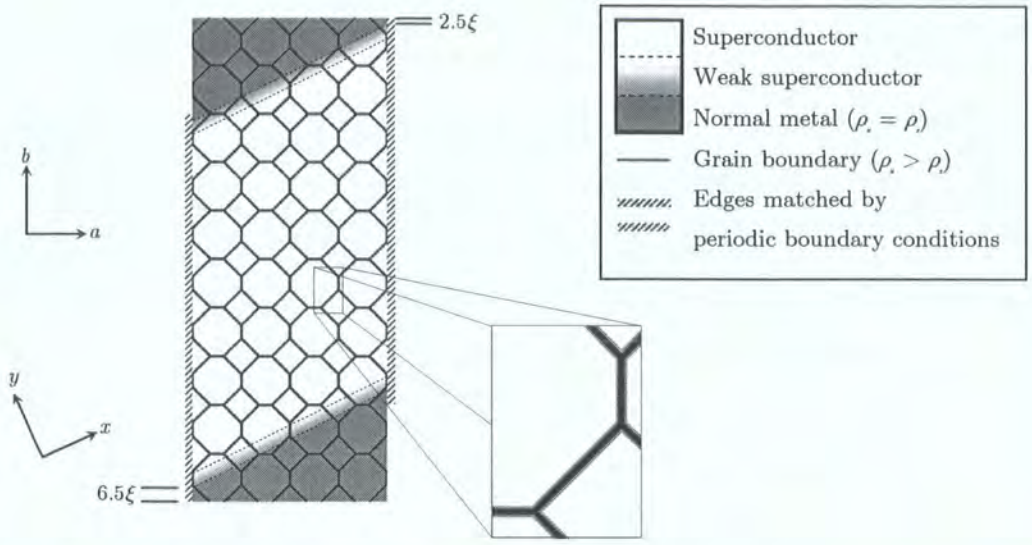

Figure 8.3: Scale drawing of the 'hub' simulated 2D polycrystalline superconductor, or a cross-section of a simulated 3D polycrystalline superconductor

equivalent, both being normal to the plane of study in 2D calculations, and being the direction along which the H-field is applied. In 3D calculations, true periodic boundary conditions are applied along the c/z-axis, and the problem of matching effects can be reduced further by applying the external field along a direction other than along the c/z-axis.

To prevent states which are a local energy maximum forming due to point symmetry of the system, the N material thicknesses at the b-extrema has also set to be unequal (one is 2.5ξ while the other is 6.5ξ). Since ψ tends rapidly to zero within the outer N layers this should have negligible effect on the physics of the system, but an overall mathematical asymmetry to the system is introduced which prevents fluxons artificially 'blocking' each other in the centre of the system.

8.3.3 Dealing with surface barriers

J is obtained from the y-dependence of the local field B (summed over x) and finding dB/dy using a least-squares-fitting method – this gives J via Maxwell's equations as described in Bean's critical state model[24]. This measures the *bulk* J_c of the superconductor, without regard to the effect of the surface barrier. Nevertheless, to further suppress any effect of surface barrier on the calculated bulk J_c values, an S' layer 10ξ thick along with an thin N layer are

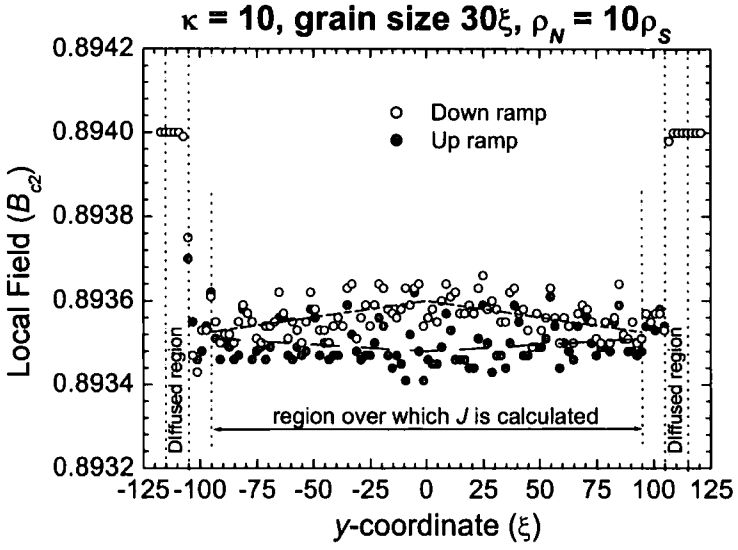

Figure 8.4: Raw field data obtained from simulations of the 'hub' system at $H = 0.894H_{c2}$ with fitted symmetric Bean profiles

added at the y-extrema to lower the barrier, and the outermost regions on either side of the core superconductor are ignored when calculating J_c. An example Bean profile for the hub system ($\kappa = 10$, grain size 30ξ, $\rho_N = 10\rho_S$) at an applied field $H = 0.894H_{c2}$ is shown in Fig. 8.4 – the straight-line profiles indicate the region in y across which J_c is measured.

8.4 Obtaining J_c for low E-fields

8.4.1 Metastable States

There are an innumerable number of possible fluxon configurations for the polycrystalline superconductor which are stable. As the applied magnetic field is ramped up or down, the superconductor passes through these metastable states. Fluxons enter (or leave) at the edges, steepening the Bean profile and thus increasing the current density J. This occurs until the metastable state becomes unstable, at which point fluxons move down the energy gradient towards or away from the centre until another metastable state is reached.

8.4.2 Computing J_c by a 'branching' approach

One problem with obtaining J_c computationally is that the ramping of the applied magnetic field up or down generates an electric field, and that the field ramping rates practical in

computations corresponding to E-fields that are nine orders of magnitude higher than those used in experimental measurements – for a superconductor with $\kappa \approx 20$, $H_{c2} \approx 10$T and $\rho_S \approx 1$ $\mu\Omega$ m, $E = 10$ μV m^{-1} – a commonly-used experimental criterion[94-96] for J_c – corresponds to $E \approx 2 \times 10^{-12}\ H_{c2}\rho_S/\kappa^2\xi$. Ramping through the entire field range from zero to H_{c2} at the extremely slow ramp rate corresponding to such an E-field is obviously totally impractical, as it would ~ 10^{15} iterations to ramp from zero to H_{c2}, which on our current computers would take several million years to complete.

To solve this problem, we have adopted an approach where a 'mainline' run sweeps up and down relatively quickly through the field range. 'Branch runs' then hold the H-field constant allowing the superconductor to equilibrate starting from the flux configuration calculated for that field during the mainline run, with no electric field present except that generated internally during equilibration. Each branch run reaches a different metastable state, with an associated J_c value corresponding to an E-field reached at the end of the branch. In typical examples of calculations seen here, the mainline run corresponds to an E-field of $E_{mainline} = 1.25 \times 10^{-3}\ H_{c2}\rho_S/\kappa^2\xi$. The E-field at the end of the branches varies from branch to branch, as the length of the branches is fixed in time, but is typically of order $E_{branches} \sim 4 \times 10^{-8}\ H_{c2}\rho_S/\kappa^2\xi$. This is still much higher than experimentally-measured values, but is nevertheless orders of magnitude less than would be practicable in a direct calculation.

8.4.3 Choice of initial conditions, grain boundary thickness and field range

The initial condition for the calculations is a simple flux-line lattice, obtained by equilibration in a superconductor homogenous except for 0.5ξ-wide normal strips along the x-edges of the grid. This preliminary equilibration takes place at the starting applied field over $250t_0$, beginning in the Meissner state (for upward ramping) or the normal state (for downward ramping). The order parameter and vector potential from this calculation are then applied to the polycrystalline structure and the system is allowed to equilibrate over $1000t_0$ before the ramping of the applied field begins. Note that in Fig. 8.5, $t = 0$ is to the time when field ramping starts.

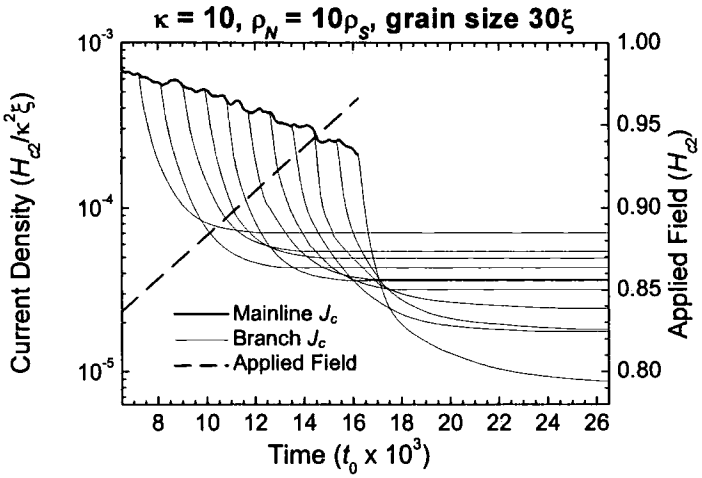

Figure 8.5: Time evolution of mainline and branch calculations in the high-field range for a κ = 10 superconductor with 30ξ grains separated by $\rho_N = 10\rho_S$ boundaries

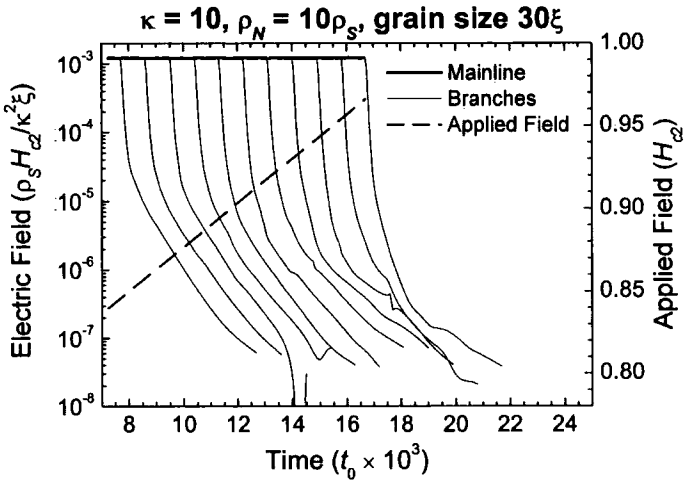

Figure 8.6: Electric fields associated with mainline and branch-line data shown in Fig. 8.5

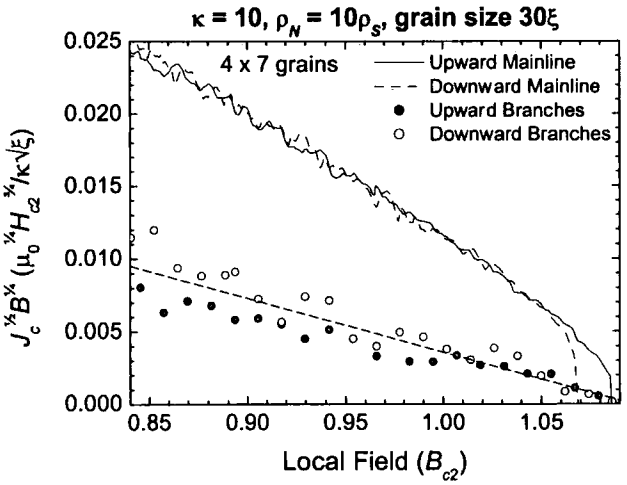

Figure 8.7: Kramer plot in the field range $0.84H_{c2}$ – $1.09H_{c2}$ for a κ = 10 superconductor with 30ξ grains separated by $\rho_N = 10\rho_S$ grain boundaries. As in experimental results, the J_c values obtained from the downward ramp are greater than those from the upward ramp.

As described in section 7.6, a trilayer-junction model is more realistic than a single junction when modelling a grain boundary. In all computations in this chapter and in Chapter 9, the grain boundaries are modelled as trilayer junctions with an inner thickness of 1ξ and an outer thickness of 2ξ. Thicker grain boundaries would not only decrease J_c values considerably possibly complicating measurements due to slower equilibration (cf section 7.1.2), but would also reduce the total proportion of superconducting material within the system, while thinner boundaries cannot reasonably be used as the computations are discretized in units of 0.5ξ.

We shall first investigate J_c in a $\kappa = 10$ superconductor with a grain unit cell size of 30ξ and an inner boundary resistivity $\rho_N = 10\rho_S$. Consistency tests will focus on the high-field regime, in the range $0.84H_{c2} < H < 1.09H_{c2}$. Once the computational method is judged reliable for this limited field range, it is extended to the entire field range from zero to $1.1H_{c2}$, first for this specific system towards the end of this chapter, and then for a range of grain sizes and κ and ρ_N/ρ_S values in Chapter 9. The results from this first set of measurements are shown in Figs. 8.5, 8.6 and 8.7.

8.4.4 Grid size dependence of J_c

Before the computational values of J_c can be trusted, they must also be shown to be completely general, rather than specific to the specific size of superconductor used in the calculation. It seemed reasonable that there should be at least 4 grains of superconductor in the *a*-direction, and at least 200ξ, of superconductor (here we use 7 grains – 210ξ of superconductor) in the *b*-direction. Tests were made in which the *a*- and *b*-dimensions of the superconducting region were doubled – the results of these tests are shown in Fig. 8.8. These tests confirm that the superconductor dimensions of 4 grains (120ξ) are sufficient in the *a*-direction for our purposes. When the size of the system is doubled in the *b*-direction, the computed J_c for the branch lines falls by 35%. This is not ideal, but the computational expense of increasing the *y*-dimension further would be prohibitive, as we go on to investigate the effect of changing the Ginzburg-Landau parameter κ, the grain boundary resistivity, and the size of the superconductor grains.

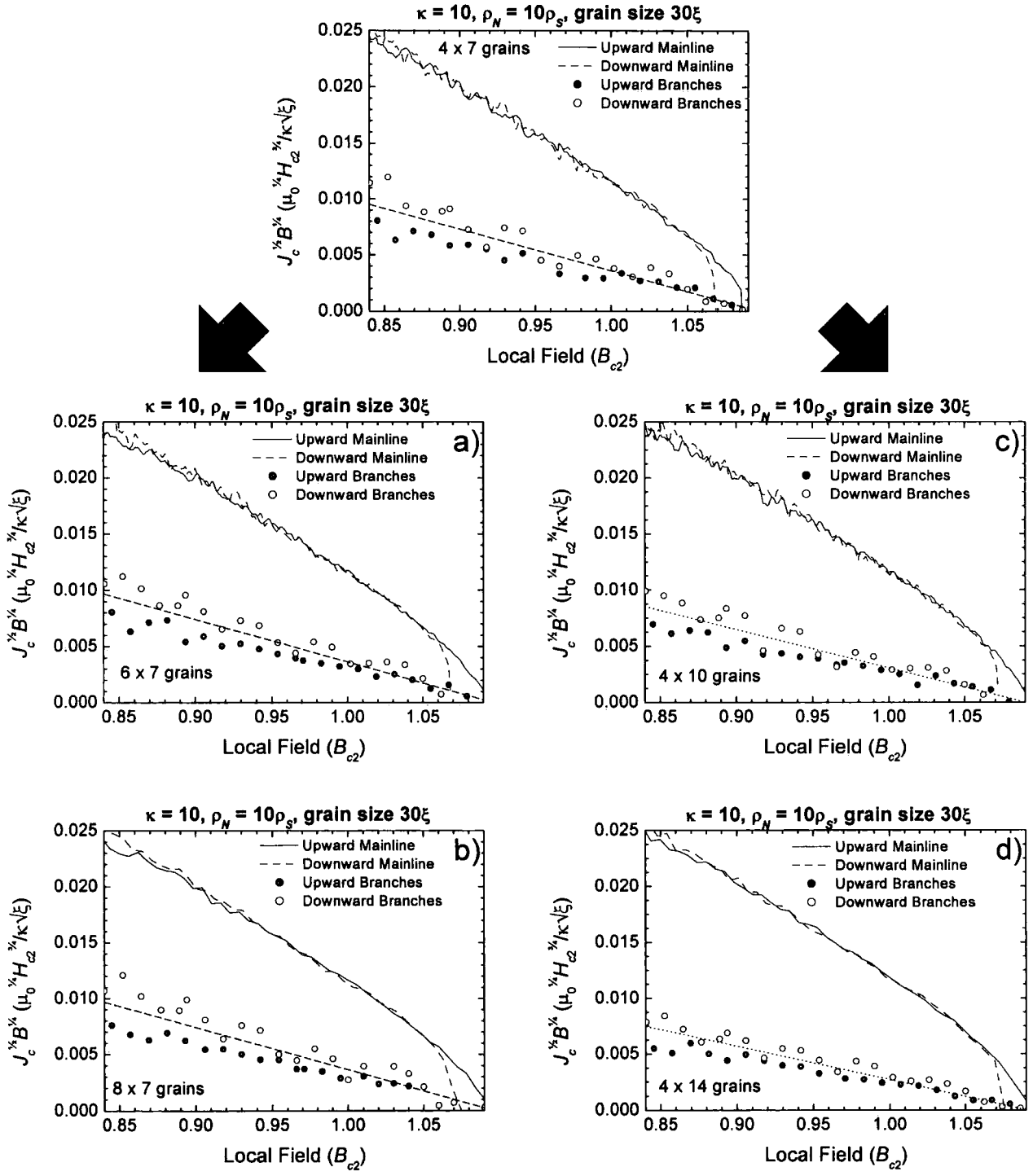

Figure 8.8: Effect of sample dimensions on J_c, expressed as Kramer plots in the field range $0.84H_{c2}$ – $1.09H_{c2}$ for a κ = 10.superconductor with 30ξ grains separated by $\rho_N = 10\rho_S$ grain boundaries. The top graph is a duplicate of Fig. 8.7, while the left branch increases the number of grains in the a-direction from 4 to a) 6 and b) 8, and the right branch increases the number of grains in the b-direction from 7 to c) 10 and d) 14. The high-E 'mainline' J values have negligible dependence on a- or b-dimensions. The low-E 'branch' J values have no a-dimension dependence, but do decrease as the b-dimension increases.

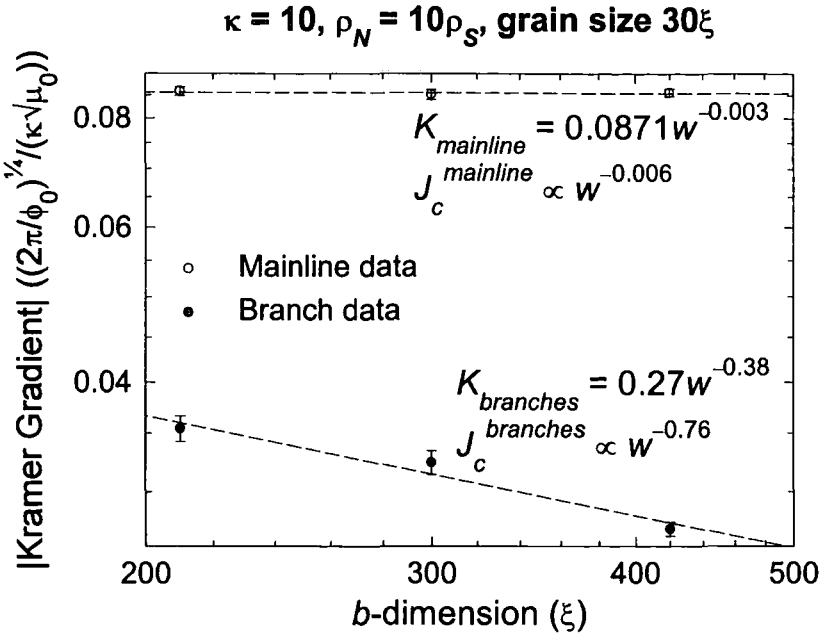

Figure 8.9.: Kramer gradient of 'mainline' (high-E) and 'branch' (low-E) as a function of sample width for a $\kappa = 10$ superconductor with 30ξ grains separated by $\rho_N = 10\rho_S$ trilayer grain boundaries (note that both axes are logarithmic).

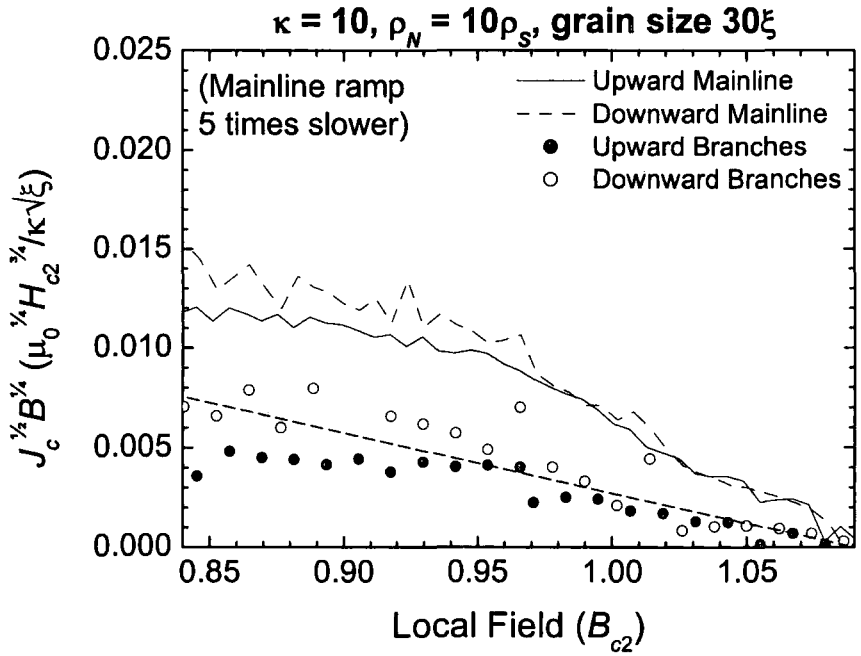

Figure 8.10: Kramer plots in the field range $0.84H_{c2}$ – $1.09H_{c2}$ for a $\kappa = 10$.superconductor with 30ξ grains separated by $\rho_N = 10\rho_S$ grain boundaries with the mainline ramp rate reduced to 20% of the value in Fig, 7.5a.

In fact, the width-dependence of the branch data is consistent with a width dependence of

$$J_c \propto w^{-0.76} \tag{8.3}$$

as shown by plotting the Kramer gradient as a function of width in Fig. 8.9. The mainline data shows negligible width dependence.

8.4.5 Effect of changing the mainline ramp rate

Before carrying out large-scale calculations of J_c it is important to determine to determine that the granular system can carry a bulk supercurrent at all, rather than merely a resistive current. This was checked by computing J_c at differing E fields and confirming that the E-field dependence of J_c is non-ohmic. The data plotted in Fig. 8.10 was calculated under the same conditions as that of Fig. 8.7, except that the ramping rate of the mainline was five times slower (via Maxwell's equations, this corresponds to reducing the E-field in the system by 80%). This decreases the observed mean bulk current density by $\approx$ 30%, consistent with a non-linear E-J characteristic.

8.4.6 Grid resolution dependence of J_c

The default $0.5\xi \times 0.5\xi$ grid spacing gave accurate results for the thickness dependences of J_c for single junctions in Chapter 7, but it is necessary to check that this is sufficient for the polycrystalline system. The calculations of Fig. 8.7 are repeated for the finer grid spacings of $0.33\xi \times 0.33\xi$ and $0.25\xi \times 0.25\xi$ – the results are shown in Fig. 8.11. The computed H_{c2} is closer to the analytic value than in the previous runs, which overestimated it by about 7%. This highlights a tendency for grid discretization in TDGL computations to cause overestimation of H_{c2}. However, the important results – the gradient of the Kramer line – remains unaffected by the change in grid discretization.

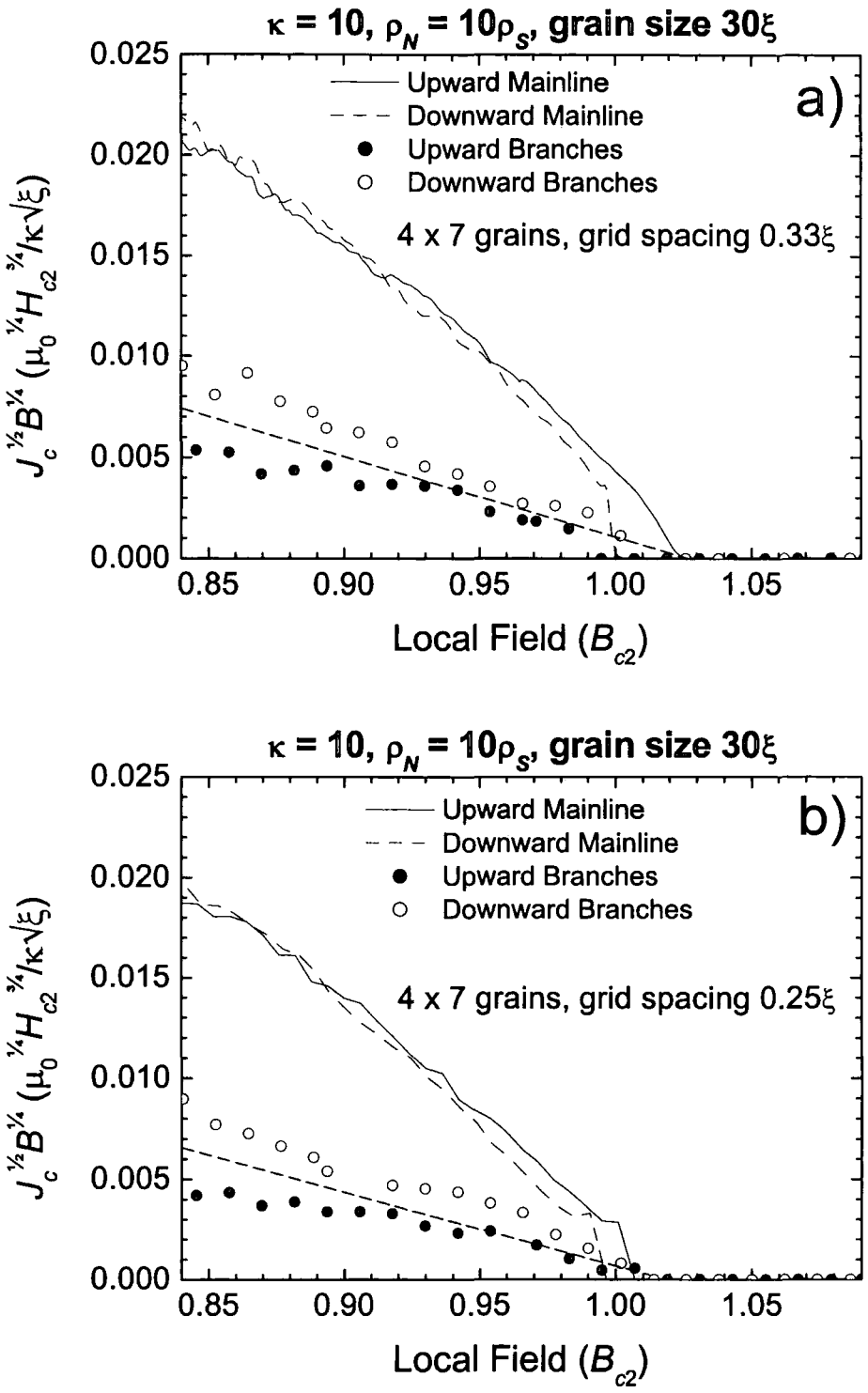

Figure 8.11: Kramer plots in the field range $0.84H_{c2}$ – $1.09H_{c2}$ for a $\kappa = 10$.superconductor with 30ξ grains separated by $\rho_N = 10\rho_S$ grain boundaries with grid spacing reduced to a) 0.33ξ and b) $0.25\ \xi$.

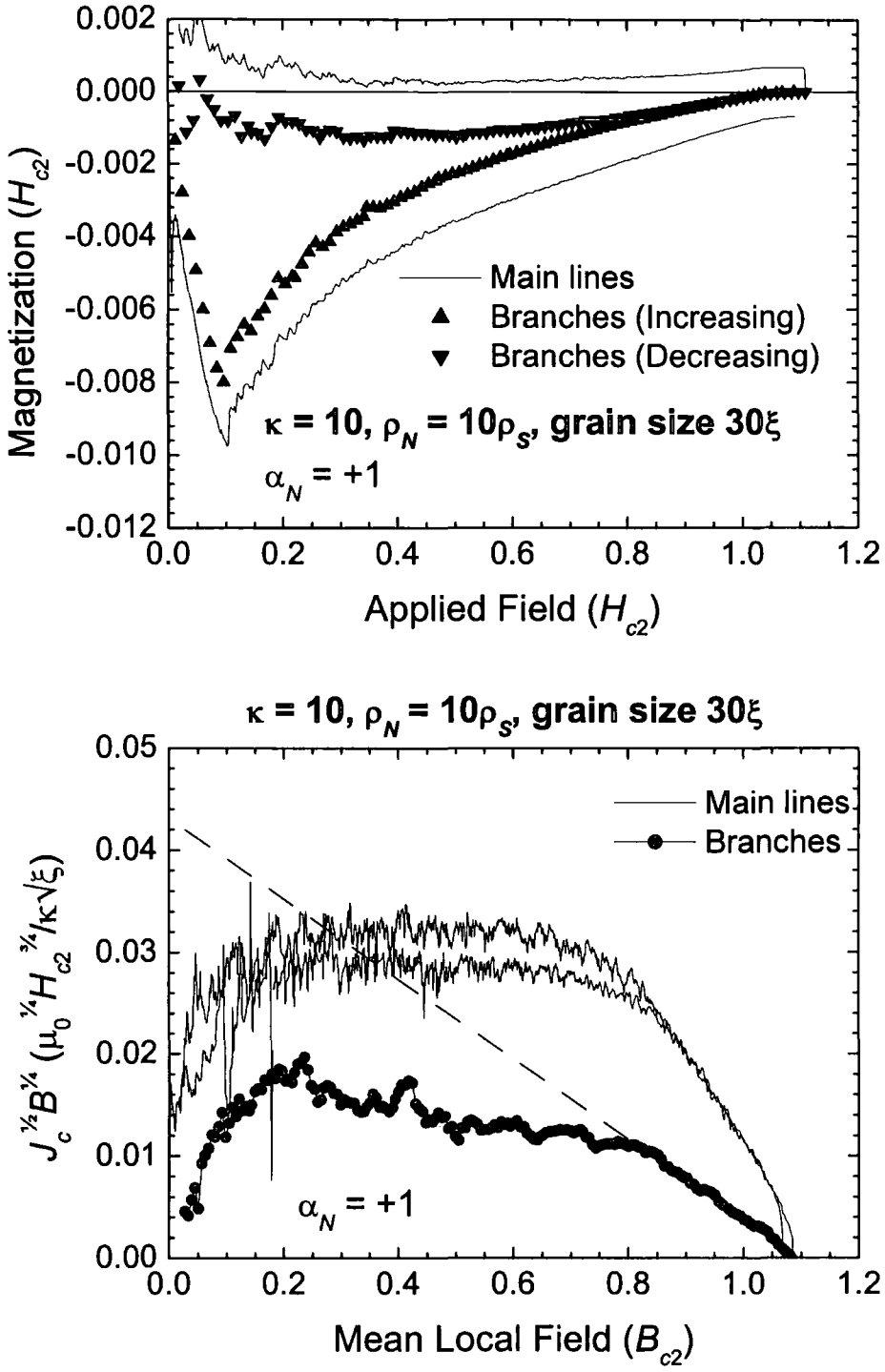

Figure 8.12: Magnetization and Kramer plots for a $\kappa = 10$ polycrystalline system with 30ξ grains and $\rho_N = 10\rho_S$ trilayer grain boundaries (inner thickness 1ξ, outer thickness 2ξ).

8.5 Using the branching method over the full field range

Now that the branching method has been confirmed to work for a single applied field, it can now be used to calculate the critical current density across the entire field range from zero to H_{c2}. The rate at which the applied field is ramped up and down for these calculations corresponds to an E-field of $1.25 \times 10^{-3}\ H_{c2}\rho_S/\kappa^2\xi$ – this is the same as the ramping rate used in Figs. 8.5-8.7. While in the single-point consistency tests raw J_c values obtained from individual branches (corresponding to a different metastable state of the system) were plotted, for computations over the full field range the 'branch' J_c is obtained using a 9-point moving average is plotted. The magnetization and J_c results from these calculations are shown in Fig. 8.12.

8.6 Computational resource requirements

8.6.1 Machines used for computation

The 2D granular superconductor simulations were conducted on several types of computer. In initial tests, a 400MHz Sun UltraSPARC machine was used. However, it soon became clear that this was not up to the task as running a full field range calculation at $\rho_N = 10\rho_S$, grain size 5ξ(this is a relatively small calculation) required 718 CPU hours. Since a maximum of 8 CPUs could be used at any one time, this machine was judged insufficient for our purposes.

We therefore decided to use multiple PCs for the calculation – the 'branching' structure of the new method was ideal for this as the branches could be distributed among the PCs available. Our code was compiled under Windows XP using the Salford Fortran compiler. A typical specification of PC used here was a 1.7GHz Pentium 4 PCs with 512 MB of RAM. With between 30 and 80 PCs being used in total, these calculations were now practicable.

Later on in the course of our work a 256-processor cluster, equipped with 2GHz Opteron processors became available. This machine was faster than the PCs processor-for-processor and jobs were sometimes executed with up to 204 processors in use at any one time. In addition, this machine could be run continuously, whereas the PCs could only be run overnight or at weekends, because they were required for other uses during office hours.

Each grid point in the computational system is represented by approximately 20 variables. Each complex variable occupies 16 bytes of memory, which means that a 2GB machine can run about 8 million grid points. In 2D, RAM limitations are therefore not a serious restriction, as this number of grid points gives dimensions up to ~ $200\xi \times 10{,}000\xi$. In 3D however, as the memory requirement is multiplied by the number of layers in the z-direction, memory becomes a very important limiting factor on the size of computational systems. The maximum possible grid size in 3D is ~ $100\xi \times 100\xi \times 100\xi$.

8.6.2 Calculating required CPU time

For the Opteron cluster and the PCs, the running time required to run 1000 iterations of the code was measured. A good approximation to the required running time as a function of grid size is

$$\begin{aligned} t_{1000}^{Opteron} &= 0.0032 n_a n_b \text{ CPU-seconds} \\ t_{1000}^{PC} &= \left(0.0085 n_a n_b - 22\right) \text{ CPU-seconds} \end{aligned} \tag{8.4}$$

Where n_a and n_b are the numbers of grid points in the a and b directions. For the "mainline" runs, we ramp the applied magnetic field H from zero to $1.2H_{c2}$ and back to zero over a total time period of $1.8 \times 10^5\ t_0$. The timestep we use is dependent on the resistivity ratio ρ_N/ρ_S as higher ratios impair the stability of the algorithm:

$$\delta t = \tfrac{1}{2} \min\left(\frac{\rho_N}{\rho_S}, \frac{\rho_S}{\rho_N}\right). \tag{8.5}$$

This gives a total number of iterations for the mainline of

$$i_{mainline} = 3.6 \times 10^5 \max\left(\frac{\rho_N}{\rho_S}, \frac{\rho_S}{\rho_N}\right) \tag{8.6}$$

Combining this with the running-time figures we get mainline running times of

$$\begin{aligned} t_{mainline}^{Opteron} &= \frac{n_a n_b}{3125} \max\left(\frac{\rho_N}{\rho_S}, \frac{\rho_S}{\rho_N}\right) \text{ CPU-hours} \\ t_{mainline}^{PC} &= \left(\frac{n_a n_b}{1175} - 2.2\right) \max\left(\frac{\rho_N}{\rho_S}, \frac{\rho_S}{\rho_N}\right) \text{ CPU-hours} \end{aligned} \tag{8.7}$$

In our computations we typically calculate a total of 200 branches starting from the up and down mainlines. Branches typically run over a simulated time period of $5000t_0$, but for low

ρ_N/ρ_S values a longer duration is needed as the decay in the E-field over the length of the branch is slower. For a system with $\rho_N > \rho_S$ we can write the total number of iterations required for the calculation of all branches as:

$$i_{branches} = 2\times 10^6 \max\left(\frac{\rho_N}{\rho_S}, 5\right) \tag{8.8}$$

This gives branch running times of

$$\begin{aligned} t_{branches}^{Opteron} &= \frac{n_a n_b}{562}\max\left(\frac{\rho_N}{\rho_S}, 5\right) \text{ CPU-hours} \\ t_{branches}^{PC} &= \left(\frac{n_a n_b}{212} - 12.2\right)\max\left(\frac{\rho_N}{\rho_S}, 5\right) \text{ CPU-hours} \end{aligned} \tag{8.9}$$

For a very small-grain system (grain size 5ξ), there were 5 superconducting grains in the a-direction and 20 in the b-direction. Once the normal diffusion layers, the outer normal layers, the angle between the a-b and x-y axes is taken into account, the total grid size is given by $n_a = 50$, $n_b = 288$. Substituting these into (8.7) and (8.9) gives the CPU time figures for a $\rho_N = 10\rho_S$ system of:

$$\begin{aligned} &t_{mainline}^{Opteron}(\text{grain } 5\xi) = 46.1 \text{ CPU-hours}, \quad t_{mainline}^{PC}(\text{grain } 5\xi) = 100.6 \text{ CPU-hours} \\ &t_{branches}^{Opteron}(\text{grain } 5\xi) = 256.2 \text{ CPU-hours}, \quad t_{branches}^{PC}(\text{grain } 5\xi) = 557.2 \text{ CPU-hours} \end{aligned} \tag{8.10}$$

For a system with larger grains (30ξ), the number of superconducting grains was reduced to 4 in the a-direction and 7 in the b-direction in the interest of reducing computational expense. The corresponding values of n_a and n_b are 240 and 598 respectively. For a $\rho_N = 10\rho_S$ system the calculated CPU time figures are:

$$\begin{aligned} &t_{mainline}^{Opteron}(\text{grain } 30\xi) = 459.3 \text{ CPU-hours}, \quad t_{mainline}^{PC}(\text{grain } 30\xi) = 1199 \text{ CPU-hours} \\ &t_{branches}^{Opteron}(\text{grain } 30\xi) = 2554 \text{ CPU-hours}, \quad t_{branches}^{PC}(\text{grain } 30\xi) = 6648 \text{ CPU-hours} \end{aligned} \tag{8.11}$$

The code was not written to run a single job on multiple processors. This means that running the mainline as only 2 jobs was not practical for large grain sizes, as it would require 230 hours of wall time to complete (on the Opteron cluster). Instead each ramp (from zero to H_{c2} and from H_{c2} to zero) was split into eight chunks. Due to the need to overlap these chunks in order to mimic the magnetization profile of a single ramp, this increased the total CPU time

for the mainlines to 695.8 CPU-hours (on the Opteron cluster) but reduced the wall time to 43.5 hours, as the work is now shared by 16 processors.

8.7 Conclusion

A means has been established to numerically calculate the bulk critical current density J_c for a simulated granular superconductor. This method obtains J_c in a magnetization measurement, with a 'branching' procedure to achieve E-fields much lower than would be feasible in a direct computation. The use of a magnetization method also permits the use of periodic boundary conditions, which would not be possible in a transport method.

It has been found that to obtain bulk H_{c2} values approximately equal (within 10%) of the analytic value, the boundaries between the grains of the polycrystalline material should be of 'trilayer' structure as explained in Section 7.6. To avoid the calculated J_c values being unduly affected by surface barriers at the material edges, T_c is gradually decreased to zero over a distance of several coherence lengths, and its value is calculated using Bean profiles, rather than from the irreversible magnetization component. To simplify the analysis of the data it was decided to use a regular structure of 'grains'. The potential problem of matching effects that this could cause is minimized by setting the edges of the superconductor at an oblique angle to the grain structure.

This chapter has considered a $\kappa = 10$ superconductor with grains 30ξ across, where the resistivity ρ_N of the inner part of the trilayer junction is $10\rho_S$ (ρ_S is the normal state resistivity of the superconductor). This initial test has demonstrated that there are two field-dependence regimes for J_c, with the boundary at approximately 0.8 H_{c2}. However, the computational results still have some errors compared with experimental data. The spatial discretization of the superconductor necessary for computation has caused H_{c2} to be over-estimated by approximately 8% (although the field dependence of J_c in the high-field regime is not affected by the discretization). The low-field J_c results also have retained a dependence on the width of the superconductor, which is not the case for a real polycrystalline superconductor. In the next chapter, this method will be used to calculate J_c as a function of applied field for a range of κ values, grain boundary properties and grain sizes.

9 J_c in Polycrystalline Systems

9.1 Introduction

In this penultimate chapter we bring this thesis to a conclusion by studying J_c in simulated polycrystalline superconductors. Our focus throughout will be on the Kramer-like reduced-field dependence of J_c in fields near H_{c2}, and for this reason our J_c data shall be plotted in the form of Kramer plots – $J_c^{1/2}B^{1/4}$ versus B. Section 9.2 is an overview of the TDGL model and considers all the independent variables which could be changed in a simulation of a polycrystalline superconductor. In sections 9.3 through 9.6 we present computational results demonstrating how the system magnetization and J_c change with grain size, kappa, grain boundary properties and temperature – these will help us to determine the functional form of J_c. We define our 'hub' system as one where $T = \frac{1}{2}T_c$, $\kappa = 10$, the grain size is $30\xi(T = \frac{1}{2}T_c)$ and each grain boundary is a normal-metal trilayer with a $1\xi(T = \frac{1}{2}T_c)$-thick $\rho_N = 10\rho_S$ inner layer and two $\frac{1}{2}\,\xi(T = \frac{1}{2}T_c)$-thick $\rho_N = \rho_S$ outer layers on either side. Section 9.3 studies the effect of varying grain size in the range from 5ξ to 40ξ while keeping the other parameters at their 'hub' values, while section 9.4 investigates the effect of changing κ, the grain-boundary resistivity or the temperature., with the other parameters retaining their 'hub' values. A diagram of the 'hub' system is shown in Figure 9.1.

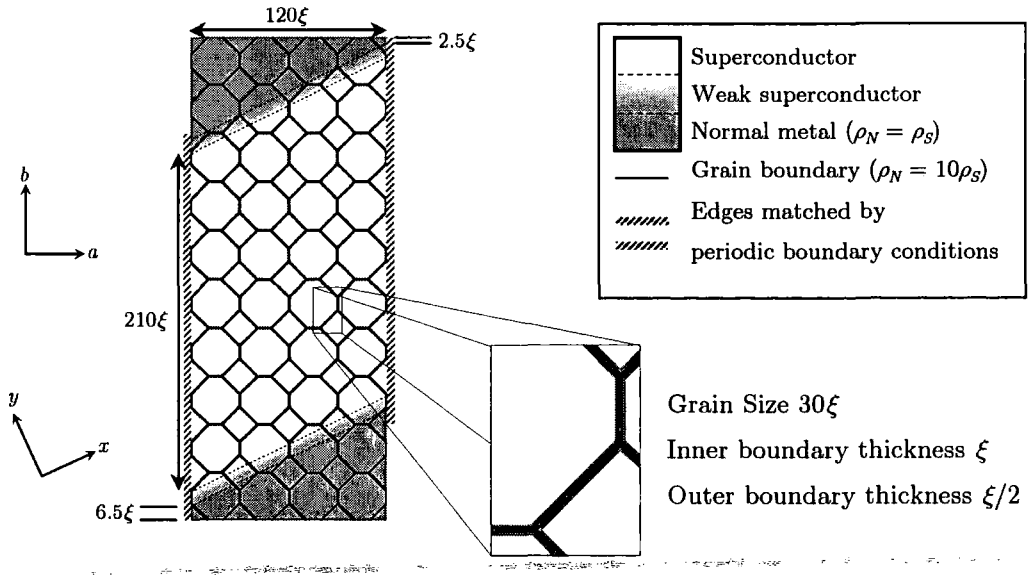

Figure 9.1: Scale drawing of the 'hub' simulated 2D polycrystalline superconductor

Section 9.5 studies the effect of grain-boundary engineering – either by removing one outer layer along the diagonally-aligned boundaries, or by removing the outer layers of the trilayer boundary completely to introduce H_{c3} effects. Section 9.6 summarizes our 2D results, while Sec. 9.7 extends our work to three-dimensional systems, comparing their magnetization and J_c behaviour with that of similar two-dimensional systems. Section 9.8 uses computer graphics to show the spatial distribution of the order parameter and the dissipation in both 2D and 3D simulated systems, while Sec. 9.9 compares our computational results with data obtained from experimental work. We overview an existing theoretical model to obtain a functional form for J_c and F_p given by flux shear along grain boundaries in Sec. 9.10 before extending this model in Sec. 9.11 to account for three dimensional systems, and the distortion of fluxons occupying grain boundaries. We then discuss our work further in Section 9.12, before summarizing the chapter as a whole in Sec. 9.13.

9.2 Independent variables

If we check the normalized TDGL equations (3.63) and (3.64) we see that κ is the only parameter for the main superconductor which can fundamentally change the behaviour of a superconductor in isolation from other materials. Equations (3.66) and (3.67) for the normal metal add three extra parameters relating to the grain boundaries: the grain boundary pair-breaking coefficient α_N, the resistivity ratio ρ_N/ρ_S and the diffusivity ratio D_N/D_S. As in our work in Chapter 5, it is assumed that the density of states $g(\epsilon_F)$ in the grain boundaries is the same as in the bulk superconductor: this relates the resistivity and diffusivity ratios by:

$$\frac{D_N}{D_S} = \left(\frac{\rho_N}{\rho_S}\right)^{-1} \tag{9.1}$$

In experimental work the pair-breaking coefficient can only be changed directly by means of changing the temperature T. Equation (3.63) and (3.64) are normalized to ξ and λ at the current temperature. If we assume $T_c = 0$ in the grain boundaries, and then normalize equations (3.63) and (3.66) to a normalization temperature T_N, rather than the current temperature, we get:

Bulk superconductor:
$$\frac{\partial\hat{\psi}}{\partial t} = -\frac{1}{\zeta'}\left[\left(\left|\hat{\psi}\right|^2 - \frac{T_c - T}{T_c - T_N}\right) + \left(\frac{\nabla}{i} - \mathbf{A}\right)^2\right]\hat{\psi} \tag{9.2}$$

Grain boundaries:
$$\frac{\partial\hat{\psi}}{\partial t} = -\frac{1}{\zeta'}\left[\left(\left|\hat{\psi}\right|^2 + \frac{T}{T_c - T_N}\right) + \frac{D_N}{D_S}\left(\frac{\nabla}{i} - \mathbf{A}\right)^2\right]\hat{\psi} \tag{9.3}$$

In addition to these parameters are those related to the system's geometry: the length X and width Y of the superconductor, the grain size G and the grain boundary thickness d (inner thickness d_1 and outer thickness d_2). The changeable parameters are summarized in the table below (those parameters which we have chosen to study are underlined). For most calculations d_1 and $d_2$will remain fixed at ξ and 2ξ respectively, as the discretization imposed by the computation it would be extremely difficult to fine tune these thicknesses, and coarse changes would have too great an effect on the system.

Symbol	Property	Notes
$\underline{\kappa}$	Kappa	Affects λ in normalized units ($\lambda = \kappa\xi$)
$\underline{T}$	Temperature	Affects ξ, λ and α_N
$\underline{\rho_N/\rho_S}$	Relative grain boundary resistivity	–
D_N/D_S	Relative grain boundary diffusivity	Set to $(\rho_N/\rho_S)^{-1}$ to keep $g(\epsilon_F)$ constant
$\underline{G}$	Grain size	G/ξ affected by temperature
d_1	Inner grain boundary thickness	d_1/ξ affected by temperature
d_2	Outer grain boundary thickness	d_2/ξ affected by temperature
X	Superconductor length	X/ξ affected by temperature
Y	Superconductor width	Y/ξ affected by temperature

Table 9.1: Free parameters in TDGL simulation of granular superconductor with trilayer grain boundaries.

9.3 Effect of grain size on magnetization and J_c

9.3.1 Small Grain Size regime

We shall begin our investigation on the effect of grain size on polycrystalline superconductor J_c by looking at small-grain materials (grain size $< 10\xi$). In all systems investigated in Sec. 9.3, the parameters other than grain size are set to their 'hub' values as explained in Sec. 9.1. For these small grain sizes, it is not energetically favourable for fluxons to enter the grains, and thus the fluxons are completely confined to the grain boundaries.

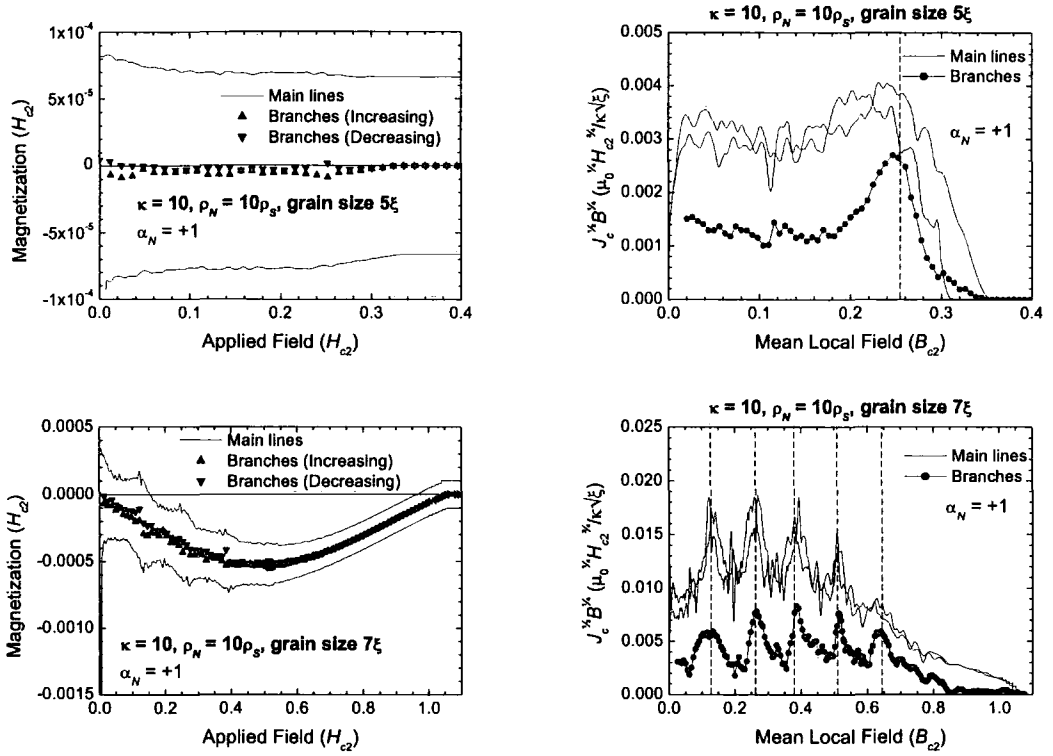

Figure 9.2: Field dependence of M and J_c for a $\rho_N = 10\rho_S$ trilayer-junction polycrystalline model with $\kappa = 10$ and grain sizes 5ξ and 7ξ

Figure 9.2 shows the magnetization and J_c for superconductors with grain sizes of 5ξ and 7ξ. – the mainline E-field is $6.19 \times 10^{-4}\ H_{c2}\rho_S/\kappa^2\xi$ in both cases. The J_c characteristic has peaks which are marked on the plots with dashed lines. These peaks occur at fields where the number of fluxons per 'triple point' (points in the lattice structure where three grains meet, as seen in Fig. 9.1) is a whole number of quarters. In the 7ξ grain size case, there exist five such peaks, at $0.13H_{c2}$, $0.26H_{c2}$, $0.38H_{c2}$, $0.51H_{c2}$ and $0.64H_{c2}$. These peaks represent increasing integer number of fluxons per unit cell (each unit cell contains four triple-points). In the 5ξ grain size case, the normal metal which makes up the grain boundaries (inner and outer layers) is a significant fraction of the total material within the system. The pair breaking which occurs in this normal material and the proximity effect force the effective H_{c2} down to only 35% of the value for the homogenous superconductor. This also means that only the first peak is visible, equivalent to one fluxon per unit cell, at $0.25H_{c2}$.

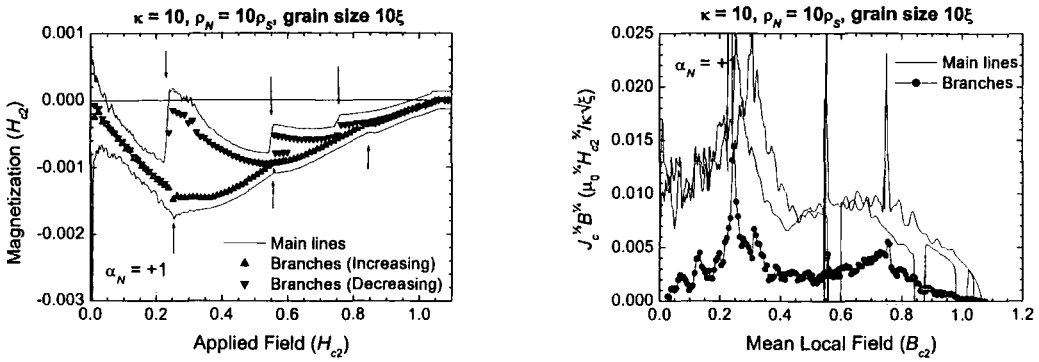

Figure 9.3: Magnetization characteristics for $\rho_N = 10\rho_S$ trilayer-junction polycrystalline models with $\kappa = 10$ and a grain sizes of 10ξ. The arrows show changes in the number of fluxons per grain

9.3.2 Transitional Grain Size regime

Figure 9.3 shows the effect of increasing the grain size to 10ξ (the mainline E-field is kept at $6.19 \times 10^{-4}\ H_{c2}\rho_S/\kappa^2\xi$). The grains themselves are now large enough to accommodate a small number of fluxons each. The magnetization characteristic has acquired 'steps' at specific fields at which the number of fluxons per grain (this is the same for all grains in this system) abruptly increases or decreases by one. Figure 9.4 demonstrates this for the downward ramp through $0.56H_{c2}$ – each grain contains two fluxons above this field, but only one below. This 'stepped magnetization' behaviour has been observed previously in TDGL computations of single mesoscopic superconductors[39], and is also similar to the work in Chapter 6.

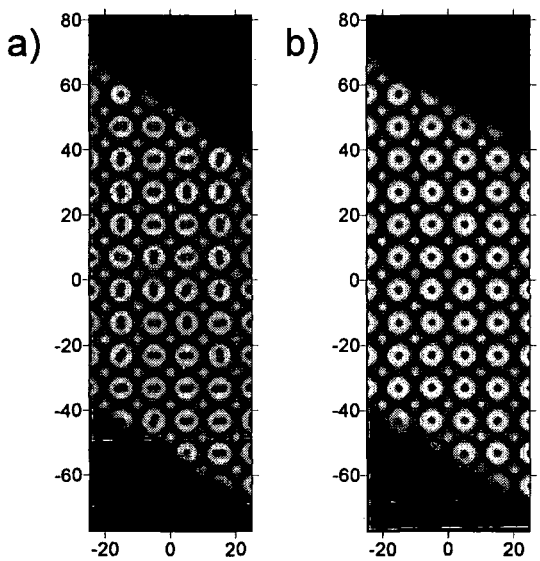

Figure 9.4: Comparison of order parameter on downward ramp for $\rho_N = 10\rho_S$ trilayer-junction polycrystalline models with $\kappa = 10$ and a grain sizes of 10ξ – $H =$ a) $0.632H_{c2}$ b) $0.5H_{c2}$

9.3.3 Large Grain Size regime

When the grain size is increased further to 20ξ or more, the number of 'steps' in the magnetization curve increases until they can no longer be distinguished, and a smooth curve is restored. Figure 9.5 shows M and J_c for superconductors with grain sizes of 20ξ, 30ξ and 40ξ. The mainline E-fields are $1.24 \times 10^{-3}\ H_{c2}\rho_S/\kappa^2\xi$, $1.25 \times 10^{-3}\ H_{c2}\rho_S/\kappa^2\xi$ and $1.67 \times 10^{-3}\ H_{c2}\rho_S/\kappa^2\xi$ respectively. Typical branch E-fields are $4 \times 10^{-8}\ H_{c2}\rho_S/\kappa^2\xi$ in the high-field regime (see Fig. 8.6) and $2 \times 10^{-8}\ H_{c2}\rho_S/\kappa^2\xi$ in $H_{c2}\rho_S/\kappa^2\xi$ in the low-field regime.

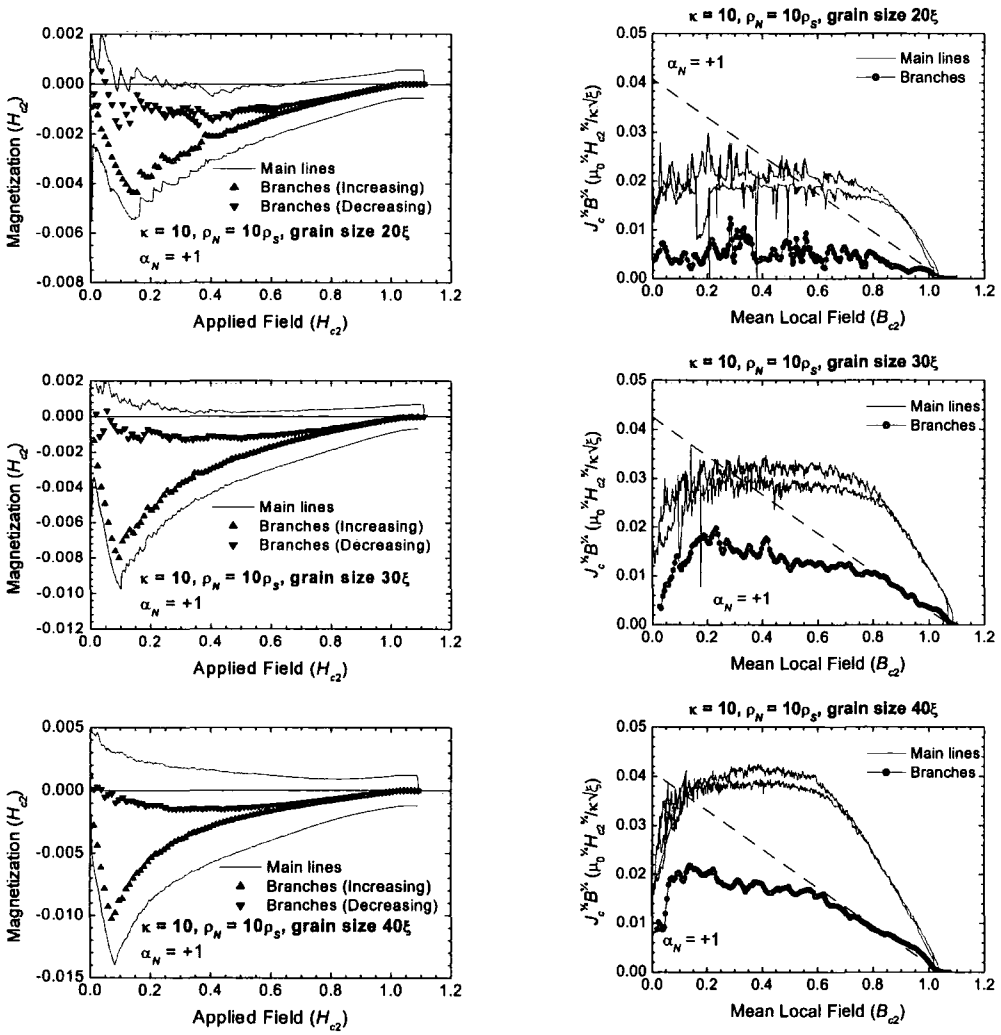

Figure 9.5: Field dependence of M and J_c for a $\rho_N = 10\rho_S$ trilayer-junction polycrystalline model with $\kappa = 10$ and grain sizes $\geq 20\xi$

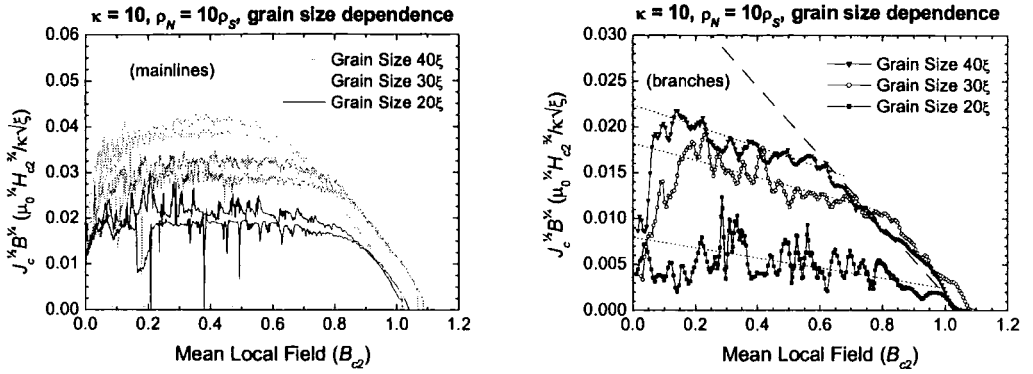

Figure 9.6: Comparison of Kramer plots for grain sizes of 20ξ, 30ξ and 40ξ ($\kappa = 10$, $\rho_N = 10\rho_S$, $T = 0.5T_c$)

The critical current curve now has two parts – on a Kramer plot these can be fitted to straight lines of differing gradients. In the high-field regime J_c has a strong, monotonic field dependence and is approximately independent of grain size, while at lower fields J_c has a weaker and more erratic field dependence, and increases as grain size increases (unlike in experimentally-measured 3D superconductors[4,21]). Figure 9.5 combines all the mainline (high-E) and branch (low-E) Kramer plots into a single pair of graphs, in which the grain-size independence of J_c in high B fields is made clear.

Experimental observations[97] as a function of field, temperature and strain on highly-optimized Nb_3Sn wires have given the expression for the pinning force F_p:

$$F_p \approx \frac{1}{100\sqrt{2\pi\phi_0}} \frac{B_{c2}^{5/2}}{\mu_0\kappa^2} b^{1/2}(1-b)^2 \approx 1.6\times10^{-3}\sqrt{\frac{2\pi}{\phi_0}} \frac{B_{c2}^{5/2}}{\mu_0\kappa^2} b^{1/2}(1-b)^2 \qquad (9.4)$$

This experimental result is depicted in Figs. 9.4 and 9.5 as a long-dashed straight line, and is remarkably close to the computational results in the high-field regime. However, the dependences of J_c on κ and B_{c2} have not been explicitly checked yet. In the next section we investigate these dependences, along with the dependence of J_c on the grain boundary resistivity. For Nb_3Al, a similar expression results[98], but the prefactor is 1.4×10^{-3} rather than 1.6×10^{-3}. All the data in section 9.4 use the same E-fields as used for the grain size 30ξ data in this section.

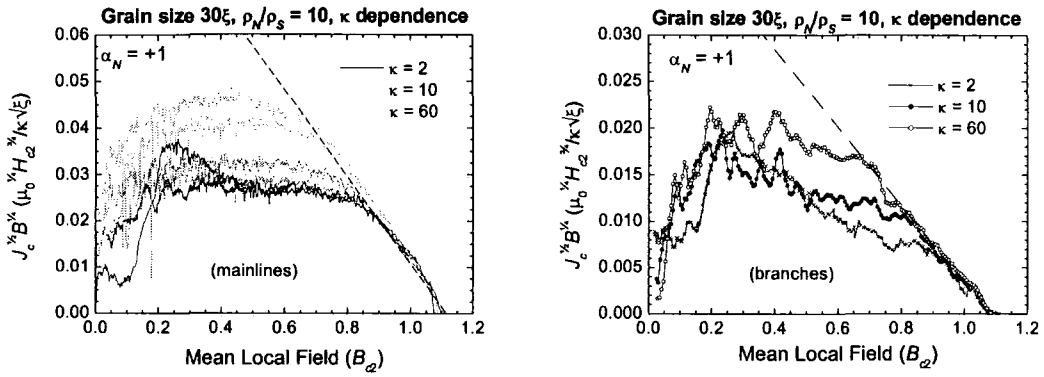

Figure 9.7: Kramer plots for κ values of 2, 10 and 60 (Grain size 30ξ, $\rho_N = 10\rho_S$, $T = 0.5T_c$)

9.4 Effect of κ, ρ_N/ρ_S and T on 2D magnetization and J_c

9.4.1 Effect of changing κ

In Figure 9.7 we compare J_c values for $\kappa = 2, 10$ and 60. Since these graphs plot J_c normalized by the factor $\left(B_{c2}^{3/2}/\mu_0\kappa^2\right)\sqrt{2\pi/\phi_0}$, it is implied that the pinning force in the high-field regime follows

$$F_p \propto \frac{1}{\kappa^2} b^{1/2}(1-b)^2 . \tag{9.5}$$

This is consistent with both the Fietz-Webb[26] and the Kramer[30] scaling laws, and with the Dew-Hughes work[25] on flux pinning in all geometries. However, the transition field where the superconductor transitions from the intermediate-field regime to the Kramer regime decreases significantly as κ increases, from $\approx 0.9B_{c2}$ at $\kappa = 2$ to $\approx 0.7B_{c2}$ at $\kappa = 60$.

9.4.2 Effect of changing ρ_N/ρ_S

The next stage in investigating the mechanism behind current criticality in granular superconductors was to check the dependence of J_c on the properties of the grain boundaries. With κ fixed at 10 and the grain size at 30ξ, grain boundaries with resistivities ρ_N of $2\rho_S$, $5\rho_S$, $10\rho_S$ and $20\rho_S$ were compared. Figure 9.8 shows the effect of changing grain boundary resistivity – three field regimes can be seen.

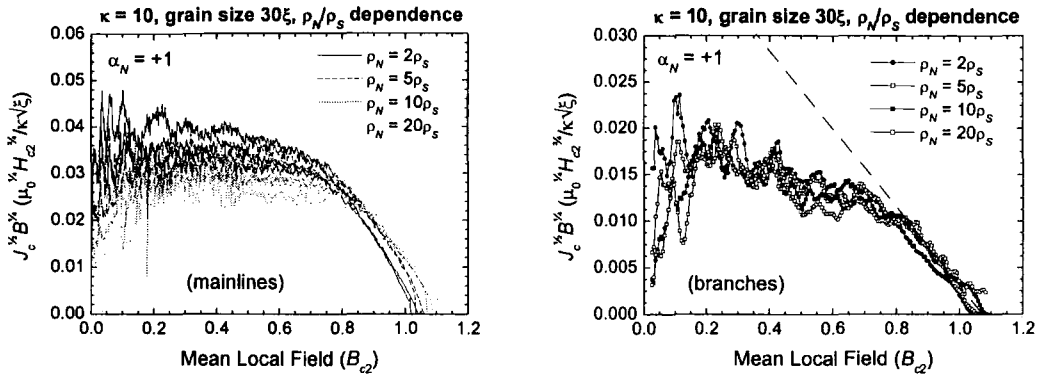

Figure 9.8: Comparison of Kramer plots for mainlines and branches for ρ_N values of $2\rho_S$, $5\rho_S$, $10\rho_S$ and $20\rho_S$ ($\kappa = 10$, grain size 30ξ, $T = 0.5T_c$)

- **Low fields ($B < 0.2B_{c2}$):** J_c strongly decreases as ρ_N increases
- **Intermediate fields ($0.2B_{c2} < B < 0.8B_{c2}$):** J_c has little dependence on ρ_N/ρ_S
- **High fields ($B > 0.8B_{c2}$):** The effective upper critical field B_{c2}^* increases slightly above B_{c2}^{homogen} for high ρ_N/ρ_S, but the Kramer gradient has little ρ_N/ρ_S dependence.

This shows that behaviour of the grain boundaries as Josephson junctions (as studied in Chapter 7) is not a significant factor in determining J_c in large-grain superconductors (except perhaps in very low applied fields), as $J_{D,J}$ for the $\rho_N = 2\rho_S$ case is about 50 times that for the $\rho_N = 20\rho_S$ case (see Sections 7.2.2 and 7.6.2).

9.4.3 Effect of changing temperature

The scaling laws used by Fietz-Webb and Kramer also include a dependence on H_{c2}, which is temperature dependent. In much experimental work, the H_{c2} dependence of J_c and F_p is determined by determining the H_{c2} and maximum pinning force at a range of different temperatures[30], then plotting these on a log-log plot. However, this method does not work with data such as our 2D computational results since the Kramer-like field dependence of J_c only exists at fields above ~ 0.7 H_{c2}. Instead we use the gradient of $J_c^{1/4}B^{1/4}$ in the high-field regime to calculate the H_{c2}-dependence of J_c.

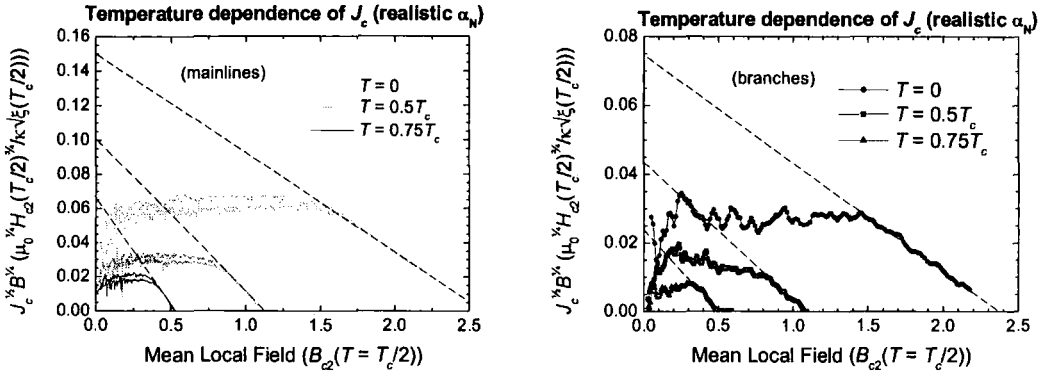

Figure 9.9: Kramer plots showing temperature dependence of J_c on ($\kappa = 10$, $\rho_N = 10\rho_S$, grain size $30\xi(T = 0.5T_c)$).

Figure 9.9 shows the effect of changing temperature on the critical current density of the $\kappa = 10$ superconductor with $\rho_N = 10\rho_S$ grain boundaries. If the dashed lines on these graphs (fitted to the high-field J_c data) were parallel, then this would suggest that $F_p \propto B_{c2}^{5/2}$, consistent with the normalization. In fact the lines are not parallel and the field dependence has the B_{c2} dependences

$$\begin{aligned} J_c^{branches} &\propto B_{c2}^{0.85} b^{-1/2} (1-b)^2 \quad \left(F_p^{branches} \propto B_{c2}^{1.85} b^{1/2} (1-b)^2\right) \\ J_c^{mainline} &\propto B_{c2}^{0.5} b^{-1/2} (1-b)^2 \quad \left(F_p^{mainline} \propto B_{c2}^{1.5} b^{1/2} (1-b)^2\right) \end{aligned} \tag{9.6}$$

It may be noted that as T decreases, the coherence length also decreases relative to the discretization length, increasing the discretization-related error (see Fig. 8.11) in the apparent B_{c2} value (where J_c becomes zero) relative to the Ginzburg-Landau analytic values, which are $0.5B_{c2}(T = T_c/2)$ for $T = 0.75T_c$, $B_{c2}(T = T_c/2)$ for $T = 0.5T_c$ and $2B_{c2}(T = T_c/2)$ for $T = 0$.

9.5 Grain Boundary Engineering

9.5.1 Changing the Grain Boundary Structure

We decided to investigate the effect of modifying the structure of the diagonal grain boundaries on the magnetization and J_c of the granular superconductor. Specifically, the diagonal trilayer boundaries were replaced with bilayer boundaries – this is demonstrated diagrammatically in Fig. 9.10. The first check on the effect of this modification to the system was to check the dependence of J_c on grain size for this new system. The dependence of J_c on ρ_N/ρ_S was also checked.

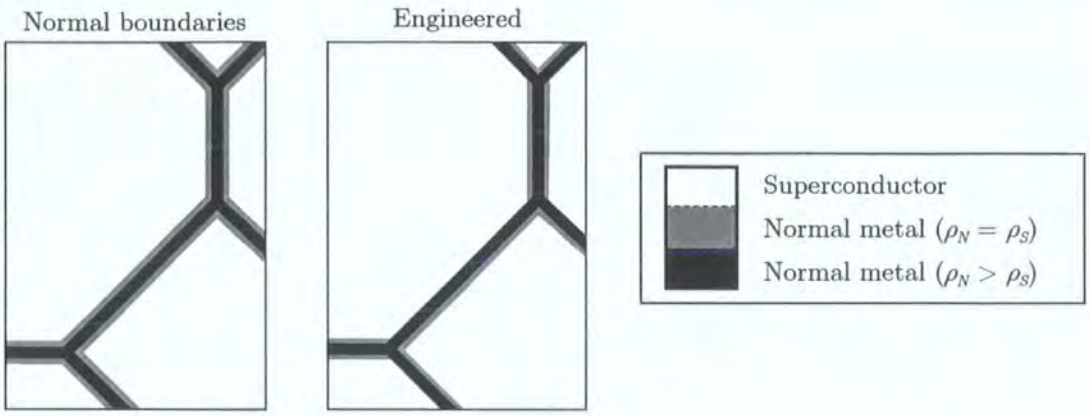

Figure 9.10: Changes in the grain boundary structure resulting from grain boundary engineering

J_c for the engineered boundaries is shown as a function of grain size and normal-state resistivity in Figure 9.11. It can be seen that these engineered boundaries increase J_c at low fields, while not affecting J_c in the high-field limit. J_c increases for low B-fields because a fluxon travelling along the grain boundaries in this system is not only subjected to flux shear forces, but also to increased pinning forces at those triple points where it moves from a thicker grain boundary section to a thinner one. These low-field results are also slightly dependent on ρ_N/ρ_S dependence, because increasing ρ_N/ρ_S makes it more difficult for the fluxon core to diffuse into the outer layers of the grain boundary (due to the reduction in the proximity effect). When the fluxon is more strictly confined within the inner part of the trilayer boundary, the presence or absence of outer layers has less effect and thus the pinning force is reduced.

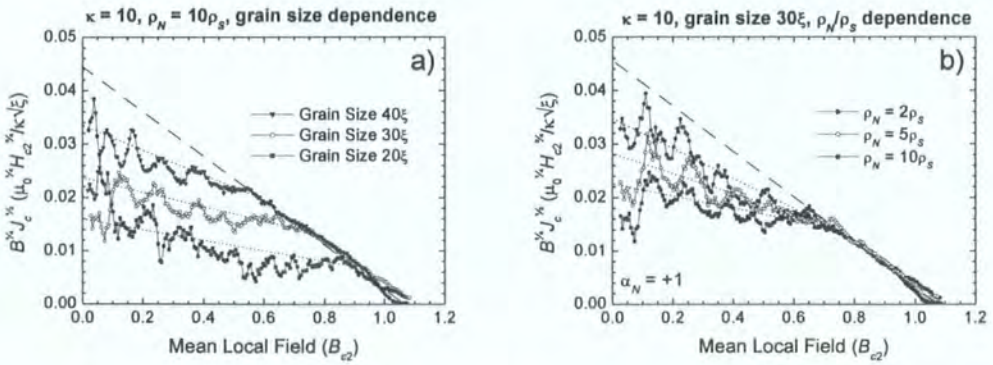

Figure 9.11: Dependence of branch J_c values on a) grain size and b) ρ_N/ρ_S in systems with thin bilayer diagonal boundaries($\kappa = 10$, $\rho_N = 10\rho_S$, $\alpha_N = +1$)

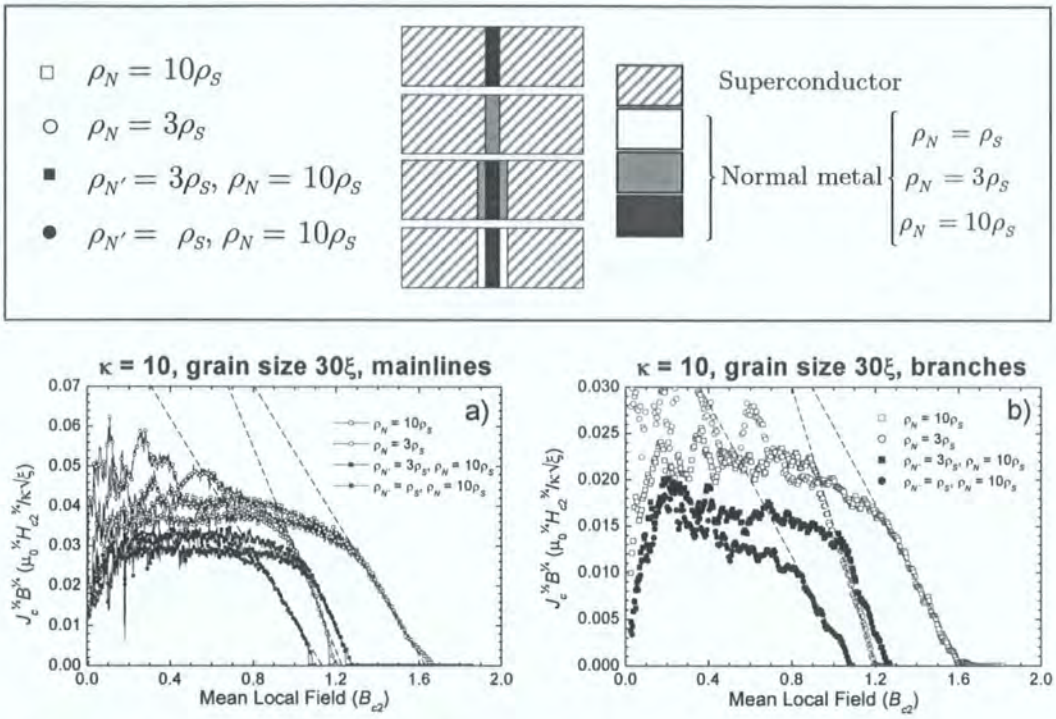

Figure 9.12: Kramer plots for a) mainline and b) branch J_c of a $\kappa = 10$ superconductor with 30ξ grains separated by four types of grain boundary (two monolayer and two trilayer). The upper caption demonstrates the differing types of grain boundaries used.

9.5.2 Introducing Surface Field Effects

If the outer $\rho_N = \rho_S$ layers of the trilayer are omitted (leaving a monolayer of thickness ξ), or are replaced by outer layers of higher resistivity, surface sheaths of enhanced superconductivity will form along the edges of the grains which will persist even above B_{c2}. This will have a major effect on the J_c of a polycrystalline superconductor. It is expected[67] that higher resistivity normal layers will give higher values of the effective upper critical field B_{c2}^*.

Figure 9.12 plots J_c from both mainline (high-E) and branch (low-E) data for four different types of grain boundary, shown diagrammatically in the key above. As expected, the effective upper critical field B_{c2}^* is highest for monolayer boundaries of resistivity $10\rho_S$. The gradient of the Kramer lines for the system with $\rho_N = 10\rho_S$ grain boundaries is very similar to that for the 'hub' trilayer system, and gives a B_{c2}^* dependence which may be combined with the B_{c2} dependence from section 9.4.3:

$$F_p^{(2D\text{-}branches)} \propto \frac{B_{c2}^{*2.85}}{B_{c2}} b^{*1/2}\left(1-b^*\right)^2 \tag{9.7}$$

$$F_p^{(2D\text{-}mainlines)} \propto \frac{B_{c2}^{*2.65}}{B_{c2}^{1.15}} b^{*1/2}\left(1-b^*\right)^2. \tag{9.8}$$

However the gradient of the data on the Kramer plot is increased for intermediate H_{c2}^* values, such as those for the $\rho_N = 3\rho_S$ monolayer or the $\rho_N = 3\rho_S$ and $\rho_N = 10\rho_S$ trilayer. This can be considered equivalent to an increase in the F_p prefactor of up to 50% for the mainlines, and of up to 80% for the branches. Since we cannot use any power law to fully describe the data in Fig. 9.12, we shall from now on consider only the case of $B_{c2}^* = B_{c2}$. This is acceptable because for any given experimental sample the structure and electrical properties of the grain boundaries are clearly not re-engineered during the course of the measurements.

9.6 Summary of 2D computational data

The J_c results for 2D granular superconductors suggest that there are two different mechanisms determining J_c, with a crossover at a reduced field dependent on grain size.

- The *low-field regime* J_c increases with increasing grain size, and has a complicated field dependence with many peaks and troughs. If the thickness of the grain boundaries is constant, the low-field J_c has little dependence on the boundary ρ_N/ρ_S, but if the grain boundary varies in thickness along is length low-field J_c is increased, and this increase is greater for low ρ_N/ρ_S.
- The *high-field regime* exhibits a J_c with a much simpler field dependence, independent of grain size and ρ_N/ρ_S and which follows an approximately $b^{-1/2}(1-b)^2$ dependence.

When the reduced field and kappa dependence (equation (9.5)) is combined with the B_{c2} dependence (equation (9.6)) and the width dependence (equation (8.3)), we get the following expressions for the high-field regime:

$$F_p^{(2D\text{-}mainlines)} = 7.3\times10^{-3} B_{c2}\left(T_c/2\right)\left[\frac{B_{c2}^{1.5}(T)}{\mu_0\kappa^2}\sqrt{\frac{2\pi}{\phi_0}}\right] b^{1/2}(1-b)^2. \tag{9.9}$$

$$F_p^{(2D\text{-}branches)} = 7.3\times10^{-2} B_{c2}^{0.27}\left(T_c/2\right)\left[\left(\frac{\phi_0}{2\pi w^2}\right)^{0.38}\frac{B_{c2}^{1.85}(T)}{\mu_0\kappa^2}\sqrt{\frac{2\pi}{\phi_0}}\right] b^{1/2}(1-b)^2 \tag{9.10}$$

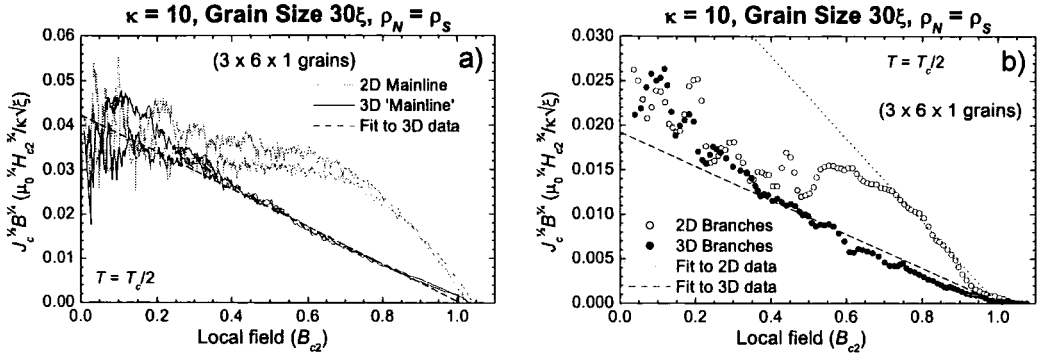

Figure 9.13: Kramer plot comparing a) mainline (high-E) and b) branch (low-E) J_c for 2D and 3D $\kappa = 10$ superconductors with 30ξ grains separated by $\rho_N = \rho_S$ barriers.

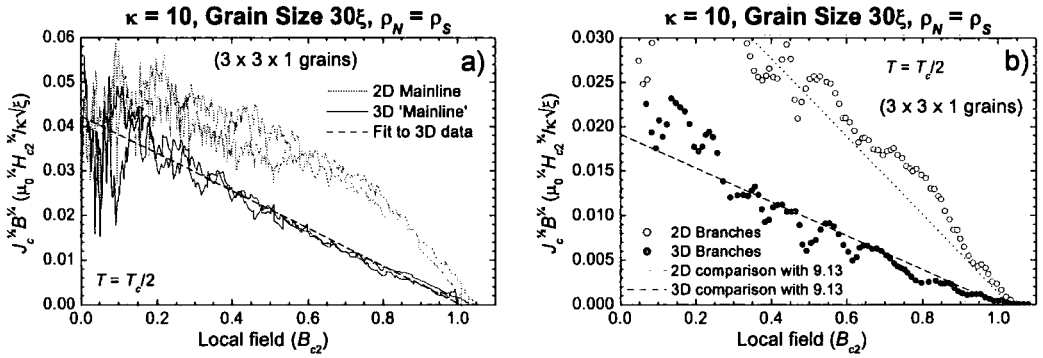

Figure 9.14: Kramer plots of 3D mainline and branch data with the superconductor width halved compared to Fig. 9.13

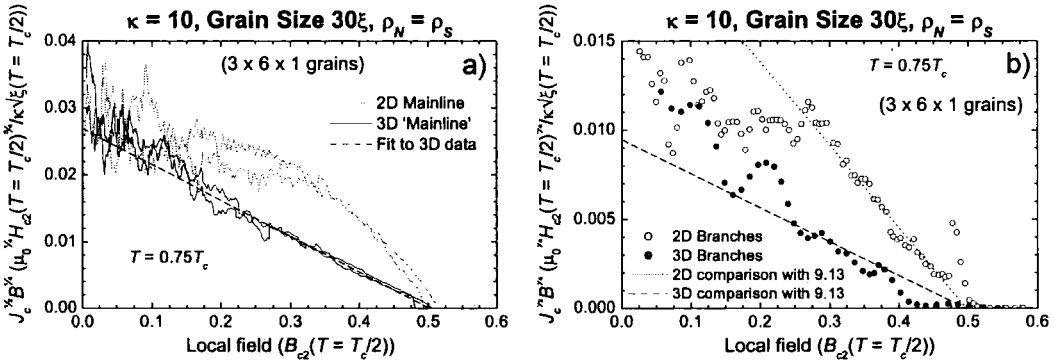

Figure 9.15: Kramer plots of 3D mainline and branch data with the upper critical field H_{c2} halved compared to Fig. 9.13

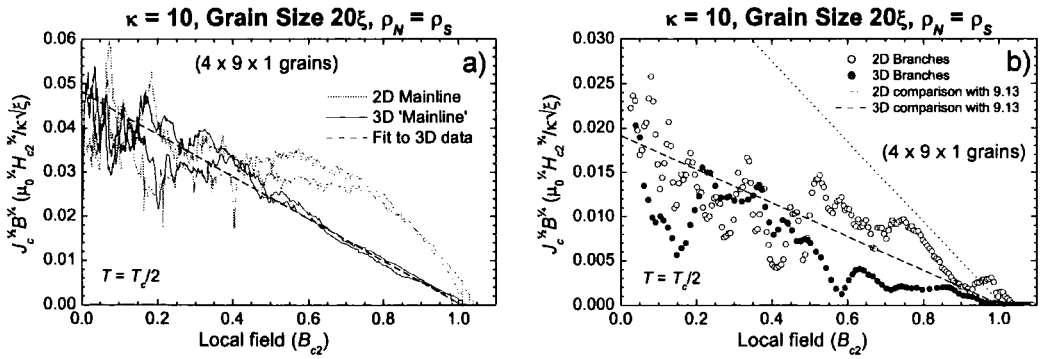

Figure 9.16: Kramer plots of 3D mainline and branch data with the grain size reduced from 30ξ to 20ξ (the mainline E-field is twice that for figures 9.13-9.15)

9.7 3D computational data

It is important to be able to simulate a full three-dimensional granular superconductor in order to compare its behaviour both with that of the two-dimensional superconductors previously mentioned, and more importantly with the behaviour of experimentally-observed superconductors. However, there are some severe restrictions imposed by the computational requirements of 3D computation, in terms of both processing and RAM requirements. Given a 2 GHz processor with 2GB RAM available, the maximum practicable dimensions for 3D computation of the 'hub' system (grain size 30ξ) are $3 \times 6 \times 1$ grains ($90\xi \times 180\xi \times 30\xi$). Since the mainline data in our method is not easily divisible into chunks spanning the field range it would take too long to run a complete mainline in 3D. We solve this problem by running branch runs only, with a 2D mainline run used to provide (z-independent) initial conditions for the 3D computations. For 'mainline' 3D runs the same E-field is maintained as in the 2D mainline, while in the 'branch' runs E is equilibrated towards zero. Another problem is that the stability of the numerical algorithm is compromized in 3D, which means that only calculations with $\rho_N = \rho_S$ grain boundaries are practicable. We therefore set a new 'hub' for 3D calculations of $T = T_c/2$, $\kappa = 10$, and grains 30ξ across (as for the 2D calculations), but with a smaller grid size and $\rho_N = \rho_S$. We investigate the effect on J_c of changing sample width, temperature and grain size.

Mainline and branch-line data for the new 'hub' are presented in Fig. 9.13. The values of J_c in the 3D system are lower than for the equivalent 2D system, and it is clear that the 3D J_c follows the Kramer dependence of $J_c \propto b^{-1/2}(1-b)^2$ throughout the entire field range, which is unlike the reduced-field dependence of J_c in the 2D polycrystalline system and more like the reduced-field dependence of ΔM in Sections 5.4 and 5.5. However, below $0.4H_{c2}$ J_c increases slightly above the value predicted by fitting a simple $J_c \propto b^{-1/2}(1-b)^2$ dependence – as does ΔM in the systems studied in Section 5.5. In the high-field regime, J_c in the 3D system is about 20% of the 2D J_c value.

Figure 9.14 shows that both high E-field and low E-field J_c in the 3D system are width-independent, as both sets of data fit to the same equivalent Kramer lines as the data in Fig. 9.13. Figure 9.15 shows data for the same system with the temperature increased to $0.75T_c$, at which B_{c2} is halved compared to $T = 0.5T_c$. It shows that while the 3D exponent for the high-E mainline data is approximately 1.5, as for the 2D mainlines, the low-E branch exponent is close to the Kramer value of 2.5, as a Kramer gradient independent of H_{c2} corresponds to $F_p \propto B_{c2}^{5/2}$. In Figs. 9.14 and 9.15, a Kramer reduced-field dependence $F_p \propto b^{1/2}(1-b)^2$ is observed throughout the field range for the 3D data, as in Fig. 9.13.

Figure 9.16 shows the effect of reducing the grain size from 30ξ to 20ξ. The mainline J_c, is very similar to that in Fig. 9.13 and the Kramer reduced-field dependence is maintained. However, as in the 2D system, the branch J_c values are much lower than those for the system with 30ξ grains. This shows that the decrease in J_c with decreasing grain size is not unique to 2D. However, the calculations in Figs. 9.8 and 9.15 both of which halve B_{c2} relative to its hub value do not show a similar reduction in J_c, despite having a larger ξ and λ (due to the lower B_{c2}) and therefore a smaller relative grain size. This suggests that the collapse of J_c in the small-grain systems is caused by the large volume fraction of the material occupied by normal metal. From the data in Figs. 9.13 – 9.16, the mainline and branch-line F_p values for the 3D system can thus be summarized as

$$F_p^{(3D\text{-}mainlines)} = 1.8\times10^{-3} B_{c2}\left(T_c/2\right)\frac{B_{c2}^{1.5}(T)}{\mu_0\kappa^2}\sqrt{\frac{2\pi}{\phi_0}}b^{1/2}(1-b)^2. \qquad (9.11)$$

$$F_p^{(3D\text{-}branches)} = 3.6\times10^{-4}\,\frac{B_{c2}^{2.5}(T)}{\mu_0\kappa^2}\sqrt{\frac{2\pi}{\phi_0}}b^{1/2}(1-b)^2 \qquad (9.12)$$

9.8 Visualization of moving fluxons

9.8.1 2D Visualizations

To determine the mechanism limiting J_c in simulated 2D superconductors it was decided to pass a transport current through the system and note where fluxons move and where dissipation occurs. Two applied fields are investigated in the 2D hub system – $H = 0.430H_{c2}$ representing the low-field regime and $H = 0.942H_{c2}$ in the high-field regime. Test transport currents are chosen such that in each case, only one of the two mechanisms responsible for dissipation in this system could operate – this is clarified in Fig. 9.17. Using the end of the branch runs in Fig. 9.5 (ie the hub) as the initial conditions the transport current is linearly ramped up to the target value over a time period of $10^4\ t_0$, and then held constant for another $10^4\ t_0$.

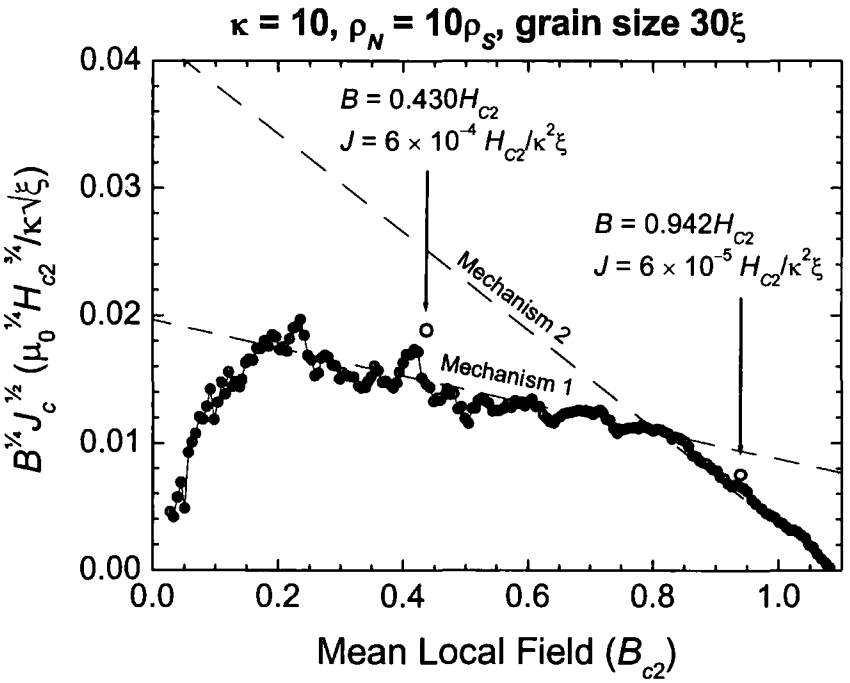

Figure 9.17: Choices of B and J for visualization calculations used to determine mechanism of current criticality in 2D granular superconductor

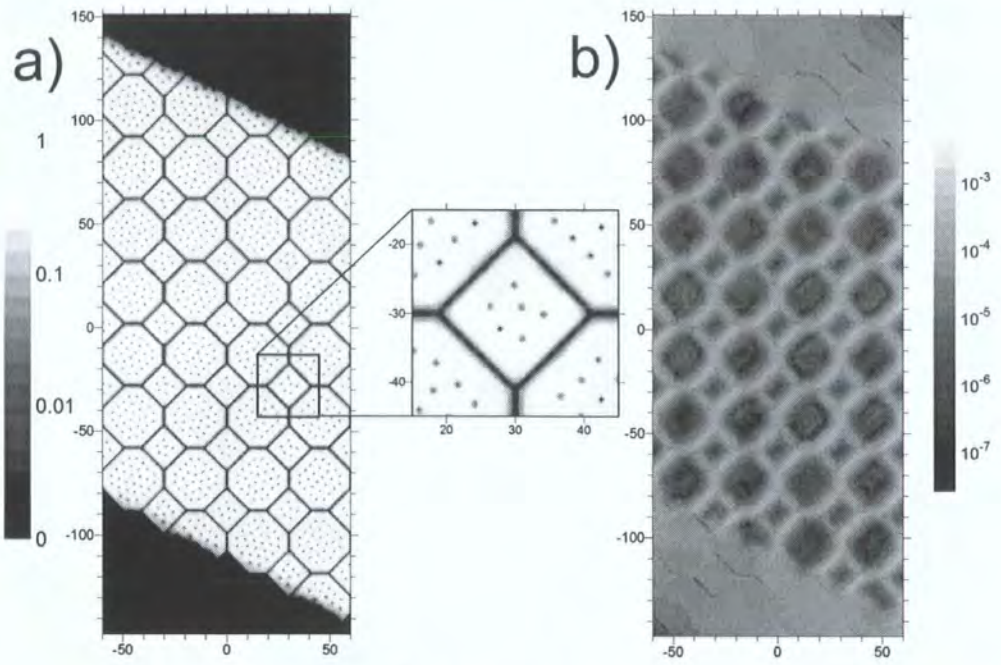

Figure 9.18: Snapshots of a) $\left|\hat{\psi}\right|^2$ and b) $|J_N|$ in units of $H_{c2}/\kappa^2\xi$ for a $\kappa = 10$ superconductor with 30ξ grains separated by $\rho_N = 10\rho_S$ trilayer grain boundaries at $H = 0.430H_{c2}$ and $J = 6 \times 10^{-4}\ H_{c2}/\kappa^2\xi$. Dissipation results from the motion of fluxons along the grain boundaries. Both $\left|\hat{\psi}\right|^2$ and $|J_N|$ are shaded according to logarithmic scales.

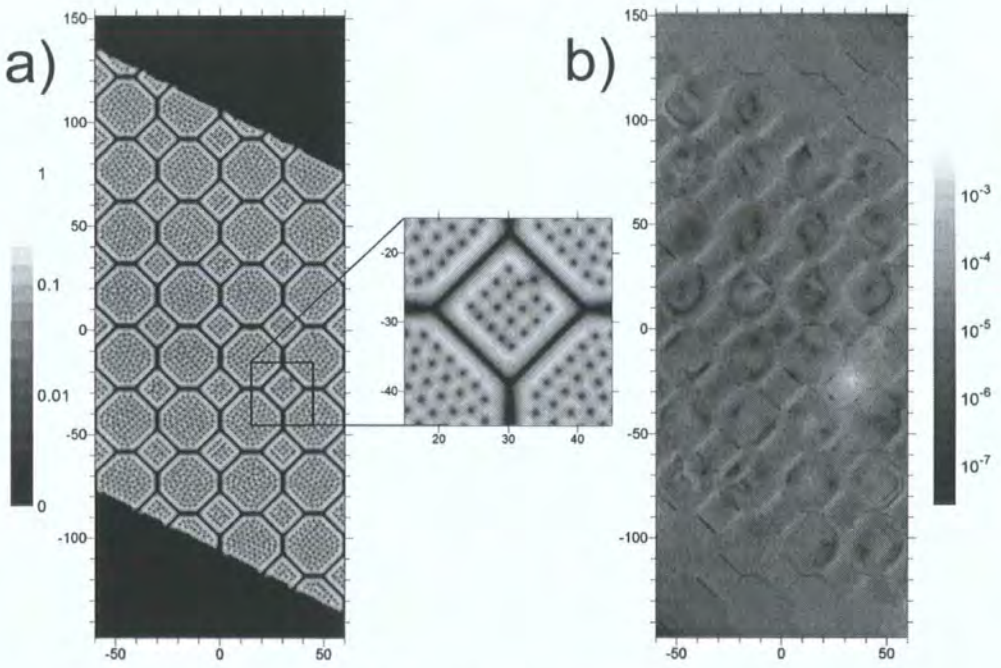

Figure 9.19: Snapshots of a) $\left|\hat{\psi}\right|^2$ and b) $|J_N|$ for a $\kappa = 10$ superconductor with 30ξ grains separated by $\rho_N = 10\rho_S$ trilayer grain boundaries at $H = 0.942H_c$ and $J = 6 \times 10^{-5}\ H_{c2}/\kappa^2\xi$. A fluxon can be seen entering the grain in the enlarged region and in the normal current plot. Both $\left|\hat{\psi}\right|^2$ and $|J_N|$ are shaded according to logarithmic scales.

Figure 9.18 is a snapshot of the superconductor at the end of the $0.430H_{c2}$ run – in the enlarged inset fluxons are distinguishable within the grain boundaries. Additionally, an animated movie of the system depicted in Fig. 9.18 showed that the fluxons within the grain boundaries moved while the fluxons inside the grains remained stationary. This therefore confirms that in the low-field regime, J_c is determined by flux shear within grain boundaries. The test run at $0.942H_{c2}$ was less definitive, as $\left|\hat{\psi}\right|^2$ within the grain boundaries was so heavily suppressed that individual fluxons were not discernible there, even with $\left|\hat{\psi}\right|^2$ shaded according to a logarithmic scale. At this field the lower J_c means equilibrium is slower, which meant that the system's Bean profile did not fully equilibrate within the run – the consequences are seen clearly in Fig. 9.19, which shows a fluxon entering a grain from its grain boundary: this is shown in the inset and is visible as a bright spot in the normal current plot. However, it was still clear that most of the dissipation within the system was within the grain boundaries, thus suggesting along with the lack of dependence of J_c on grain size, that flux shear is also the dominant critical state mechanism in the high-field regime.

9.8.2 3D Visualizations

Equations (9.11) and (9.12) show the 3D systems which we simulated computationally have F_p and J_c values which are about 20% of those for the equivalent 2D systems, given by equations (9.9) and (9.10) respectively. In order to investigate the behaviour of flux within 3D systems, we take snapshots of cross-sections of the 'hub' 3D system of Fig. 9.13. Snapshots of the order parameter are made in the XY and YZ planes, and of the magnitude of the normal current in the XY plane.

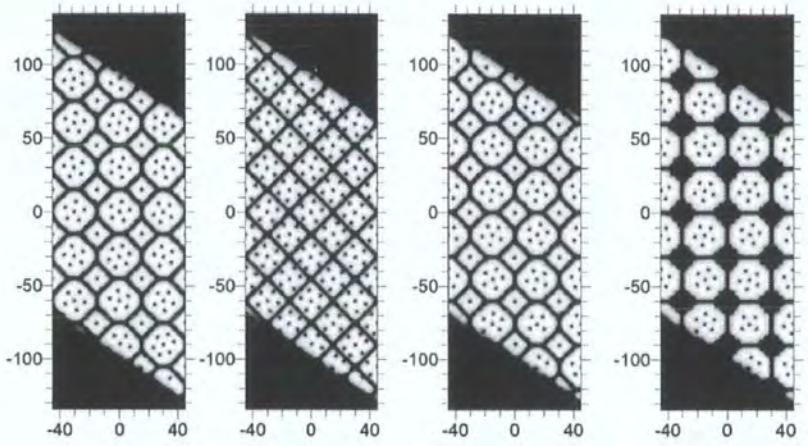

Figure 9.20: XY cross-sections of $\left|\hat{\psi}\right|^2$ for 3D $\kappa = 10$ superconductor with 30ξ grains separated by 2ξ-thick $\rho_N = \rho_S$ grain boundaries at $H = 0.151 H_{c2}$. Compared to a 2D run at the same field there are more fluxons within the grains.

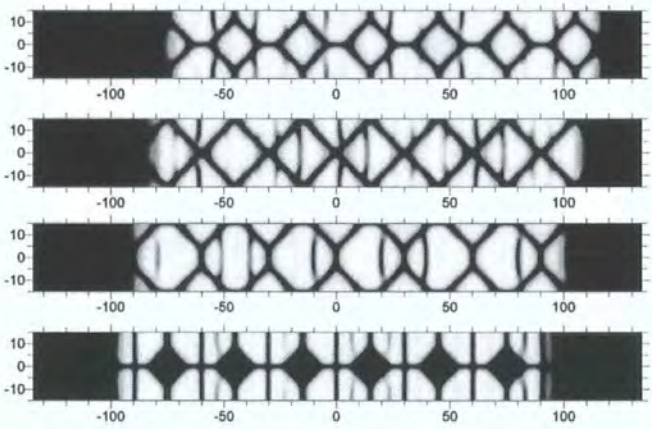

Figure 9.21: YZ cross-sections of $\left|\hat{\psi}\right|^2$ for 3D $\kappa = 10$ superconductor with 30ξ grains separated by 2ξ-thick $\rho_N = \rho_S$ grain boundaries at $H = 0.151 H_{c2}$. The fluxons within the grains are almost straight, but other fluxons bend to stay within the grain boundaries.

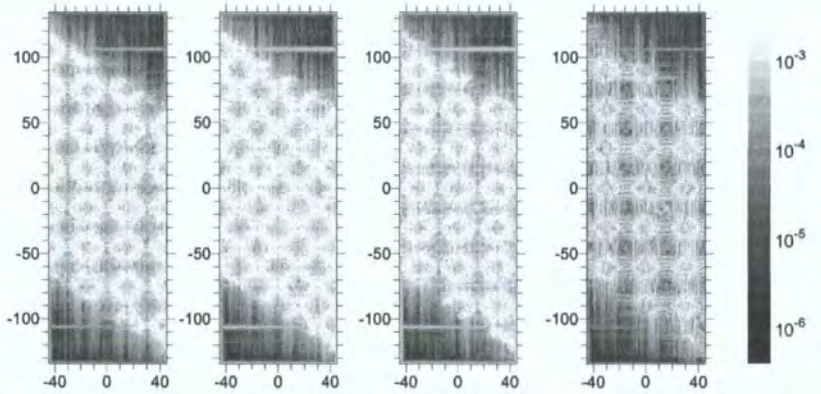

Figure 9.22: XY cross-sections of $|J_N|$ in units of $H_{c2}/\kappa^2\xi$ for a 3D $\kappa = 10$ superconductor with 30ξ grains separated by 2ξ-thick $\rho_N = \rho_S$ grain boundaries at $H = 0.151 H_{c2}$. The horizontal and vertical streaks within the normal regions are a computational artefact.

Figures 9.20 and 9.21 show that in the 3D system, fluxons passing through the interior of the grains do not show any major curvature within the grains, although they do deviate sharply as they enter the grain boundaries, and also prefer to bend slightly towards the normal axis on approach to a grain boundary. It can be seen from Figure 9.22 in the 3D system that most of the dissipation is within the grain boundaries. Just as with the similar findings in 2D (Figure 9.18) this suggests that the fluxons which move through the system above J_c are confined entirely to the grain boundaries. However, since this system also includes fluxons penetrating through the grains (which do not themselves move), the system geometry suggests that the moving grain boundary fluxons must cut through the stationary grain fluxons wherever the latter pass through the grain boundaries. We shall return to the issue of flux cutting later in this chapter.

9.9 Comparison with experimental results

The $b^{½}(1 - b)^2$ reduced field dependence of the pinning force, observed for our 2D computational systems in the high-field regime and in our 3D computational systems throughout the entire field range, is also observed in most experimental polycrystalline materials, including the A15 materials, niobium nitride and the Chevrel-phase materials.

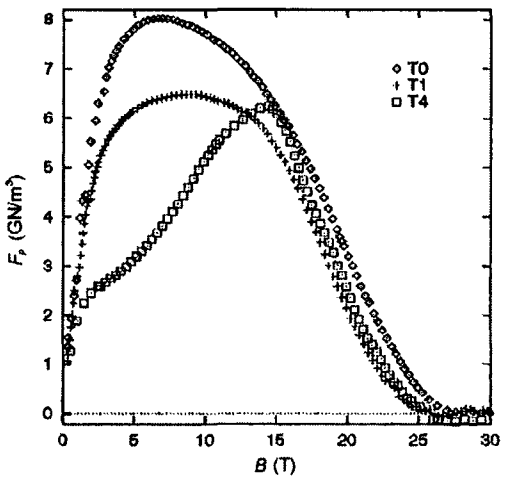

Figure 9.23: Bulk volume pinning force F_p at 4.2 K for three $SnMo_6S_8$ samples fabricated using different thermal treatments[99].

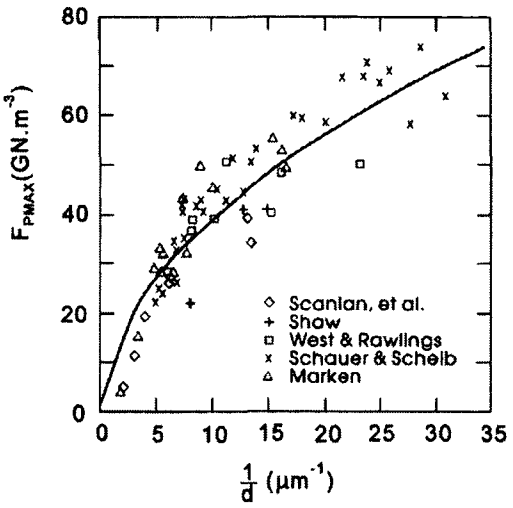

Figure 9.24: Maximum pinning force per unit volume at 4.2 K as a function of reciprocal grain size in filamentary bronze-route Nb_3Sn[21].

In our 2D computations two mechanism for F_p were observed, a low-field mechanism where J_c affected by grain size, and a mechanism independent of grain size for applied fields close to B_{c2}. Figure 9.30 shows F_p as a function of field for Chevrel-phase samples of differing microstructures, in which a microstructure-dependent low-field regime crosses over with a universal high-field regime, strongly reminiscent of Figs. 9.6 and 9.17. This behaviour is also observed in Nb_3Sn samples studied extensively by Kramer[100]. However, Fig. 9.31, which plots maximum F_p as a function of reciprocal grain size for Nb_3Sn wires and tapes with different microstructures, shows that J_c decreases with increasing grain size, which is opposite to that observed in our 2D computations.

Although our 2D computational results predict a B_{c2} scaling law exponent $n \approx 1.85$, our 3D result correctly predict the exponent $n \approx 2.5$ observed in experiments. We must note that though in some experimental data the raw B_{c2} exponent of F_p is closer to 2 than 2.5, this is because the temperature dependence of κ_1 ($F_p \propto 1/\kappa_1^2$) is sometimes not properly considered. In the BCS (weak-coupling) limit[101], $\kappa_1(0) = 1.19\kappa_1(T_c)$, while in strong-coupling superconductors, the temperature dependence is stronger[98] – $\kappa_1(0)$ can be as high as $1.6\kappa_1(T_c)$.

Superconductor	n_{raw}	$n_{corrected}$
Nb-25% Zr[30]	1.9	-
Nb_3Sn tapes (RCA, GE)[30]	1.95	-
Nb_3Sn (MJR)[102]	-	3.07
Nb_3Sn (Bronze-route)[102]	-	2.46
Nb_3Sn (Internal-tin)[102]	-	2.34
Jelly-roll Nb_3Al[98]	2.18	2.60
$(NbTa)_3Sn$ filaments[32]	-	2.5
Nanocrystalline $PbMo_6S_8$[103]	-	2.35
MgB_2[104]	2	-

Table 9.2: H_{c2} exponents for various superconducting materials

When this is taken into account, the true value of n is close to 2.5 for most experimental samples (except the MJR wires, which have n closer to 3). A comparison between the raw B_{c2} exponent n_{raw} and the exponent corrected for the temperature-dependence of κ, $n_{corrected}$ for various experimental measurements is shown in Table 9.2.

9.10 Standard flux-shear calculation for F_p

Many researchers have investigated models of the critical state in superconductors in which some fluxons remain stationary, while other fluxons shear past them. The famous Kramer paper[30] model from 1973 was based on fluxons shearing past other fluxons pinning by point pinning sites, while in the late 1980s both Dew-Hughes[27] and Pruymboom[105,106] considered flux shear along grain boundaries. Pruymboom studied thin films of NbN grown on top of a substrate of Nb_3Ge, with etched channels providing preferential paths for flux motion – either straight lines parallel to the Lorentz force[105] or honeycomb and brick-wall patterns[106]. Such model systems are ideal for investigating flux shear with minimal interference from intrinsic material parameters.

In the following calculations, we shall essentially follow Pruymboom's method for systems in high magnetic fields. When a superconductor contains weak-pinning channels of with W, an expression can be derived for the shear-limited F_p based on these channels[30,105]

$$F_p = \frac{2G_1G_2\tau_{\max}}{W_{eff}} \tag{9.13}$$

Here τ_{max} is the FLL shear modulus, W_{eff} is the effective width of the weak-pinning channels and G_1 and G_2 are geometrical factors. For a 2D FLL with an isotropic shear modulus, $G_2 = 1$ (this factor is for 3D systems, and is considered in Sec. 9.11.2) and τ_{max} is given by[107]

$$\tau_{max} = A C_{66} \tag{9.14}$$

where the shear modulus C_{66} is given by the Brandt expression (3.9) and A is the fraction of the flux-line spacing a_0 through which a fluxon must move before the elastic limit of the lattice is exceeded. Brandt's analytic calculation[108] of A, based on the free energy difference between hexagonal and square FLLs, gave $A = 0.044$, while an experimental determination of A based on measurements of the peak effect observed in 2D collective-pinning experiments[109] gave $A \approx 0.047$. G_1 is a geometric enhancement factor[106] allowing for the fact that fluxons in grain boundaries are prevented from entering the grains by a large pinning force, and that only the projected component of the Lorentz force boundaries along the grain boundary can move the fluxon in this direction. G_1 can thus be written as

$$G_1 = \frac{L_{tot}}{L_{||}} \tag{9.15}$$

which is the ratio of the total channel length L_{tot} to the component of the channel length $L_{||}$ parallel (projected in the direction of) to the Lorentz force. For the 2D grain structure shown in Fig. 9.1 which we used for our computations, it can be shown when θ is the angle between the y-axis (along which the Lorentz force acts) and the b-axis (along which the grain boundary structure is aligned), G_1 is given by:

$$G_1 = \frac{2 + 6\sqrt{2}}{|\sin\theta| + |\cos\theta| + 3\sqrt{2}\left(\left|\sin\left(\theta + \pi/4\right)\right| + \left|\sin\left(\theta - \pi/4\right)\right|\right)} \tag{9.16}$$

The four terms in the denominator represent the contributions from the four distinct grain boundary sections in our system illustrated in Fig. 9.1, namely parallel to the a-axis, parallel to the b-axis, and diagonal from top-left to bottom-right and from top-right to bottom-left respectively. G_1 is plotted as a function of θ in Figure 9.25.

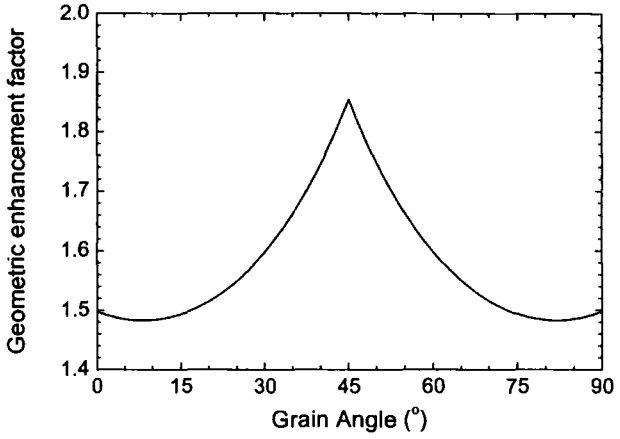

Figure 9.25: Geometric enhancement factor G_1 for 2D computational system as a function of angle

Most of our 2D polycrystalline simulations set $\theta = \tan^{-1}(½) \approx 26.5°$, which gives $G = 1.563$. Substituting this G_1 value, (9.14) and (3.9) into (9.13), with $A = 0.044$, gives F_p as

$$F_p = 1.72\times10^{-2}\,\frac{B_{c2}^2}{\mu_0\kappa^2}\,\frac{1}{W_{eff}}\exp\left(\frac{b-1}{3\kappa^2 b}\right)b(1-0.29b)(1-b)^2 \qquad (9.17)$$

The effective width W_{eff} for a system with grain boundaries of thickness d is given by Pruymboom[105,106]:

$$W_{eff}^{\uparrow} = d + 2a_0, \quad W_{eff}^{\downarrow} = d + \sqrt{3}a_0 \qquad (9.18)$$

These differing values of W_{eff} explain the results from Chapter 8 in which J_c is seen to be higher for a decreasing magnetic field than for an increasing field.

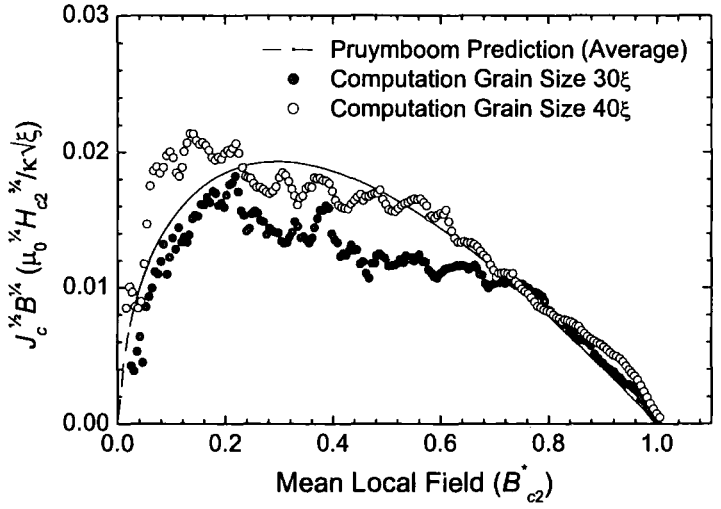

Fig ure 9.26: Kramer plot comparing computational results with Pruymboom prediction

Taking an average value $\bar{W}_{eff}^{\uparrow} = d + 2\left(\frac{3}{4}\right)^{1/4} a_0$, and the value of $d = 2\xi$ used in our computational system, we get the following expression for F_p:

$$F_p = 6.6\times10^{-3}\frac{B_{c2}^{5/2}}{\mu_0\kappa^2}\frac{b^{3/2}(1-0.29b)}{b^{1/2}+\sqrt{2\pi}}\exp\left(\frac{b-1}{3\kappa^2 b}\right)\sqrt{\frac{2\pi}{\phi_0}}(1-b)^2 \tag{9.19}$$

which can be approximated by

$$F_p \approx 1.5\times10^{-3}\frac{B_{c2}^{5/2}}{\mu_0\kappa^2}\sqrt{\frac{2\pi}{\phi_0}}b^p(1-b)^q \tag{9.20}$$

where $p = 1.29$ and we have set $q = 2$.

This expression is compared with some of our TDGL computational results in Figure 9.26. It can be seen that this expression has a remarkable agreement with the 2D TDGL data, at least in the high-field regime.

The 'knee' which was observed in our own TDGL computational results was also observed in Pruymboom's experimental results[105]. The reduced field at the 'knee' where the transition between the two mechanisms occurs is given empirically by

$$b_{knee} \approx 4\sqrt{\frac{\xi}{D}} \qquad (D > 16\xi) \tag{9.21}$$

Below b_{knee}, the arrangement of fluxons within each grain is determined mainly by the shape of the grain itself. This causes F_p to be reduced from the value given by the continuum model of (9.19), and also introduces oscillations in the value of F_p which are associated with the number of fluxons per grain interior as a function of B (this is obscured some what in our 2D system, as there are grains of two different sizes). Above b_{knee} the number of fluxons in the grain is large enough that the positions of the fluxons near the edge is determined more by fluxon-fluxon interactions. b_{knee} decreases with increasing grain size because larger grains can each hold more fluxons.

9.11 Further development of the flux-shear model

9.11.1 Introduction

The Pruymboom result based the model of flux shear along grain boundaries gives remarkably good agreement with the 2D computational results seen earlier in this chapter. The Pruymboom model is a purely 2D model, and in its original form does not consider geometric aspects specific to 3D systems. Also, the Pruymboom calculation predicts a value of p of 1.29 (see equation (9.20)) at $b \sim 0.38$, a value much higher that the $p \sim 0.5$ observed experimentally in the technically important A15 materials[27,97,98], or indeed in our 3D computational results (see equations (9.11) and (9.12)). This section is concerned with two attempts to amend the Pruymboom model to fix these deficiencies: a second geometrical factor to account for non-parallel fluxons in 3D systems, and a model of distorted fluxons within grain boundaries which reduces p to a value more comparable with experimental results.

9.11.2 Second geometrical factor for 3D systems

In order to consider a 3D system, we introduce a second geometrical factor, G_2, that accounts for the fact that the grain boundary fluxons are not always parallel to those within the grains. It can be expected that that the dependence of the flux shear force on the angle between the moving fluxon and the stationary fluxons is sharply peaked, because if the moving and stationary fluxons are not parallel, segments of the moving fluxon would be exposed to forces from the stationary fluxons which would cancel out when averaged along its length. In a 3D system, we can begin with the assumption that the only segments of the flux lines in grain boundaries subject to flux shear forces are those parallel to the applied field, with fluxons in all other faces moving freely unimpeded by flux shear forces.

In our 3D grain structure, each of the grains of grain size D (defined as the distance between opposite square faces) is a truncated octahedron with six square faces each of area $D^2/8$ (two of which are orthogonal to the applied field, the other four are parallel) and eight hexagonal faces each of area $3\sqrt{3}D^2/16$ (and which are each at an angle of $\approx 35°$ to the applied field). If

flux shear forces only apply to fluxons in the square faces parallel to the applied field, the flux shear force is reduced by the factor

$$G_2 = \frac{4\left(D^2/8\right)}{6\left(D^2/8\right)+8\left(3\sqrt{3}D^2/16\right)} = \frac{2}{3+6\sqrt{3}} = 0.149 \qquad (9.22)$$

G_2 obtained from high-field TDGL computational results, either by dividing the 3D mainline F_p (9.11) by the 2D mainline F_p (9.9), or from dividing the equivalent branch F_p values in (9.12) and (9.10), is approximately 0.2. Hence this provides a simple explanation for the factor-5 reduction in F_p in the 3D computational results compared to the 2D computational results. A consideration in considering the difference between G_2 for the computation and this simple model is that the dependence of the flux shear force on the angle between moving and stationary fluxons, while sharply peaked at zero angle, is not zero for any non-zero angle.

9.11.3 The effect of grain boundary fluxon distortion on F_p

Since the value of p is predominantly determined by low-field data, and since the Kramer-like dependence of both our 2D computational data and Pruymboom's 2D experimental data does not extend to these low fields, the value of p for this data is unconfirmed. However, the $p \approx 1.29$ given by the Pruymboom analytic model is very different from the $p \approx 0.5$ typically observed experimentally and confirmed by the 3D computational results shown in Figs. 9.13 through 9.16. In this section we describe a possible explanation for the reduction of p from that quoted by the Pruymboom model, which would apply for both 2D and 3D systems.

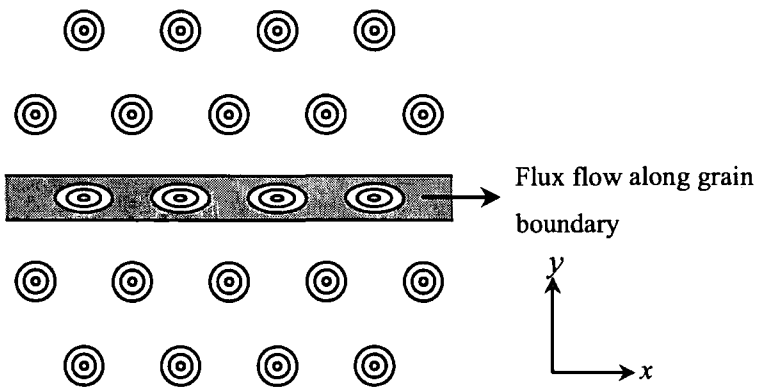

Figure 9.27: Flux shear along a grain boundary. Only the fluxons within the grain boundary move, while the grain fluxons are held stationary by the grain boundaries.

Figure 9.27 shows a row of fluxons moving along a grain boundary parallel to the x-axis. It is assumed that all the grain boundary fluxons are moving together, so the forces from the neighbouring fluxons within the grain boundary cancel.

It is to be expected that since the fluxons within the grain boundary are constrained in the y-direction, and are in a region where the order parameter is depleted (and thus the effective coherence length and penetration depth are much larger than within the grains), that the fluxons are elongated in the x-direction. At low fields, where the fluxon-fluxon spacing a_0 is much larger than the elongated fluxon dimension, the distortion of the fluxons in the grain boundaries has little effect on F_p. At high fields F_p is significantly reduced because the distorted fluxons in the grain boundaries experience force components from the grain fluxons that partially cancel. Such reasoning leads to terms that account for the fluxon distortion of the form $(a_0/\gamma)^n$ where n is positive and γ increases as the distortion decreases. This in turn reduces the value of p. A more mathematically rigorous approach is now considered below.

We approximate the force from the grain fluxons on a fluxon within the grain boundary by a sinusoidal potential. For a flux line within the grain boundary, displaced by X from its equilibrium position, we thus write the force per unit length of fluxon as:

$$F \quad (X) = -F \quad ^{\max} \sin \frac{2\pi X}{a_0} \tag{9.23}$$

In the London limit, the field associated with a fluxon at position $\mathbf{R}$ is given by the equation[19]:

$$\lambda^2 \nabla \times \nabla \times \mathbf{B} + \mathbf{B} = \phi_0 \delta_2 (\mathbf{r} - \mathbf{R}) \hat{\mathbf{z}} \tag{9.24}$$

We posit that the fluxons within the grain boundary are distorted by the presence of this grain boundary and that the field for these distorted fluxons is instead given by

$$\lambda^2 \nabla \times \nabla \times \mathbf{B} + \mathbf{B} = \phi_0 f_{dist} (x - R_x) \delta_2 (y - R_y) \hat{\mathbf{z}} \tag{9.25}$$

where $f_{dist}(x)$ is an even function for which $\int_{-\infty}^{\infty} f_{dist}(x)\,dx = 1$. We suggest that this type of distortion is more likely to simulate the effect of a normal-metal grain boundary on a fluxon core than the standard anisotropic Ginzburg-Landau model[110], as it affects the core significantly while having little effect on the B-field from any individual fluxon at a distance

of λ or more away from the core. We can find the effect on the field **B** within the fluxon by means of Fourier transforms. Since $\nabla.\mathbf{B} = 0$, we can transform (9.25) into a scalar equation:

$$B - \lambda^2 \nabla^2 B = \phi_0 f_{dist}\left(x - R_x\right)\delta_2\left(y - R_y\right) \tag{9.26}$$

Taking Fourier transforms of both sides ($\mathfrak{F}$ = Fourier transform operator) we get

$$\mathfrak{F}(B) = \frac{\phi_0 \mathfrak{F}\left(f_{dist}\left(x - R_x\right)\right)}{1 - \lambda^2 \mathbf{k}^2} = \frac{\mathfrak{F}\left(B_{no-dist}\right)\mathfrak{F}\left(f_{dist}\left(x - R_x\right)\right)}{\sqrt{2\pi}} \tag{9.27}$$

where $B_{no\text{-}dist}$ is the scalar magnetic field associated with an un-distorted fluxon. We can thus write the field of the distorted fluxon as

$$\mathbf{B} = \frac{\phi_0}{2\pi\lambda^2}\left(K_0\left(\frac{|\mathbf{r} - \mathbf{R}|}{\lambda}\right) * f_{dist}\left((\mathbf{r} - \mathbf{R}).\hat{\mathbf{x}}\right)\right)\hat{\mathbf{z}} \tag{9.28}$$

where * is the convolution operator $\left(f(x) * g(x) = \int_{-\infty}^{\infty} f(x')g(x - x')dx'\right)$. Similarly, the energy (and thus the force) associated with the distorted fluxon is also given by the convolution operator[19]:

$$F = \frac{1}{2\mu_0}\int \mathbf{B}^2 + \lambda^2 |\nabla \times \mathbf{B}|^2 d^2\mathbf{r} = \frac{1}{2\mu_0}\int \left(\mathbf{B} + \lambda^2 \nabla \times \nabla \times \mathbf{B}\right).\mathbf{B}\, d^2\mathbf{r}$$

$$= \frac{\phi_0}{2\mu_0}\int \left|\mathbf{B}\left(x\hat{\mathbf{x}} + \mathbf{R}.\hat{\mathbf{y}}\right)\right| f_{dist}\left(x - \mathbf{R}.\hat{\mathbf{x}}\right)dx$$

$$= \frac{\phi_0}{2\mu_0}\left[|\mathbf{B}(\mathbf{r})| * f_{dist}\left(\mathbf{r}.\hat{\mathbf{x}}\right)\right]_{\mathbf{r}=\mathbf{R}} \tag{9.29}$$

The force per unit length of distorted fluxon $F_{dist}(X)$ is thus given by

$$F_{dist}(X) = -F^{\max}\left(\sin\frac{2\pi X}{a_0} * f_{dist}(X)\right) = -F_{dist}^{\max}\sin\frac{2\pi X}{a_0} \tag{9.30}$$

The 'stretching' of the fluxon causes the force on it from the fluxons in the grains to be reduced. We determine the value of $F_{dist}^{\max}/F^{\max}$ by solving (9.30). Again by using Fourier transforms (k is a dummy variable) we obtain:

$$\frac{F_{dist}^{\max}}{F^{\max}} = \sqrt{2\pi}\mathfrak{F}\left(f_{dist}(X)\right)\Big|_{k=\frac{2\pi}{a_0}} = \int_{-\infty}^{\infty} f_{dist}(X)\cos\frac{2\pi X}{a_0}dX \tag{9.31}$$

Example values of $F_{dist}^{\max}/F^{\max}$ for four different trial functions are shown in Table 9.3 (the prefactors on the f_{dist} expressions are needed to ensure $\int_{-\infty}^{\infty} f_{dist}(x)dx = 1$). We use γ as a parameter to set the magnitude of the fluxon's distortion. The distortion of the fluxon thus

adds an additional term, dependent on the ratio a_0/γ. Since a_0 is dependent on reduced field b, this changes the field dependence of F_p if γ is field-independent. In Table 9.3 we write the factor F_{dist}^{max}/F^{max} to explicitly include the reduced field b.

	$f_{dist}(x)$	F_{dist}^{max}/F^{max}
1.	$\frac{1}{\gamma\sqrt{\pi}}\exp\left(-\frac{x^2}{\gamma^2}\right)$	$\exp\left(-\frac{\pi\sqrt{3}\gamma^2}{4\xi^2}b\right)$
2.	$\frac{\gamma}{\pi\left(x^2+\gamma^2\right)}$	$\exp\left(-\frac{3^{1/4}\sqrt{\pi}\gamma}{\xi}b^{1/2}\right)$
3.	$\frac{1}{\pi\gamma}K_0\left(\frac{\lvert x\rvert}{\gamma}\right)$	$\left(1+\frac{\pi\sqrt{3}\gamma^2}{\xi^2}b\right)^{-1/2}$
4.	$\frac{1}{2\gamma}\exp\left(-\frac{\lvert x\rvert}{\gamma}\right)$	$\left(1+\frac{\pi\sqrt{3}\gamma^2}{\xi^2}b\right)^{-1}$

Table 9.3: Effect of various distortion functions f_{dist} on the field dependence of F_p.

All of these functions reduce the value of p. It can be seen that function 3 reduced p by 0.5, while function 4 – the mod-exponential function $\frac{1}{2\gamma}\exp\left(-\frac{|x|}{\gamma}\right)$ – reduces p by 1. Since the field from a fluxon decays quasi-exponentially according to the K_0 function, it would be expected that functions 3 and 4 in Table 9.3 are more likely to give meaningful field dependences than the quite different decays of functions 1 or 2.

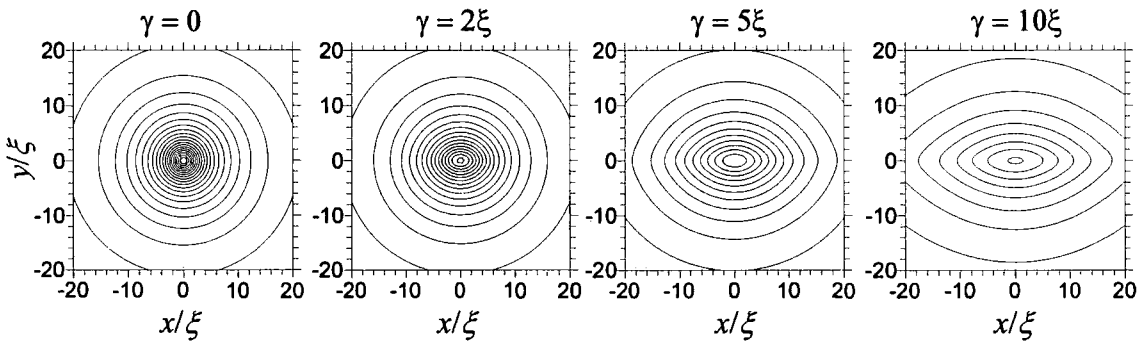

Figure 9.28: Contour plots of **B** (the contours are spaced at intervals of 10^{-3} B_{c2}) for isolated fluxons distorted by convolving the fluxon field with $f_{dist} = \frac{1}{2\gamma}\exp\left(-|x|/\gamma\right)$. As γ increases, the fluxon is stretched in the x-direction.

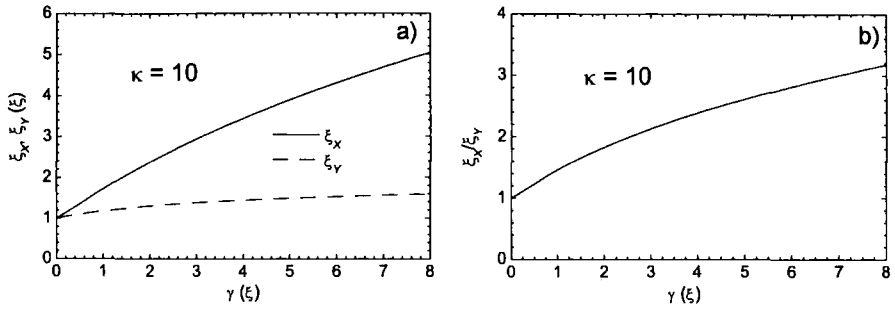

Figure 9.29: a) Effective coherence lengths ξ_X and ξ_Y if a distorted fluxon as a function of γ, b) Effective fluxon anisotropy ξ_X/ξ_Y

Function 4, which decreases p by one, may be a reasonable function of x to convolve with the undistorted fluxon structure because when the structure of an undistorted fluxon is integrated over all y, the resulting x-dependence is mod-exponential $\left(\int_{-\infty}^{\infty} B(x,y)\,dy = \frac{\phi_0}{2\lambda}\exp\left(-\frac{|x|}{\lambda}\right)\right)$, although this is clearly not a rigorous justification. Figure 9.28 shows examples of distorted fluxons for three values of γ in a $\kappa = 10$ superconductor, compared with a undistorted fluxon. The fluxon core expands in both x- and y-directions (though more in the x-direction), while the effective penetration depth (the distance over which the vortex current decays) increases in the x-direction and decreases in the y-direction.

Since our calculation describing the effect of distorting the grain boundary fluxons is based on a London model, we do not have an expression for the order parameter associated with our distorted fluxons. To obtain equivalent coherence lengths in the x and y directions for our distorted fluxons, we must therefore rely on their magnetic field profiles. We use a result obtained by Clem[84] for the structure of a single fluxon to define effective coherence lengths ξ_X and ξ_Y for the distorted fluxon in the x- and y-directions in a way which compared them correctly to ξ for an undistorted fluxon. In the Clem approximation, the size of the fluxon core is defined using the variational parameter ξ_v, which in the high-κ limit is both the point of inflection along the magnetic field profile, and equal to $\xi\sqrt{2}$, where ξ is the standard Ginzburg-Landau coherence length. Using this we define ξ_X and ξ_Y

$$\frac{d^2}{dx^2}\left(\mathbf{B}\left(\xi_X\sqrt{2}\hat{\mathbf{x}}\right)\right) = \mathbf{0}, \qquad \frac{d^2}{dy^2}\left(\mathbf{B}\left(\xi_Y\sqrt{2}\hat{\mathbf{y}}\right)\right) = \mathbf{0} \tag{9.32}$$

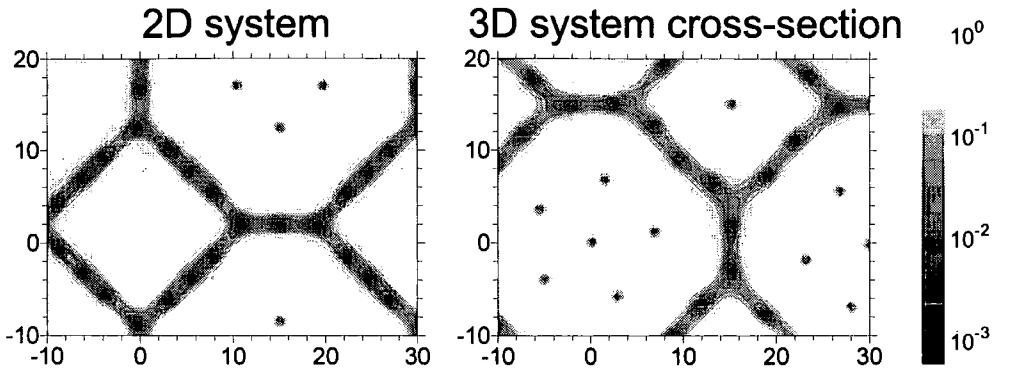

Figure 9.30: Comparison of $\left|\hat{\psi}\right|^2$ of grain-boundary fluxons in 2D and 3D $\kappa = 10$ superconductors with 30ξ grains separated by 2ξ-thick $\rho_N = \rho_S$ grain boundaries. The 2D system is at $0.156H_{c2}$ while the 3D system is at $0.151H_{c2}$

ξ_X and ξ_Y are plotted for $\kappa = 10$ as a function of γ in Figure 9.29a. It can be seen that both effective coherence lengths increase with γ (these increases are similar to those which would be expected for grain boundary fluxons, as the grain boundary itself depresses ψ). However, ξ_X increases more than ξ_Y. Figure 9.29b explicitly shows the anisotropy ξ_X/ξ_Y as a function of γ. It can thus be seen that a relatively small anisotropy ξ_X/ξ_Y can correspond to a rather large γ value, and thus to a field dependence of F_p which is consistent with $F_p \propto b^{1/2}(1-b)^2$ at all but the lowest values of reduced field b.

In Fig. 9.30 we compare equivalent slices of the order parameter through 2D and 3D superconductors with the same grain size and grain boundary type. It can be determined from visual inspection of the contours that the 2D and 3D grain boundary fluxons are of broadly similar shape. However, it is not possible to obtain an accurate γ value from these visualizations. Visual inspection of the contour line $\left|\hat{\psi}\right|^2 = 0.018$ gives aspect ratio of the grain boundary fluxon cores $\xi_X/\xi_Y = 2.2 \pm 0.2$, which corresponds to a γ/ξ value of 3.3 ± 0.8, while a similar inspection of the contour line $\left|\hat{\psi}\right|^2 = 0.001$ gives aspect ratio of the grain boundary fluxon cores $\xi_X/\xi_Y = 1.2 \pm 0.2$, which corresponds to a γ/ξ value of 0.4 ± 0.4 (this is because closer to the core the grain boundary edge has less effect making the local behaviour more isotropic). Nevertheless, the $\gamma^2 b$ dependence of the reduction in F_p resulting from the mod-exponential fluxon distortion function is enough to change the F_p dependence to $b^{1/2}(1-b)^2$ over about 90% of the field range.

Model	Force F_p per unit volume
Pinning at surfaces[25] (Dew-Hughes 1974)	$F_p = \frac{B_{c2}^2}{4\mu_0\kappa^2 D} b^{1/2}(1-b)^2$
Pinning at surfaces[27] (Dew-Hughes 1987)	$F_p = \frac{\pi\sqrt{3}B_{c2}^2}{16\mu_0\kappa^2 D} b(1-b)$
Flux shear past point pinning sites[30] (Kramer, Labusch[31] C_{66})	$F_p = 2.8\times10^{-4}\frac{B_{c2}^{5/2}}{\mu_0\kappa^2}\sqrt{\frac{2\pi}{\phi_0}}\frac{1}{\left(1-a_0/d\right)^2} b^{1/2}(1-b)^2$
Flux shear past point pinning sites[30] (Kramer, Brandt[33] C_{66})	$F_p = 3.9\times10^{-4}\frac{B_{c2}^{5/2}}{\mu_0\kappa^2}\sqrt{\frac{2\pi}{\phi_0}}\frac{1-0.29b}{\left(1-a_0/d\right)^2}\exp\left(\frac{b-1}{3\kappa^2 b}\right) b^{3/2}(1-b)^2$
Maximum shear strength of lattice[27] (Dew-Hughes 1987)	$F_p = \frac{B_{c2}^2}{8\pi\mu_0\kappa^2(D-a_0)}\exp\left(\frac{b-1}{3\kappa^2 b}\right) b(1-0.29b)(1-b)^2$
Flux shear along grain boundaries in 2D[105] (Pruymboom 1988)	$F_p \approx 1.5\times10^{-3}\frac{B_{c2}^{5/2}}{\mu_0\kappa^2}\sqrt{\frac{2\pi}{\phi_0}} b^{1.29}(1-b)^2$
Collective pinning model[34] (Larkin-Ovchinnikov)	$F_p = \frac{n_p^2 f_p^4}{16 a_0^3 C_{44} C_{66}^2}$
2D TDGL computational results (equations (9.9) and (9.10))	$F_p^{high-E} = 7.3\times10^{-3} B_{c2}\left(T_c/2\right)\left[\frac{B_{c2}^{1.5}(T)}{\mu_0\kappa^2}\sqrt{\frac{2\pi}{\phi_0}}\right] b^{1/2}(1-b)^2$
	$F_p^{low-E} = 7.3\times10^{-2} B_{c2}^{0.27}\left(T_c/2\right)\left[\left(\frac{\phi_0}{2\pi w^2}\right)^{0.38}\frac{B_{c2}^{1.85}(T)}{\mu_0\kappa^2}\sqrt{\frac{2\pi}{\phi_0}}\right] b^{1/2}(1-b)^2$
3D TDGL computational results (equations (9.11) and (9.12))	$F_p^{high-E} = 1.8\times10^{-3} B_{c2}\left(T_c/2\right)\frac{B_{c2}^{1.5}(T)}{\mu_0\kappa^2}\sqrt{\frac{2\pi}{\phi_0}} b^{1/2}(1-b)^2$
	$F_p^{low-E} = 3.6\times10^{-4}\frac{B_{c2}^{2.5}(T)}{\mu_0\kappa^2}\sqrt{\frac{2\pi}{\phi_0}} b^{1/2}(1-b)^2$
Experimental measurement[97] on Nb_3Sn	$F_p = 1.6\times10^{-3}\frac{B_{c2}^{2.5}}{\mu_0\kappa^2}\sqrt{\frac{2\pi}{\phi_0}} b^{1/2}(1-b)^2$
Experimental measurement[98] on Nb_3Al	$F_p = 1.4\times10^{-3}\frac{B_{c2}^{2.5}}{\mu_0\kappa^2}\sqrt{\frac{2\pi}{\phi_0}} b^{1/2}(1-b)^2$

Table 9.4: Pinning forces per unit volume from various sources (D = grain size, d = point pin flux separation). Note that for our 'hub' computational system $w = 187.8\xi$ and thus the low-E 2D data closely matches the Nb_3Sn experimental data.

9.12 Discussion

Table 9.2 gives the force per unit volume F_p from our computational results, and from various analytical models and experimental sources. It can be seen that for the width $w = 188.7\xi$ used in our 2D computations, our high-field 2D computational data gave a good correspondence in magnitude with 2D experimental data, but our 3D computational data was about a factor of 5 too low. This could possibly be due to an increase in F_p resulting from the fact that while our computational systems are completely regular in arrangement, real polycrystalline superconductors have randomly shaped grains. Another possibility is that the process of optimizing in technological superconductors modifies the grain boundaries to significant H_{c3} effects which also increase J_c, like our computational systems in Fig. 9.12.

A more challenging problem is to solve the discrepancies between theoretical models and the data given by both experiments and TDGL computer simulations. We have found that the original Pruymboom 2D analytic model, based on flux shear along grain boundaries, gives good agreement in magnitude at high magnetic fields with our 2D computational results, and rather remarkably with the 3D experimental results. However, its predicted value of p is much higher than that observed from low-field data both in 3D experiments and in our 3D computational results. We have found no way to reduce this value of p without also reducing the magnitude of F_p at high fields. One possibility is that the Brandt value of $A = 0.044$ is appropriate for shear in a bulk flux-line lattice, but not for that of a single row of fluxons – it is possible that the higher Frenkel prediction of $A = 1/(2\pi)$ would be appropriate instead, which would allow a distortion term to be introduced without reducing the magnitude of F_p in high fields. A second possibility for reducing p is that the original Pruymboom result is indeed correct for 2D, and that in 3D, G_2 is somehow field-dependent, decreasing from ≈ 1 at low fields to ≈ 0.2 near B_{c2}. A third, more unlikely possibility, is that field dependence of C_{66} itself changes in a system where a single row of fluxons shears through a flux-line lattice.

9.13 General Conclusions

We have used computational modelling to study the critical current density in 2D and 3D polycrystalline superconductors. We have investigated the effects of grain size, kappa, grain boundary resistivity and temperature on the system behaviour. In our 2D computation we have found two mechanisms which determine J_c: low-field mechanism dependent on the grain size and kappa and a high-field mechanism independent of these where the pinning force has a Kramer-like field dependence. We also found that the resistivity of the grain boundary interiors does not affect J_c.

In 3D we have found correct dependences for reduced field, kappa, B_{c2} corresponding to those observed experimentally and although the prefactor is only one third to one fifth of that for optimized technological superconductors – although we have some evidence that this may be due to the enhancement of J_c in technological materials by H_{c3} effects, investigated by grain boundary engineering in some of our 2D computations.

We have observed visualizations of the order parameter and the dissipation in both 2D and 3D. These confirm that in 2D flux shear along grain boundaries is the primary mechanism determining J_c, while showing for the first time in 3D that dissipation results from fluxons which are almost entirely confined to the grain boundaries, while the fluxons within the grains are almost straight, and do not move.

Following the visualization we investigated the Pruymboom 2D model of flux shear along grain boundaries. This gave reasonably good agreement with our 2D computational results, but we have still not found a way of adapting it to 3D which gives both the correct magnitude of J_c and the correct reduced-field dependence.

10 Future work

10.1 Improving the computational code

The Fortran codes I have used in the course were originally designed for use on a single processor. Some calculations have been carried out using shared-memory (OpenMP) parallelization: this kind of parallelization is easy to implement starting from a single-processor code, but such parallelization is limited. This suggests that one of the first objectives of further development should be to rewrite the code in a form suitable for distributed-memory (MPI) parallelization. This would achieve two goals:

- **Efficient parallel working on all multiprocessor machines:** It would permit the code to run on multiple processors on machines incapable of shared-memory parallel working (eg Beowulf-style clusters). On machines which can perform shared-memory calculations, distributed-memory working is generally more efficient.
- **Distribution of memory:** It would allow the simulation of systems which are too large to be simulated using the memory available to a single processor. This would allow us to simulate 3D systems larger than currently possible.

Both of these benefits are of great significance for the 'mainline' segment of a 'mainline + branches' style calculation of J_c. For the 'branches' part of the calculation, the second benefit is still important, while the first is less so as parallelization can be achieved even more efficiently by running many branches simultaneously, each occupying a different single processor. The first benefit would also be very useful if investigating a new unfamiliar system, as a small number of branches (such that multiple processors could be devoted to each branch) could be calculated more quickly than with single-processor code.

To improve the efficiency within the 'branch' part of the calculations, a change in the computational algorithm may be the best approach. The 'branch' part of the calculations involves fixing the applied H field at a constant value and allowing the system to equilibrate. Only the final equilibrated state is considered important, not the intermediate states.

Once a properly parallelized 3D code is available, we would extend the work in Chapter 9 to investigate the kappa and grain size dependences of J_c more thoroughly.

10.2 New candidate systems for further study

The granular structure studied in Chapters 8 and 9 is equivalent to materials such as the A15 niobium compounds such as Nb_3Sn and Nb_3Al, and to the Chevrel-phase superconductors. However that still leaves many classes of material uncovered. In addition, the computational system was deliberately simplified by making its granular structure completely regular. In both 2D and 3D this suggests the following classes of system for future study:

- Superconductors with irregular grain structures, which are more similar to real polycrystalline materials.
- A superconductor with *d*- or *p*-wave electron pairing. In these materials the conventionally-used *s*-wave Ginzburg-Landau equations no longer apply – more complex versions must be substituted[111,112].
- Superconductors with grains elongated in the direction of current flow. These correspond to the 'ribbons' seen in NbTi alloy[113] and are expected to lead to a completely different reduced-field dependence. It would be very useful to find the grain aspect ratio at which the flux-shear mechanism gives way to the pin-breaking mechanism.

In the specific case of 3D computation, many more possibilities for future research are opened up:

- 3D Superconductors where grain boundaries are predominantly in the direction of the applied field, but not continuous (eg stacks of prisms with cross-sections in the XY plane, but offset from each other). This will give a better insight as to how three-dimensionality affects flux shear.
- Superconductors where the electron effective mass is anisotropic[114] – this would perhaps simulate the behaviour of MgB_2 or even YBCO.

- Superconductor where c-axis conduction is Josephson-coupled. This is the Lawrence-Doniach[115] model, which describes BSCCO and many other cuprate superconductors.

Appendix - Codes used in computation

A.1 Introduction

All TDGL computation codes are written in FORTRAN 90, and update a file with the extension `.continue` containing a snapshot of the current data each time a line of data is outputted. This allows a job to be restarted at the last good position after any failure in the running of the code.

A.2 2D codes, used in coating and junction tests (Chapters 5 and 7)

The same code is used for both coating and junction computations. For the coating tests in Chapter 5, the junction is deleted by setting its thickness to zero in the input file.

- **Name of executable: TDGL-2C**
- **Source files:**
  - `0declarat.f90` – variables are declared here. It is prefaced with a zero to ensure it is the first file to be compiled.
  - `calcul.f90` – solves the TDGL equations
  - `currents.f90` – calculates supercurrent and normal current
  - `gibbs.f90` – calculates the Gibbs energy (this is used mostly to detect breakdown of stability on code)
  - `inicol.f90` – initial conditions are set up here
  - `magnet.f90` – calculates B from the link variables
  - `main.f90` – 'front end' concerned with input and output
  - `voltage.f90` – calculates voltage across the junction (this output is ignored in no-junction computations)

A.3 2D codes used in polycrystalline J_c computations (Chapters 8 and 9)

The same code is used for both coating and junction computations. For the coating tests in Chapter 5, the junction is deleted by setting its thickness to zero in the input file. This code gives the option of outputting .input and .continue files at specified intervals, which is crucial for running the 'branching' J_c calculations as described in Section 7.4.2.

- **Name of executable: TDGL-2C-8CN**

- **Source files:**
  - `0declarat.f90` – variables are declared here
  - `calcul.f90`
  - `gibbs.f90`
  - `inicol-8n.f90` – initial conditions are set up here. This contains two routines, `inico0` which sets up the very start of the run, and `inicol` which creates the granular microstructure.
  - `magnet.f90` – calculates B from the link variables. The old routines from `current.f90` are now incorporated into `magnet.f90`
  - `main.f90`

Earlier versions of the polycrystalline code were **TDGL-2C-8C** (which gave the data in Section 8.4) and **TDGL-2C-8** (which had the grains separated with single junctions rather than trilayer junctions)

A.4 3D code (Chapter 9)

This code simulates 3D polycrystalline systems, as seen in Section 8.6. To save memory, this code does not allow spatially-varying values of ρ.

- **Name of executable: TDGL-3C-NORHO**
- **Source files:**
  - `0declarat.f90` – variables are declared here. Macros for calculating B are also here, replacing `magnet.f90`
  - `calcul.f90`
  - `gibbs.f90`
  - `inicol.f90` – initial conditions are set up here. This contains two routines, `inico0` which sets up the very start of the run, and `inicol` which creates the granular microstructure.

    `main.f90` – the old routines from `currents.f90` are incorporated into `main.f90`.

References

[1] J. Bardeen, L. N. Cooper, and J. R. Schrieffer, Phys. Rev. **108**, 1175 (1957).

[2] J. G. Bednorz and K. A. Müller, Z. Phys. B **64**, 189 (1986).

[3] Conectus, http://www.conectus.org/xxmarket.html (2001).

[4] W. Schauer and W. Schelb, IEEE Transactions on Magnetics **17**, 374 (1981).

[5] H. K. Onnes, Communications from the Physical Laboratory of the University of Leiden **124C**, 21 (1911).

[6] J. File and R. G. Mills, Phys. Rev. Lett. **10**, 93 (1963).

[7] W. Meissner and R. Ochsenfeld, Naturwissenschaften **21**, 787 (1933).

[8] R. C. Weast, M. J. Astle, and W. H. Beyet, *Handbook of Chemistry and Physics*, 69th Edition ed. (CRC Press, Boca Raton, FL, 1989).

[9] W. Y. Liang, J. Phys. C - Solid State **10**, 11365 (1998).

[10] F. London and H. London, Proc Roy Soc (London) **A149**, 71 (1935).

[11] G. M. Éliashberg, Sov. Phys. JETP **11**, 696 (1960).

[12] J. P. Carbotte, Rev. Mod. Phys. **62**, 1027 (1990).

[13] V. L. Ginzburg and L. D. Landau, Zh. Eksp. Teor. Fiz. **20**, 1064 (1950).

[14] A. A. Abrikosov, Sov. Phys. JETP **5**, 1174 (1957).

[15] W. H. Kleiner, L. M. Roth, and S. H. Autler, Phys. Rev. **133**, A1226 (1964).

[16] L. P. Gor'kov, Sov. Phys. JETP **7**, 505 (1958).

[17] L. P. Gor'kov, Sov. Phys. JETP **9**, 1364 (1959).

[18] L. P. Gor'kov, Sov. Phys. JETP **10**, 998 (1960).

[19] M. Tinkham, *Introduction to Superconductivity*, 2nd ed. (McGraw-Hill Book Co., Singapore, 1996).

[20] R. R. Hake, Phys. Rev. **158**, 356 (1967).

[21] D. P. Hampshire, Physica C **296**, 153 (1998).

[22] P. J. Lee, http://www.asc.wisc.edu/plot/plot.htm (2002).

[23] C. P. Bean, Phys. Rev. Lett. **8**, 250 (1962).

[24] C. P. Bean, Rev. Mod. Phys. **36**, 31 (1964).

[25] D. Dew-Hughes, Philos. Mag. **30**, 293 (1974).

[26] W. A. Fietz and W. W. Webb, Phys. Rev. **178**, 657 (1969).

[27] D. Dew-Hughes, Philos. Mag. B **55**, 459 (1987).

[28] A. M. Campbell and J. E. Evetts, Adv. Phys. **21**, 395 (1972).

[29] E. J. Kramer and H. C. Freyhardt, J. Appl. Phys. **51**, 4930 (1980).

[30] E. J. Kramer, J. Appl. Phys. **44**, 1360 (1973).

[31] R. Labusch, Phys. Stat. Solid. **32**, 439 (1969).

[32] D. P. Hampshire, H. Jones, and E. W. J. Mitchell, IEEE Trans. Magn. **21**, 289 (1985).

[33] E. H. Brandt, Phys. Stat. Solid. B **77**, 551 (1976).

[34] A. I. Larkin and Y. N. Ovchinnikov, J. Low Temp. Phys. **34**, 409 (1979).

[35] T. Y. Hsiang and D. K. Finnemore, Phys. Rev. B **22**, 154 (1980).

[36] L. Dobrosavljevic-Grujic and Z. Radovic, Supercond. Sci. Tech. **6**, 537 (1993).

[37] C. P. Bean and J. D. Livingston, Phys. Rev. Lett. **12**, 14 (1964).

[38] J. Matricon and D. Saint-James, Phys. Lett. **24A**, 241 (1967).

[39] A. D. Hernández and D. Domínguez, Phys. Rev. B **65**, 144529 (2002).

[40] R. Kato, Y. Enomoto, and S. Maekawa, Phys. Rev. B **47**, 8016 (1993).

[41] K. D. Usadel, Phys. Rev. Lett. **25**, 507 (1970).

[42] G. Eilenberger, Z. Phys. **214**, 195 (1968).

[43] Z. G. Ivanov, M. Y. Kuprianov, K. K. Likharev, S. V. Meriakri, and O. V. Snigirev, Sov. J. Low Temp. Phys. **7**, 274 (1981).

[44] K. R. Biagi, V. G. Kogan, and J. R. Clem, Phys. Rev. B **32**, 7165 (1985).

[45] Z. Radovic, M. Ledvij, and L. Dobrosavljevic-Grujic, Phys. Rev. B **43**, 8613 (1991).

[46] J. B. Ketterson and S. N. Song, *Superconductivity* (Cambridge University Press, 1999).

[47] A. Schmid, Physik der Kondensierte Materie **5**, 302 (1966).

[48] C.-R. Hu and R. S. Thompson, Phys. Rev. B **6**, 110 (1972).

[49] L. P. Gor'kov and G. M. Eliashberg, Sov. Phys. JETP **27**, 328 (1968).

[50] R. Kato, Y. Enomoto, and S. Maekawa, Phys. Rev. B **44**, 6916 (1991).

[51] H. Frahm, S. Ullah, and A. T. Dorsey, Phys. Rev. Lett. **66**, 3067 (1991).

[52] M. Machida and H. Kaburaki, Phys. Rev. Lett. **71**, 3206 (1993).

[53] M. Machida and H. Kaburaki, Phys. Rev. B **50**, 1286 (1994).

[54] K. J. M. Moriarty, E. Myers, and C. Rebbi, Computer Physics Communications **54**, 272 (1989).

[55] T. Winiecki, PhD Thesis, University of Durham, 2001.

[56] W. H. Press, B. P. Flannery, S. A. Teukolsky, and W. T. Vetterling, *Numerical Recipes in Fortran: The Art of Scientific Computing*, 2nd edition ed. (Cambridge University Press2nd edition, 1992).

[57] J. Crank and P. Nicolson, Proceedings of the Cambridge Philosophical Society **43**, 50 (1946).

[58] W. F. Ames, *Numerical Methods for Partial Differential Equations* (Academic Press Inc., San Diego, 1992).

[59] T. Winiecki and C. S. Adams, J. Comput. Phys. **179**, 127 (2002).

[60] E. H. Brandt, Phys. Rev. B **58**, 6506 (1998).

[61] E. H. Brandt, Phys. Rev. B **60**, 11939 (1999).

[62] T. Winiecki and C. S. Adams, Phys. Rev. B **65**, 104517 (2001).

[63] D. Y. Vodolazov, Phys. Rev. B **62**, 8691 (2000).

[64] M. Machida and H. Kaburaki, Phys. Rev. Lett. **74**, 1434 (1995).

[65] M. Machida and H. Kaburaki, Phys. Rev. Lett. **75**, 3178 (1995).

[66] R. Kato, Y. Enomoto, and S. Maekawa, Physica C **227**, 387 (1994).

[67] J. P. Hurault, Phys. Lett. **20**, 587 (1966).

[68] P. G. De Gennes, Solid State Commun. **3**, 127 (1965).

[69] G. Carty, M. Machida, and D. P. Hampshire, Phys. Rev. B **71**, 144507 (2005).

[70] J. E. Evetts, Phys. Rev. B **2**, 95 (1970).

[71] E. H. Brandt, Rep. Prog. Phys. **58**, 1465 (1995).

[72] G. Blatter, M. V. Feigelman, V. B. Geshkenbein, A. I. Larkin, and V. M. Vinokur, Rev. Mod. Phys. **66**, 1125 (1994).

[73] Y. Iijima and K. Matsumoto, Supercond. Sci. Tech. **13**, 68 (2000).

[74] E. H. Brandt, Phys. Rev. Lett. **78**, 2208 (1997).

[75] L. Kramer, Z. Phys. **259**, 333 (1973).

[76] A. M. Campbell, J. E. Evetts, and D. Dew-Hughes, Philos. Mag. **18**, 313 (1968).

[77] G. R. Love, Philos. Mag. **21**, 1003 (1970).

[78] M. Konczykowski, L. I. Burlachkov, Y. Yeshurun, and F. Holtzberg, Phys. Rev. B **43**, 13707 (1991).

[79] P. K. Mishra, G. Ravikumar, V. C. Sahni, M. R. Koblischka, and A. K. Grover, Physica C **269**, 71 (1996).

[80] M. Pissas, E. Moraitakis, D. Stamopoulos, G. Papavassiliou, V. Psycharis, and S. Koutandos, Journal of Superconductivity **14**, 615 (2001).

[81] H. A. Ullmaier and W. F. Gauster, J. Appl. Phys. **37**, 4519 (1966).

[82] G. P. van der Mey, P. H. Kes, and D. De Klerk, Physica B **95**, 369 (1978).

[83] E. Kreyszig, *Advanced Engineering Mathematics*, Seventh ed. (Wiley, New York, 1993).

[84] J. R. Clem, J. Low Temp. Phys. **18**, 427 (1975).

[85] P. G. De Gennes, *Superconductivity in Metals and Alloys* (Addison Wesley Publishing Company, Redwood City, California, 1989).

[86] M. Abramovitz and I. Stegun, *Handbook of Mathematical Functions* (New York : Dover, 1970).

[87] S. Senoussi, M. Ousséna, G. Collin, and I. A. Campbell, Phys. Rev. B **37**, 9792 (1988).

[88] R. A. Ferrell and R. E. Prange, Phys. Rev. Lett. **10**, 479 (1963).

[89] C. P. Poole, H. A. Farach, and R. J. Creswick, *Superconductivity* (Academic Press Inc, San Diego, California, 1995).

[90] R. Fehrenbacher, V. B. Geshkenbein, and G. Blatter, Phys. Rev. B **45**, 5450 (1992).

[91] C. S. Owen and D. J. Scalapino, Phys. Rev. **164**, 538 (1967).

[92] A. V. Nikulov and Y. D. Remisov, Supercond. Sci. Tech. **3**, 312 (1991).

[93] J. W. Ekin, Cryogenics **20**, 611 (1980).

[94] D. M. J. Taylor, S. A. Keys, and D. P. Hampshire, Cryogenics **42**, 109 (2002).

[95] B. Seeber, in *Handbook of Applied Superconductivity*, edited by B. Seeber (IOP Publishing, Bristol, 1998), p. 307.

[96] S. A. Keys and D. P. Hampshire, in *Handbook of Superconducting Materials*; *Vol. 2*, edited by D. Cardwell and D. Ginley (IOP Publishing, Bristol, 2003), p. 1297.

[97] S. A. Keys and D. P. Hampshire, Supercond. Sci. Tech. **16**, 1097 (2003).

[98] S. A. Keys, N. Koizumi, and D. P. Hampshire, Supercond. Sci. Tech. **15**, 991 (2002).

[99] L. A. Bonney, T. C. Willis, and D. C. Larbalestier, J. Appl. Phys. **77**, 6377 (1995).

[100] E. J. Kramer, J. Elec. Mat. **4**, 839 (1975).

[101] E. Helfand and N. R. Werthamer, Phys. Rev. **147**, 288 (1966).

[102] D. M. J. Taylor and D. P. Hampshire, Supercond. Sci. Tech. **18**, S241 (2005).

[103] H. J. Niu and D. P. Hampshire, Phys. Rev. B **69**, 174503 (2004).

[104] N. Sakamoto, T. Akune, Y. Matsumoto, H. R. Khan, and K. Lüders, Physica C **426-431**, 726 (2005).

[105] A. Pruymboom, P. H. Kes, E. van der Drift, and S. Radelaar, Phys. Rev. Lett. **60**, 1430 (1988).

[106] A. Pruymboom, P. Kes, E. Drift, and S. Radelaar, Appl. Phys. Lett. **52**, 662 (1988).

[107] E. H. Brandt, Phys. Rev. Lett. **50**, 1599 (1983).

[108] E. H. Brandt, J. Low Temp. Phys. **24**, 427 (1976).

[109] R. Wördenweber, P. H. Kes, and C. C. Tsuei, Phys. Rev. B **33**, 3172 (1986).

[110] G. Blatter, V. B. Geshkenbein, and A. I. Larkin, Phys. Rev. Lett. **68**, 875 (1992).

[111] Y. Ren, J. Xu, and C. S. Ting, Phys. Rev. Lett. **74**, 3680 (1995).

[112] J. X. Zhu, C. S. Ting, J. L. Shen, and Z. D. Wang, Phys. Rev. B **56**, 14093 (1997).

[113] L. D. Cooley, P. Lee, and D. C. Larbalestier, in *Handbook of Superconducting Materials*; *Vol. 1*, edited by D. Cardwell and D. Ginley (IOP Publishing, Bristol, 2002), p. 603.

[114] G. R. Tilley, P. Phys. Soc. Lond. **86**, 289 (1965).

[115] W. E. Lawrence and S. Doniach, in *Theory of layer structure superconductors*, Kyoto, 1971 (Academic press of Japan), p. 361.